APPLIED NEUROIMAGING - EDITOR'S PICK 2022

EDITED BY: Jan Kassubek
PUBLISHED IN: Frontiers in Neurology

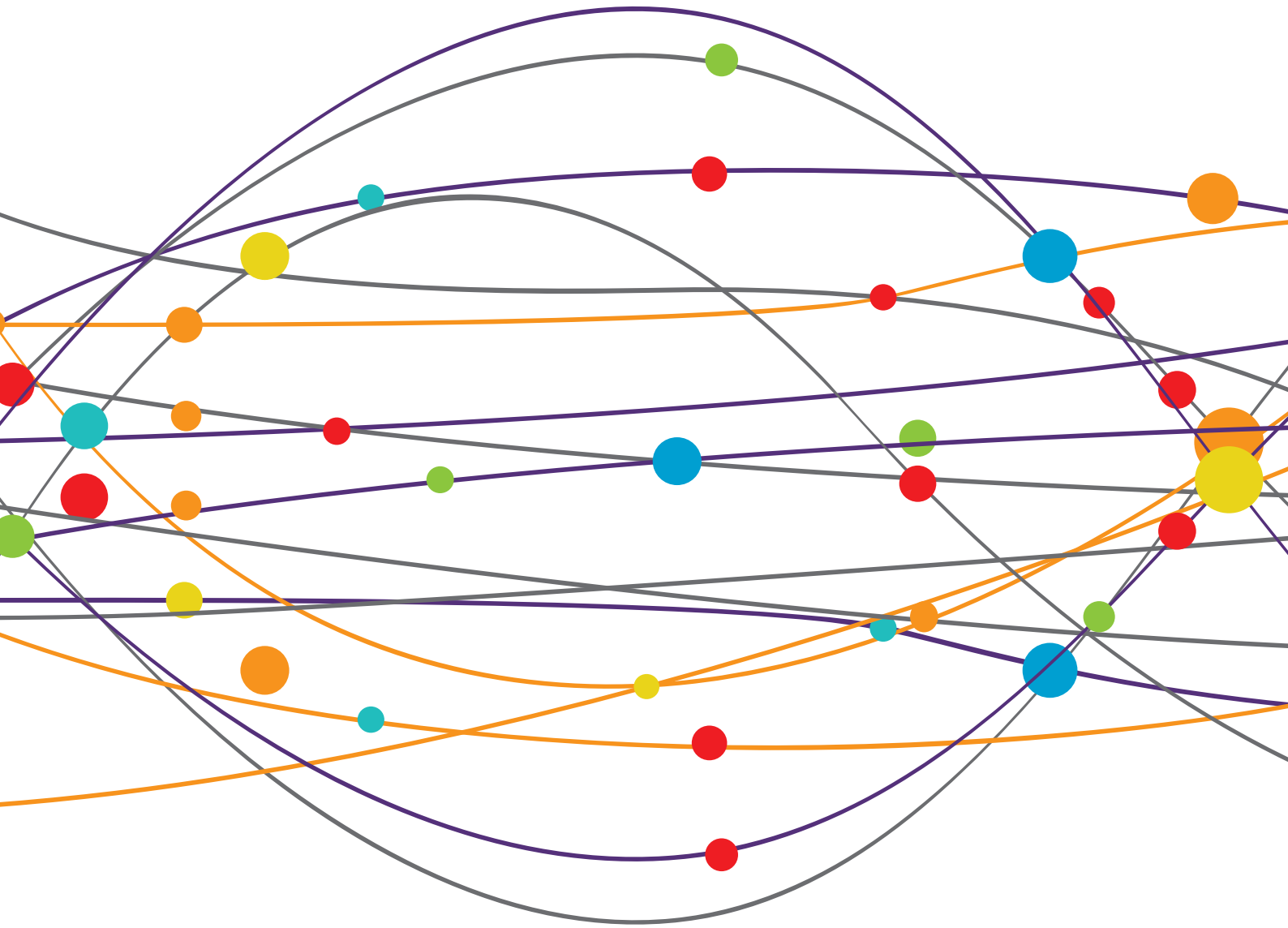

frontiers Research Topics

frontiers

ISSN 1664-8714
ISBN 978-2-88976-705-2
DOI 10.3389/978-2-88976-705-2

About Frontiers

Frontiers is more than just an open-access publisher of scholarly articles: it is a pioneering approach to the world of academia, radically improving the way scholarly research is managed. The grand vision of Frontiers is a world where all people have an equal opportunity to seek, share and generate knowledge. Frontiers provides immediate and permanent online open access to all its publications, but this alone is not enough to realize our grand goals.

Frontiers Journal Series

The Frontiers Journal Series is a multi-tier and interdisciplinary set of open-access, online journals, promising a paradigm shift from the current review, selection and dissemination processes in academic publishing. All Frontiers journals are driven by researchers for researchers; therefore, they constitute a service to the scholarly community. At the same time, the Frontiers Journal Series operates on a revolutionary invention, the tiered publishing system, initially addressing specific communities of scholars, and gradually climbing up to broader public understanding, thus serving the interests of the lay society, too.

Dedication to Quality

Each Frontiers article is a landmark of the highest quality, thanks to genuinely collaborative interactions between authors and review editors, who include some of the world's best academicians. Research must be certified by peers before entering a stream of knowledge that may eventually reach the public - and shape society; therefore, Frontiers only applies the most rigorous and unbiased reviews.
Frontiers revolutionizes research publishing by freely delivering the most outstanding research, evaluated with no bias from both the academic and social point of view. By applying the most advanced information technologies, Frontiers is catapulting scholarly publishing into a new generation.

What are Frontiers Research Topics?

Frontiers Research Topics are very popular trademarks of the Frontiers Journals Series: they are collections of at least ten articles, all centered on a particular subject. With their unique mix of varied contributions from Original Research to Review Articles, Frontiers Research Topics unify the most influential researchers, the latest key findings and historical advances in a hot research area! Find out more on how to host your own Frontiers Research Topic or contribute to one as an author by contacting the Frontiers Editorial Office: frontiersin.org/about/contact

APPLIED NEUROIMAGING - EDITOR'S PICK 2022

Topic Editor:
Jan Kassubek, University of Ulm, Germany

Citation: Kassubek, J., ed. (2022). Applied Neuroimaging - Editor's Pick 2022. Lausanne: Frontiers Media SA. doi: 10.3389/978-2-88976-705-2

Table of Contents

frontiers in Neurology

ORIGINAL RESEARCH
published: 13 January 2020
doi: 10.3389/fneur.2019.01382

MR Elastography-Based Assessment of Matrix Remodeling at Lesion Sites Associated With Clinical Severity in a Model of Multiple Sclerosis

Shuangqing Wang[1,2†], *Jason M. Millward*[1,3†], *Laura Hanke-Vela*[1†], *Bimala Malla*[1], *Kjara Pilch*[1], *Ana Gil-Infante*[1], *Sonia Waiczies*[3], *Susanne Mueller*[4,5], *Philipp Boehm-Sturm*[4,5], *Jing Guo*[6], *Ingolf Sack*[6] and *Carmen Infante-Duarte*[1*]

[1] Charité – Universitätsmedizin Berlin, Corporate Member of Freie Universität Berlin, Humboldt-Universität zu Berlin, and Berlin Institute of Health, Institute for Medical Immunology, Berlin, Germany, [2] Department of Neurology, Shenzhen University General Hospital, Shenzhen University Clinical Medical Academy, Shenzhen, China, [3] Berlin Ultrahigh Field Facility, Max Delbrück Center for Molecular Medicine, Berlin, Germany, [4] Department of Experimental Neurology and Center for Stroke Research, Charité – Universitätsmedizin Berlin, Corporate Member of Freie Universität Berlin, Humboldt-Universität zu Berlin, and Berlin Institute of Health, Berlin, Germany, [5] NeuroCure Cluster of Excellence and Charité Core Facility 7T Experimental MRIs, Charité – Universitätsmedizin Berlin, Corporate Member of Freie Universität Berlin, Humboldt-Universität zu Berlin, and Berlin Institute of Health, Berlin, Germany, [6] Department of Radiology, Charité - Universitätsmedizin Berlin, Corporate Member of Freie Universität Berlin, Humboldt-Universität zu Berlin, and Berlin Institute of Health, Berlin, Germany

Magnetic resonance imaging (MRI) with gadolinium based contrast agents (GBCA) is routinely used in the clinic to visualize lesions in multiple sclerosis (MS). Although GBCA reveal endothelial permeability, they fail to expose other aspects of lesion formation such as the magnitude of inflammation or tissue changes occurring at sites of blood-brain barrier (BBB) disruption. Moreover, evidence pointing to potential side effects of GBCA has been increasing. Thus, there is an urgent need to develop GBCA-independent imaging tools to monitor pathology in MS. Using MR-elastography (MRE), we previously demonstrated in both MS and the animal model experimental autoimmune encephalomyelitis (EAE) that inflammation was associated with a reduction of brain stiffness. Now, using the relapsing-remitting EAE model, we show that the cerebellum—a region with predominant inflammation in this model—is especially prone to loss of stiffness. We also demonstrate that, contrary to GBCA-MRI, reduction of brain stiffness correlates with clinical disability and is associated with enhanced expression of the extracellular matrix protein fibronectin (FN). Further, we show that FN is largely expressed by activated astrocytes at acute lesions, and reflects the magnitude of tissue remodeling at sites of BBB breakdown. Therefore, MRE could emerge as a safe tool suitable to monitor disease activity in MS.

Keywords: magnetic resonance elastography, experimental autoimmune encephalomyelitis, extracellular matrix, fibronectin, gadolinium-based contrast agent, multiple sclerosis

OPEN ACCESS

Edited by:
Itamar Ronen,
Leiden University, Netherlands

Reviewed by:
Mark Wagshul,
Albert Einstein College of Medicine, United States
Shadi Othman,
University of the Pacific, United States

****Correspondence:***
Carmen Infante-Duarte
carmen.infante@charite.de

[†] These authors have contributed equally to this work

Specialty section:
This article was submitted to Applied Neuroimaging, a section of the journal Frontiers in Neurology

Received: *04 March 2019*
Accepted: *16 December 2019*
Published: *13 January 2020*

Citation:
Wang S, Millward JM, Hanke-Vela L, Malla B, Pilch K, Gil-Infante A, Waiczies S, Mueller S, Boehm-Sturm P, Guo J, Sack I and Infante-Duarte C (2020) MR Elastography-Based Assessment of Matrix Remodeling at Lesion Sites Associated With Clinical Severity in a Model of Multiple Sclerosis. Front. Neurol. 10:1382. doi: 10.3389/fneur.2019.01382

INTRODUCTION

Multiple sclerosis (MS) is a chronic inflammatory disease of the central nervous system (CNS) that represents the most common cause of non-traumatic disability in young adults. MS is considered to be an autoimmune disease in which self-reactive immune cells gain access to the CNS leading to myelin destruction and neuronal damage and the subsequent formation of multifocal lesions (1). These pathological hallmarks are also characteristic for experimental autoimmune encephalomyelitis (EAE), which is the prototypical model for MS (2).

In MS, clinical relapses correlate with the development of perivenular inflammatory lesions inside the CNS. Lesion monitoring is commonly required to make an accurate diagnosis and to monitor disease progression and response to treatment. Typically, new lesions are visualized using gadolinium-based contrast agents (GBCA) on MRI. During active inflammatory processes, GBCA cross the leaking blood-brain barrier (BBB), enter the CNS parenchyma, and alter the magnetic properties of the tissue, reducing the T1 relaxation time. Generally, the more severe the inflammatory activity, the greater the burden of GBCA-enhancement on post-contrast T1-weighted scans (3). However, GBCA-MRI has limitations due to safety reasons and lack of sensitivity. We previously showed in EAE that certain lesions may remain undetectable by GBCA (4, 5). Furthermore, there are emerging concerns that GBCA may deposit in the tissue after repeated applications (6).

Magnetic resonance elastography (MRE) could represent a promising alternative to the use of GBCA. MRE provides information about the mechanical properties of tissues (7, 8) by analyzing their response to oscillatory shear stress (9). Using MRE, we reported on reduced brain viscoelasticity in patients with clinically isolated syndrome (10) as well as patients with established relapsing-remitting (11) and chronic-progressive (12) MS. Brain tissue softening was also observed in patients with a neuromyelitis optical spectrum disorder (NMOSD) (13). However, the mechanisms underlying brain softening in patients remain elusive. Our aim is therefore to dissect these mechanisms using animal models of neuroinflammation. Application of MRE in the cuprizone mouse model of demyelination demonstrated that brain softening was associated with demyelination (14). The observed reduction of brain viscoelasticity in this model was not related to tissue inflammation. However, in the EAE model of MS, we previously showed that inflammation was associated with reduced brain elasticity on MRE (15, 16).

In the present study, we evaluated the capacity of MRE to reveal acute inflammatory activity and disease severity, comparing sagittal MRE with conventional GBCA-MRI in the relapsing-remitting EAE model. Furthermore, we aimed to clarify the nature of the tissue alterations at lesion sites by examining changes to the extracellular matrix (ECM). For this we concentrated attention on the proteoglycan fibronectin (FN), as it has been shown to accumulate within perivascular lesions, and correlate with the degree of inflammation (17, 18). We thereby endeavor to improve our understanding of pathological changes detected by MRE but not by conventional GBCA-MRI.

METHODS

Animals

All procedures were approved by the Animal Welfare Department of the State Office of Health and Social Affairs Berlin (LAGeSo), in accordance with national and international guidelines to minimize discomfort to animals (86/609/EEC). Experimental SJL mice (Charles River Laboratories, Sulzfeld, Germany) were housed in the central animal facility of the Charité—Universitätsmedizin Berlin. All animals were kept in a temperature- and humidity-controlled colony room and maintained on a light/dark cycle of 12/12 h with *ad libitum* access to food and water. Over multiple experiments, mice were divided into two groups, EAE ($n = 25$) and non-manipulated healthy control ($n = 7$).

Experimental Autoimmune Encephalomyelitis (EAE)

To induce EAE (2, 19), SJL mice were immunized subcutaneously with 250 μg proteolipid protein (PLP) peptide 139-151 (purity 95%; Pepceuticals, Leicester, UK) and 800 μg *Mycobacterium tuberculosis* H37Ra (Difco, Franklin Lakes, NJ, USA) emulsified in 100 μl Complete Freund's adjuvant (CFA) and 100 μl phosphate-buffered saline (PBS). Pertussis toxin (250 ng per mouse; List, Biological Laboratories, Campbell, CA, USA) was injected intraperitoneally on the day of immunization (day 0) and again 2 days later (day 2). After immunization, mice were monitored daily for clinical signs and scored as follows: 0, no disease; 0.5, tail paresis; 1, tail paralysis; 1.5, tail paralysis and righting reflex weakness; 2, hind limb paralysis (one limb); 2.5 Hind limb paralisis and paresis of the other hind limb; 3, paraplegia; 4, paraplegia with forelimb weakness or paralysis; 4.5, moribund with tetraparesis or tetraplegia; and 5, dead.

In vivo Scans

In vivo MRE and MRI scans were performed as described previously (16) on a 7 T Bruker Pharmascan 70/16 rodent MR scanner (Bruker Biospin, Ettlingen, Germany), running Paravision 5.1 software, with a 20 mm RF quadrature volume head coil (RAPID Biomedical GmbH, Rimpar, Germany). Mice were anesthetized with 1.5–2.0% isoflurane in 30% O_2 and 70% N_2O administered via face mask, with continuous respiration monitoring using a pressure-sensitive pad placed on the thorax (Small Animal Instruments Inc., Stony Brook, NY, USA). The animals were placed on a bed with circulating heated water to maintain constant body temperature. In those animals investigated by both MRE and MRI, the MRE measurements were acquired first, followed by GBCA-MRI after 24 h.

Magnetic Resonance Elastography (MRE)

The MRE images were acquired in one 2 mm midsagittal slice as described previously (16). Mechanical vibration was generated by an air-cooled electromagnetic Lorentz coil in the fringe field of the MRI scanner. Vibrations were initiated by a trigger pulse from the control unit of the MRI scanner, and transferred to the animal through a carbon fiber piston, which was connected to the bite bar transducer. The transducer was gimbaled through

a rubber bearing and retaining bracket at the temperature-controlled mouse bed. A plastic disk held up the entire setup in the center of the magnet bore (16).

The timing of the vibration was defined and recorded by a fast low-angle shot (FLASH) sequence especially made for MRE measurement. The direction of the motion sensitizing gradient (MSG), with a strength of 285 mT/m, a frequency of 900 Hz, and 9 periods, was maintained parallel to the principal axis of the magnetic field (maximum amplitude of the mechanical driver was 10 microns). To compensate for the static phase contributions, phase difference images were calculated from two images differing in the sign of the MSG. Frequency amplitude and the number of cycles were controlled by a waveform generator connected via an audio amplifier to the driving coil. Additional scan parameters were as follows: TE = 14.3 ms; TR array = 166.0 ms; slice thickness = 2.0 mm; matrix = 128, FOV = 25 mm; two averages; eight dynamic scans over a vibration period and an acquisition time of 12 min.

MRE Data Analysis

Complex wave images corresponding to the harmonic drive frequency were extracted by temporal Fourier transformation of the unwrapped phase-difference images. To reduce noise, in addition to the Butterworth band pass filter, a spatiotemporal directional filter was applied to the wave images (20). The spatiotemporal filter filtered waves that were propagating from bottom-to-top in the sagittal slice. A 2D-Helmholtz inversion was performed to the filtered data, yielding the complex shear modulus G* and the magnitude modulus $|G^*| = \text{abs}(G^*)$. The calculated spatially averaged G*-values were represented by the real part of the complex shear modulus $G' = \text{Re}(G^*)$, known as the storage modulus that represents tissue elasticity, and the imaginary part $G'' = \text{Im}(G^*)$, which is the loss modulus representing tissue viscosity. The magnitude, storage and loss moduli were expressed in pascals (Pa). The loss factor calculated as the phase angle phi = arctan (G″/ G′) represents the fluidity of the tissue, which is the degree of viscosity relative to elasticity and is interpreted as being sensitive to the architecture of viscoelastic networks in biological tissues (21). In addition to calculating values for the storage and loss moduli for the entire sagittal slice, the brain was separated into two regions of interest divided at the junction between the cerebrum and the cerebellum.

Magnetic Resonance Imaging (MRI)

T1 maps were generated using a saturation recovery RAREVTR method, in which the repetition time (TR) was varied to acquire a series of axial T1 weighted images, from which the T1 map was produced. Scan parameters were as follows: TE = 8.3 ms; TR array = 230, 460, 1061, 1485, 2080, 3080 and 7500 ms; flip angle = 90°/180°; RARE factor = 2; slice thickness = 1.0 mm; matrix = 128, FOV = 1.92 cm; NA = 1, 10 slices, scan time = 17 min 44 sec. After acquiring the pre-contrast T1 map, the animals were administered 0.2 mmol/kg gadopentate dimeglumine (Gd-DTPA, Magnevist, Bayer Vital GmbH, Leverkusen, Germany) by intravenous injection. After 5 min, the post-contrast T1 maps were acquired using the same parameters as above. Data acquisition was done with ParaVision 5.1 (Bruker Biospin, Germany). The raw data files were exported as NIFTI image files, and analyzed in ImageJ v. 1.51 (NIH, open source). A region of interest (ROI) defining the brain was manually traced for all 10 slices, and the mean T1 value of each ROI calculated. The mean T1 from all 10 slices was determined for each animal, and the post-contrast mean was subtracted from the pre-contrast mean, to yield the difference—delta T1. The delta T1 was used for the statistical analysis.

In addition, T1-weigthed images were acquired as described previously (22). As a complimentary method, we also calculated the T1 signal intensity change directly from the T1-weighted images. An ROI defining the brain was manually traced for 20 slices and the mean signal intensity (SI) value of each ROI was calculated. The mean SI from all 20 slices was determined for each animal in both pre- and post-contrast, calculated as: signal intensity change (SI%) = [(SI post-contrast—SI pre-contrast)/SI pre-contrast] * 100.

Tissue Processing

Mice were sacrificed 1 day after MRE and MRI measurements. Animals were deeply anesthetized with ketamine/xylazine, then transcardially perfused with PBS. Twenty-five brains were extracted and 19 of them were cut sagittally in two symmetrical halves. Half of the brain was postfixed in 4% paraformaldehyde (PFA) overnight at 4°C and then PBS washed, followed by 30% sucrose in PBS, soaking until the tissue sunk to the bottom. Meanwhile, the other half of the brain was reserved for RNA extraction. For histological analysis, brain tissue was embedded in O.C.T., frozen in methylbutane with dry ice, and stored at −80°C. For analysis, frozen tissues were cut into 12 μm coronal or sagittal cryosections and stored at 4°C.

Histology and Immunofluorescence

For Immunostaining, brain sections were permeabilized and blocked with PBS containing 10% normal goat serum, 10% bovine serum albumin and 0.3% Triton TM X-100 for 1 h at room temperature. Sections were incubated overnight at 4°C with the primary antibodies diluted in PBS. Primary antibodies included: rabbit anti-fibronectin, 1:200 (Millipore ab2033); mouse anti-EIIIA-fibronectin, 1:200 (Abcam ab6328); chicken anti-GFAP, 1:500 (Abcam ab4674). For double labeling immunostaining, primary antibodies were incubated sequentially. For staining with the mouse anti-EIIIA-fibronectin (IST9), we used a mouse on mouse (M.O.M.) kit from Vector Laboratories. After staining with primary antibodies, sections were washed with PBS and incubated with Alexa Fluor (488 or 647, 594)-conjugated secondary antibodies (1:400) at room temperature for 2 h, followed by 4′,6-diamidino-2-phenylindole (DAPI) to visualize cell nuclei. Sections were imaged using a Zeiss Axio Observer fluorescence microscope or a laser-scanned confocal microscope (LSM 710, Carl Zeiss, Jena, Germany).

Quantitative Reverse-Transcription PCR

The brain tissue for PCR was divided into two portions, the anterior (cerebral) and posterior (cerebellar) region, according to the MRE scanning regions. Total RNA was extracted from the tissue by using the Trizol method. The

RNA was reverse transcribed, and quantitative PCR (qPCR) carried out as described previously, using an ABI Prism 7000 SequenceDetection System (Applied Biosystems, Darmstadt, Germany) (16). Primers and probes were from Eurofins MWG Operon (Ebersberg, Germany), and the sequences used were as followed: Fibronectin, forward *5′-ATCATTTCATGCCAAC CAGTT-3′*, reverse *5′-TCGCACTGGTAGAAGTTCCA-3′*, probe *5′FAM-CCGACGAAGAGCCCTTACAGTTCCA-3′*TAMRA. Neurocan, forward *5′-GGTGTGCGCACTGTGTA-3′*, reverse *5′-CATGTTGTGCTGTATGGTGATG-3′*, probe *5′FAM-TTCGACGCCTACTGCTTCCGAG-3′*TAMRA. Brevican, forward *5′-AGAACCGCTTCAATGTCTACTG-3′*, reverse *5′-ACTGTGACAATGGCCTCAAG-3′*, probe *5′FAM-ACTCTGCC CATCCCTCTGCTTC-3′*TAMRA. Glypican5, forward *5′-GAGA CACTTGCCAACAGAAGA-3′*, reverse *5′-GGGCAGCCAATT CATTAACAC-3′*, probe *5′FAM-CATGGGTCCTTCTATGGTGG CCTG-3′*TAMRA. 18s, served as the endogenous reference, forward *5'-TTCGAACGTCTGCCCTATCAA-3′*, reverse *5′-TCCC CGTCACCCATGGT-3′*, probe *5′FAM- TGATGTTTATTGACAA CACGCTTTACTTTATACCTGAAGA-3′*TAMRA. We used the $2^{-\Delta\Delta C_T}$ method to analyze the results.

Statistical Analysis

Data were analyzed by unpaired two-tailed *t*-test, paired two-tailed *t*-test or repeated-measures analysis of variance (ANOVA), as appropriate. The non-parametric Spearman correlation was used to assess correlation between MRE parameters and EAE score. Pearson correlation was used to assess correlation between imaging parameters, and between MRE parameters and the PCR or immunostaining quantification data. Analysis was done using GraphPad Prism v.5.01. (GraphPad software, La Jolla, CA, USA). $^{*}p < 0.05$, $^{**}p < 0.01$, $^{***}p < 0.001$.

RESULTS

During Relapsing-Remitting EAE, Brain Viscoelasticity Is Altered Particularly in the Cerebellum

To assess the sensitivity of the sagittal MRE protocols in the SJL EAE model (16), we monitored mechanical brain changes in SJL mice immunized with PLP. Mice developed a typical relapsing-remitting disease course, showing first clinical signs by 9–10 days after immunization, reaching peak disease 3–4 days later (day 12-14 p.i.; **Figure 1A**). MRE measurements were performed at day 14 post-immunization, when clinical signs of disease were well-established and coinciding with the expected disease peak. MRE data were acquired in one 2 mm midsagittal slice and confirmed our previous MRE data in relapsing-remitting EAE acquired in coronal slices (15). We observed that at day 14–15 p.i. the overall viscoelasticity of the tissue (|G*| magnitude modulus) as well as the storage modulus G' (elasticity) and the loss modulus G" (viscosity) were significantly diminished in EAE mice compared to controls (**Figures 1B–D**). No alteration of the phase angle (loss factor) was observed (**Figure 1E**), indicating that the overall architecture of the brain tissue was not affected by acute inflammation.

We previously showed in C57/BL6 mice that different brain regions also show distinct viscoelastic properties (16). However, it remained unclear whether this was also applicable in the

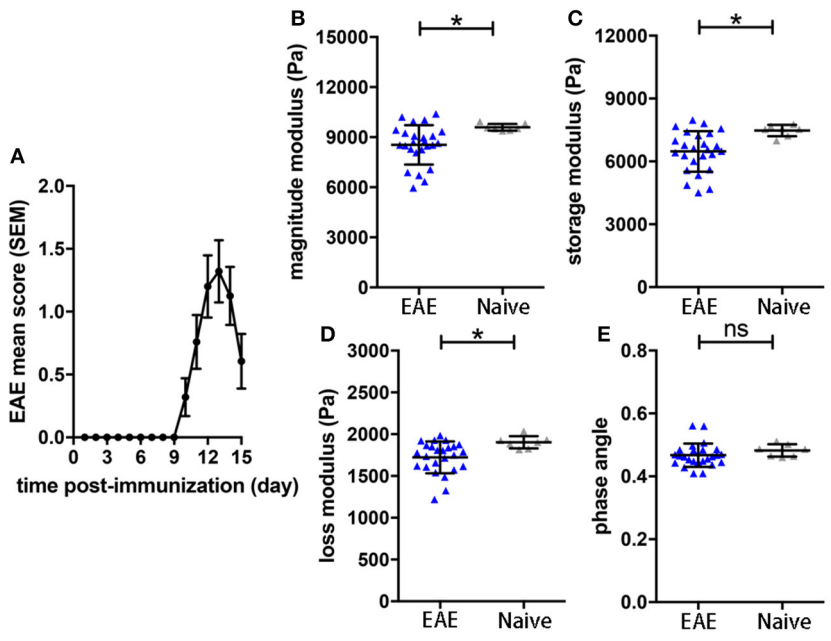

FIGURE 1 | Brain viscoelasticity in EAE and control mice. **(A)** EAE clinical course of SJL mice immunized with PLP. EAE mice reached the maximal score at day 12–14 after immunization, mean with SEM. At days of expected peak disease, EAE mice showed significant reductions of **(B)** magnitude modulus, **(C)** storage and **(D)** loss modulus, compared to healthy controls. **(E)** No alteration of the phase angle was observed in EAE mice. Unpaired two-tailed *t*-test, $^{*}p < 0.05$, mean ± SD.

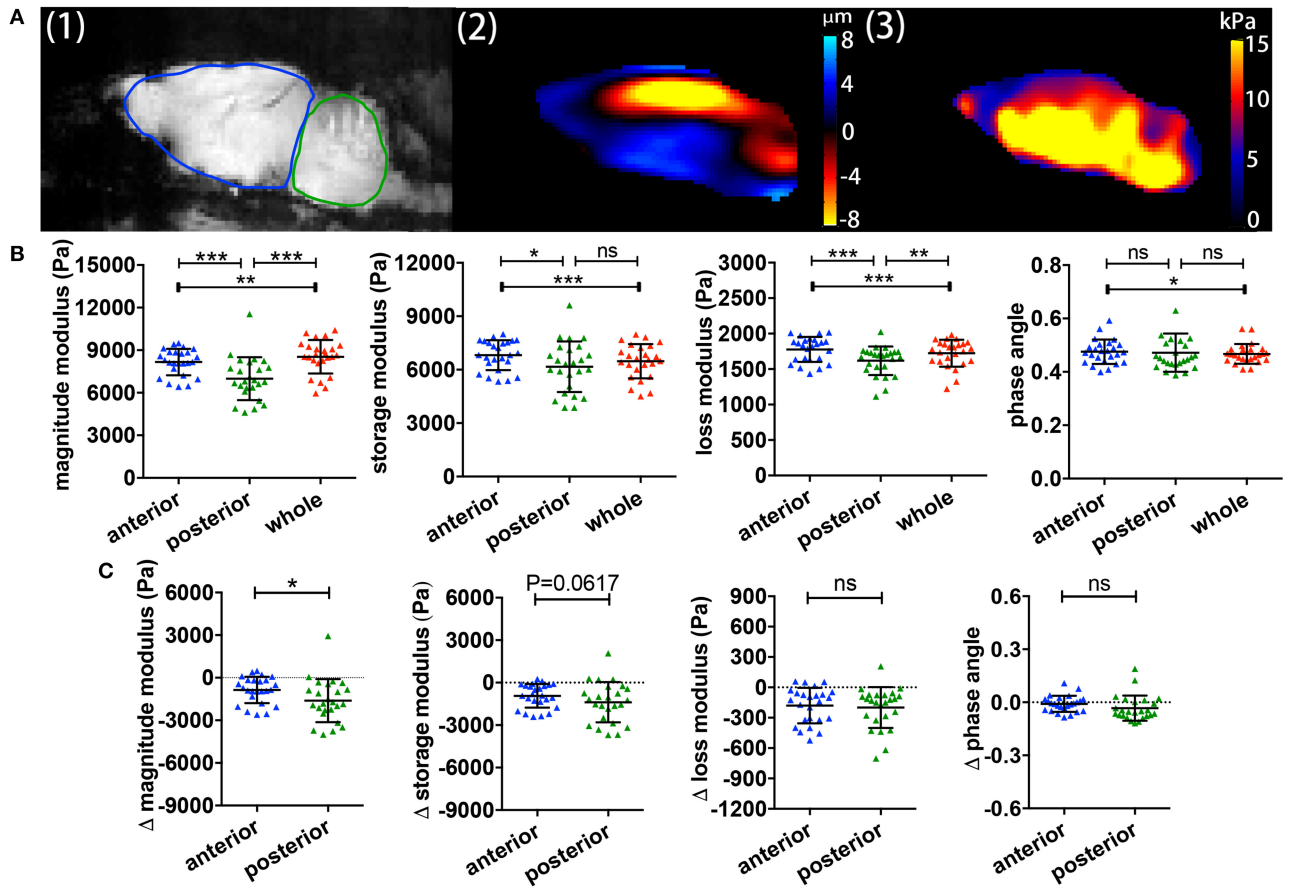

FIGURE 2 | Comparisons of regional brain viscoelasticity. **(A)** Sagittal views of an EAE mouse brain showing a representative magnitude image with definitions of the cerebrum/anterior (red) and cerebellum/posterior (blue) regions (1), a wave (deflection) image (2) and a map of the complex modulus superimposed on the magnitude image (3). **(B)** Comparison of the viscoelastic properties of the posterior/cerebellar region with the anterior region and the whole brain during inflammation. Repeated measures ANOVA, $^{*}p < 0.05$, $^{**}p < 0.01$, $^{***}p < 0.001$. **(C)** Delta MRE values at the time of the expected disease peak normalized to the values of age- and gender-matched healthy animals. The magnitude modulus—i.e., the tissue rigidity—is particularly diminished in the posterior region (cerebellum) compared to the anterior region (cerebrum). Data from five independent experiments $n = 25$. Paired two-tailed t-test, $^{*}p < 0.05$, mean ± SD.

SJL EAE model, and whether different brain regions may also differ in the MRE values during relapsing-remitting EAE. A representative example of a midsagittal slice from a SJL EAE mouse is shown in **Figure 2A**, illustrating the magnitude image A (1), the wave deflection image A (2) and the magnitude of the complex shear modulus $|G^*|$ A (3). The acquisition of MRE data in midsagittal slices permits the separate analysis of the anterior region (cerebrum) and the posterior brain region (cerebellum) (ROIs in **Figure 2A**-1). The results show that during EAE, the cerebellum shows a striking reduction of the magnitude, storage and loss moduli, when compared with the cerebrum or the whole brain (**Figure 2B**). The phase angle remained stable in the investigated regions. Furthermore, to estimate the effect of disease in these two different brain regions, we calculated the viscoelastic changes of the EAE tissue in relation to sex and age matched healthy controls. **Figure 2C** demonstrates that viscoelastic values at the time of the expected peak of EAE were decreased in both regions when normalized to healthy mice, as indicated by mean difference $\Delta|G^*| < 0$, indicating that during EAE both regions undergo a "softening" of the tissue. Nevertheless, the magnitude modulus decreased more strikingly in the cerebellum, consistent with the fact that this region is more affected by inflammatory pathology than the cerebrum in the SJL EAE model.

Sagittal MRE Measurements Show a Correlation Between Mechanical Brain Properties and Clinical Disability in the Relapsing-Remitting EAE Model

It is well-established in both MS patients (23) and EAE (24), that MRI measurements do not always correlate with clinical disability. Using MRE acquired in the sagittal plane, we observed statistically significant correlations between the magnitude and storage moduli and the clinical score on the day of MRE acquisition, $p = 0.0117$, $r = -0.6306$ and $p = 0.0373$, $r = -0.5411$, respectively (**Figures 3A,B**). No significant correlations between loss modulus, phase angle and

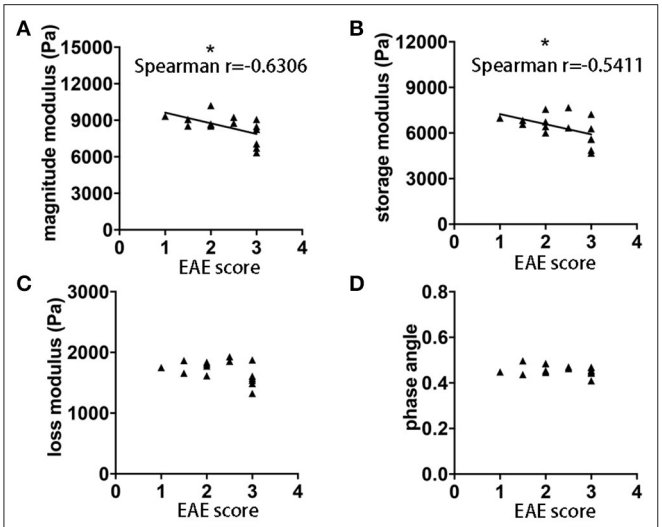

FIGURE 3 | Correlation of EAE clinical score and whole brain viscoelasticity. **(A)** Negative correlation was observed between clinical disability and magnitude modulus ($p = 0.0117$, $r = -0.6306$) as well as **(B)** storage modulus ($p = 0.0373$, $r = -0.5411$). No correlation was observed with **(C)** loss modulus and **(D)** phase angle. Data from five independent experiments, including only symptomatic mice, $n = 15$. Spearman correlation, $^*p < 0.05$.

EAE score were observed ($p = 0.1211$ and $r = -0.4179$, $p = 0.6189$ and $r = -0.1399$, respectively **Figures 3C,D**). These results indicate that there is an association between brain softening and more severe clinical signs in EAE mice.

MRE Does Not Correlate With Gadolinium Enhancement in Acute EAE

Contrast agent-based MRI represents the standard MR tool in MS to detect acute inflammatory lesions (25). Therefore, we asked whether the intensity of gadolinium (Gd) enhancement in brain MRI also correlated with clinical disability and MRE values in the SJL EAE model. We acquired axial and coronal T1-weighted images before and after intravenous injection of 0.2 mmol/kg Gd contrast agent, 24 h subsequent to the MRE scans. Brain lesions in active EAE are unevenly distributed in space, and are highly diffuse, lacking clear boarders. In order to better evaluate the extent of these diffuse lesions, we generated T1 maps to yield a quantitative measure of brain tissue contrast changes resulting from GBCA leakage across the blood-brain barrier. The T1 values were averaged from ROIs defining the entire brain, in order to obtain a global metric of Gd enhancement in the whole brain. Representative images illustrating the T1 maps pre- and post-contrast are shown **Figure 4A**. As expected, the post-contrast T1 values for all animals were significantly reduced, compared to the pre-contrast values (data not shown). Contrary to expectations, there was no statistically significant correlation between the delta T1 and the magnitude modulus ($p = 0.8797$, $r = 0.05181$, **Figure 4B**) or between T1 signal intensity changes directly obtained from the whole brain T1-weighted images and MRE values ($p = 0.3402$, $r = 0.2315$, **Figure 4C**). Accordingly, no significant correlation was observed between T1 signal intensity changes and EAE scores of the mice ($p = 0.2325$, $r = -0.4195$, **Figure 4D**).

Reduction of Viscoelasticity Correlates With an Increased Expression of FN

In view of the correlation between acute inflammatory events and loss of brain stiffness as measured by MRE, we considered whether viscoelastic changes may reflect processes of molecular remodeling that occur during the formation of brain lesions. Here we found that reduced viscoelasticity during EAE was significantly correlated with increased gene expression of FN in brain tissue, $p = 0.0041$, $r = -0.9473$ (**Figure 5A**). This correlation was robust, and was also confirmed in a separate analysis using frozen tissue from our previous study in SJL EAE acquiring MRE data in the coronal orientation (15), $p = 0.0163$, $r = -0.6737$ (**Figure 5B**).

To assess whether this association may involve changes of other components of the ECM, we investigated the gene expression of other key ECM proteoglycans, associated with the BBB (eg. glypican 5), or with the perineuronal and interstitial matrix (e.g., neurocan and brevican). No significant correlation was observed between brain viscoelasticity and the expression of these key proteoglycans, $p = 0.9755$ and $r = -0.01632$, $p = 0.3062$ and $r = -0.5056$, $p = 0.8671$ and $r = -0.08886$, respectively (**Figure 5C**).

FN Deposits Are Predominantly Found in Perivascular Areas, and Reduced Viscoelasticity Correlates With Increased FN Protein Expression

To confirm that FN gene expression is associated with protein deposits, we performed immunohistochemical analysis in the corresponding tissue, and demonstrated that at the time of the expected peak of EAE severity FN was highly expressed in perivascular areas (**Figure 6A**). In agreement with the gene expression data, reduced viscoelasticity correlated with increased FN immunofluorescence intensity (**Figure 6B**). In particular, a significant correlation was observed with the magnitude modulus and storage modulus ($p = 0.0083$, $r = -0.8447$ and $p = 0.0127$, $r = -0.8201$, respectively); whereas, no correlation of FN immunostaining with the loss modulus or phase angle could be detected ($p = 0.1766$, $r = -0.5301$ and $p = 0.2889$, $r = -0.4290$, respectively).

FN present in the lesions may arise either from the circulating plasma Fn (pFn), deposited following BBB disruption, or synthesized locally by glial cells (cellular cFn). These two FN variants contain alternatively spliced domains, EIIIA and EIIIB. To clarify the source of the FN observed in EAE, we used an anti EIIIA-FN antibody (IST9), which only recognizes cellular FN, in combination with the broad-spectrum anti-FN antibody. The staining of cellular FN showed a consistently overlapping pattern with the total FN, indicating that the main source of the perivascular FN deposits was indeed cellular, rather than circulating pFn (**Figure 6C**). The co-staining of FN with the astrocytic marker GFAP further indicated that not only astroglia

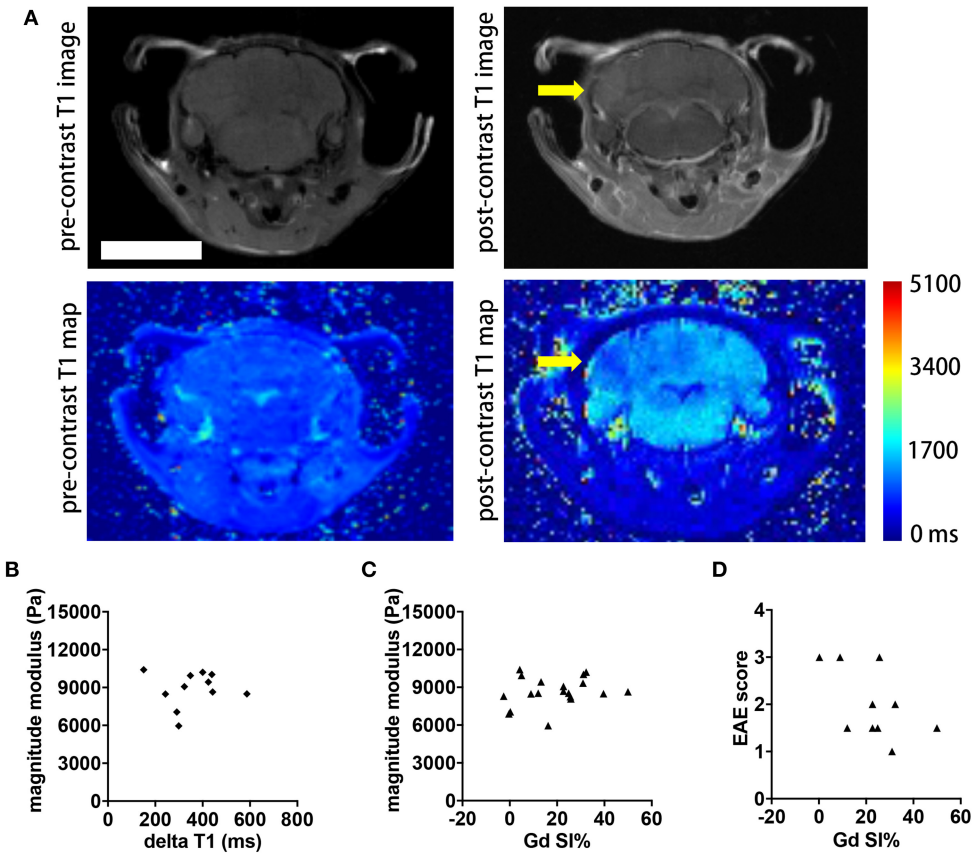

FIGURE 4 | Comparison of whole brain contrast-enhancing lesion burden with whole brain viscoelasticity. **(A)** Representative T1-weighted MR images pre- (left) and post- (right) GBCA administration. A diffuse contrast-enhancing lesion is seen in the cerebellum (arrow). T1 map pre- and post-contrast with T1 relaxation time in ms. Scale bar = 5 mm. **(B)** Delta T1 (mean pre-contrast minus mean post-contrast) did not correlate with the magnitude modulus (Pearson correlation, $p = 0.8797$, $r = 0.05181$). **(C)** T1 signal intensity changes (SI%) obtained from the T1-weighted images following Gd application showed no correlation with the magnitude modulus (Pearson correlation, $p = 0.3402$, $r = 0.2315$). **(D)** There was no significant correlation between SI% and the EAE score (Spearman correlation, $p = 0.2325$, $r = -0.4195$). Data from two independent experiments, $n = 11$ and $n = 19$ in **(B–D)**, respectively.

but also endothelial cells may be major sources of FN production in the lesion sites (**Figure 6D**).

DISCUSSION

In this study, we investigated the capacity of MRE to detect acute inflammatory events in the mouse brain during relapsing-remitting EAE. MRE investigations were performed together with T1-weighted MRI using GBCA and were correlated with clinical disability. Furthermore, we assessed the association between MRE values and molecular aspects of extracellular matrix remodeling at the sites of inflammatory lesions.

Studies using MRE to show changes in brain tissue stiffness in the context of pathology should consider the baseline values of normal brain, though it is crucial to take into consideration technical differences among various research groups. For example, Murphy et al. used a higher stimulation frequency (1,500 Hz), yielding higher mouse brain stiffness values (25.0 kPa) (26). Other studies using stimulation frequencies similar to the setup in the current study show that the values we obtained are within the range of other published values [reviewed in Table 1 of Bertalan et al. (27)]. Consistent with our previous studies using coronal MRE (15), we show here that MRE using sagittal slices in SJL EAE revealed a decrease in the overall brain viscoelasticity at the time of the expected peak of disease, compared to the corresponding healthy controls. Furthermore, confirming our data in C57/BL6 mice (16), we demonstrated also in SJL mice that the cerebellum is softer than the cerebrum, and that these regional differences were maintained during EAE. In the SJL model, it is well-documented that the cerebellum is especially susceptible to blood-brain-barrier disruption and lesion formation (28). This together with the significant softening of the cerebellum suggests that areas of high inflammatory activity are especially well-identified by MRE. However, confirming the sensitivity of the sagittal MRE scans for visualizing whole brain inflammation, we observed a significant correlation between whole-brain brain viscoelasticity and EAE clinical score. No correlation was established between cerebellar viscoelasticity and EAE score. Thus, although changes

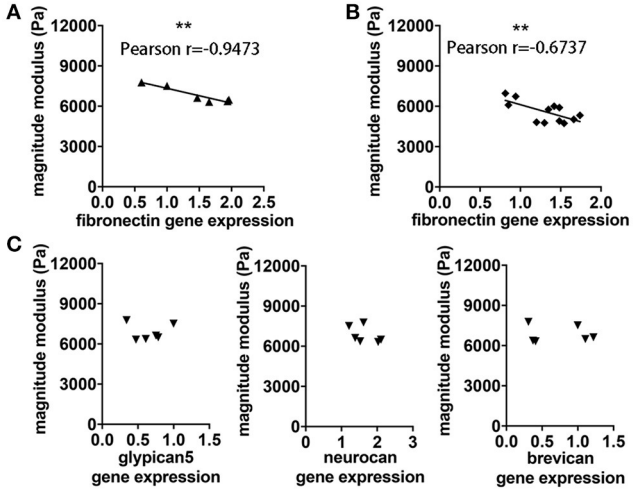

FIGURE 5 | Association between viscoelastic changes and expression of FN. **(A)** The degree of reduction of cerebellar rigidity (magnitude modulus) at time of the expected EAE peak is associated with increased expression of FN assessed by qPCR, $p = 0.0041$, $r = -0.9473$. **(B)** The same association between magnitude modulus and fibronectin expression was found using frozen tissue from our previous study in SJL EAE with coronal MRE. $P = 0.01163$, $r = -0.6737$. **(C)** No correlation was observed between cerebellar magnitude modulus and gene expression of other ECM components of the cerebellum including glypican5, neurocan and brevican, respectively. Pearson correlation, $^{**}p < 0.01$. Data from two independent experiments, including only symptomatic mice, $n = 12$ and $n = 6$ in **(A–C)**, respectively.

in the cerebellum are relevant and pronounced, they do not seem to reflect all the processes that ultimately determine the clinical EAE signs.

To date, GBCA-MRI represents the standard approach to identify BBB breakdown in MS patients and also in animal models (29–31). However, there is increasing concern from recent studies and case reports pointing out potential toxic side effects of GBCA (32), thus motivating the desire for alternative MRI methods that can both better detect and improve understanding of the nature of the pathology during disease. In the active EAE model, GBCA-enhancing lesions are numerous, but rather small and diffusely distributed, and are thus inherently difficult to quantify using T1-weighted images. Therefore, we used T1 mapping to yield an unbiased, quantitative readout of the burden of lesion activity in the entire brain—a strategy that was recently applied in a mouse brain tumor model (33). Using the delta T1 averaged over the entire brain as a metric of BBB disruption also avoids potential sampling bias that might occur when attempting to quantify lesions in selected brain slices, given the uneven distribution of brain lesions in SJL EAE. Contrary to our expectations, there was no significant correlation between the overall magnitude of GBCA-enhancing lesions and the whole-brain MRE parameters. This underscores the complex nature of multiple pathological processes that occur simultaneously in EAE. It may be that the relationship between viscoelastic changes and GBCA-enhancement cannot be detected with a simple linear correlation. This may reflect that the disease processes that lead to viscoelastic changes have different kinetics from those of acute BBB disruption and active lesions. This remains a topic for further investigations.

Inflammatory lesions are not only defined by enhanced endothelial permeability and disruption of the BBB, but also by astroglial activation and remodeling of the extracellular matrix components (34). In particular FN-mediated signaling seems to promote vascular remodeling during demyelinating disease (35). Therefore, we investigated the relationship between alteration of mechanical properties of the brain and expression of FN, as an indicator for neurovascular junction remodeling during lesion formation. Our data indicate that reduction of brain viscoelasticity is indeed associated with an overall increase of FN expression in the brain tissue (36, 37).

FN is a multidomain glycoprotein binding to cell-surface-receptors, mostly integrins, and to the ECM and appears in two forms: plasma and cellular FN. Cellular FN is secreted as a soluble covalent dimer, and in a complicated process in which the FN molecule undergoes different conformational changes, is assembled into a stable matrix (38). Our data point to a cellular source of the FN deposits detected in the perivascular areas. FN fibers were in close proximity to the reactive astrocytes, confirming previous reports that glia cells are major producers of the protein (39). However, further studies are required to determine the sources of FN. So far, we could not exclude other cellular sources such as brain endothelial cells. Additionally, we observed that FN deposits characterized disturbed BBB with enhanced perivascular space and astrocyte endfoot detachment. Thus, although the FN fibers are extremely elastic (40), and might be expected to contribute to enhanced tissue elasticity, in this context their presence might reflect an assembly of processes involved in disruption of the neurovascular unit at the lesion sites. This may lead to tissue softening, due to enhanced endothelial permeability, alteration of blood flow, enlargement of the perivascular spaces, inflammation or astrocytic endfeed detachment.

Importantly, the correlation of MRE data with FN deposition could also be confirmed in brain tissue from our previous MRE study in SJL animals, in which MRE data was acquired using a coronal slice (15). In contrast, no correlation was found between MRE values and other ECM components such neurocan, brevican, or glypican, which are reported to be relevant for neuroinflammation, but which do not directly reflect the process of acute lesion formation (36, 37). Furthermore, we found that deposits of FN are prominent around inflamed vessels and that the presence of FN also correlated with the overall softening of the brain tissue at acute EAE.

Altogether our study sheds light on the mechanism of brain softening due to inflammation. Previous studies in mouse models and patients have demonstrated *in vivo* that brain tissue becomes softer during the progression of neuroinflammatory processes. Our data demonstrate that some of these observations might be explained by mechanisms involving the enhancement of perivascular spaces and astrocyte endfoot detachment leading to weaker couplings between the neuronal-vascular networks, and reduced tissue stiffness. This might also explain the high sensitivity of MRE to processes of acute inflammation and

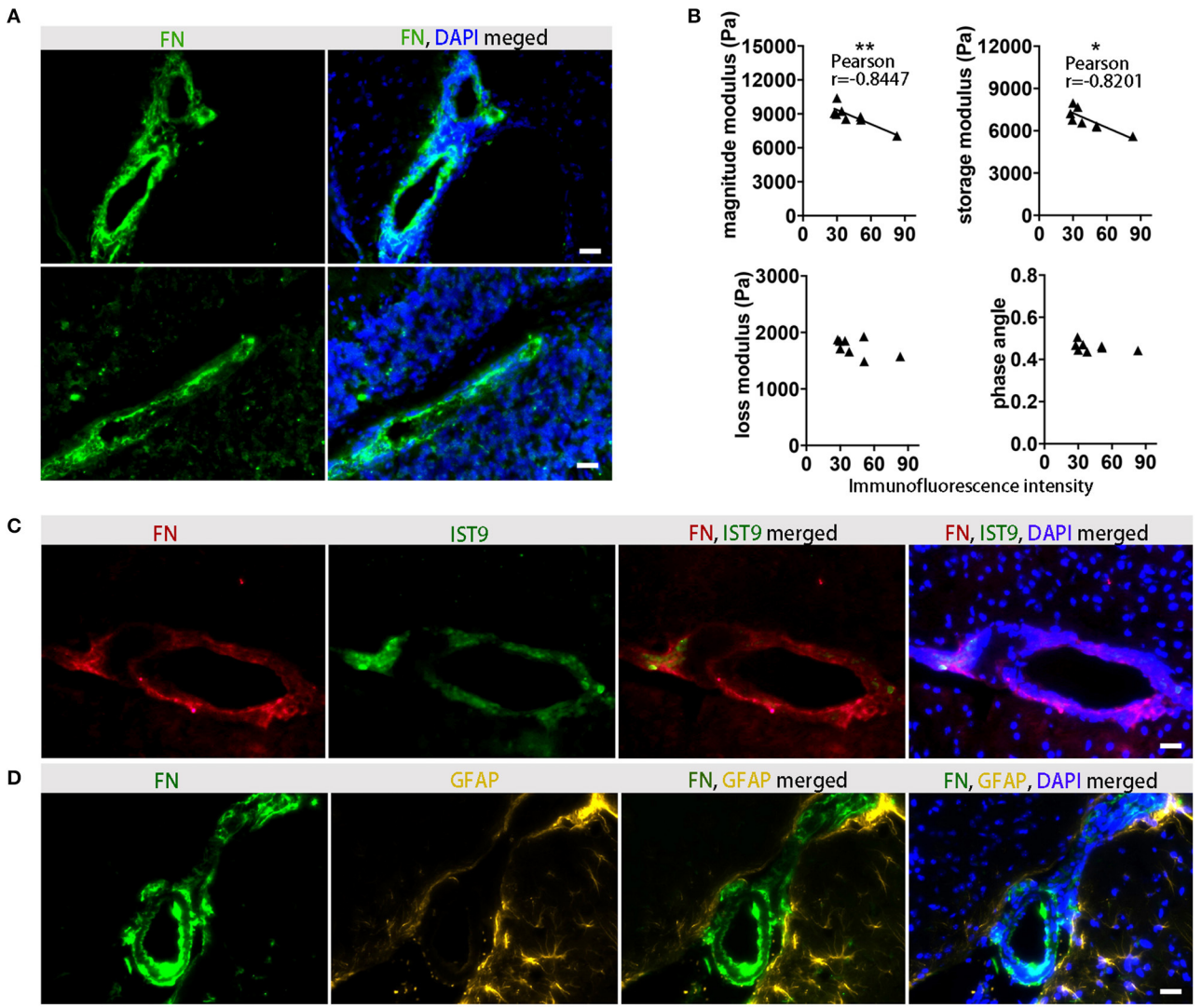

FIGURE 6 | Association between viscoelastic changes and histological detection of FN. **(A)** Immunofluorescence staining indicates a perivascular distribution of FN (green) in inflamed midbrain (top) and cerebellum (bottom). Staining of FN deposits are green and cell nuclei are blue, scale ba $r = 100\,\mu m$. **(B)** Correlation between MRE parameters and FN immunofluorescence in EAE animals at days of expected peak disease. Data from two independent experiments, including only symptomatic mice, $n = 8$. Pearson correlation, $^{**}p < 0.01$, $^{*}p < 0.05$. **(C)** Immunostaining with anti-FN for detection of overall fibronectin (red), and anti-EIIIA-FN for detection of cellular FN (IST9, green) indicates that perivascular FN deposits are secreted by cells. Cell nuclei are blue. Scale bar $= 100\,\mu m$. **(D)** Immunostaining of FN (green) and the astrocytic marker GFAP (yellow) shows perivascular astrocytes adjacent to the FN deposits in the EAE brain. Cell nuclei are blue. Scale bar $= 100\,\mu m$.

lesion formation in the brain when compared to GBCA-MRI. The application of MRE in mouse models of brain disease is an emerging field. Future experiments to evaluate how well MRE can predict disease development in the pre-onset phase, or to identify tissue changes and accurately reflect disease severity during clinical relapse and remission, hold promise. Further technical developments that will allow faster acquisition times to obtain MRE data covering the entire mouse brain with reasonable scan times, as well as improvements in spatial resolution will be essential to advance our understanding of the complex processes occurring during neuroinflammation. The results of the present study lay a foundation for such upcoming studies to investigate in more detail the temporal and spatial changes of tissue mechanics in relation with lesion development.

DATA AVAILABILITY STATEMENT

The raw data supporting the conclusions of this article will be made available by the corresponding author, without undue reservation, to any qualified researcher.

ETHICS STATEMENT

This study was carried out in accordance with the recommendations of national and international guidelines

to minimize discomfort to animals (86/609/EEC. The protocol was approved by the Animal Welfare Department of the State Office of Health and Social Affairs Berlin (LAGeSo).

AUTHOR CONTRIBUTIONS

CI-D, SWan, JM, LH-V, JG, and IS designed the study. SWan, JM, LH-V, BM, KP, and AG-I carried out the experiments and measurements. SM and PB-S developed the 7 Tesla MRI setup. SWan, JM, JG, BM, and SWai worked on the analysis. SWan, JM, LH-V, and CI-D wrote the manuscript with the assistance of all other co-authors.

FUNDING

This work was supported by grants of the German Research Foundation (Deutsche Forschungsgemeinschaft, DFG) to CI-D and IS (IN 156/4-1; SA 901/16-1 and SFB 1340/B05, project number 372486779) GRK 2260 BIOQIC, and the DFG Cluster of Excellence NeuroCURE (Exc 257). Funding to SM and PB-S was provided by the German Federal Ministry of Education and Research (BMBF, Center for Stroke Research Berlin 01EO1301), the BMBF under the ERA-NET NEURON scheme (01EW1811), and the German Research Foundation (DFG, Project 428869206 and EXC NeuroCure). We further acknowledge support from the German Research Foundation (DFG) and the Open Access Publication Fund of Charité – Universitätsmedizin Berlin.

ACKNOWLEDGMENTS

We thank Natascha Asselborn for expert technical assistance. SWan acknowledges financial support from China Scholarship Council.

REFERENCES

1. Weissert, R. The immune pathogenesis of multiple sclerosis. *J Neuroimmune Pharmacol*. (2013) 8:857–66. doi: 10.1007/s11481-013-9467-3
2. Robinson P, Harp CT, Noronha A, Miller SD. The experimental autoimmune encephalomyelitis (EAE) model of MS: utility for understanding disease pathophysiology and treatment. *Handb Clin Neurol*. (2014) 122:173–89. doi: 10.1016/B978-0-444-52001-2.00008-X
3. Miller DH, Grossman RI, Reingold SC, McFarland HF. The role of magnetic resonance techniques in understanding and managing multiple sclerosis. *Brain*. (1998) 121:3–24. doi: 10.1093/brain/121.1.3
4. Tysiak E, Asbach P, Aktas O, Waiczies H, Smyth M, Schnorr J, et al. Beyond blood brain barrier breakdown - *in vivo* detection of occult neuroinflammatory foci by magnetic nanoparticles in high field MRI. *J Neuroinflammation*. (2009) 6:20. doi: 10.1186/1742-2094-6-20
5. Wuerfel E, Infante-Duarte C, Glumm R, Wuerfel JT. Gadofluorine M-enhanced MRI shows involvement of circumventricular organs in neuroinflammation. *J Neuroinflammation*. (2010) 7:70. doi: 10.1186/1742-2094-7-70
6. Gulani V, Calamante F, Shellock FG, Kanal E, Reeder SB, International Society for Magnetic Resonance in Medicine. Gadolinium deposition in the brain: summary of evidence and recommendations. *Lancet Neurol*. (2017) 16:564–70. doi: 10.1016/S1474-4422(17)30158-8
7. Bigot M, Chauveau F, Beuf O, Lambert SA. Magnetic resonance elastography of rodent brain. *Front Neurol*. (2018) 9:1010. doi: 10.3389/fneur.2018.01010
8. Muthupillai R, Lomas DJ, Rossman PJ, Greenleaf JF, Manduca A, Ehman RL. Magnetic resonance elastography by direct visualization of propagating acoustic strain waves. *Science*. (1995) 269:1854–7. doi: 10.1126/science.7569924
9. Hirsch S, Braun J, Sack I. *Magnetic Resonance Elastography: Physical Background And Medical Applications*. Weinheim: Wiley-VCH (2017). doi: 10.1002/9783527696017
10. Fehlner, Behrens JR, Streitberger KJ, Papazoglou S, Braun J, Bellmann-Strobl J, et al. Higher-resolution MR elastography reveals early mechanical signatures of neuroinflammation in patients with clinically isolated syndrome. *J Magn Reson Imaging*. (2016) 44:51–8. doi: 10.1002/jmri.25129
11. Wuerfel J, Paul F, Beierbach B, Hamhaber U, Klatt D, Papazoglou S, et al. MR-elastography reveals degradation of tissue integrity in multiple sclerosis. *Neuroimage*. (2010) 49:2520–5. doi: 10.1016/j.neuroimage.2009.06.018
12. Streitberger KJ, Sack I, Krefting D, Pfuller C, Braun J, Paul F, et al. Brain viscoelasticity alteration in chronic-progressive multiple sclerosis. *PLoS ONE*. (2012) 7: e29888. doi: 10.1371/journal.pone.0029888
13. Streitberger KJ, Fehlner A, Pache F, Lacheta A, Papazoglou S, Bellmann-Strobl J, et al. Multifrequency magnetic resonance elastography of the brain reveals tissue degeneration in neuromyelitis optica spectrum disorder. *Eur Radiol*. (2017) 27:2206–15. doi: 10.1007/s00330-016-4561-6
14. Schregel K, Wuerfel E, Garteiser P, Gemeinhardt I, Prozorovski T, Aktas O, et al. Demyelination reduces brain parenchymal stiffness quantified *in vivo* by magnetic resonance elastography. *Proc Natl Acad Sci USA*. (2012) 109:6650–5. doi: 10.1073/pnas.1200151109
15. Riek K, Millward JM, Hamann I, Mueller S, Pfueller CF, Paul F, et al. Magnetic resonance elastography reveals altered brain viscoelasticity in experimental autoimmune encephalomyelitis. *Neuroimage Clin*. (2012) 1:81–90. doi: 10.1016/j.nicl.2012.09.003
16. Millward JM, Guo J, Berndt D, Braun J, Sack I, Infante-Duarte C. Tissue structure and inflammatory processes shape viscoelastic properties of the mouse brain. *NMR Biomed*. (2015) 28:831–9. doi: 10.1002/nbm.3319
17. Sobel RA, Mitchell ME. Fibronectin in multiple sclerosis lesions. *Am J Pathol*. (1989) 135:161–8.
18. Stoffels JM, de Jonge JC, Stancic M, Nomden A, van Strien ME, Ma D, et al. Fibronectin aggregation in multiple sclerosis lesions impairs remyelination. *Brain*. (2013) 136:116–31. doi: 10.1093/brain/aws313
19. Glatigny S, Bettelli E. Experimental Autoimmune Encephalomyelitis (EAE) as Animal Models of Multiple Sclerosis (MS). *Cold Spring Harb Perspect Med*. (2018) 8:a028977. doi: 10.1101/cshperspect.a028977
20. Oliphant TE, Manduca A, Ehman RL, Greenleaf JF. Complex-valued stiffness reconstruction for magnetic resonance elastography by algebraic inversion of the differential equation. *Magn Reson Med*. (2001) 45:299–310. doi: 10.1002/1522-2594(200102)45:2<;299::AID-MRM1039>;3.0.CO;2-O
21. Sack, Jöhrens K, Wuerfel J, Braun J. Structure-sensitive elastography: on the viscoelastic powerlaw behavior of *in vivo* human tissue in health and disease. *Soft Matter*. (2013) 9:5672–80. doi: 10.1039/c3sm50552a
22. Millward M, Schnorr J, Taupitz M, Wagner S, Wuerfel JT, Infante-Duarte C. Iron oxide magnetic nanoparticles highlight early involvement of the choroid plexus in central nervous system inflammation. *ASN Neuro*. (2013) 5:e00110. doi: 10.1042/AN20120081
23. Barkhof F. The clinico-radiological paradox in multiple sclerosis revisited. *Curr Opin Neurol*. (2002) 15:239–45. doi: 10.1097/00019052-200206000-00003
24. Wuerfel, Tysiak E, Prozorovski T, Smyth M, Mueller S, Schnorr J, et al. Mouse model mimics multiple sclerosis in the clinico-radiological paradox. *Eur J Neurosci*. (2007) 26:190–8. doi: 10.1111/j.1460-9568.2007.05644.x
25. Kaunzner UW, Gauthier SA. MRI in the assessment and monitoring of multiple sclerosis: an update on best practice. *Ther Adv Neurol Disord*. (2017) 10:247–61. doi: 10.1177/1756285617708911
26. Murphy C, Curran GL, Glaser KJ, Rossman PJ, Huston J III, Poduslo JF, et al. Magnetic resonance elastography of the brain in a mouse model

of Alzheimer's disease: initial results. *Magn Reson Imaging*. (2012) 30:535–9. doi: 10.1016/j.mri.2011.12.019
27. Bertalan G, Guo J, Tzschatzsch H, Klein C, Barnhill E, Sack I, et al. Fast tomoelastography of the mouse brain by multifrequency single-shot MR elastography. *Magn Reson Med*. (2019) 81:2676–87. doi: 10.1002/mrm.27586
28. Tonra JR. Cerebellar susceptibility to experimental autoimmune encephalomyelitis in SJL/J mice: potential interaction of immunology with vascular anatomy. *Cerebellum*. (2002) 1:57–68. doi: 10.1080/147342202753203096
29. Pirko Johnson AJ. Neuroimaging of demyelination and remyelination models. *Curr Top Microbiol Immunol*. (2008) 318:241–66. doi: 10.1007/978-3-540-73677-6_10
30. Levy H, Assaf Y, Frenkel D. Characterization of brain lesions in a mouse model of progressive multiple sclerosis. *Exp Neurol*. (2010) 226:148–58. doi: 10.1016/j.expneurol.2010.08.017
31. Tommasin S, Gianni C, De Giglio L, Pantano P. Neuroimaging techniques to assess inflammation in multiple sclerosis. *Neuroscience*. (2017) 403:4–16. doi: 10.1016/j.neuroscience.2017.07.055
32. Fraum TJ, Ludwig DR, Bashir MR, Fowler KJ. Gadolinium-based contrast agents: a comprehensive risk assessment. *J Magn Reson Imaging*. (2017) 46:338–53. doi: 10.1002/jmri.25625
33. Herrmann K, Erokwu BO, Johansen ML, Basilion JP, Gulani V, Griswold MA, et al. Dynamic quantitative T1 mapping in orthotopic brain tumor xenografts. *Transl Oncol*. (2016) 9:147–54. doi: 10.1016/j.tranon.2016.02.004
34. Voskuhl RR, Peterson RS, Song B, Ao Y, Morales LB, Tiwari-Woodruff S, et al. Reactive astrocytes form scar-like perivascular barriers to leukocytes during adaptive immune inflammation of the CNS. *J Neurosci*. (2009) 29:11511–22. doi: 10.1523/JNEUROSCI.1514-09.2009
35. Boroujerdi, Welser-Alves JV, Milner R. Extensive vascular remodeling in the spinal cord of pre-symptomatic experimental autoimmune encephalomyelitis mice; increased vessel expression of fibronectin and the alpha5beta1 integrin. *Exp Neurol*. (2013) 250:43–51. doi: 10.1016/j.expneurol.2013.09.009
36. Haylock-Jacobs S, Keough MB, Lau L, Yong VW. Chondroitin sulphate proteoglycans: extracellular matrix proteins that regulate immunity of the central nervous system. *Autoimmun Rev*. (2011) 10:766–72. doi: 10.1016/j.autrev.2011.05.019
37. Lorentzen R, Melum E, Ellinghaus E, Smestad C, Mero IL, Aarseth JH, et al. Association to the Glypican-5 gene in multiple sclerosis. *J Neuroimmunol*. (2010) 226:194–7. doi: 10.1016/j.jneuroim.2010.07.003
38. Schwarzbauer E, DeSimone DW. Fibronectins, their fibrillogenesis, and *in vivo* functions. *Cold Spring Harb Perspect Biol*. (2011) 3:a005041. doi: 10.1101/cshperspect.a005041
39. Stoffels JM, Hoekstra D, Franklin RJ, Baron W, Zhao C. The EIIIA domain from astrocyte-derived fibronectin mediates proliferation of oligodendrocyte progenitor cells following CNS demyelination. *Glia*. (2015) 63:242–56. doi: 10.1002/glia.22748
40. Ohashi T, Kiehart DP, Erickson HP. Dynamics and elasticity of the fibronectin matrix in living cell culture visualized by fibronectin-green fluorescent protein. *Proc Natl Acad Sci USA*. (1999) 96:2153–8. doi: 10.1073/pnas.96.5.2153

Conflict of Interest: The authors declare that the research was conducted in the absence of any commercial or financial relationships that could be construed as a potential conflict of interest.

frontiers in Neurology

ORIGINAL RESEARCH
published: 24 January 2020
doi: 10.3389/fneur.2020.00018

Functional Characterization of Atrophy Patterns Related to Cognitive Impairment

*Gereon J. Schnellbächer[1], Felix Hoffstaedter[2,3], Simon B. Eickhoff[2,3], Svenja Caspers[2,4,5], Thomas Nickl-Jockschat[6,7], Peter T. Fox[8,9], Angela R. Laird[10], Jörg B. Schulz[1,2,5], Kathrin Reetz[1,2,5] and Imis Dogan[1,2,5]**

[1] Department of Neurology, RWTH Aachen University, Aachen, Germany, [2] Research Centre Jülich, Institute of Neuroscience and Medicine (INM-1, INM-7, INM-11), Jülich, Germany, [3] Institute of Systems Neuroscience, Medical Faculty, Heinrich Heine University, Düsseldorf, Germany, [4] Institute for Anatomy I, Medical Faculty, Heinrich Heine University, Düsseldorf, Germany, [5] JARA-BRAIN, Jülich-Aachen Research Alliance, Jülich, Germany, [6] Iowa Neuroscience Institute, Carver College of Medicine, University of Iowa, Iowa City, IA, United States, [7] Department of Psychiatry, Carver College of Medicine, University of Iowa, Iowa City, IA, United States, [8] Research Imaging Center, University of Texas Health Science Center, San Antonio, TX, United States, [9] Research Service, South Texas Veterans Administration Medical Center, San Antonio, TX, United States, [10] Department of Physics, Florida International University, Miami, FL, United States

OPEN ACCESS

Edited by:
Hans-Peter Müller,
University of Ulm, Germany

Reviewed by:
Yann Quidé,
University of New South Wales, Australia
Kimberly Louise Ray,
University of Texas at Austin, United States

***Correspondence:**
Imis Dogan
idogan@ukaachen.de

Specialty section:
This article was submitted to Applied Neuroimaging, a section of the journal Frontiers in Neurology

Received: 02 October 2019
Accepted: 08 January 2020
Published: 24 January 2020

Citation:
Schnellbächer GJ, Hoffstaedter F, Eickhoff SB, Caspers S, Nickl-Jockschat T, Fox PT, Laird AR, Schulz JB, Reetz K and Dogan I (2020) Functional Characterization of Atrophy Patterns Related to Cognitive Impairment. Front. Neurol. 11:18. doi: 10.3389/fneur.2020.00018

Introduction: Mild cognitive impairment (MCI) is a heterogenous syndrome considered as a risk factor for developing dementia. Previous work examining morphological brain changes in MCI has identified a temporo-parietal atrophy pattern that suggests a common neuroanatomical denominator of cognitive impairment. Using functional connectivity analyses of structurally affected regions in MCI, we aimed to investigate and characterize functional networks formed by these regions that appear to be particularly vulnerable to disease-related disruptions.

Methods: Areas of convergent atrophy in MCI were derived from a quantitative meta-analysis and encompassed left and right medial temporal (i.e., hippocampus, amygdala), as well as parietal regions (precuneus), which were defined as seed regions for connectivity analyses. Both task-based meta-analytical connectivity modeling (MACM) based on the BrainMap database and task-free resting-state functional MRI in a large cohort of older adults from the 1000BRAINS study were applied. We additionally assessed behavioral characteristics associated with the seed regions using BrainMap meta-data and investigated correlations of resting-state connectivity with age.

Results: The left temporal seed showed stronger associations with a fronto-temporal network, whereas the right temporal atrophy cluster was more linked to cortico-striatal regions. In accordance with this, behavioral analysis indicated an emphasis of the left temporal seed on language generation, and the right temporal seed was associated with the domains of emotion and attention. Task-independent co-activation was more pronounced in the parietal seed, which demonstrated stronger connectivity with a frontoparietal network and associations with introspection and social cognition. Correlation analysis revealed both decreasing and increasing functional connectivity with higher age that may add to pathological processes but also indicates compensatory mechanisms of functional reorganization with increasing age.

Conclusion: Our findings provide an important pathophysiological link between morphological changes and the clinical relevance of major structural damage in MCI. Multimodal analysis of functional networks related to areas of MCI-typical atrophy may help to explain cognitive decline and behavioral alterations not tractable by a mere anatomical interpretation and therefore contribute to prognostic evaluations.

Keywords: temporal lobe, parietal lobe, meta-analytical connectivity modeling, resting-state functional connectivity, aging, cognition, neurodegeneration

INTRODUCTION

Mild cognitive impairment (MCI) is a syndrome marked by a cognitive deficit greater than expected considering age and education level and without relevant impact on daily activities (1–3). MCI is a heterogeneous condition with varying operational definitions, presumably originating from different etiologies and, importantly, may be the precursor of emerging dementia with an annual conversion rate of up to 10% (4, 5). Hence, improving our understanding of early processes of cognitive decline, behavioral symptoms, and degenerative alterations is highly relevant, particularly given that dementia is often caused by irreversible cell degeneration.

Structural brain changes may be observed at an early stage of cognitive decline (6, 7). In order to identify the common neuroanatomical substrates of MCI as a widely defined syndrome, Nickl-Jockschat et al. (8) performed a quantitative meta-analysis of voxel-based morphometry (VBM) studies comparing MCI patients diagnosed via the Petersen criteria (1, 9) with healthy controls. Consistent structural changes across studies were found in three clusters mainly encompassing bilaterally the hippocampus and amygdala, and the parietal precuneus (8). Gray matter reductions in the amygdala, hippocampus and thalamus were additionally associated with decreased cognitive performance (8). Although different pathologies may underlie MCI, this convergent temporo-parietal atrophy pattern can be considered to reflect a common neuropathological denominator of cognitive impairment (8). However, a comprehensive understanding of the clinical profile linked to such alterations should consider the complex interactions within neuronal circuits formed by or emanating from areas susceptible to disease pathology. This is particularly true given the notion that neurogenerative disorders represent diseases with distinct patterns of network disintegration (10, 11). Moreover, neurodegenerative diseases have been described as "nexopathies" (Latin nectere, tie) referring to the spread of pathogenic protein abnormalities via large-scale brain networks and differential intrinsic network vulnerability (12). In this context, the regions of convergent volume loss in MCI identified by Nickl-Jockschat et al. (8), which are also parts of the default mode network (DMN), can be considered as network nodes particularly vulnerable in MCI. Computational models have emphasized the role of structural network hubs as highly interconnected neural regions that are important for the integration and segregation of brain networks (13, 14). A disruption of such circuits due to morphological changes will be detrimental to network functionality, which in turn may likely lead to clinical manifestations going beyond a merely anatomical interpretation of circumscribed atrophic regions.

In the current study we aimed to functionally and behaviorally characterize the atrophy pattern previously observed in MCI and delineate ensuing functional networks connected to these regions that are prone to disruption in MCI. To achieve this, regions of convergent volume loss as identified by Nickl-Jockschat et al. (8) were defined as seed regions and subjected to functional connectivity modeling using different modalities. (i) First, functional connectivity was assessed using task-based meta-analytical connectivity modeling (MACM), which identifies stimuli-driven networks during task performance using an extensive amount of meta-data of functional imaging studies stored in the BrainMap database (15). (ii) Second, we employed task-free resting-state functional MRI (fMRI) data of a large sample of older healthy probands derived from the 1000BRAINS study (16) to assess endogenously controlled functional connectivity profiles coupled with respective atrophy seeds. This non-clinical cohort enabled the identification of characteristic networks that are expected to co-activate with our seed regions in an aging population and may be disrupted when morphological changes occur. Additionally, the combination of both approaches allowed the analysis of convergence between both task-driven and task-independent functional networks related to the regions of atrophy, representing a more robust estimation of "core" connectivity profiles across different modalities (17). (iii) In a further step, again using meta-data from BrainMap we aimed to behaviorally characterize the atrophy nodes by inferring from the specific behavioral domains and paradigms that consistently elicited activation in these regions in previously published functional imaging studies. (iv) Finally, as MCI is an age-associated disease and there are connectivity alterations with increasing age (18), we performed correlation analyses between age and resting-state connectivity of MCI-typical atrophy regions. This allows a better differentiation between age-related connectivity changes and those expected to be associated with MCI.

Given the several definitions of the MCI syndrome over the last decades, we note that in the current study we focused on the definition by Petersen (9) that any cognitive domain may be affected. While different causes other than neurodegenerative processes (e.g., vascular diseases, depression) may lead to MCI, use of this broader definition enables the characterization of an early temporo-parietal atrophy pattern representing a common neuropathological substrate of cognitive impairment (8).

MATERIALS AND METHODS

Seed Regions: Regions of Convergent Atrophy in MCI

Functional connectivity analysis was based on seed regions identified by Nickl-Jockschat et al. (8), representing areas of common consistent atrophy in MCI (**Figure 1A**). In this previously published coordinate-based meta-analysis, 22 VBM studies comparing in total 917 MCI patients (predominantly amnestic MCI) with 809 healthy controls were included and three supra-threshold clusters of convergent atrophy in MCI were identified: The largest cluster (cluster extent k_E: 2407 voxels, MNI-coordinates of cluster maxima in x/y/z: −22/−8/−22) was localized in the left medial temporal lobe, including the hippocampus (cornu ammonis) and laterobasal amygdala. The second cluster (k_E: 1984 voxels, 24/−8/−20) was located on the right temporal lobe encompassing the laterobasal amygdala, fascia dentata of the hippocampus and parahippocampal gyrus. The third cluster (k_E: 269 voxels, 2/-54/32) was mainly located in the precuneus extending to the posterior cingulate cortex [PCC; (8)].

Task-Based Meta-Analytic Connectivity Modeling (MACM)

Task-based functional connectivity of MCI-typical atrophy seeds was calculated via meta-analytic connectivity modeling [MACM; (20–22)] based on the BrainMap database [www.brainmap.org; (15, 23, 24)]. By examining the functional connectivity profile of co-activations reported across the entire brain, we aimed to identify functional networks connected with these atrophy regions and therefore most likely to be disrupted in patients with MCI.

MACM assesses the brain-wide co-activation pattern of an anatomical region across a large number of functional neuroimaging results in healthy individuals stored in BrainMap (please see Section Behavioral Characterization for more information on paradigm classes and behavioral domains) and identifies significant areas of above-chance co-activation with this seed region. For this, all eligible experiments reporting at least one activation focus of within-subject effects between conditions were identified. Using the activation likelihood estimation (ALE) approach, convergence across these brain-wide foci was tested for identifying consistent co-activation (i.e., task-based functional connectivity) with the respective seed (15, 25–27). The reported foci were treated as centers of 3D Gaussian probability distributions reflecting the spatial uncertainty associated with each reported set of coordinates (25). The probabilities of all foci reported in the experiments were then combined for every voxel and a modeled activation (MA) map was drawn (27). The union of these maps yielded voxel-wise ALE scores describing the level of convergence at each location in the brain, which were compared to a null-distribution (26). Non-parametric *p*-values for each meta-analysis were thresholded at a cluster-level corrected family-wise error (cFWE) of $p < 0.05$ (uncorrected at the voxel-level with $p < 0.001$). Additionally, we performed contrast analyses of network connectivity between seed regions to assess divergent connectivity profiles between the three atrophy seeds (28). Thereby we aimed to delineate networks showing stronger functional connectivity with one seed region in particular compared to the remaining ones. Contrast analysis results were thresholded at a posterior probability of $p > 0.95$ ($k_E \geq 50$ voxels) for a true difference between the two samples (17). All results were anatomically labeled by reference to probabilistic cytoarchitectonic maps of the human brain implemented in the SPM Anatomy Toolbox (29).

Task-Independent "Resting-State" Connectivity Modeling

We further performed seed-voxel-wise connectivity analysis of each atrophy seed using resting-state functional MRI (rs-fMRI) data from the 1000BRAINS study (16). The 1000BRAINS study is a longitudinal large-scale imaging study that investigates functional and structural variability of the aging brain, providing a unique source of imaging data in a large sample of healthy older adults. Hence, in order to delineate functional connectivity profiles across different modalities, we examined endogenously controlled resting-state networks co-activating with our seed regions in addition to rather externally-driven task-based connectivity (17). The large 1000BRAINS dataset of older healthy adults further gave us the opportunity to investigate the effect of aging on the functional connectivity of those areas demonstrating morphological changes in MCI.

For the current analysis, we used data from 637 healthy older subjects (mean age 66.7 ± 6.3 SD years, range: 55–85 years; 50.2% male; formal school years 9.9 ± 2.1; vocational/higher education 3.9 ± 2.7 years) with no history of neurological or psychiatric disorders. Only subjects with a score of at least 13 points (mean 15.5 ± 1.9 SD; range: 13–18) in the cognitive screening tool DemTect (30) indicating no signs of early dementia were included. Resting-state fMRI scans of 11:30 min duration were performed while eyes were closed, light switched off, and with the instruction to let the mind wander without thinking of anything in particular and not to fall asleep. Gradient-echo echoplanar images (EPI) were acquired on a 3T Siemens Tim Trio MR scanner (Erlangen, Germany) with the following sequence parameters: TR = 2.2 s, TE = 30 ms, FoV = 200 × 200 mm^2, flip angle = 90°, voxel resolution = 3.1 × 3.1 × 3.1 mm^3, 36 slices. Physiological and movement artifacts were removed from the data using FIX [FMRIB's ICA-based Xnoiseifier, implemented in FSL; (31)]. FIX decomposes the data into independent components using FSL melodic and classifies noise components using distinct spatial and temporal features, which are then regressed out of the raw fMRI data. Further processing was performed using SPM12 (http://www.fil.ion.ucl.ac.uk/spm/) and in-house Matlab tools. Images were normalized to the MNI template (32) and smoothed with a 5 mm FWHM Gaussian kernel. In order to reduce spurious correlations, variance that could be explained by nuisance variables was removed, i.e., the six motion parameters derived from image realignment, the first derivate from the realignment parameters, and the mean tissue class signals (gray matter, white matter, CSF) per time-point obtained by averaging across voxels (33, 34). Finally, using a bandpass filter we examined frequencies between 0.01 and 0.08 Hz as meaningful resting-state signal will predominantly be found in these frequencies (35).

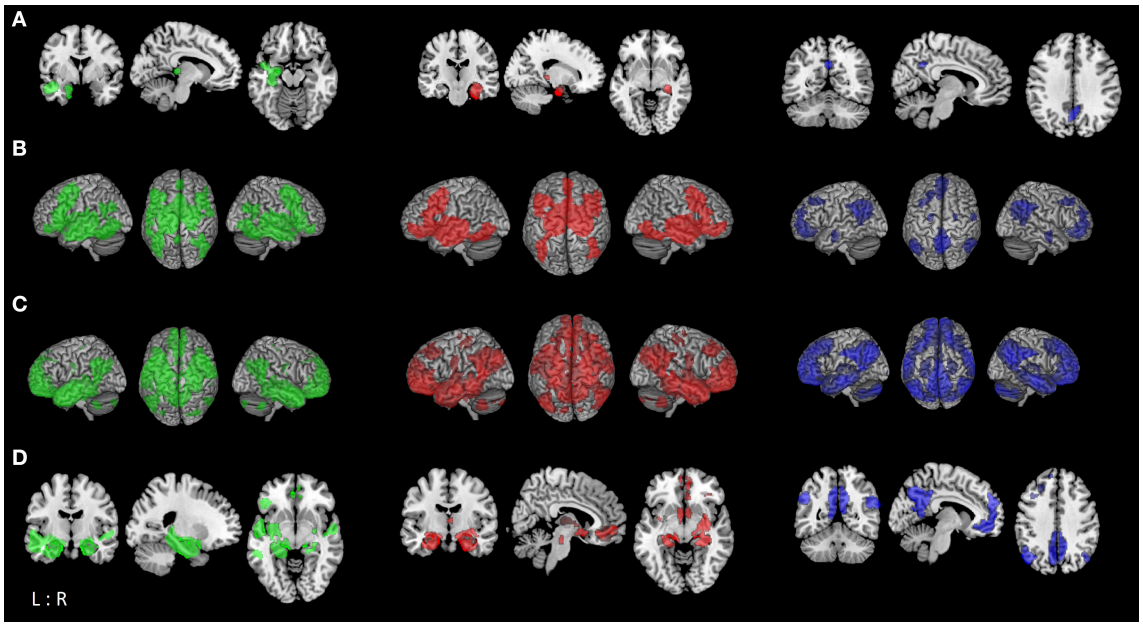

FIGURE 1 | Functional connectivity modeling of MCI-atrophy seeds. **(A)** Location of the seed regions (*left (green)*: left temporal seed; *middle (red)*: right temporal seed; *right (blue)*: parietal seed [same color coding for **(B–D)**]) showing convergent evidence of atrophy as revealed by coordinate-based meta-analysis across voxel-based morphometry studies in MCI (8). **(B)** Task-based brain-wide co-activation maps of the respective seed regions as revealed by meta-analytic connectivity modeling (MACM; cluster-level FWE corrected at $p < 0.05$, $p < 0.001$ at voxel-level). **(C)** Resting-state connectivity of respective seeds (FWE corrected at $p < 0.05$). **(D)** Conjunction between MACM and resting-state connectivity of respective seed regions using minimum statistic (19).

Statistical analysis was performed in correspondence to the MACM analysis as described above. Pearson correlation coefficients were transformed into Fisher's Z-scores in a connectivity matrix and tested for consistency across subjects in a second-level ANOVA with age included as a nuisance regressor. We first assessed resting-state connectivity of each atrophy seed separately (FWE corrected at voxel-level with $p < 0.05$). Subsequently, we performed contrast analyses between connectivity networks of the MCI-related atrophy seeds, and additionally calculated correlations between voxel-wise co-activation of each seed region and age (cFWE corrected $p < 0.05$, $p < 0.001$ at voxel-level).

Conjunction of Task-Based MACM and Task-Free Resting-State Functional Connectivity

We performed conjunction analyses between resting-state and task-based (MACM) functional connectivity maps of seed regions using the minimum statistics (19). The aim here was to identify the brain-wide co-activation profile of each atrophy area in both task-related and task-free states yielding a more robust and mode-independent delineation of networks functionally connected to the seed regions (17, 36).

Behavioral Characterization

For further differentiation of the seed regions affected in MCI a behavioral characterization was performed. MCI-related atrophy clusters were submitted to functional profiling using meta-data of the BrainMap database. In the BrainMap taxonomy, behavioral domains (BD) describe the specific mental process isolated by the statistical contrast of each archived neuroimaging experiment (23) and include the main categories of cognition, action, perception, emotion, interoception, as well as their related subcategories. Additionally, paradigm classes (PC) define the specific tasks employed in the experiment (for a complete list of taxonomy cf. http://brainmap.org/scribe/). Each cluster was analyzed regarding its associated behavioral domain and paradigm class by computing conditional probabilities (forward [P(activation | domain or paradigm)] and reverse inference [P(domain or paradigm | activation)]) (17, 36). For forward inference, significant over-representation of BD and PC in the experiments activating the respective seed region relative to the overall chance of finding activation in that particular seed across the BrainMap database was assessed using a binomial test at $p < 0.05$, FDR corrected (20, 28). For the reverse inference, a seed's functional profile was determined by identifying the most probable BD and PC given activation in a particular cluster using chi-square tests ($p < 0.05$, FDR corrected) (20). Statistical overrepresentation of a specific behavioral domain and paradigm class allowed the identification of the functional role of the selected seed region (36).

RESULTS

Task-Based Functional Connectivity of Seed Regions (MACM)

The co-activation patterns revealed by MACM were similar for the left and right temporal seed, and demonstrated convergent

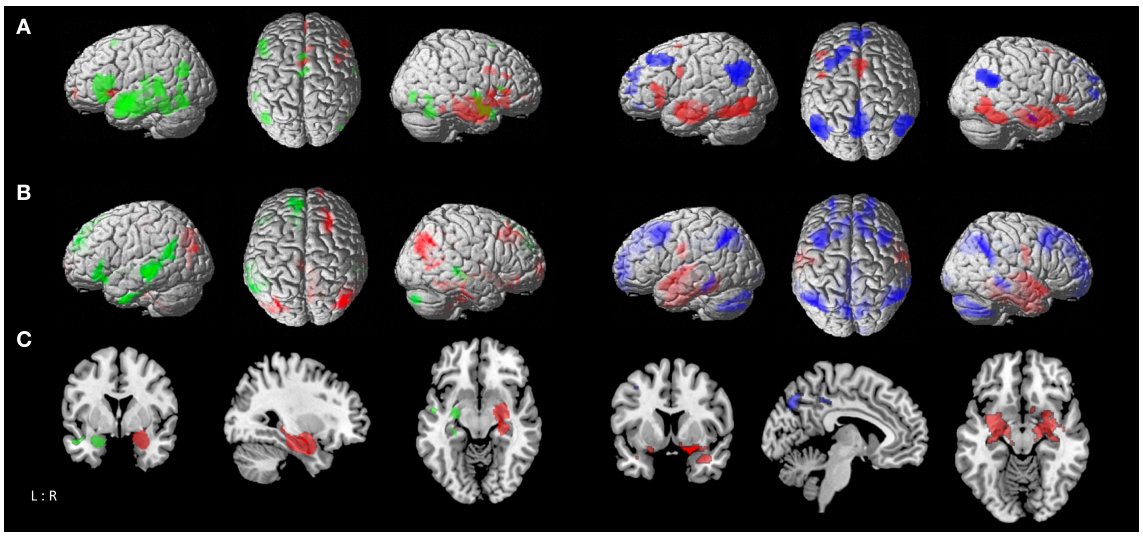

FIGURE 2 | Comparison of functional connectivity maps between atrophy seeds. **(A)** *left*: MACM contrasts between left and right temporal seeds, with *green* areas showing stronger connectivity to left temporal seed, and *red* areas showing stronger connectivity to right temporal seed; *right*: MACM contrasts of parietal seed against the conjunction of left and right temporal seeds, with *blue* areas showing stronger connectivity to parietal seed, and *red* areas showing stronger connectivity to both right and left temporal seeds. **(B)** *left*: Resting-state connectivity contrasts between left and right temporal seeds; *right*: contrast of parietal seed against the conjunction of left and right temporal seeds [color coding as in A]. **(C)** Conjunction of MACM and resting-state contrast maps; *left*: contrasts between left and right temporal seeds; *right*: contrast of parietal seed against the conjunction of left and right temporal seeds [color coding as in **(A)**].

connectivity with the hippocampus, amygdala, thalamus, and striatum (caudate nucleus, putamen), and cortically in the posterior medial frontal gyrus (supplementary motor area, SMA), inferior frontal gyrus, middle orbital and rectal gyrus, insula, fusiform gyrus (FG4, FG2), right inferior temporal and inferior occipital gyrus, as well as cerebellum (lobule VI). The left temporal seed additionally demonstrated co-activation with bilateral middle and inferior temporal areas, left cerebellum (lobule VI), left inferior parietal lobe (IPL, mainly PGa, PFm), parietal operculum and precuneus. MACM of the parietal cluster showed convergent co-activation with the precuneus, posterior cingulate cortex (PCC), middle orbital and rectal gyrus, superior medial and anterior cingulate cortex (ACC), IPL (PGa, PFm, PGp), angular gyrus, left middle and superior frontal gyrus, right middle temporal gyrus as well as amygdala and hippocampus (**Figure 1B**; **Table S-1**).

In the statistical comparison of both temporal seeds the left temporal cluster showed in contrast to the contralateral one stronger connectivity with the bilateral fusiform gyrus (FG3, FG4), middle temporal gyrus and cerebellum (lobules VI-VII), left inferior temporal and frontal gyrus, inferior occipital and angular gyrus. The right temporal seed had a stronger focus on the bilateral basal ganglia (caudate nucleus, putamen, pallidum), middle orbital gyrus and right middle cingulate cortex. Contrasting both temporal seeds with the parietal one delineated co-activation of temporal seeds in the bilateral hippocampus, amygdala, striatum, fusiform gyrus, inferior occipital gyrus, middle cingulate cortex, cerebellum (lobule VI) and the left inferior frontal gyrus. The parietal seed revealed stronger convergence compared to the temporal seeds in the middle orbital and rectal gyrus areas, superior medial frontal and ACC, angular gyrus, and left middle and superior frontal gyrus (**Figure 2A**; **Table S-2**).

Task-Free Functional Connectivity of Seed Regions (Resting-State fMRI)

Resting-state connectivity modeling results of the left and right temporal seeds were again very similar, both showing co-activation with the hippocampus, amygdala, thalamus, precuneus, PCC, angular and middle temporal gyrus, fusiform (FG3, FG4) and rectal gyrus. On the other hand, the right temporal seed co-activated with the superior frontal gyrus, pre- and post-central gyrus, right superior occipital and angular gyrus. While both seeds showed connectivity with cerebellar lobules IX-X and VIIa, the left temporal seed additionally co-activated with lobules IV–VI. The parietal seed exhibited a more widespread connectivity pattern than in the MACM analysis. This included orbital gyri, cingulate cortex, medial frontal and fronto-insular cortex, angular gyrus, middle and inferior temporal gyrus, hippocampus and amygdala, and the cerebellar lobule IX (**Figure 1C**; **Table S-3**).

Contrasting the left temporal seed with the contralateral one delineated stronger co-activation in the middle temporal gyrus, left inferior and superior frontal gyrus, insula, angular gyrus, inferior temporal gyrus, putamen, and right cerebellum (lobule VIIa), while the right temporal seed delineated more right-hemispheric convergence in the temporal and fusiform gyrus (FG4, FG3), angular gyrus, precuneus and middle cingulate cortex, middle and superior frontal gyrus, middle orbital gyrus, and cerebellum (lobule IX, X), as well as the bilateral striatum (caudate nucleus and putamen). The temporal seeds had a stronger focus in comparison to the parietal one on

TABLE 1 | Functional connectivity of MCI-atrophy seeds.

Cluster #	k_E	MNI co-ordinates*			Lat.	Macroanatomical and cytoarchitectonic region
		x	y	z		
Temporal left						
Cluster 1	5375	−24	−12	−34	L	Hippocampus (CA, EC, SUB, DG), parahippocampal gyrus, amygdala (LB, SF, CM), thalamus, superior and middle temporal gyrus, fusiform gyrus, insula lobe
Cluster 2	1962	42	14	−34	R	Hippocampus (CA, EC, SUB, DG), amygdala (LB, SF, CM), thalamus, superior and middle temporal gyrus
Cluster 3	399	−42	26	−16	L	Inferior frontal gyrus (p. opercularis, p. orbitalis)
Cluster 4	292	−8	−56	6	L	Precuneus, PCC, calcarine gyrus
Cluster 5	255	−48	−68	16	L	Middle temporal gyrus
Cluster 6	116	−2	40	−20	L	Rectal gyrus
Cluster 7	79	40	−44	−28	R	Fusiform gyrus
Cluster 8	66	4	42	−20	R	Rectal gyrus
Temporal right						
Cluster 1	3307	30	−10	−31	R	Hippocampus (CA, SUB, DG, EC, HATA), amygdala (LB, SF, CM), thalamus, fusiform gyrus, pallidum, putamen
Cluster 2	2379	−24	−12	−32	L	Hippocampus (CA, SUB, DG, EC, HATA), amygdala (LB, SF, CM), thalamus, fusiform gyrus, parahippocampal gyrus
Cluster 3	300	42	−48	−28	R	Fusiform gyrus
Cluster 4	240	2	42	−22	R	Rectal gyrus
Cluster 5	160	−2	42	−22	L	Rectal gyrus
Cluster 6	114	42	26	18	R	Inferior frontal gyrus (p. orbitalis)
Cluster 7	91	6	−2	0	R/L	Medial thalamus
Cluster 8	52	46	−74	−2	R	Inferior occipital gyrus
Precuneus						
Cluster 1	1442	−10	−56	2	L	Precuneus, PCC, MCC, lingual gyrus
Cluster 2	1221	−52	−68	14	L	Angular gyrus. IPL
Cluster 3	1052	10	−56	10	R	Precuneus, PCC, MCC, calcarine gyrus
Cluster 4	962	−2	46	−22	L	Rectal gyrus, middle orbital gyrus, ACC
Cluster 5	805	50	−70	16	R	Angular gyrus, IPL
Cluster 6	527	−36	18	40	L	Superior and middle frontal gyrus
Cluster 7	354	2	42	−20	R	Rectal gyrus
Cluster 8	168	56	−8	−28	R	Middle temporal gyrus

*Conjunction of both task-based (MACM) and task-free (resting-state) functional connectivity maps of each MCI-atrophy seed (cluster-level FWE corrected at $p < 0.05$; cluster-forming threshold $p < 0.001$). *Cluster-maxima in MNI space. k_E, cluster extent; Lat., laterality; L, left; R, right; CA, cornu ammunis; EC, entorhinal cortex; SUB, subiculum; DG, dentate gyrus; HATA, hippocampus–amygdala-transition-area; LB, laterobasal; SF, superficial; CM, centromedial; MCC, middle cingulate cortex; PCC, posterior cingulate cortex.*

the post-central gyrus, fusiform gyrus (FG3, FG4), superior temporal gyrus, and left inferior temporal gyrus in addition to hippocampal and amygdalae regions. The parietal seed on the other hand had more pronounced connectivity with the precuneus, ACC and PCC, superior and middle frontal gyrus, angular gyrus, middle temporal gyrus, thalamus and cerebellar lobules (**Figure 2B**; **Table S-4**).

TABLE 2 | Comparison of functional connectivity maps of MCI-atrophy seeds.

Cluster #	k_E	MNI co-ordinates*			Lat.	Macroanatomical and cytoarchitectonic region
		x	y	z		
Contrast: Left > right temporal seed						
Cluster 1	290	−57	−37	1	L	Middle temporal gyrus
Cluster 2	205	−48	28	−5	L	Inferior frontal gyrus (p. orbitalis)
Cluster 3	17	−30	−6	−6	L	Putamen
Contrast: Right > left temporal seed						
Cluster 1	105	38	−12	−12	R	Thalamus, putamen
Cluster 2	39	21	−27	−3	R	Thalamus
Cluster 3	31	−8	−4	−12	L	Caudate nucleus
Cluster 4	23	10	16	−14	R	Caudate nucleus
Contrast: [right and left] temporal seeds > parietal seed						
Cluster 1	1059	−26	−12	−34	L	Hippocampus (CA, SUB), amygdala (LB, SF, CM), fusiform gyrus
Cluster 2	991	28	−8	−34	R	Hippocampus (CA, SUB), amygdala (LB, SF, CM), fusiform gyrus
Cluster 3	181	−36	−48	−26	L	Fusiform gyrus
Cluster 4	112	40	−44	−28	R	Fusiform gyrus
Contrast: Parietal seed > [right and left] temporal seeds						
Cluster 1	217	−58	−54	30	L	Angular gyrus
Cluster 2	177	−8	−72	32	L	Precuneus
Cluster 3	175	−36	18	40	L	Middle frontal gyrus
Cluster 4	80	60	−50	24	R	Angular gyrus
Cluster 5	23	−6	−34	40	L	MCC

*Conjunction of both task-based (MACM) and task-free (resting-state) functional connectivity maps of each MCI-atrophy seed (cluster-level FWE corrected $p < 0.05$, $p < 0.001$ at voxel-level). *Cluster-maxima in MNI space. k_E, cluster extent; Lat., laterality; L, left; R, right; CA, cornu ammunis; EC, entorhinal cortex; SUB, subiculum; DG, dentate gyrus; HATA, hippocampus–amygdala-transition-area; LB, laterobasal; SF, superficial; CM, centromedial, MCC, middle cingulate cortex.*

Conjunction of Task-Based and Task-Free Functional Connectivity

To outline a more robust and mode-independent co-activation profile of each atrophy area we performed conjunction analyses between resting-state and MACM maps of seed regions. Here we found convergent co-activation with the left temporal cluster in the left inferior frontal gyrus, insula, PCC and precuneus, bilateral middle, and superior temporal gyrus in addition to the hippocampus, amygdala, and thalamus. The fusiform gyrus (FG3, FG4), rectal gyrus and left parahippocampal gyrus were co-activated with both temporal clusters, while the right inferior frontal and occipital gyrus, putamen, and pallidum demonstrated connectivity only with the ipsilateral temporal seed. The parietal cluster demonstrated convergent connectivity with the precuneus, PCC and ACC, angular gyrus, rectal/middle orbital gyrus, left middle and superior frontal gyrus, and right middle temporal gyrus (**Figure 1D**; **Table 1**). Conjunction analysis of

all three seed regions across modalities revealed common co-activation within the bilateral rectal gyrus and hippocampus.

Contrasting both temporal seeds, the left temporal cluster revealed stronger co-activation with the left putamen, middle temporal gyrus, as well as inferior frontal gyrus. The right temporal cluster showed more co-activation in the right putamen, thalamus and bilateral caudate nucleus. Both right and left temporal seeds exhibited stronger connectivity compared with the parietal seed in the hippocampus, amygdala, and fusiform gyrus. The parietal seed demonstrated co-activation primarily in cortical structures including the left middle frontal gyrus and middle occipital gyrus, and bilateral angular gyrus (**Figure 2C**; **Table 2**).

Behavioral Characterization of Seed-Regions

Behavioral characterization of the MCI-atrophy seeds using meta-data from the BrainMap database indicated that activation in the left temporal cluster in contrast to the right temporal seed was elicited by cognitive domains related to language syntax, speech and semantics as well as motor learning. The right temporal cluster showed high probability of activation in the domains of emotion and attention. Activation was more likely in the left temporal cluster given paradigm classes of naming, action observation, drawing and figurative language as well as syntactic discrimination (**Figure 3A**), while the right temporal cluster demonstrated a focus on the paradigm class of reward. In order to outline distinctive behavioral associations of temporal vs. parietal atrophy regions, we contrasted both temporal seeds against the parietal seed and found predominance of the domains perception (gustation and olfaction), action (observation), and cognition (memory) for the temporal clusters. Paradigms were classical conditioning, olfactory discrimination, action observation, encoding, and affective pictures. Activation in the parietal cluster was elicited given the domains social cognition and perception of motion, and paradigm classes of semantic discrimination, episodic recall, passive listening, and theory of mind (**Figure 3B**).

Age-Dependent Functional Connectivity of Seed-Regions

Resting-state functional connectivity decreased with higher age between the left temporal cluster and the hippocampus, amygdala, orbitofrontal area, medial frontal cortex, fusiform gyrus, middle and inferior temporal gyrus, angular gyrus, and precuneus. A similar pattern was observed for the right temporal seed, which additionally showed negative associations with age in precentral and post-central gyrus, while the connectivity of the left temporal seed with right temporal areas was negatively correlated with age. The parietal seed only revealed a decrease in connectivity to the anterior insula with higher age (**Figure 4A**; **Table 3**). We also found positive correlations between age and resting-state connectivity. Both the left and right temporal seed showed increased connectivity with higher age mainly with the lateral prefrontal cortex, inferior parietal lobe, insula and cerebellum (lobules VI, VIIa). The parietal cluster demonstrated increased co-activation with the middle temporal gyrus, middle occipital gyrus, angular gyrus and the precuneus with higher age (**Figure 4B**; **Table 3**).

DISCUSSION

Based on convergent morphological changes in MCI, we conducted task-based and task-free connectivity analyses and identified neural networks giving further insight into the pathophysiological relevance of structural damage in MCI. For each atrophy seed, we observed widespread but also distinct connectivity patterns and respective behavioral characteristics. While the left temporal seed showed stronger associations with a fronto-temporal network and an emphasis on language generation, the right temporal atrophy cluster was more linked to cortico-striatal regions and the domains of emotion and attention. The parietal seed demonstrated strong connectivity within the DMN, in particular with frontoparietal regions and was associated with introspection and social cognition. These networks suggest increased vulnerability in MCI due to beginning degenerative processes in important hub centers functionally connected to these areas and may underlie the heterogeneous clinical picture in this syndrome. Correlation analysis revealed both decreasing and increasing functional connectivity of atrophy seeds with higher age that may augment pathological processes but also indicates potential compensatory mechanisms of functional reorganization.

Functional Connectivity of Temporal Atrophy Seeds

Investigations into cerebral network characteristics are important for our understanding of neurodegenerative diseases, in particular given the notion of disease spreading along neuronal pathways rather than by spatial proximity (37, 38). More important than proximity seems to be the functional association with certain hub regions of the brain (39). To this end we assessed functional connectivity patterns of regions at risk in MCI that may facilitate identification of disease-related network disruptions. Functional connectivity analysis of temporal seeds revealed widespread but also distinct patterns of co-activation related to each temporal seed. In particular the *right* temporal seed showed convergent co-activation with a fronto-striatal network including orbitofrontal regions, the caudate nucleus, putamen and pallidum. This is of clinical importance since the striatum is involved not merely in motor functions but also in executive control and motivational processes, such as experience of reward and punishment (40–42). Convergent functional connectivity of the right temporal seed with the medial orbitofrontal cortex (OFC) additionally suggests a functional link to emotional control and reward processing (43–45). According to the hypothesis of network-spreading in neurodegenerative diseases, functionally connected regions are subject to a higher risk of disease-related vulnerability. Hence, this convergent functional connectivity pattern of morphologically affected right temporal regions may help to explain the high prevalence

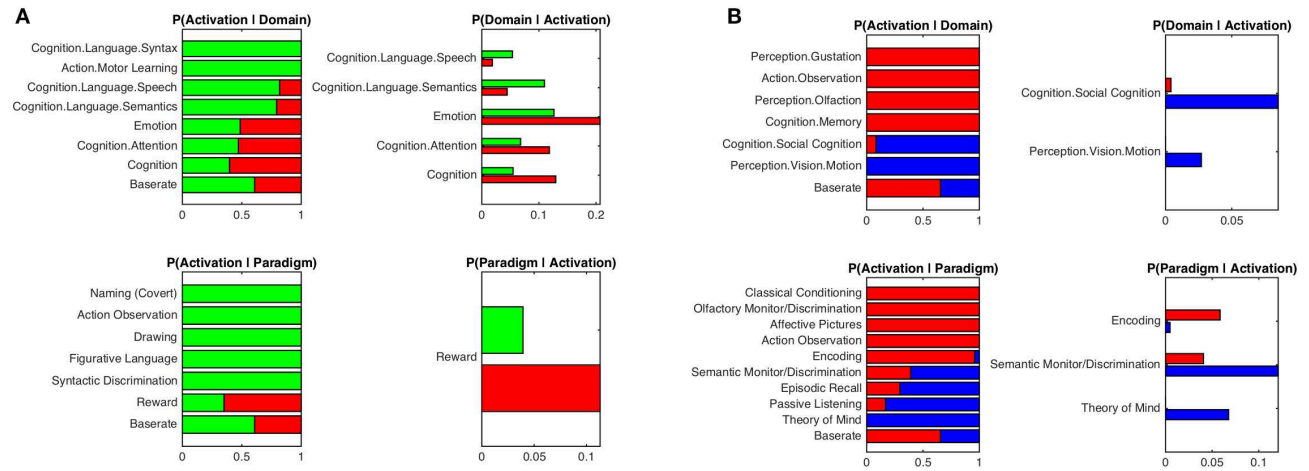

FIGURE 3 | Functional characterization of atrophy seeds by behavioral domains and paradigm classes. **(A)** Functional characterization by behavioral domains and paradigm classes of left temporal seed (*green*) in contrast to right temporal seed (*red*). **(B)** Functional characterization by behavioral domains and paradigm classes of parietal seed (*blue*) in contrast to the conjunction of left and right temporal seeds (*red*). Bar plots show significant associations (at $p < 0.05$, FDR corrected) of behavioral domains and paradigm classes from the BrainMap meta-data given observed brain activity (and vice versa); the x-axis indicates relative probability values.

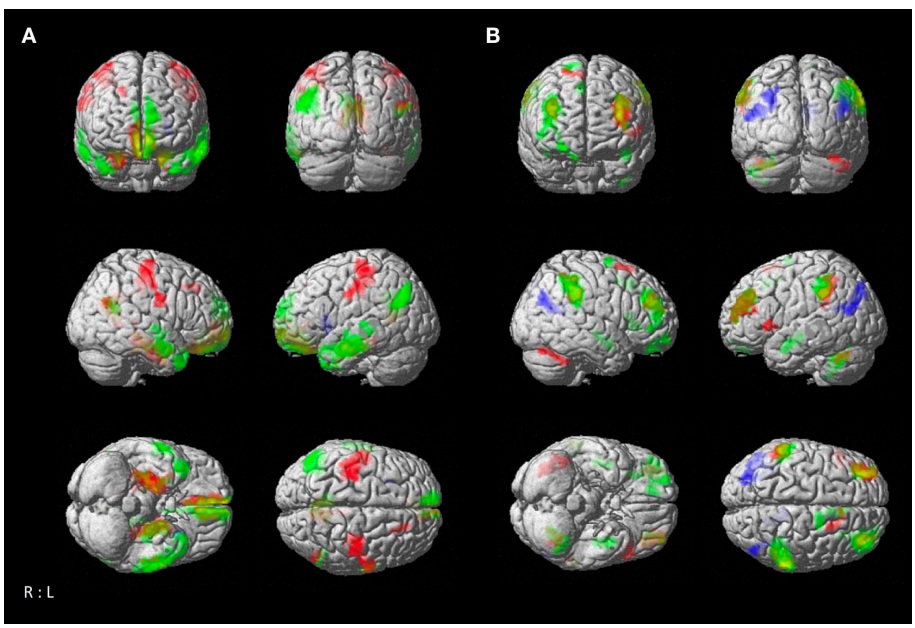

FIGURE 4 | Resting-state connectivity correlation of atrophy seeds with age. **(A)** Negative correlation between age and brain-wide resting-state connectivity of seeds (*green*: left temporal seed; *red*: right temporal seed; *blue*: parietal seed). **(B)** Positive correlation between age and brain-wide resting-state connectivity of seeds with age [color coding as in **(A)**]. Results are cluster-level FWE corrected at $p < 0.05$ ($p < 0.001$ at voxel-level).

of psychiatric disorders such as depression in MCI patients (46), since neuronal pathways responsible for the generation of reward experiences and emotional control mechanisms may be disrupted. Behavioral analysis based on BrainMap meta-data emphasized these results showing associations of the right temporal seed with the paradigm class of reward, and the domains of emotion and attention. Nonetheless, the domain of emotion and reward processes are not entirely independent from each other and can be interlinked in the BrainMap taxonomy, whereby a clear distinction between studies eliciting activation in this region is difficult.

The *left* temporal seed on the other hand had a stronger functional connectivity with a fronto-temporal network, and behavioral decoding of the left temporal seed supported an emphasis on speech, semantic and syntax. Semantic deficiencies have been reported in MCI-patients (47) and can be observed

TABLE 3 | Resting-state fMRI connectivity correlations with age.

k_E	MNI co-ordinates*			Lat.	Anatomical region	k_E	MNI co-ordinates*			Lat.	Anatomical region
	x	y	z				x	y	z		
Left temporal seed: Negative correlation						**Positive correlation**					
1385	−4	64	−8	L	Middle orbital, rectal gyrus, superior medial gyrus	1163	60	−36	36	R	Angular gyrus
1108	−60	−6	−22	L	Middle and inferior temporal gyrus	791	36	50	28	R	Middle frontal gyrus, inferior frontal gyrus
845	−26	−14	−22	L	Hippocampus (DG, SUB, CA, HATA), amygdala (CM, SF), parahippocampal gyrus	527	−32	46	32	L	Middle frontal gyrus
835	−50	−70	36	L	Angular gyrus	440	−56	−36	52	L	Inferior parietal lobe, supramarginal gyrus
633	−8	−54	10	L	Precuneus, PCC, calcarine gyrus	397	−28	−62	−30	L	Cerebellum (Crus 1, VI, VIIa)
488	18	−8	−20	R	Hippocampus (HATA, SUB, CA), amygdala (SF, LB), fusiform gyrus	283	−40	0	−20	L	Insula
449	2	38	−22	R	Rectal gyrus, middle orbital gyrus	178	26	60	−16	R	Middle orbital gyrus, superior orbital gyrus
372	6	−52	16	R	Precuneus, calcarine gyrus	173	6	20	46	R	Superior medial gyrus
351	62	0	−20	R	Middle and superior temporal gyrus	138	44	−12	−10	R	Superior temporal gyrus, insula
256	40	12	−36	R	Medial temporal pole	130	34	20	12	R	Insula lobe
140	4	62	10	R	Superior medial gyrus, ACC	115	20	−4	70	R	Superior frontal gyrus
130	48	−54	18	R	Middle temporal gyrus, angular gyrus						
102	−66	−24	2	L	Middle temporal gyrus						
Right temporal seed: Negative correlation						**Positive correlation**					
1197	20	−8	−22	R	Hippocampus (CA. SUB, DG), amygdala (LB, CM), fusiform gyrus	706	−32	50	30	L	Middle frontal gyrus, inferior frontal gyrus (p. triangularis)
1119	−36	−28	58	L	Precentral gyrus (Area 4a), post-central gyrus(1,3b)	367	−56	−42	52	L	Angular gyrus
774	6	−54	14	R	Precuneus, calcarine gyrus, lingual gyrus, PCC	282	38	−70	−24	R	Cerebellum (Crus 1, VIIa)
704	4	50	−16	R	Rectal, middle orbital gyrus, superior medial gyrus	273	64	−40	42	R	Supramarginal gyrus, angular gyrus
694	−22	−12	−24	L	Hippocampus (CA, DG, SUB, HATA, EC), amygdala (LB, SF, CM), fusiform gyrus	256	36	38	24	R	Middle frontal gyrus
573	46	−20	58	R	Post-central gyrus (1, 3b), precentral gyrus (4a, p)	197	−34	−56	−30	L	Cerebellum (Crus 1, VI, VIIa)
454	−4	64	−6	L	Middle orbital gyrus, rectal gyrus, ACC	126	−48	20	4	L	Inferior frontal gyrus (p. triangularis)
422	−10	−56	10	L	Precuneus, PCC	108	18	18	64	R	Superior frontal gyrus
258	56	−14	44	R	Post-central gyrus (Area 1, 3b)						
114	50	−60	28	R	Angular gyrus						
107	22	30	42	R	Middle and superior frontal gyrus						
106	−62	−2	−22	L	Middle and inferior temporal gyrus						
Parietal seed: Negative correlation						**Positive correlation**					
98	−26	14	6	L	Insula lobe	610	−52	−68	16	L	Middle temporal, middle occipital, angular gyrus
						260	44	−68	28	R	Middle occipital, angular, middle temporal gyrus
						159	16	−44	28	R	Precuneus, PCC

*Correlation between age and resting-state fMRI connectivity of each MCI-atrophy seed (cluster-level FWE corrected at $p < 0.05$; cluster-forming threshold $p < 0.001$). *Cluster-maxima in MNI space. k_E, cluster extent; Lat., laterality; L, left; R, right; CA, cornu ammunis; EC, entorhinal cortex; SUB, subiculum; DG, dentate gyrus; HATA, hippocampus–amygdala-transition-area; LB, laterobasal; SF, superficial; CM, centromediale; ACC, anterior cingulate cortex; PCC, posterior cingulate cortex; Id, insular dysgranular area; Ig, insular granular area; IPL, inferior parietal lobule.*

in neurodegenerative dementias. In particular, the convergent co-activation with the left inferior frontal gyrus, both in task-dependent and task-independent analysis, suggests susceptibility in pathways playing a role in speech generation, and accords with observed vulnerability to atrophy of the inferior frontal gyrus in patients with Alzheimer's disease (48). Task-dependent analysis additionally revealed functional connectivity between the left temporal seed and cerebellar lobule VI and VII. This is of interest as the cerebellum is involved in a broad range of cognitive domains (49–51). Particularly right lobule VI, which connects to the left cerebral hemisphere, is involved in language processes (52). Hence, disruptions in these pathways emanating from left temporal degeneration may be susceptible to functional impairment as observed in MCI. Interestingly, in case of temporal lobe epilepsy with hippocampal atrophy morphometric changes in the cerebellum have been described before (53). Task-independent co-activation with the left and the right temporal seeds was found in lobule IX of the cerebellum, which has been described as being part of the default-mode network (DMN) (54). In the parietal lobe we further found pronounced co-activation with structures of the DMN such as the angular gyrus, which is considered to be a connecting hub and involved in memory functions, theory of mind and social cognition (55, 56). Altered DMN connectivity has been consistently reported in Alzheimer's disease, and based on longitudinal studies the strength of interregional connectivity seems to decrease when MCI patients convert to dementia (11). While targeted studies need to further evaluate the specific diagnostic and prognostic value of network alterations for the course of MCI, the functional connectivity profiles of the temporal seeds offer a framework to characterize possible network damage in MCI and neural correlates of subsequent MCI-related neuropsychological deficits. The delineated convergence patterns of functional connectivity indicate differential networks formed by each atrophy seed and related to specific behavioral symptoms. While the left temporal seed had a stronger convergence with a fronto-temporal network associated with speech generation, on the contralateral site connectivity patterns encompassed rather striatal and orbitofrontal regions indicating a role in emotional control.

Functional Connectivity of the Parietal Atrophy Seed

The precuneus and PCC as well as the hippocampus are part of the "rich club" of highly interconnected hub centers of the brain (13, 57), which is known for its integrative long-range connections and plays a major role in the brains ability to perform cognitive functions. The PCC and precuneus are vital parts of the DMN and abnormalities have been reported in a range of different diseases such as Alzheimer's disease (11, 58–61), schizophrenia, autism and depression (56, 62). The ventral PCC is associated with internally focused states and the dorsal part with externally directed attention (63). The precuneus is involved in monitoring and execution of spatially guided behavior, mental imagery and episodic memory retrieval (64, 65). The PCC and precuneus share intensive connections with each other and are considered as the "posterior" part of the DMN (66). Unsurprisingly, the parietal seed demonstrated a much more pronounced and widespread task-independent than task-dependent connectivity pattern including the medial prefrontal cortex, fronto-insular cortex, middle and inferior temporal gyri, hippocampus, amygdala and the posterior part of the cerebellum. The difference between those two modes illustrates the behavioral specificity of this cluster and emphasizes its role in introspection and non-directional cerebral activity. Especially functional convergence of the PCC and the ventromedial prefrontal cortex is suggestive of DMN activity (67). Task-dependent co-activation was located in the middle orbital and superior medial gyrus, left middle frontal gyrus, inferior parietal lobe, hippocampus and amygdala. Behavioral decoding showed for the parietal seed compared to the temporal clusters a significant probability for the domains of social cognition and motion perception, and the paradigms of theory of mind, semantic discrimination, episodic recall and passive listening. This reflects the parietal cluster's role in the DMN as well as in memory functions and understanding of speech. The overlap between the domain of social cognition and areas active during resting state has been described before and is being interpreted that both social cognitive processes and the resting state are linked to introspection (68). Given the DMN's known function in autobiographical remembering (18) memory deficits in MCI may also be linked to parietal volume reductions and ensuing functional network disruptions. In summary, the significance of morphological changes in the precuneus and the PCC particularly lies in their role as integrative hub regions in the brain. Network dysfunction in the case of damage to hub regions is more detrimental than in the case of less interconnected structures (57). Given the broad overlap of structures of the DMN and epicenters of connectivity, disruptions of these hubs will likely compromise network communication and the brain's ability to integrate information, which seems to be in particular at risk in case of MCI.

Effects of Aging on Functional Connectivity

Next, we investigated age-related connectivity of MCI-typical atrophy regions and found decreasing co-activation between temporal seeds and the medial frontal, medial parietal and middle and inferior temporal regions with higher age, while connectivity to lateral prefrontal and parietal cortex increased in older subjects. The shift of higher functional connectivity in older individuals from the OFC to the dorsolateral prefrontal cortex (DLPFC) is in line with previous literature that described greater age differences in OFC-sensitive cognitive tasks in comparison to DLPFC tasks supporting the notion that the OFC is susceptible to earliest age-related changes (69). Furthermore, a posterior/anterior-shift of task-dependent activation has been described with aging in which activation shifts from parietal and occipital regions toward prefrontal areas implicating compensatory recruitment of prefrontal regions due to age-related sensory-processing deficits (70, 71). Age-related increases in brain activity, however, do not only involve the frontal lobe, but have also been reported for parietal structures (70, 71). Our analysis showed a pattern of decreasing task-independent connectivity between the temporal

seeds and parietal, medial orbitofrontal and temporal regions with higher age, whereas connectivity to the lateral PFC and inferior parietal regions (supramarginal gyrus) increased. Hence, the age-dependent posterior-anterior shift may to some extent also apply to connectivity changes at rest, as also previously reported by Roski et al. (72). Interestingly, temporal seeds further demonstrated an increase of connectivity with cerebellar lobules VI and VII suggesting that the cerebellum might be involved in adaptive processes of the aging brain. However, it is important to note that we cannot infer based on our current analysis in healthy individuals if such a compensation strategy is also maintained in MCI or already overcome by MCI-related pathological changes. On the other hand, given that patients with MCI exhibit cognitive deficits without relevant impact on daily living, it seems reasonable that such a neural reorganization pattern may contribute to preserve functional maintenance in MCI, which needs to be addressed in future imaging studies comparing MCI and healthy aging.

Finally, we found mainly positive correlations between age and connectivity of the parietal cluster with the middle occipital gyrus, middle temporal gyrus, and angular gyrus. Decreasing connectivity with higher age could only be found in the insula, in contrast to the more widespread pattern of age-related decline of connectivity of the temporal clusters. In accordance with this, the PCC is known for its relatively good preservation in age (73), and seems to be subject to relatively fewer alterations in normal aging than pathological processes such as Alzheimer's disease and MCI (74). Additionally, the increasing connectivity within parietooccipital areas with higher age may also reflect an age-dependent loss of functional specialization (e.g., sensory-processing functions) in terms of a dedifferentiation process and decrease in intra-network distinctiveness. This notion of neural dedifferentiation has been postulated for cognitive functioning in the aging brain [e.g., (75)] and was also shown for resting-state connectivity (72), which may likely be augmented due to MCI-related morphological changes and network disruptions constricting the brains ability to adapt to the aging process.

LIMITATIONS AND CONCLUSIONS

Based on structurally-affected areas in MCI that are consistent across studies, we investigated ensuing functional alterations emanating from this degenerative pattern as well as their possible clinical relevance. However, it is important to note that our approach relies upon networks derived from healthy brain functioning and likely interfering with structural damage typically observed in MCI. Hence, it does not allow conclusions regarding the degree of disruptions in functional networks, disease-stage dependent effects, or any causality, but rather delineates circuits formed by nodes affected in MCI and potentially disrupted in this disease. The knowledge of these connections and their clinical impact is important and relevant as they give further insights into the functional architecture of cognitive impairment. This also pertains to our correlation analysis between functional connectivity and age in healthy individuals as discussed above. While we were able to outline age-dependent task-free functional alterations in an aging population derived from the 1000BRAINS study, this was not possible for the meta-analytical task-dependent analysis, which would have allowed further insights on age-related co-activation patterns under cognitive demand. In addition, it is noteworthy that the large database of the 1000BRAINS study was designed to allow investigations into age-related variability in brain structure and function in the general population with a focus on the aging brain. Nevertheless, we cannot rule out a certain sampling bias in particular pertaining to the here used cohort of older healthy subjects that may affect generalizability to the general aging population. Another limitation is the fact that MCI is a heterogenous syndrome with different etiologies possibly underlying mental decline, whereas precise diagnostic evaluation encompasses the measurement of biomarkers like amyloid and tau-proteins in the cerebrospinal fluid. On the other hand, given that the here used definition of MCI was not bound to a certain etiology and functional analyses were based on shared morphologically affected regions, our findings relate to network patterns associated with these nodes as a common denominator of cognitive decline (8). Hence, the here delineated functional profiles in task-free and task-driven states offer a framework to characterize the pathophysiological impact of atrophy loci found in patients with cognitive impairment. Functional connectivity analysis in concordance with behavioral characterization and previous literature demonstrated susceptibility of functional disruption in networks responsible for language generation, emotional control, theory of mind as well as non-directional cerebral activity. These areas may also have an increased vulnerability to disease spreading along network lines in neurodegenerative diseases compromising integrative capabilities of the brain, which are essential for global cognitive functioning, as well as age-related adaptive processes. These findings help to understand the ensuing clinical relevance of structural damage in MCI beyond memory deficits.

DATA AVAILABILITY STATEMENT

Datasets supporting the conclusions of this article will be made available to qualified researchers on request.

ETHICS STATEMENT

The studies involving human participants were reviewed and approved by the University of Duisburg-Essen. The patients/participants provided their written informed consent to participate in this study.

AUTHOR CONTRIBUTIONS

SE, AL, PF, KR, and ID conceived and designed the study. GS, FH, SE, and ID analyzed the data. GS, KR,

and ID interpreted the data. GS drafted the manuscript. SE, SC, TN-J, AL, JS, KR, and ID critically reviewed the manuscript.

FUNDING

KR was funded by the German Federal Ministry of Education and Research (BMBF 01GQ1402). ID was supported by the START-Program (08/16) of the Faculty of Medicine at the RWTH Aachen University.

SUPPLEMENTARY MATERIAL

The Supplementary Material for this article can be found online at: https://www.frontiersin.org/articles/10.3389/fneur.2020.00018/full#supplementary-material

REFERENCES

1. Petersen RC, Smith GE, Waring SC, Ivnik RJ, Tangalos EG, Kokmen E. Mild cognitive impairment: clinical characterization andoutcome. *Arch Neurol*. (1999) 56:303–8. doi: 10.1001/archneur.56.3.303
2. Petersen RC, Doody R, Kurz A, Mohs RC, Morris JC, Rabins PV. Current concepts in mild cognitive impairment. *Arch Neurol*. (2001) 58:1985–92. doi: 10.1001/archneur.58.12.1985
3. Gauthier S, Reisberg B, Zaudig M, Petersen RC, Ritchie K, Broich K, et al. Mild cognitive impairment. *Lancet*. (2006) 367:1262–70. doi: 10.1016/S0140-6736(06)68542-5
4. Bruscoli M, Lovestone S. Is MCI really just early dementia? A systematic review of conversion studies. *Int Psychogeriatr*. (2004) 16:129–40. doi: 10.1017/S1041610204000092
5. Mitchell AJ, Shiri-Feshki M. Rate of progression of mild cognitive impairment to dementia–meta-analysis of 41 robust inception cohort studies. *Acta Psychiatr Scand*. (2009) 119:252–65. doi: 10.1111/j.1600-0447.2008.01326.x
6. DeKosky ST, Scheff SW. Synapse loss in frontal cortex biopsies in Alzheimer's disease: Correlation with cognitive severity. *Ann Neurol*. (1990) 27:457–64. doi: 10.1002/ana.410270502
7. Persson J, Nyberg L, Lind J, Larsson A, Nilsson LG, Ingvar M, et al. Structure-function correlates of cognitive decline in aging. *Cereb Cortex*. (2006) 16:907–15. doi: 10.1093/cercor/bhj036
8. Nickl-Jockschat T, Kleiman A, Schulz JB, Schneider F, Laird AR, Fox PT, et al. Neuroanatomic changes and their association with cognitive decline in mild cognitive impairment: a meta-analysis. *Brain Struct Funct*. (2012) 217:115–25. doi: 10.1007/s00429-011-0333-x
9. Petersen RC. Mild cognitive impairment as a diagnostic entity. *J Intern Med*. (2004) 256:183–94. doi: 10.1111/j.1365-2796.2004.01388.x
10. Pievani M, Filippini N, van den Heuvel MP, Cappa SF, Frisoni GB. Brain connectivity in neurodegenerative diseases–from phenotype to proteinopathy. *Nat Rev Neurol*. (2014) 10:620–33. doi: 10.1038/nrneurol.2014.178
11. Hohenfeldt C, Werner CJ, Reetz K. Resting-state connectivity in neurodegenerative disorders: is there potential for an imaging biomarker? *Neuroimage Clin*. (2018) 18:849–70. doi: 10.1016/j.nicl.2018.03.013
12. Warren JD, Rohrer JD, Schott JM, Fox NC, Hardy J, Rossor MN. Molecular nexopathies: a new paradigm of neurodegenerative disease. *Cell Press*. (2013) 36:561–9. doi: 10.1016/j.tins.2013.06.007
13. Sporns O. Structure and function of complex brain networks. *Dialogues Clin Neurosci*. (2013) 15:247–62.
14. Cohen JR, D'Esposito M. The segregation and integration of distinct brain networks and their relationship to cognition. *J Neurosci*. (2016) 36:12083–94. doi: 10.1523/JNEUROSCI.2965-15.2016
15. Laird AR, Eickhoff SB, Kurth F, Fox PM, Uecker AM, Turner JA,et al. ALE meta-analysis workflows via the brainmap database: progress towards a probabilistic functional brain atlas. *Front Neuroinform*. (2009) 9:3–23. doi: 10.3389/neuro.11.023.2009
16. Caspers S, Moebus S, Lux S, Pundt N, Schütz H, Mühleisen TW, et al. Studying variability in human brain aging in a population-based German cohort-rationale and design of 1000BRAINS. *Front Aging Neurosci*. (2014) 14:149. doi: 10.3389/fnagi.2014.00149
17. Rottschy C, Caspers S, Roski C, Reetz K, Dogan I, Schulz JB, et al. Differentiated parietal connectivity of frontal regions for "what" and "where" memory. *Brain Struct Funct*. (2013) 218:1551–67. doi: 10.1007/s00429-012-0476-4
18. Spreng RN, Wojtowicz M, Grady CL. Reliable differences in brain activity between young and old adults: a quantitative meta-analysis across multiple cognitive domains. *NeurosciBiobehav Rev*. (2010) 34:1178–94. doi: 10.1016/j.neubiorev.2010.01.009
19. Nichols T, Brett M, Andersson J, Wagner T, and Poline JB. Valid conjunction inference with the minimum statistic.*Neuroimage*. (2005) 25:653–60. doi: 10.1016/j.neuroimage.2004.12.005
20. Laird AR, Eickhoff SB, Li K, Robin DA, Glahn DC, Fox PT. Investigating the functional heterogeneity of the default mode network using coordinate-based meta-analytic modeling. *J Neurosci*. (2009) 29:14496–505. doi: 10.1523/JNEUROSCI.4004-09.2009
21. Eickhoff SB, Jbabdi S, Caspers S, Laird AR, Fox PT, Zilles K, et al. Anatomical and functional connectivity of cytoarchitectonic areas within the human parietal operculum. *The Journal of Neuroscience*. (2010) 30: 6409–21. doi: 10.1523/JNEUROSCI.5664-09.2010
22. Fox PT, Lancaster JL, Laird AR, Eickhoff SB. Meta-analysis in human neuroimaging: computational modeling of large-scale databases. *Annu Rev Neurosci*. (2014) 37:409–34. doi: 10.1146/annurev-neuro-062012-170320
23. Laird AR, Fox PM, Eickhoff SB, Turner JA, Ray KL, McKay DR,et al. Behavioral interpretations of intrinsic connectivity networks. *J Cogn Neurosci*. (2011) 23:4022–37. doi: 10.1162/jocn_a_00077
24. Laird AR, Lancaster JL, Fox PT. BrainMap: the social evolution of a human brain mapping database. *Neuroinformatics*. (2005) 3:65–78. doi: 10.1385/NI:3:1:065
25. Eickhoff SB, Laird AR, Grefkes C, Wang LE, Zilles K, Fox PT. Coordinate-based ALE meta-analysis of neuroimaging data: a random-effects approach based on empirical estimates of spatial uncertainty. *Hum Brain Mapp*. (2009) 30:2907–26. doi: 10.1002/hbm.20718
26. Eickhoff SB, Bzdok D, Laird AR, Kurth F, Fox PT. Activation Likelihood Estimation meta-analysis revisited. *Neuroimage*. (2012) 59:2349–61. doi: 10.1016/j.neuroimage.2011.09.017
27. Turkeltaub PE, Eickhoff SB, Laird AR, Fox M, Wiener M, Fox P. Minimizing within-experiment and within-group effects in Activation Likelihood Estimation meta-analyses. *Hum Brain Mapp*. (2012) 33:1–13. doi: 10.1002/hbm.21186
28. Eickhoff SB, Bzdok D, Laird AR, Roski C, Caspers S, Zilles K, et al. Co-activation patterns distinguish cortical modules, their connectivity and functional differentiation. *Neuroimage*. (2011) 57, 938–949. doi: 10.1016/j.neuroimage.2011.05.021
29. Eickhoff SB, Paus T, Caspers S, Grosbras MH, Evans AC, Zilles K, et al. Assignment of functional activations to probabilistic cytoarchitectonic areas revisited. *Neuroimage*. (2007) 36:511–21. doi: 10.1016/j.neuroimage.2007.03.060
30. Kalbe E, Kessler J, Calabrese P, Smith R, Passmore AP, Brand M, et al. DemTect: a new, sensitive cognitive screening test to support the diagnosis of mild cognitive impairment and early dementia. *Int J GeriatrPsychiatry*. (2004) 19:136–43. doi: 10.1002/gps.1042
31. Salimi-Khorshidi G, Douaud G, Beckmann CF, Glasser MF, Griffanti L, Smith SM. Automatic denoising of functional MRI data: combining independent

component analysis and hierarchical fusion of classifiers. *Neuroimage*. (2014) 90:449–68. doi: 10.1016/j.neuroimage.2013.11.046
32. Ashburner J, Friston KJ. Unified segmentation. *Neuroimage*. (2005) 26:839–51. doi: 10.1016/j.neuroimage.2005.02.018
33. Satterthwaite TD, Elliott MA, Gerraty RT, Ruparel K, Loughead J, Calkins ME, et al. An improved framework for confound regression and filtering for control of motion artifact in the preprocessing of resting-state functional connectivity data. *Neuroimage*. (2013) 64:240–56. doi: 10.1016/j.neuroimage.2012.08.052
34. Fox MD, Zhang D, Snyder AZ, Raichle ME. The global signal and observed anticorrelated resting state brain networks. *J Neurophysiol*. (2009) 101:3270–83. doi: 10.1152/jn.90777.2008
35. Fox MD, Raichle ME. Spontaneous fluctuations in brain activity observed with functional magnetic resonance imaging. *Nat Rev Neurosci*. (2007) 8:700–11. doi: 10.1038/nrn2201
36. Dogan I, Eickhoff CR, Fox PT, Laird AR, Dogan I, Schulz JB, et al. Functional connectivity modeling of consistent cortico-striatal degeneration in Huntington's disease, NeuroImage: *NeuroimageClin*. (2015) 7:640–52. doi: 10.1016/j.nicl.2015.02.018
37. Warren JD, Rohrer JD, Hardy J. Disintegrating brain networks: from syndromes to molecular nexopathies. *Neuron*. (2012) 73:1060–2. doi: 10.1016/j.neuron.2012.03.006
38. Raj A, Kuceyeski A, Weiner M. A network diffusion model of disease progression in dementia. *Neuron*. (2012) 73:1204–15. doi: 10.1016/j.neuron.2011.12.040
39. Zhou J, Gennatas ED, Kramer JH, Miller BL, Seeley WW. Predicting regional neurodegeneration from the healthy brain functional connectome. *Neuron*. (2012) 73:1216–27. doi: 10.1016/j.neuron.2012.03.004
40. Di Martino A, Scheres A, Margulies DS, Kelly AM, Uddin LQ, Shehzad Z, et al. Functional connectivity of human striatum: a resting state FMRI study. *Cereb Cortex*. (2008) 18:2735–47. doi: 10.1093/cercor/bhn041
41. Smith KS, Tindell AJ, Aldridge JW, Berridge KC. Ventral pallidum roles in reward and motivation. *Behav Brain Res*. (2009) 196:155–67. doi: 10.1016/j.bbr.2008.09.038
42. Postuma RB, Dagherm A. Basal ganglia functional connectivity based on a meta-analysis of 126 positron emission tomography and functional magnetic resonance imaging publications. Cereb *Cortex*. (2006) 16:1508–21. doi: 10.1093/cercor/bhj088
43. Hahn A, Stein P, Windischberger C, Weissenbacher A, Spindelegger C, Moser E, et al. Reduced resting-state functional connectivity between amygdala and orbitofrontal cortex in social anxiety disorder. *Neuroimage*. (2011) 56:881–9. doi: 10.1016/j.neuroimage.2011.02.064
44. Bechara A, Damasio A, Damasio H, Anderson S. Insensitivity to future consequences following damage to human prefrontal cortex. *Cognition*. (1994) 50:7–15. doi: 10.1016/0010-0277(94)90018-3
45. Bechara A, Damasio H, Damasio A. Emotion, decision making and the orbitofrontal cortex. *Cerebral Cortex*. (2000) 10:295–307. doi: 10.1093/cercor/10.3.295
46. Ismail Z, Elbayoumi H, Fischer CE, Hogan DB, Millikin CP, Schweizer T, et al. Prevalence of depression in patients with mild cognitive impairment: a systematic review and meta-analysis. *JAMA Psychiatry*. (2017) 1:58–67. doi: 10.1001/jamapsychiatry.2016.3162
47. Guidi M, Paciaroni L, Paolini S, Scarpino O, Burn DJ. Semantic profiles in mild cognitive impairment associated with Alzheimer's and Parkinson's diseases. *Funct Neurol*. (2015) 30:113–8. doi: 10.11138/fneur/2015.30.2.113
48. Thomann PA, Pantel J, Wüstenberg T, Giesel FL, Seidl U, Schönknecht P, et al. Structural MRI-findings in mild cognitive impairment and Alzheimer's disease. *Psychogeriatria Polska*. (2005) 2:1–12.
49. Schmahmann JD, Sherman JC. The cerebellar cognitive affective syndrome. *Brain*. (1998) 121:561–79. doi: 10.1093/brain/121.4.561
50. Stoodley LR, Schmahmann JD. Evidence for topographic organization in the cerebellum of motor control versus cognitive and affective processing. *Cortex*. (2010) 46:831–44. doi: 10.1016/j.cortex.2009.11.008
51. Reetz K, Dogan I, Rolfs A, Binkofski F, Schulz JB, Laird AR, et al. Investigating function and connectivity of morphometric findings — exemplified on cerebellar atrophy in spinocerebellar ataxia 17 (SCA17). *Neuroimage*. (2012) 62:1354–66. doi: 10.1016/j.neuroimage.2012.05.058
52. Stoodley CJ, Valera EM, Schmahmann JD. Functional topography of the cerebellum for motor and cognitive tasks: an fMRI study. *Neuroimage*. (2012) 59:1560–70. doi: 10.1016/j.neuroimage.2011.08.065
53. Keller SS, Wieshmann UC, Mackay CE, Denby CE, Webb J, Roberts N. Voxel based morphometry of grey matter abnormalities in patients with medically intractable temporal lobe epilepsy: effects of side of seizure onset and epilepsy duration. *J Neurol Neurosurg Psychiatry*. (2002) 73:648–55. doi: 10.1136/jnnp.73.6.648
54. Habas C, Kamdar N, Nguyen D, Prater K, Beckmann CF, Menon V, et al. Distinct cerebellar contributions to intrinsic connectivity networks. *J Neurosci*. (2009) 29:8586–94. doi: 10.1523/JNEUROSCI.1868-09.2009
55. Seghier ML. The angular gyrus multiple functions and multiple subdivisions. *Neuroscientist*. (2012) 19:43–61. doi: 10.1177/1073858412440596
56. Buckner RL, Andrews-Hanna JR, and Schacter DL. The brain's default network: anatomy, function, and relevance to disease. *Ann N Y AcadSci*. (2008) 1124:1–38. doi: 10.1196/annals.1440.011
57. Van den Heuvel MP, Sporns O. Rich-club organization of the human connectome. *J Neurosci*. (2011) 31:15775–86. doi: 10.1523/JNEUROSCI.3539-11.2011
58. Raichle ME, MacLeod AM, Snyder AZ, Powers WJ, Gusnard DA, and Shulman GL. A default mode of brain function. *PNAS*. (2001) 98:676–82 doi: 10.1073/pnas.98.2.676
59. Greicius MD, Srivastava G, Reiss AL, Menon V. Default-mode network activity distinguishes Alzheimer's disease from healthy aging: evidence from functional MRI. *Proc Natl AcadSci USA*. (2004) 101:4637–42. doi: 10.1073/pnas.0308627101
60. Buckner RLMemory and executive function in aging and AD: multiple factors that cause decline and reserve factors that compensate. *Neuron*. (2004) 44:195–208. doi: 10.1016/j.neuron.2004.09.006
61. Buckner RL, Sepulcre J, Talukdar T, Krienen FM, Liu H, Hedden T, et al. Cortical hubs revealed by intrinsic functional connectivity: mapping, assessment of stability, and relation to Alzheimer's disease. *J Neurosci*. (2009) 29:1860–73. doi: 10.1523/JNEUROSCI.5062-08.2009
62. Greicius M. Resting state functional connectivity in neuropsychiatric disorders. *Curr Opin Neurol*. (2008) 21:424–30. doi: 10.1097/WCO.0b013e328306f2c5
63. Leech R, Sharpe DJ. The role of the posterior cingulate cortex in cognition and disease. *Brain*. (2014) 137:12–32. doi: 10.1093/brain/awt162
64. Zhang S, Li CS. Functional connectivity mapping of the human precuneus by resting state fMRI. *Neuroimage*. (2012) 59:3548–62. doi: 10.1016/j.neuroimage.2011.11.023
65. Wagner AD, Shannon BJ, Kahn I, Buckner RL. Parietal lobe contributions to episodic memory retrieval. *Trends Cogn Sci*. (2005) 9:445–53. doi: 10.1016/j.tics.2005.07.001
66. Yang Z, Chang C, Xu T, Jiang L, Handwerker DA, Castellanos FX, et al. Connectivity trajectory across lifespan differentiates the precuneus from the default network. *NeuroImage*. (2014) 89:45–56. doi: 10.1016/j.neuroimage.2013.10.039
67. Greicius MD, Krasnow B, Allan L, Reiss AL, Menon V. Functional connectivity in the resting brain: a network analysis of the default mode hypothesis. *PNAS*. (2003) 100:253–8. doi: 10.1073/pnas.0135058100
68. Schilbach L, Bzdok D, Timmermans B, Fox PT, Laird AR, Vogeley K, et al. Introspective minds: using ALE meta-analyses to study commonalities in the neural correlates of emotional processing, social & unconstrained cognition. *PLoS ONE*. (2012) 7:30920. doi: 10.1371/journal.pone.0030920
69. Resnick SM, Lamar M, and Driscoll, I. Vulnerability of the orbitofrontal cortex to age-associated structural and functional brain changes. *Ann N Y AcadSci*. (2007) 1121:562–75. doi: 10.1196/annals.1401.027
70. Davis SW, Dennis NA, Daselaar SM, Fleck MS, Cabeza R. Que PASA? The posterior-anterior shift in aging. *Cereb Cortex*. (2008) 18:1201–9. doi: 10.1093/cercor/bhm155
71. Grady CL, McIntosh AR, Craik FI. Age-related differences in the functional connectivity of the hippocampus during memory encoding. *Hippocampus*. (2003) 13:572–86. doi: 10.1002/hipo.10114
72. Roski C, Caspers S, Langner R, Laird AR, Fox PT, Zilles K, et al. Adult age-dependent differences in resting-state connectivity within and between

visual-attention and sensorimotor networks. *Front Aging Neurosci.* (2013) 5:67. doi: 10.3389/fnagi.2013.00067

73. Kalpouzos G, Chetelat G, Baron J, Landeau B, Mevel K, Godeau C, et al. Voxel-based mapping of brain gray matter volume and glucose metabolism profiles in normal aging. *Neurobiol Aging.* (2009) 30:112–24. doi: 10.1016/j.neurobiolaging.2007.05.019
74. Mann S, Hazlett EA, Byne W, Hof PR, Buchsbaum MS, Cohen BE, et al. Anterior and posterior cingulate cortex volume in healthy adults: effects of aging and gender differences. *Brain Res.* (2011) 15:18–29. doi: 10.1016/j.brainres.2011.05.050
75. Li SC, Lindenberger U, Sikstrom S. Aging cognition: from neuromodulation to representation. *Trends Cogn Sci.* (2001) 5:479–86. doi: 10.1016/s1364-6613(00)01769-1

Conflict of Interest: The authors declare that the research was conducted in the absence of any commercial or financial relationships that could be construed as a potential conflict of interest.

The reviewer KR declared a past co-authorship with several of the authors AL, PF, and SE to the handling Editor.

frontiers in Neurology

ORIGINAL RESEARCH
published: 24 January 2020
doi: 10.3389/fneur.2019.01359

Differences Between Interictal and Ictal Generalized Spike-Wave Discharges in Childhood Absence Epilepsy: A MEG Study

*Qi Shi[1], Tingting Zhang[1], Ailiang Miao[1], Jintao Sun[1], Yulei Sun[1], Qiqi Chen[2], Zheng Hu[3], Jing Xiang[4] and Xiaoshan Wang[1]**

[1] Department of Neurology, The Affiliated Brain Hospital of Nanjing Medical University, Nanjing Medical University, Nanjing, China, [2] MEG Center, The Affiliated Brain Hospital of Nanjing Medical University, Nanjing, China, [3] Department of Neurology, Nanjing Children's Hospital, Nanjing, China, [4] Division of Neurology, MEG Center, Cincinnati Children's Hospital Medical Center, Cincinnati, OH, United States

OPEN ACCESS

Edited by:
Peter Sörös,
University of Oldenburg, Germany

Reviewed by:
James Christopher Young,
University of Melbourne, Australia
Pauly Ossenblok,
Eindhoven University of Technology, Netherlands
Elisa Cainelli,
University of Padova, Italy

***Correspondence:**
Xiaoshan Wang
lidou2005@126.com

Specialty section:
This article was submitted to Applied Neuroimaging, a section of the journal Frontiers in Neurology

Received: 09 July 2019
Accepted: 09 December 2019
Published: 24 January 2020

Citation:
Shi Q, Zhang T, Miao A, Sun J, Sun Y, Chen Q, Hu Z, Xiang J and Wang X (2020) Differences Between Interictal and Ictal Generalized Spike-Wave Discharges in Childhood Absence Epilepsy: A MEG Study. Front. Neurol. 10:1359. doi: 10.3389/fneur.2019.01359

Purpose: To investigate the differences between interictal and ictal generalized spike-wave discharges (GSWDs) for insights on how epileptic activity propagates and the physiopathological mechanisms underlying childhood absence epilepsy (CAE).

Methods: Twenty-five patients with CAE were studied using magnetoencephalography (MEG). MEG data were digitized at 6,000 Hz during the interictal and ictal GSWDs. GSWDs were analyzed at both neural magnetic source levels and functional connectivity (FC) in multifrequency bands: delta (1–4 Hz), theta (4–8 Hz), alpha (8–12 Hz), beta (12–30 Hz), gamma (30–80 Hz), ripple (80–250 Hz), and fast ripple (250–500 Hz). Brain FC was studied with the posterior cingulate cortex/precuneus (PCC/pC) as the seed region.

Results: The magnetic source of interictal GSWDs mainly locates in the PCC/pC region at 4–8 and 8–12 Hz, while that of ictal GSWDs mainly locates in the medial frontal cortex (MFC) at 80–250 Hz. There were statistically significant differences between interictal and ictal GSWDs ($p < 0.05$). The FC network involving the PCC/pC showed strong connections in the anterior-posterior pathways (mainly with the frontal cortex) at 80–250 Hz during ictal GSWDs, while the interictal GSWDs FC were mostly limited to the posterior cortex region. There was no significant difference in the magnetic source strength among interictal and ictal GSWDs at all bandwidths.

Conclusions: There are significant disparities in the source localization and FC between interictal and ictal GSWDs. Low-frequency activation in the PCC/pC during inhibition of seizures possibly relates to the maintenance of consciousness during interictal GSWDs. High-frequency oscillations (HFOs) of the MFC during CAE may associate with the inducing or occurrence of GSWDs. Weakened network connections may be in favor of preventing overexcitability and relates to the termination of GSWDs.

Keywords: childhood absence epilepsy (CAE), generalized spike-wave discharges (GSWDs), interictal and ictal period, Magnetoencephalography (MEG), multi-frequency bands

INTRODUCTION

Childhood absence epilepsy (CAE) is a type of idiopathic generalized epilepsy (IGE) characterized as episodes of unresponsiveness and generalized spike and wave discharges (GSWDs) on scalp electroencephalogram (EEG) of 3–4 Hz (1). When the duration of GSWDs was more than 4 s, the typical symptoms can be observed clinically, whereas the GSWDs lasting <4 s (interictal GSWDs) are usually asymptomatic (2). The seizures are thought to be relative to abnormal interplays in thalamocortical network (3–5), which affects patient awareness (6). The global workspace (GW) theory proposes that information is processed in an unconscious manner when numerous modular cerebral networks are synchronized activity. However, consciousness would be formed if the corresponding neural population is mobilized through top-down attention amplification into a state of self-sustaining activity, which involves many neurons distributed throughout the brain (7). The consciousness system has cortical and subcortical components, most notably being the medial, lateral, and orbital frontal cortex; anterior and posterior cingulate cortex (ACC, PCC); medial parietal (precuneus, pC) cortex; lateral temporal-parietal association cortex; basal forebrain; thalamus; and the upper brain stem activating systems (involved in higher order association) (8). Network inhibition hypothesis proposes that the subcortical arousal systems are inhibited by spread of seizure-related activity, which generates sleep-like or coma-like slow-wave activity in the bilateral frontoparietal association cortex and leads to disturbance of consciousness (1). A subset of these localized in the medial frontal cortex (MFC), PCC/pC, and inferior temporal makes up the default mode network (DMN), a state of resting brain function (9). These brain areas usually show decreased activity during attention-demanding tasks and become increasingly active during inattention to mental tasks or the external environment (10, 11). Also, the prefrontal cortex, anterior cingulate, and parietal cortex are important in creating the assumptive brain-scale workspace. Currently, the most accepted generation mechanisms of SWDs are cortico-reticular theory and cortical focus theory. The former assumes that the SWDs are closely related to the thalamocortical mechanism that generates sleep spindles (5, 12). The latter assumes that there is a focal area (pC, prefrontal and parietal cortex regions) active before occurrence of SWDs (13). Then cortical and thalamic alternating resonance (the cortical and thalamus in turn drives each other) produces SWDs. The integrity of the network is a prerequisite in both theories. Accordingly, the DMN, which integrates cognitive and emotional processing (14), is disturbed during absence seizures (15). Previous works studying GSWDs with EEG-fMRI have shown that the frontal, parietal regions, thalamus, and DMN (9) are changed with blood oxygen level-dependent (BOLD) signals (9, 16–18) in absence seizures (19–23). Disorders of consciousness may thus be caused by selective bilateral cortical and subcortical networks (5, 24) through abnormal patterns of neural activity (1).

It is well-known that typical GSWDs originate from paroxysmal oscillations in corticothalamic networks, but the underlying mechanism is still unclear (5, 25, 26). The appearance of BOLD changes related to GSWDs in the PCC/pC may imply that this region has an important role in the pathogenesis of CAE (27, 28). This might indicate that alteration of the PCC/pC with levels of activity is relevant to the changes of GSWD. However, the exact interplay between the cortical and subcortical structures should be further explored. The present study aimed to investigate the difference of magnetic source localization and FC between the interictal and ictal GSWDs in various frequency bands in CAE patients using MEG, which has better spatial resolution comparing with EEG and higher temporal resolution than magnetic resonance imaging (MRI) (29).

To the best of our knowledge, there have been some studies on the frequency-dependent nature of CAE. The connectivity networks and sources during the evolvement of SWDs with spatial and temporal profiles were described (30). Tenney et al. revealed that different ictal connectivities in pretreatment were related with response to antiepileptic treatment (31). And the changes of the effective connectivity (EC) network in specific frequency during interictal period were reported by Wu et al. (32). However, in our study, we try to investigate the differences between interictal and ictal GSWDs using FC and sources. The findings may contribute to our understanding of the physiopathological mechanism underlying consciousness disorders and mechanisms that sustain epileptic discharge.

METHODS

Subjects

Forty-two CAE patients aged 5–14 years old were recruited from the Department of Neurology at the Nanjing Children's Hospital and Nanjing Brain Hospital during March 2012–December 2018. The research received approval from the medical ethics committees of Nanjing Medical University, Nanjing Brain Hospital and Nanjing Children's Hospital. The inclusion criteria were (1) typical CAE consistent with the International League Against Epilepsy Seizure Classification (2017) diagnosed by a neurologist; (2) bilaterally synchronous 3–4 Hz SWDs on a normal background EEG; (3) normal physical and neurological examination; (4) no abnormal brain MRI; and (5) head movement <5 mm during MEG recordings. Patients were excluded if they met any of the following criteria: (1) history of other major neurologic or psychiatric diseases or severe systemic disease; (2) having metal implants that interfere with MEG data, such as pacemakers or cochlear devices; (3) incompatibility in keeping head motionless during MRI scans or MEG recordings. Of the 42 CAE patients recruited, 17 were excluded due to excessive head movements or absence of GSWDs. Accordingly, 25 subjects (7 males, 18 females) fulfilled our inclusion criteria and were eligible for the study. This study was approved by the medical ethics committees of the Nanjing Medical University, Nanjing Children's Hospital, and Nanjing Brain Hospital. All subjects and their guardians were informed about the purpose of this study and signed their written informed consent.

MEG

All participants were asked to reduce sleeping time before MEG recordings to raise the probability of absence of seizures during

data recordings. MEG data were recorded in a magnetically shielded room with a whole-head CTF MEG system with 275 channels (VSM Medical Technology Company, Canada) at the MEG Center at the Nanjing Brain Hospital. Background noises were routinely measured by MEG before the experiment in an empty room. Before data acquisition, three coils were attached to the pre-auricular points and nasion of each subject to aid head localization relative to the MEG coordinate system. All subjects were asked to stay still (avoiding swallowing or teeth clenching) and close their eyes slightly in a supine position. Participants were monitored with an audiovisual system during MEG recording. Tolerance for head movement before and after acquisition was limited to 5 mm for each recording. Head localization was accurate to within 1 mm. The sampling rate was 6,000 Hz with noise cancelation of third-order gradients. A minimum of six consecutive epochs, each with a duration of 2 min, were recorded for each subject. If no GSWDs were recorded in the first three files, we will make the patient blow a slip of paper for a while to hyperventilate, which will increase the chance of seizure.

MRI

All 25 subjects have informed consent to undergo MRI with a 3.0T scanner (Siemens, Germany). Three fiduciary markers were attached to the same pre-auricular points and nasion used for MEG. All anatomical landmarks digitized during MEG were identifiable in the MRI.

Data Analyses

Informed by previous studies (32–35), MEG data without noise or artifacts (>6 pT) were filtered with a band pass filter of 1–4 Hz. And the MEG waveform segments showing GSWDs indicative of absence epilepsy were thereafter marked. In this study, we try to investigate the differences between interictal and ictal GSWDs in CAE. Only the GSWDs with an interictal period of <4 s (2, 21) and an ictal period of more than 10 s were selected for analysis. For segments longer than 10 s, the audiovisual system recordings were checked for subject unconsciousness to verify ictal periods. Recording the start and end times of seizure, then choosing 3 s in the middle of the seizure, which must be in the state of unconsciousness and applying it to all frequency bands for further study (because sometimes when patients presented with clinical manifestations of absence epilepsy, 3–4 Hz GSWDs would appear on the MEG earlier or later than it, so we choose the middle data of the ictal period, which would ensure that the selected study data were in the ictal period of absence epilepsy). Interictal segments were selected on both clinical observation of consciousness and presence of 3 Hz GSWDs in MEG as per the following three-step protocol: (1) waveform segments with GSWDs of 3 Hz shorter than 4 s were identified; (2) consciousness was observed via audiovisual recordings; (3) checking for the presence of ictal GSWDs before or after the chosen segments. If there was at least 30 s away from ictal segments, then the waveform was selected as interictal GSWDs data for the following analysis. An overview of MEG acquisition is presented in **Figure 1**.

MEG signals were filtered into bandwidths of 1–4 Hz (delta), 4–8 Hz (theta), 8–12 Hz (alpha), 12–30 Hz (beta), 30–80 Hz (gamma), 80–250 Hz (ripple), and 250–500 Hz (fast ripple). A notch filter of 50 Hz and harmonics were applied to eliminate power-line noise. Bandwidth segments were chosen based on our own and others' previous studies of epilepsy (35, 36). We calculated the accumulated source localization (ASI) and FC during the interictal and ictal GSWDs for 3 s time window in seven frequency bands from all patients.

ASI

ASI was defined as the volumetric summation of source activity over a period of time. ASI was localized to correlated sources

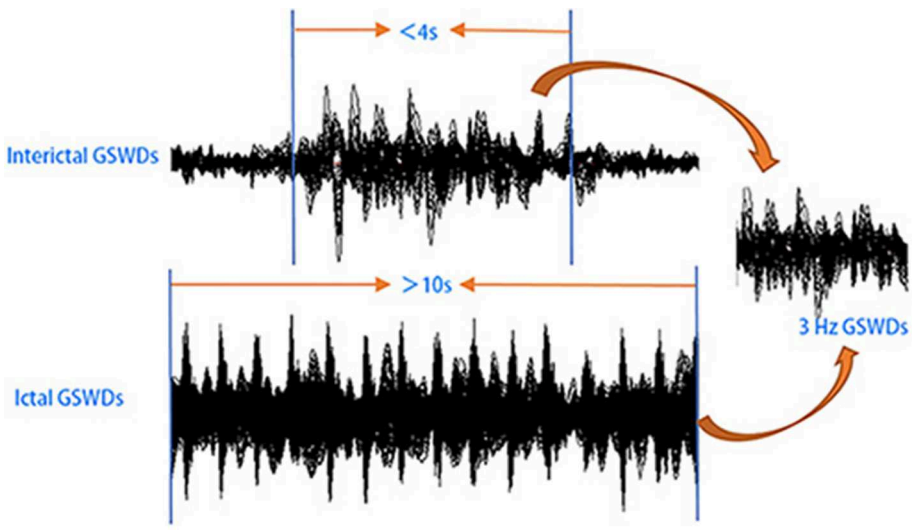

FIGURE 1 | Schematic of magnetoencephalography (MEG) data analysis. MEG waveforms were recorded from 25 patients with childhood absence epilepsy (CAE). MEG data segments with generalized spike-wave discharges (GSWDs) <4 s or >10 s were selected for further analysis.

using node-beam lead fields (37). Given that each node-beam lead field represents a form of either source-beamformer or subspace solution, the ASI had multiple source beamformers to separate correlated sources. The mathematical algorithms and validations have been described in detail (37, 38). Measurements of brain activity were enhanced by inclusion of the source activity strength. Source location was quantitated in a three-dimensional (3-D) coordinate system where the X, Y, and Z axes represented each of the three MEG fiducial points. A MEG Processor was used in the measurements of neuromagnetic source strength (37).

FC

FC was analyzed at the source level (35, 37). Each source was computed by virtual sensor waveforms using ASI algorithms. The source neural networks were estimated from the signal correlation of each pair of virtual sensors in the interictal and ictal GSWDs. Specifically, by calculating correlation coefficients, the relationship between virtual sensor signals from two source pairs is defined as follows:

$$R(X_a, X_b) = \frac{C(X_a, X_b)}{SX_a, X_b} \quad (1)$$

where R (Xa, Xb) represents the correlation of a source pair in two locations ("a" and "b"). The Xa and Xb represent the signals in two sources, which were paired for connection calculation. C (Xa, Xb) represents the mean of two source signals. Sxa and Sxb represent the standard deviation of two source signals. To avoid possible bias, we used the source-level analysis to calculate all possible connections for each two-source pair. Each pair of possible FC distributions of all voxel-based virtual sensors is registered in each participant's MRI (26, 29). To analyze the source connections, MSI-based neural networks were visualized in both axial, coronal, and sagittal views, respectively (39). Red and blue represent the excitatory and inhibitory connections, respectively. A threshold equivalent to $p < 0.05$ was used as a checkpoint to ensure the quality of the data.

$$Tp = R\sqrt{\frac{K-2}{1-R^2}} \quad (2)$$

In Equation (2), Tp is the t value of a correlation, R is the correlation of a source pair, and K is the number of data points for the connection. We used the T_p value of $p < 0.05$ as the threshold to obtain the FC network. The PCC/pC was the region of interest (ROI). The ROI was visually defined, and the template was verified by coordinates.

Statistical Analyses

The chi-squared test (or Fisher's exact test) was used to compare the source localization and FC at low-to-high bandwidth. The Student's *t*-test and Mann-Whitney test were used to compare source strength between interictal and ictal GSWDs for independent samples. A $p < 0.05$ was considered statistically significant. Bonferroni's correction was applied to all *p*-values derived from multiplicity analysis. All statistical analyses were performed with SPSS 25.0 for Windows (SPSS Inc., Chicago, IL, USA).

RESULTS

The average age of the 25 subjects at CAE onset was 7.7 ± 2.08 years. The average seizure frequency was 7.4 ± 5.36 times per day. Of 57 GSWDs recorded by MEG, 17 incomplete GSWD segments were excluded. Thus, 40 MEG segments, including 20 interictal GSWDs (without conscious disorder) and 20 ictal GSWDs (with conscious disorder), were selected from 25 subjects, with at least one segment and at most two segments of MEG data from each subject. Clinical data are presented in **Table 1**.

Source Localization

Delta (1–4 Hz)

The source of interictal GSWDs was mainly localized in the MFC ($n = 13$), PCC/pC ($n = 9$), and parietal-occipital-temporal junction (POT, $n = 7$). Ictal GSWDs were localized in the MFC ($n = 12$), POT ($n = 5$), and middle occipital cortex (MOT, $n = 5$). There were no statistically significant differences between the two groups.

TABLE 1 | Clinical data of 25 enrolled subjects with CAE.

Subject	Sex/age (F or M/years)	Duration of epilepsy (months)	Seizure frequency (times/day)	AED at the time of recording
1	F/7	1	20	None
2	F/6	12	10	None
3	M/7	25	10	VPA and LTG
4	F/10	24	5–7	LTG
5	F/8	3	20	None
6	F/9	60	2–5	None
7	M/8	2	5–8	VPA
8	F/7	4	10	VPA
9	F/5	2	7–8	None
10	F/10	10	4–5	None
11	F/9	3	15–20	None
12	M/14	6	2–3	OXC
13	F/10	11	4–5	None
14	F/5	5	1–2	None
15	F/6.5	4	5–6	None
16	F/5.5	24	6–8	OXC and LTG
17	F/5	2	10	None
18	F/6	12	8–10	VPA
19	F/8	1	4–5	VPA
20	M/7	1	0–1	VPA
21	M/10	72	4–5	VPA
22	F/8	24	0–1	VPA
23	F/6	2	5–10	None
24	M/7.5	5	2–3	VPA
25	M/8	4	10	None

F, female; M, male; VPA, valproate; OXG, oxcarbazepine; LTG, lamotrigine; CAE, childhood absence epilepsy; AED, antiepileptic drug.

Theta (4–8 Hz)

The source of interictal GSWDs was mainly localized in the PCC/pC ($n = 12$), MFC ($n = 9$), and POT ($n = 9$). Ictal GSWDs were localized in the MFC ($n = 14$), thalamus ($n = 6$), MOC ($n = 4$), and POT ($n = 4$). There were statistical differences in the PCC/pC localization of interictal and ictal GSWDs ($p < 0.05$) (**Figure 2**).

Alpha (8–12 Hz)

The source of interictal GSWDs was mainly localized in the MFC ($n = 11$), thalamus ($n = 9$), PCC/pC ($n = 8$), and POT ($n = 8$). Ictal GSWDs were mainly localized in the MFC ($n = 12$), POT ($n = 7$), and temporal cortex ($n = 4$). There were statistical differences in the PCC/pC localization of interictal and ictal GSWDs ($p < 0.005$) (**Figure 2**).

Beta (12–30 Hz)

The source of interictal GSWDs was localized in the MFC ($n = 10$), thalamus ($n = 10$), and POT ($n = 8$), whereas ictal group mainly localized in the MFC ($n = 13$), POT ($n = 7$), thalamus ($n = 7$), and temporal cortex ($n = 7$). There were no statistically significant differences between the two groups.

Gamma (30–80 Hz)

Interictal GSWDs were mainly localized in the MFC ($n = 12$), thalamus ($n = 6$) and PCC/pC ($n = 3$). Ictal GSWDs were mainly localized in the MFC ($n = 15$), temporal cortex ($n = 3$), thalamus ($n = 2$), and POT ($n = 2$). There were no statistically significant differences in the localization of interictal and ictal GSWDs.

Ripple (80–250 Hz)

Interictal GSWDs were mainly localized in the deep brain area (DBA) ($n = 8$), the MFC ($n = 4$), and temporal cortex ($n = 4$). Ictal GSWDs were localized in the MFC ($n = 11$), DBA ($n = 5$), and temporal cortex ($n = 5$). There were statistical differences in the MFC localization of interictal and ictal GSWDs ($p < 0.05$) (**Figure 3**).

Fast Ripple (250–500 Hz)

Interictal GSWDs were mainly localized in the DBA ($n = 11$), the MFC ($n = 7$), and temporal cortex ($n = 2$). Ictal GSWDs were mainly localized in the MFC ($n = 12$), temporal cortex ($n = 6$), and DBA ($n = 2$). There were statistically significant differences between interictal and ictal GSWDs ($p < 0.05$) (**Figure 3**).

Tables 2, **3** show that the neural magnetic sources were localized to PCC/pC during interictal GSWDs at 4–8 Hz ($p < 0.05$) and 8–12 Hz ($p < 0.005$). In comparison, ictal GSWDs localized in the MFC were mainly observed at 80–250 Hz ($p < 0.05$). There was no statistical difference between the two groups at all other frequency bands (1–4, 12–30, 30–80, 250–500 Hz). Moreover, the strength of brain activity shows that there is no significant difference between the two groups. The measurements of neuromagnetic peak source strength are presented in **Table 3**. The strength of activity in both groups decreased non-linearly as the frequency bands increased. The strength of activity decreased

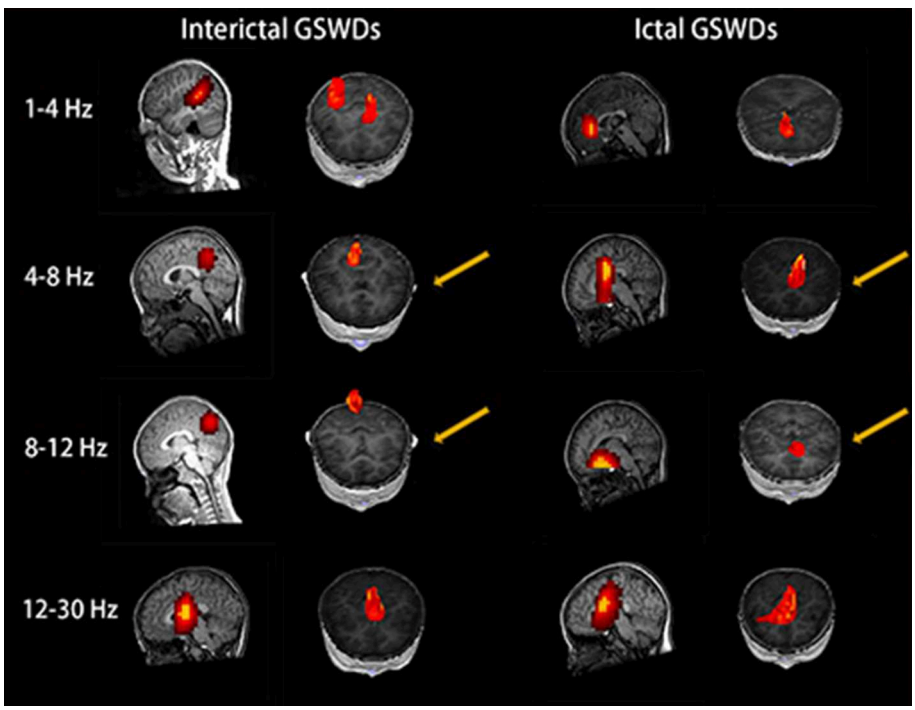

FIGURE 2 | Magnetic source images show the locations of generalized spike-wave discharges (GSWDs) in patients at 1–4, 4–8, 8–12, and 12–30 Hz. Interpatient variation withstanding, the precuneus (pC) is always activated during interictal GSWD at 4–8 and 8–12 Hz. At the same bandwidths, ictal GSWDs are mostly localized in the medial frontal cortex (MFC). Yellow arrows show the differences between the two groups.

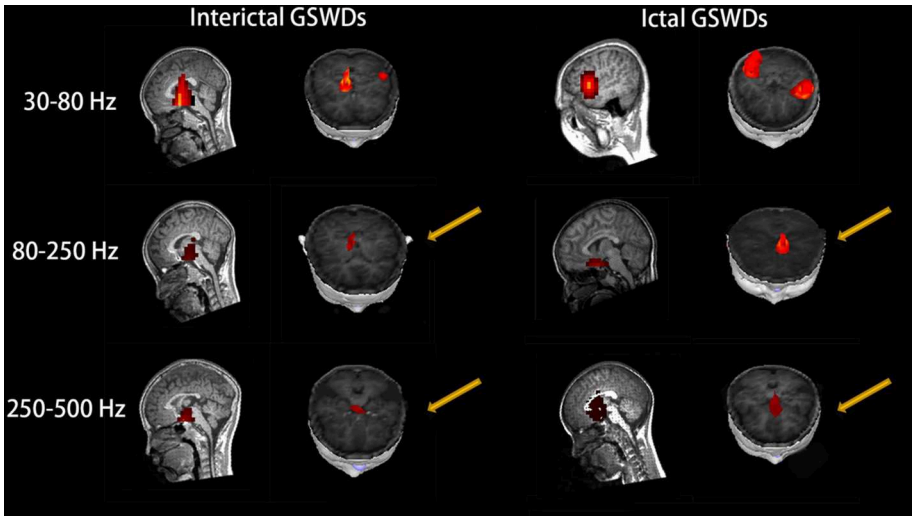

FIGURE 3 | Magnetic source images show the locations of generalized spike-wave discharges (GSWDs) in patients at 30–80, 80–250, and 250–500 Hz. At the 80–250 Hz, medial frontal cortex (MFC) are always activated during ictal GSWDs, while during interictal GSWDs, the locations are almost in the deep brain area (DBA). There are more DBA locations during interictal GSWDs when comparing with ictal GSWDs at 250–500 Hz. The yellow arrows show the differences between the two groups.

TABLE 2 | Magnetic source localization during interictal and ictal GSWD.

Frequency band (Hz)	1–4		4–8		8–12		12–30		30–80		80–250		250–500	
Group	A	B	A	B	A	B	A	B	A	B	A	B	A	B
MFC	13	12	9	14	11	12	10	13	12	15	4*	11*	7	12
TC	5	3	7	3	3	4	6	7	2	3	4	5	2	6
PCC/pC	9	4	12*	3*	8*	0*	3	1	3	0	0	0	0	0
MOC	3	5	1	4	1	1	2	4	1	1	0	0	0	0
TH	6	0	8	6	9	0	10	7	6	2	0	0	0	0
TPJ	2	2	1	1	3	0	2	0	0	0	0	0	0	0
POT	7	5	9	4	8	7	8	7	0	2	0	0	0	0
CE	1	2	2	3	4	1	0	2	1	0	3	2	0	0
DBA	0	0	0	0	0	1	0	0	2	1	8	5	11*	2*

*GSWD, generalized spike-wave discharge; A, interictal GSWDs; B, ictal GSWDs; MFC, medial frontal cortex; TC, temporal cortex; PCC, posterior cingulate cortex; pC, precuneus cortex; MOC, medial occipital cortex; TH, thalamus; TPJ, temporal-parietal junction; POT, parieto-occipito-temporal junction; CE, cerebellum; DBA, deep brain area. *Statistically significant at $p < 0.05$.*

TABLE 3 | Neuromagnetic peak source strength of interictal and ictal GSWDs.

Frequency band (Hz)	Interictal GSWDs	Ictal GSWDs	*P*-value
1–4	41.65 ± 26.95	35.91 ± 11.60	0.388
4–8	11.15 ± 4.28	13.37 ± 6.59	0.214
8–12	6.32 ± 5.09	7.13 ± 2.70	0.076
12–30	7.61 ± 5.01	7.89 ± 2.49	0.052
30–80	2.83 ± 2.48	4.35 ± 4.52	0.108
80–250	1.32 ± 2.89	2.54 ± 3.61	0.011
250–500	0.68 ± 1.18	1.45 ± 2.29	0.068

There was no significant difference after Bonferroni correction for multiple comparisons. GSWD, generalized spike-wave discharge.

between 1–4 and 4–8 Hz, 4–8 and 8–12 Hz, 12–30 and 30–80 Hz, but there was no degressive trend between 8–12 and 12–30 Hz, 30–80 and 80–250 Hz, 80–250 and 250–500 Hz in both groups (**Figure 4**).

Functional Network

There were no significant differences in the functional networks of interictal and ictal GSWDs at all frequency bands in the whole brain network when we chose PCC/pC (32) as the ROI. Notably, during interictal GSWD, the majority of CAE patients (12 of 20 segments) showed limited FC in the posterior brain region at 80–250 Hz, whereas the ictal GSWDs (15 of 20 segments) showed mostly strong connections between anterior (particularly in frontal cortex) and posterior regions at the same frequency band. The FC was significantly different between interictal and ictal GSWDs ($p = 0.001$, $p < 0.05$; **Figure 5**). However, in the other six frequency bands, both the interictal and ictal GSWDs showed FC involving anterior and posterior brain regions. There were no remarkable differences between the two groups in these bandwidths (**Figure 6**).

DISCUSSION

We herein studied the frequency-dependent neuromagnetic activities and FC during the interictal and ictal GSWDs within CAE patients using MEG. Our findings have revealed that the magnetic source localization of interictal and ictal GSWDs differs at low and high bandwidths. The FC network involving the PCC/pC showed significant differences at 80–250 Hz between interictal and ictal GSWDs. However, during

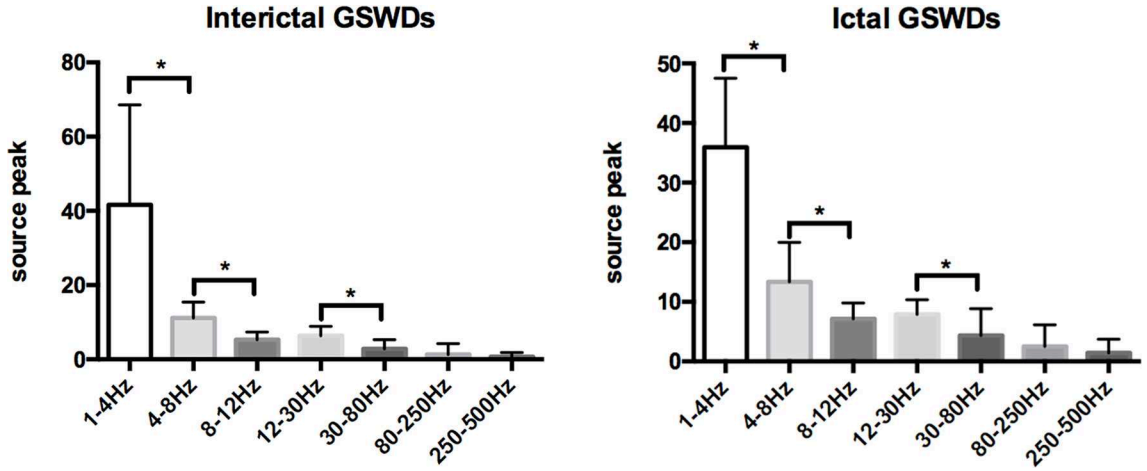

FIGURE 4 | Comparison of neuromagnetic peak source strength for seven frequency bands in interictal and ictal generalized spike-wave discharges (GSWDs). *Statistically significant at $p < 0.005$.

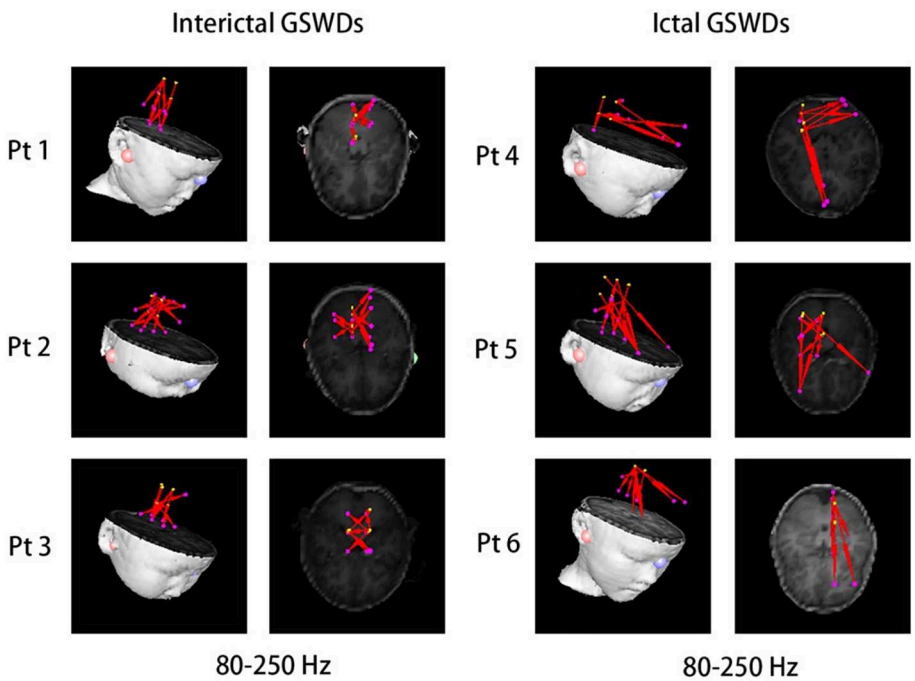

FIGURE 5 | There was significant difference in the functional connectivity (FC) [posterior cingulate cortex (PCC)/precuneus (pC) as the region of interest (ROI)] between interictal and ictal generalized spike-wave discharges (GSWDs) at 80–250 Hz. Interictal GSWDs had FC almost exclusively in the posterior cortex, whereas ictal GSWDs had strong connections in the anterior-posterior pathways (mainly with the frontal cortex).

the preliminary experiment, we found that there was no significant difference between the two groups when the frequency band was over 500 Hz, so the frequency band over 500 Hz was not included in the follow-up study. And there was no statistically significant clinical correlation between the course of epilepsy, drug therapy, and seizures frequency with the corresponding magnetic source localization and FC network in the study.

Source Localization

Recent EEG-fMRI studies have shown that the frontal cortex, pC, and thalamus are critical for generating absence seizures (31). Our study found significant PCC/pC involvement at 4–8 and 8–12 Hz during interictal GSWDs (**Table 2**; **Figure 2**), while there was less PCC/pC involvement during ictal GSWDs at the same bandwidths, thereby suggesting that the interictal neural activities in PCC/pC are higher than ictal at low-frequency

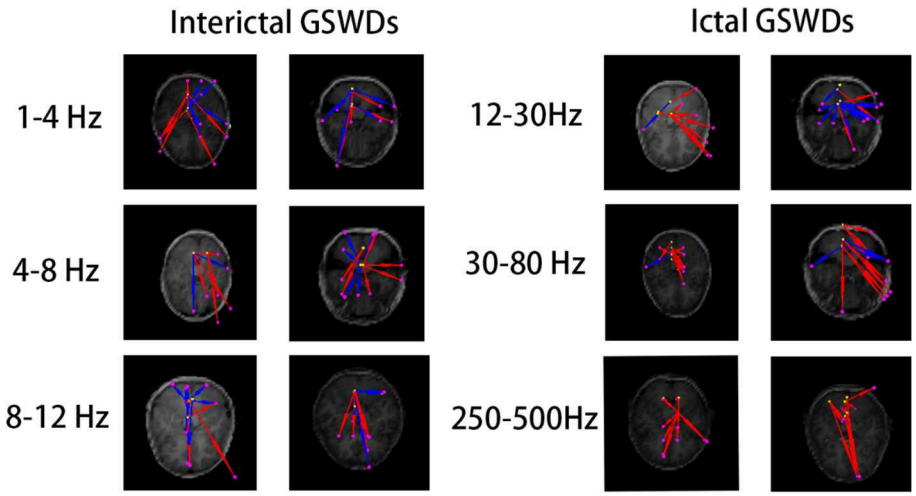

FIGURE 6 | The functional connectivity (FC) [posterior cingulate cortex (PCC)/precuneus (pC) as the region of interest (ROI)] shows no statistical differences between interictal and ictal generalized spike-wave discharges (GSWDs) at 1–4, 4–8, 8–12, 12–30, 30–80, and 250–500 Hz bandwidths.

bandwidths. A previous EEG study on resting state with low frequency revealed a decreased connectivity with the PCC in temporal lobe epilepsy (40). More recently, a MEG study of CAE patients reported that PCC/pC is markedly decreased in the low-frequency bandwidth in comparison to healthy controls (32). Furthermore, decreased BOLD signaling during GSWDs in the lateral parietal cortices was linear to the duration of EEG discharges (41). These are in agreement with our study. The PCC/pC is involved with rapidly engaging and bilaterally distributed networks for absence seizure (42), as well as the initialization of epileptic activity (36). In a related EEG-fMRI study, IGE showed that the GSWDs and functional change of the PCC may affect one other (27). Moreover, it is also a reportedly critical node in the network that correlates with consciousness in both humans and animals (43). The levels of consciousness may be relative to changes in the activity of the pC. PCC was thought to be playing a key role in the DMN, and the behavioral impairment may relate to the deactivation of pC (44). In addition, the longer the discharge, the more likely the disturbance of consciousness (45). Thus, the neural activity involving the PCC/pC may be associated with the maintenance of consciousness during interictal GSWDs and the disorder of consciousness during ictal GSWDs. Moreover, the lower-frequency pC region is necessary for a sustained and pathological oscillatory state, which is then perpetuated by the corticothalamic network. It is nonetheless possible that the lower-frequency parietal region is representative of inhibition, which has been reported during absence seizures (44).

At the same time, we also found that remarkable MFC source localization at 80–250 Hz during ictal GSWDs (n = 25, **Table 2**; **Figure 3**), while there was no obvious frontal cortex location during interictal GSWDs at 80–250 Hz. In a recent study of ictal GSWDs during CAE, it is thought that neuromagnetic GSWDs originate from the frontal lobe and thalamus (46). High-frequency oscillation (HFO) has become a new biomarker for epilepsy (47–49) because they are highly localized in the epileptogenic region. We, therefore, speculate that the frontal lobe is the focal point of epilepsy during seizure, and that interictal GSWDs diffuse neural activity generated by the interaction between the cortical and thalamus with no specific focal point. The frontal cortex has previously been demonstrated as a critical element in initiating and propagating absence seizures (34, 36, 46, 50–54) in support of the cortical focus theory (55). These findings altogether suggest that the HFOs of the frontal cortex during ictal GSWDs may be related to the generation of GSWDs (55, 56). In addition, different types of connections and/or information integration at different spatial-temporal levels require different frequencies (57). The frequency of oscillations limits the speed of information transmission. HFOs are better suited to neighboring integration, whereas lower frequencies are used to integrate information from large and/or remote areas (58).

FC Networks

On the FC networks, there were no obvious differences between the interictal and ictal GSWDs in the whole brain network at different frequency bands. However, when we chose PCC/pC as the seed region, we were surprised to find that, during interictal GSWDs, the networks showed limited FC mostly in the posterior brain region (**Figure 5**) at 80–250 Hz, whereas the ictal GSWDs showed FC mainly in networks having strong connections between anterior (particularly in frontal cortex) and posterior regions at 80–250 Hz. There were significant differences between the two groups ($p = 0.001$, $p < 0.05$).

The PCC/pC is an important part of the DMN. A study of dynamic causal modeling, for example, reported that pC has a permissive function in the epileptic network for gating GSWDs in absence seizures (27). The SWDs that are generated by the corticothalamic loop are dependent on the state of the pC region (59). It was therefore proposed that the anterior

and posterior networks oscillate asynchronously in a normal state and synchronously during transition to an ictal state (44). The posterior cortical regions may also contribute to the earliest activity associated with GSWDs (44). This may explain our finding that FC is mostly limited in the posterior cortical region during interictal GSWD. It has previously been demonstrated that weakened network connections may contribute to preventing hyperexcitability and that attenuation of network connection might be a negative feedback mechanism to prevent CAE seizures (60).

The posterior DMN is likely associated with states of awareness (9, 17, 55, 59, 61). Jing et al. reported that a large number of within- and cross-frequency form dynamics was found in secondary generalization of focal seizures (62). It is therefore possible that a cross-frequency coupling (when slow and fast oscillations interact with one another) produces absence seizures. Seizures with impairment have greater physiological intensity in widespread networks involving much of the brain. Also, comparing to seizures with spared behavior, EEG has shown greater power in widespread brain regions in seizures with impaired behavior (63). These may also explain our findings. However, the connectivity analysis of the virtual sensor activity is based on linear correlation analysis, which is one of the drawbacks of this study.

Limitations

This study has several limitations. First, the sample size is relatively small owing to the difficulty in collecting interictal data within half an hour of each patient. Second, we did not control for variations in antiepileptic drug (AED) taken by subjects, which could confound MEG recordings. Third, the software used to map the brain is not wholly reliable.

CONCLUSIONS

Our findings have revealed that the magnetic source localization and FC network differ between the interictal and ictal GSWDs in low- and high-frequency ranges. Maintenance of consciousness during interictal GSWDs may be associated with low-frequency activation in the PCC/pC region. Activation of the MFC at frequencies of 80–250 Hz during ictal GSWDs suggests that the frontal cortex is critically involved in propagating CAE. Weakened network connections in interictal GSWDs may be in favor of preventing overexcitability and relates to termination of CAE. The specific mechanisms underlying GSWDs require further study.

DATA AVAILABILITY STATEMENT

All datasets generated for this study are included in the article/supplementary material.

AUTHOR CONTRIBUTIONS

QS analyzed data and wrote this article. TZ, AM, JS, YS, and QC contributed to data analysis. ZH provided the patients. JX provided the MEG software. XW was the general responsible person of the project.

FUNDING

This work was supported by the National Natural Science Foundation of China (Grant No. 81471324, http://npd.nsfc.gov.cn/), the General Program of Natural Science Foundation of Jiangsu Province (Grant No. BK20191127) and the Health Department of Jiangsu Province (Grant Nos. H201443, H2018062).

ACKNOWLEDGMENTS

We would like to thank physicians and researchers at NBH and Nanjing Children's Hospital. We also thank all participants and their guardians for their support.

REFERENCES

1. Blumenfeld H. Impaired consciousness in epilepsy. *Lancet Neurol.* (2012) 11:814–26. doi: 10.1016/S1474-4422(12)70188-6
2. Li Q, Luo C, Yang T, Yao Z, He L, Liu L, et al. EEG-fMRI study on the interictal and ictal generalized spike-wave discharges in patients with childhood absence epilepsy. *Epilepsy Res.* (2009) 87:160–8. doi: 10.1016/j.eplepsyres.2009.08.018
3. Pittau F, Megevand P, Sheybani L, Abela E, Grouiller F, Spinelli L, et al. Mapping epileptic activity: sources or networks for the clinicians? *Front Neurol.* (2014) 5:218. doi: 10.3389/fneur.2014.00218
4. Seneviratne U, Cook M, D'Souza W. Focal abnormalities in idiopathic generalized epilepsy: a critical review of the literature. *Epilepsia.* (2014) 55:1157–69. doi: 10.1111/epi.12688
5. Meeren H, van Luijtelaar G, Lopes da Silva F, Coenen A. Evolving concepts on the pathophysiology of absence seizures: the cortical focus theory. *Arch Neurol.* (2005) 62:371–6. doi: 10.1001/archneur.62.3.371
6. Aldenkamp A, Arends J. The relative influence of epileptic EEG discharges, short nonconvulsive seizures, and type of epilepsy on cognitive function. *Epilepsia.* (2004) 45:54–63. doi: 10.1111/j.0013-9580.2004.33403.x
7. Arthuis M, Valton L, Regis J, Chauvel P, Wendling F, Naccache L, et al. Impaired consciousness during temporal lobe seizures is related to increased long-distance cortical-subcortical synchronization. *Brain.* (2009) 132(Pt 8):2091–101. doi: 10.1093/brain/awp086
8. Blumenfeld B. *Neuroanatomy Through Clinical Cases*. Sunderland, MA: Sinauer Associates (2010).
9. Raichle ME, MacLeod AM, Snyder AZ, Powers WJ, Gusnard DA, Shulman GL. A default mode of brain function. *Proc Natl Acad Sci USA.* (2001) 98:676–82. doi: 10.1073/pnas.98.2.676
10. Broyd SJ, Demanuele C, Debener S, Helps SK, James CJ, Sonuga-Barke EJ. Default-mode brain dysfunction in mental disorders: a systematic review. *Neurosci Biobehav Rev.* (2009) 33:279–96. doi: 10.1016/j.neubiorev.2008.09.002
11. Gusnard DA, Akbudak E, Shulman GL, Raichle ME. Medial prefrontal cortex and self-referential mental activity: relation to a default mode of brain function. *Proc Natl Acad Sci USA.* (2001) 98:4259–64. doi: 10.1073/pnas.071043098

12. Epilepsia GPJ. Generalized epilepsy with spike-and-wave discharge: a reinterpretation of its electrographic and clinical manifestations. The 1977 William G. Lennox Lecture, American Epilepsy Society. *Epilepsia*. (1979) 20:571–88. doi: 10.1111/j.1528-1157.1979.tb04840.x
13. Konishi T, Matsuzawa J, Hongou K, Murakami M, Yamatani M, Yagi S. Partial seizures during the course in patients with absence epilepsy. *No To Hattatsu*. (1999) 31:395–401.
14. Greicius MD, Krasnow B, Reiss AL, Menon V. Functional connectivity in the resting brain: a network analysis of the default mode hypothesis. *Proc Natl Acad Sci USA*. (2003) 100:253–8. doi: 10.1073/pnas.0135058100
15. Fransson P, Marrelec G. The precuneus/posterior cingulate cortex plays a pivotal role in the default mode network: evidence from a partial correlation network analysis. *Neuroimage*. (2008) 42:1178–84. doi: 10.1016/j.neuroimage.2008.05.059
16. Aghakhani Y. fMRI activation during spike and wave discharges in idiopathic generalized epilepsy. *Brain*. (2004) 127:1127–44. doi: 10.1093/brain/awh136
17. Gotman J, Grova C, Bagshaw A, Kobayashi E, Aghakhani Y, Dubeau F. Generalized epileptic discharges show thalamocortical activation and suspension of the default state of the brain. *Proc Natl Acad Sci USA*. (2005) 102:15236–40. doi: 10.1073/pnas.0504935102
18. Raichle ME, Mintun MA. Brain work and brain imaging. *Annu Rev Neurosci*. (2006) 29:449–76. doi: 10.1146/annurev.neuro.29.051605.112819
19. Laufs H, Hamandi K, Walker MC, Scott C, Smith S, Duncan JS, et al. EEG–fMRI mapping of asymmetrical delta activity in a patient with refractory epilepsy is concordant with the epileptogenic region determined by intracranial EEG. *Mag Reson Imaging*. (2006) 24:367–71. doi: 10.1016/j.mri.2005.12.026
20. Moeller F, Siebner HR, Wolff S, Muhle H, Granert O, Jansen O, et al. Simultaneous EEG-fMRI in drug-naive children with newly diagnosed absence epilepsy. *Epilepsia*. (2008) 49:1510–9. doi: 10.1111/j.1528-1167.2008.01626.x
21. Carney PW, Masterton RA, Harvey AS, Scheffer IE, Berkovic SF, Jackson GD. The core network in absence epilepsy. Differences in cortical and thalamic BOLD response. *Neurology*. (2010) 75:904–11. doi: 10.1212/WNL.0b013e3181f11c06
22. Salek-Haddadi A, Lemieux L, Merschhemke M, Diehl B, Allen PJ, Fish DR. EEG quality during simultaneous functional MRI of interictal epileptiform discharges. *Magn Reson Imaging*. (2003) 21:1159–66. doi: 10.1016/j.mri.2003.08.017
23. Labate A, Briellmann RS, Abbott DF, Waites AB, Jackson GD. Typical childhood absence seizures are associated with thalamic activation. *Epileptic Disord*. (2005) 7:373–7.
24. Blumenfeld H. Cellular and network mechanisms of spike-wave seizures. *Epilepsia*. (2005) 46(Suppl 9):21–33. doi: 10.1111/j.1528-1167.2005.00311.x
25. van Luijtelaar G, Sitnikova E. Global and focal aspects of absence epilepsy: the contribution of genetic models. *Neurosci Biobehav Rev*. (2006) 30:983–1003. doi: 10.1016/j.neubiorev.2006.03.002
26. Bernhardt BC, Rozen DA, Worsley KJ, Evans AC, Bernasconi N, Bernasconi A. Thalamo-cortical network pathology in idiopathic generalized epilepsy: insights from MRI-based morphometric correlation analysis. *Neuroimage*. (2009) 46:373–81. doi: 10.1016/j.neuroimage.2009.01.055
27. Vaudano AE, Laufs H, Kiebel SJ, Carmichael DW, Hamandi K, Guye M, et al. Causal hierarchy within the thalamo-cortical network in spike and wave discharges. *PLoS ONE*. (2009) 4:e6475. doi: 10.1371/journal.pone.0006475
28. Benuzzi F, Mirandola L, Pugnaghi M, Farinelli V, Tassinari CA, Capovilla G, et al. Increased cortical BOLD signal anticipates generalized spike and wave discharges in adolescents and adults with idiopathic generalized epilepsies. *Epilepsia*. (2012) 53:622–30. doi: 10.1111/j.1528-1167.2011.03385.x
29. Kotecha R, Xiang J, Wang Y, Huo X, Hemasilpin N, Fujiwara H, et al. Time, frequency and volumetric differences of high-frequency neuromagnetic oscillation between left and right somatosensory cortices. *Int J Psychophysiol*. (2009) 72:102–10. doi: 10.1016/j.ijpsycho.2008.10.009
30. Gupta D, Ossenblok P, van Luijtelaar G. Space-time network connectivity and cortical activations preceding spike wave discharges in human absence epilepsy: a MEG study. *Med Biol Eng Comput*. (2011) 49:555–65. doi: 10.1007/s11517-011-0778-3
31. Tenney JR, Kadis DS, Agler W, Rozhkov L, Altaye M, Xiang J, et al. Ictal connectivity in childhood absence epilepsy: associations with outcome. *Epilepsia*. (2018) 59:971–81. doi: 10.1111/epi.14067
32. Wu C, Xiang J, Jiang W, Huang S, Gao Y, Tang L, et al. Altered effective connectivity network in childhood absence epilepsy: a multi-frequency MEG study. *Brain Topogr*. (2017) 30:673–84. doi: 10.1007/s10548-017-0555-1
33. Xiang J, Wang Y, Chen Y, Liu Y, Kotecha R, Huo X, et al. Noninvasive localization of epileptogenic zones with ictal high-frequency neuromagnetic signals. *J Neurosurg Pediatr*. (2010) 5:113–22. doi: 10.3171/2009.8.PEDS09345
34. Tang L, Xiang J, Huang S, Miao A, Ge H, Liu H, et al. Neuromagnetic high-frequency oscillations correlate with seizure severity in absence epilepsy. *Clin Neurophysiol*. (2016) 127:1120–9. doi: 10.1016/j.clinph.2015.08.016
35. Xiang J, Tenney JR, Korman AM, Leiken K, Rose DF, Harris E, et al. Quantification of interictal neuromagnetic activity in absence epilepsy with accumulated source imaging. *Brain Topogr*. (2015) 28:904–14. doi: 10.1007/s10548-014-0411-5
36. Miao A, Tang L, Xiang J, Guan Q, Ge H, Liu H, et al. Dynamic magnetic source imaging of absence seizure initialization and propagation: a magnetoencephalography study. *Epilepsy Res*. (2014) 108:468–80. doi: 10.1016/j.eplepsyres.2014.01.006
37. Xiang J, Luo Q, Kotecha R, Korman A, Zhang F, Luo H, et al. Accumulated source imaging of brain activity with both low and high-frequency neuromagnetic signals. *Front Neuroinf*. (2014) 8:57. doi: 10.3389/fninf.2014.00057
38. Xiang J, Korman A, Samarasinghe KM, Wang X, Zhang F, Qiao H, et al. Volumetric imaging of brain activity with spatial-frequency decoding of neuromagnetic signals. *J Neurosci Methods*. (2015) 239:114–28. doi: 10.1016/j.jneumeth.2014.10.007
39. Miao A, Wang Y, Xiang J, Liu Q, Chen Q, Qiu W, et al. Ictal source locations and cortico-thalamic connectivity in childhood absence epilepsy: associations with treatment response. *Brain Topogr*. (2019) 32:178–91. doi: 10.1007/s10548-018-0680-5
40. Coito A, Genetti M, Pittau F, Iannotti GR, Thomschewski A, Holler Y, et al. Altered directed functional connectivity in temporal lobe epilepsy in the absence of interictal spikes: a high density EEG study. *Epilepsia*. (2016) 57:402–11. doi: 10.1111/epi.13308
41. Li Q, Zhou D. EEG-fMRI studies on the neural networks of the generalized spike and wave discharges: an overview. *Sheng Wu Yi Xue Gong Cheng Xue Za Zhi*. (2012) 29:179–83.
42. Youssofzadeh V, Agler W, Tenney JR, Kadis DS. Whole-brain MEG connectivity-based analyses reveals critical hubs in childhood absence epilepsy. *Epilepsy Res*. (2018) 145:102–9. doi: 10.1016/j.eplepsyres.2018.06.001
43. Vogt BA, Laureys S. Posterior cingulate, precuneal and retrosplenial cortices: cytology and components of the neural network correlates of consciousness. *Prog Brain Res*. (2005) 150:205–17. doi: 10.1016/S0079-6123(05)50015-3
44. Tenney JR, Fujiwara H, Horn PS, Vannest J, Xiang J, Glauser TA, et al. Low- and high-frequency oscillations reveal distinct absence seizure networks. *Ann Neurol*. (2014) 76:558–67. doi: 10.1002/ana.24231
45. Sadleir LG, Scheffer IE, Smith S, Carstensen B, Carlin J, Connolly MB, et al. Factors influencing clinical features of absence seizures. *Epilepsia*. (2008) 49:2100–7. doi: 10.1111/j.1528-1167.2008.01708.x
46. Tenney JR, Fujiwara H, Horn PS, Jacobson SE, Glauser TA, Rose DF. Focal corticothalamic sources during generalized absence seizures: a MEG study. *Epilepsy Res*. (2013) 106:113–22. doi: 10.1016/j.eplepsyres.2013.05.006
47. Papadelis C, Tamilia E, Stufflebeam S, Grant PE, Madsen JR, Pearl PL, et al. Interictal high frequency oscillations detected with simultaneous magnetoencephalography and electroencephalography as biomarker of pediatric epilepsy. *J Vis Exp*. (2016) 2016:54883. doi: 10.3791/54883
48. Zijlmans M, Jiruska P, Zelmann R, Leijten FS, Jefferys JG, Gotman J. High-frequency oscillations as a new biomarker in epilepsy. *Ann Neurol*. (2012) 71:169–78. doi: 10.1002/ana.22548
49. Dumpelmann M, Jacobs J, Schulze-Bonhage A. Temporal and spatial characteristics of high frequency oscillations as a new biomarker in epilepsy. *Epilepsia*. (2015) 56:197–206. doi: 10.1111/epi.12844
50. Bai X, Vestal M, Berman R, Negishi M, Spann M, Vega C, et al. Dynamic time course of typical childhood absence seizures: EEG, behavior, and functional magnetic resonance imaging. *J Neurosci*. (2010) 30:5884–93. doi: 10.1523/JNEUROSCI.5101-09.2010
51. Gupta JR, Marsh ED, Nieh HA, Porter BE, Litt B. Discrete gamma oscillations identify the seizure onset zone in some pediatric epilepsy patients. *Conf Proc IEEE Eng Med Biol Soc*. (2011) 2011:3095–8. doi: 10.1109/IEMBS.2011.6090845

52. Szaflarski JP, DiFrancesco M, Hirschauer T, Banks C, Privitera MD, Gotman J, et al. Cortical and subcortical contributions to absence seizure onset examined with EEG/fMRI. *Epilepsy Behav*. (2010) 18:404–13. doi: 10.1016/j.yebeh.2010.05.009
53. Tenney JR, Fujiwara H, Horn PS, Rose DF. Comparison of magnetic source estimation to intracranial EEG, resection area, and seizure outcome. *Epilepsia*. (2014) 55:1854–63. doi: 10.1111/epi.12822
54. Westmijse I, Ossenblok P, Gunning B, van Luijtelaar G. Onset and propagation of spike and slow wave discharges in human absence epilepsy: a MEG study. *Epilepsia*. (2009) 50:2538–48. doi: 10.1111/j.1528-1167.2009.02162.x
55. Meeren HK, Pijn JP, Van Luijtelaar EL, Coenen AM, Lopes da Silva FH. Cortical focus drives widespread corticothalamic networks during spontaneous absence seizures in rats. *J Neurosci*. (2002) 22:1480–95. doi: 10.1523/JNEUROSCI.22-04-01480.2002
56. Luttjohann A, van Luijtelaar G. The dynamics of cortico-thalamo-cortical interactions at the transition from pre-ictal to ictal LFPs in absence epilepsy. *Neurobiol Dis*. (2012) 47:49–60. doi: 10.1016/j.nbd.2012.03.023
57. Lopes da Silva F, Blanes W, Kalitzin SN, Parra J, Suffczynski P, Velis DN. Epilepsies as dynamical diseases of brain systems: basic models of the transition between normal and epileptic activity. *Epilepsia*. (2003) 44(Suppl 12):72–83. doi: 10.1111/j.0013-9580.2003.12005.x
58. Engel J Jr, da Silva FL. High-frequency oscillations - where we are and where we need to go. *Prog Neurobiol*. (2012) 98:316–8. doi: 10.1016/j.pneurobio.2012.02.001
59. Masterton RA, Carney PW, Abbott DF, Jackson GD. Absence epilepsy subnetworks revealed by event-related independent components analysis of functional magnetic resonance imaging. *Epilepsia*. (2013) 54:801–8. doi: 10.1111/epi.12163
60. Yang T, Luo C, Li Q, Guo Z, Liu L, Gong Q, et al. Altered resting-state connectivity during interictal generalized spike-wave discharges in drug-naive childhood absence epilepsy. *Hum Brain Mapp*. (2013) 34:1761–7. doi: 10.1002/hbm.22025
61. Aru J, Aru J, Priesemann V, Wibral M, Lana L, Pipa G, et al. Untangling cross-frequency coupling in neuroscience. *Curr Opin Neurobiol*. (2015) 31:51–61. doi: 10.1016/j.conb.2014.08.002
62. Jiang H, Cai Z, Worrell GA, He B. Multiple oscillatory push-pull antagonisms constrain seizure propagation. *Ann Neurol*. (2019) 86:683–94. doi: 10.1002/ana.25583
63. Guo JN, Kim R, Chen Y, Negishi M, Jhun S, Weiss S, et al. Impaired consciousness in patients with absence seizures investigated by functional MRI, EEG, and behavioural measures: a cross-sectional study. *Lancet Neurol*. (2016) 15:1336–45. doi: 10.1016/S1474-4422(16)30295-2

Conflict of Interest: The authors declare that the research was conducted in the absence of any commercial or financial relationships that could be construed as a potential conflict of interest.

frontiers in Neurology

ORIGINAL RESEARCH
published: 13 February 2020
doi: 10.3389/fneur.2019.01421

White Matter Structural Brain Connectivity of Young Healthy Individuals With High Trait Anxiety

Chunlan Yang[1], *Yining Zhang*[1], *Min Lu*[1]*, *Jiechuan Ren*[2] and *Zhimei Li*[2]

[1] College of Life Science and Bioengineering, Beijing University of Technology, Beijing, China, [2] Beijing Tiantan Hospital, Capital Medical University, Beijing, China

Background: Although functional brain connectivity in anxiety-related disorders has been studied, brain connectivity in non-clinical populations with high trait anxiety has been rarely reported. Whether structural brain connectivity changes in young healthy individuals with high trait anxiety remains unknown.

Methods: Thirty-eight young healthy individuals with high anxiety levels and 34 healthy subjects with low anxiety levels who were matched by age, gender, and educational level were recruited. Diffusion tensor images were acquired to analyze white matter connectivity. A two-sample *t*-test was used for group comparison of weighted networks and graph properties.

Results: Different connections were detected in fractional anisotropy- and fiber number-weighted networks. These connections were widely distributed in various regions, where relative significance was located in the inter-hemispheric frontal lobe, the frontal-limbic lobe in the right intra-hemisphere, and the frontal-temporal lobe in the ipsilateral hemisphere. However, no significant difference was found in fiber length-weighted network and in graph properties among the three networks.

Conclusions: The structural connectivity of white matter may be a vulnerability marker. Hence, healthy individuals with high trait anxiety levels are susceptible to anxiety-related psychopathology. The findings may help elucidate the pathological mechanism of anxiety and establish interventions for populations susceptible to anxiety disorders.

Keywords: high anxiety populations, diffusion tensor imaging, white matter, structural network, connectivity, young healthy individuals

OPEN ACCESS

Edited by:
Jan Kassubek,
University of Ulm, Germany

Reviewed by:
Costanza Gianni,
Sapienza University of Rome, Italy
Salem Hannoun,
American University of Beirut, Lebanon

***Correspondence:**
Min Lu
minlu1995@163.com

Specialty section:
This article was submitted to Applied Neuroimaging, a section of the journal Frontiers in Neurology

Received: *16 September 2019*
Accepted: *30 December 2019*
Published: *13 February 2020*

Citation:
Yang C, Zhang Y, Lu M, Ren J and Li Z (2020) White Matter Structural Brain Connectivity of Young Healthy Individuals With High Trait Anxiety. Front. Neurol. 10:1421. doi: 10.3389/fneur.2019.01421

INTRODUCTION

An increasing number of young people feel large pressure caused by the fast-paced life in our modern society. The morbidity of anxiety-related disorders has increased in recent years. Trait anxiety refers to the general traits or personality and is manifested as persistent worry and instability. Anxiety is disruptive to daily life, and long-term anxiety significantly increases the risks of developing anxiety-related disorders. We supposed that young healthy individuals with high trait anxiety level may be susceptible to anxiety-related disorders (1, 2).

The analysis of brain connectivity through graph theory and magnetic resonance imaging (MRI) has become popular in research of nervous system diseases. Previous studies demonstrated

abnormalities in brain connectivity among anxious patients. Zhu et al. found that changes in "small-world" properties in resting-state functional MRI (fMRI) are prominent among people with social anxiety disorders (3). Pacheco-Unguetti et al. found that trait anxiety is related to deficiencies in the executive control network, and attention-executive control function is impaired in adults with generalized anxiety disorder (4). Liao et al. found increased functional connectivity of the right posterior inferior temporal gyrus to the left inferior occipital gyrus, the right parahippocampal/hippocampal gyrus to the left middle temporal gyrus, and enhanced structural connectivity located in the genu of the corpus callosum among people with social anxiety disorders (5). Baur et al. found that the anterior insula and basolateral amygdala constitute a network markedly linked to anxiety (6).

In addition to an analysis using fMRI, electroencephalography (EEG) is used to detect abnormal connections in patients with anxiety disorders even at a rest state (7). However, T1-weighted imaging and diffusion tensor imaging (DTI) have been rarely used to detect structural brain connectivity. For the non-clinical population with high trait anxiety level, few neuroimaging studies have focused on brain connectivity. Our previous study used tract-based spatial statistics method to compare white matter differences among young healthy individuals with low and high trait anxiety levels (8). Alterations in the thalamus–cortical circuit and some emotion-related areas are commonly reported in anxiety-related disorders (8). In the present study, three weighted networks featured by fractional anisotropy (FA), fiber number (FN), and fiber length (FL) were analyzed; and group comparisons were performed using two-sample *t*-test to explore anatomical brain connectivity changes in a healthy population with high trait anxiety levels.

We expected to find important white matter structural connections related to trait anxiety in young healthy populations with high trait anxiety levels. These findings may provide supports for establishing a neuroimaging biomarker of susceptibility to anxiety disorders to help prevent and treat the disease.

MATERIALS AND METHODS

Subjects

Seventy-two healthy right-handed undergraduate or postgraduate students were recruited from the Southwest University Longitudinal Imaging Multimodal, Brain Data Repository (China) (http://fcon_1000.projects.nitrc.org/indi/retro/southwestuni_qiu_index.html) (9). Self-rating scores including State-Trait Anxiety Inventory (10) and Combined Raven's matrix test (CRT) (11) were measured. Subjects with trait anxiety scores exceeding 50 were classified into the high trait anxiety (HTA) group (19 males and 19 females, trait score 54.5 ± 2.628), and those with scores below 30 were classified into the low trait anxiety (LTA) group (14 males and 20 females, trait score 26.177 ± 2.516) (12). The participants were matched by age ($t = -0.567$, $p = 0.572$) and gender ($\chi^2 = 0.563$, $p = 0.453$). None of the subjects presented a history of neurological or psychiatric disorders nor underwent mental health treatment and medications. All subjects conformed to the standards of MRI scanning and provided informed written consent prior to the study. The procedures of consent and experiments were approved by the Research Ethics Committee of the Brain Imaging Center of Southwest University and agreed with the standards of the Declaration of Helsinki (1989).

Abbreviations: AAL, Automated Anatomical Labeling; ACR, anterior corona radiata; BDI, Beck Depression Inventory; CRT, combined Raven's matrix test; DTI, diffusion tensor imaging; EEG, electroencephalography; FA, fractional anisotropy; FDR, false discovery rate; FL, fiber length; fMRI, functional magnetic resonance imaging; FN, fiber number; HTA, high trait anxiety; LSAS, Liebowitz Social Anxiety Scale; LTA, low trait anxiety; MNI, Montreal Neurological Institute; MRI, magnetic resonance imaging; SPIN, Social Phobia Inventory.

Procedures

MRI Data Acquisition

All participants were scanned using a 3.0-T Siemens Trio MRI scanner (Siemens Medical, Erlangen, Germany). Diffusion-weighted imaging (DWI) for each subject was acquired with a single-shot, spin-echo, echo-planar imaging (EPI) sequence [TR/TE = 11,000/98 ms, matrix = 128 × 128, field of view (FOV) = 256 × 256 mm^2, voxel size = 2.0 × 2.0 × 2.0 mm^3, 60 axial slices, slice thickness = 2.0 mm, *b* value 1 = 0 s/mm^2, *b* value 2 = 1,000 s/mm^2] in 30 directions. The subjects were repeatedly scanned three times to increase the signal-to-noise ratio (SNR) in the DWI sequence. For each time, one $b0 = 0$ volume and 30 $b0 = 1{,}000$ volumes were acquired.

In addition, a magnetization-prepared rapid gradient echo (MPRAGE) sequence was used to acquire high-resolution T1-weighted anatomical images. T1-weighted structural images would be used as the templates of brain regions in the following data analysis procedure. The main parameters are as follows: repetition time = 1,900 ms, echo time = 2.52 ms, inversion time = 900 ms, flip angle = 9°, resolution matrix = 256 × 256, slices = 176, thickness = 1.0 mm, and voxel size = 1 × 1 × 1 mm^3. In this study, T1 images were non-linearly transformed into the Montreal Neurological Institute (MNI) space, using the ICBM152 T1 template as a reference.

Data Analysis

All imaging data were processed by PANDA software (13), a MATLAB toolbox that integrates MRIcron (https://www.nitrc.org/projects/mricron), FSL (https://fsl.fmrib.ox.ac.uk/fsl/fslwiki), and Diffusion Toolkit (http://www.trackvis.org/dtk/). The flowchart of data analysis is shown in **Figure 1**. The procedure using PANDA mainly comprises data preprocessing and construction of white matter structural network.

Image Preprocessing

In detail, the following data preprocessing steps were performed: (1) checking of image quality and converting of DICOM files into NIFTI images; (2) brain extraction and brain mask estimation; (3) cropping of images and correcting of eddy current/motion; and (4) calculation of DTI metrics (FA).

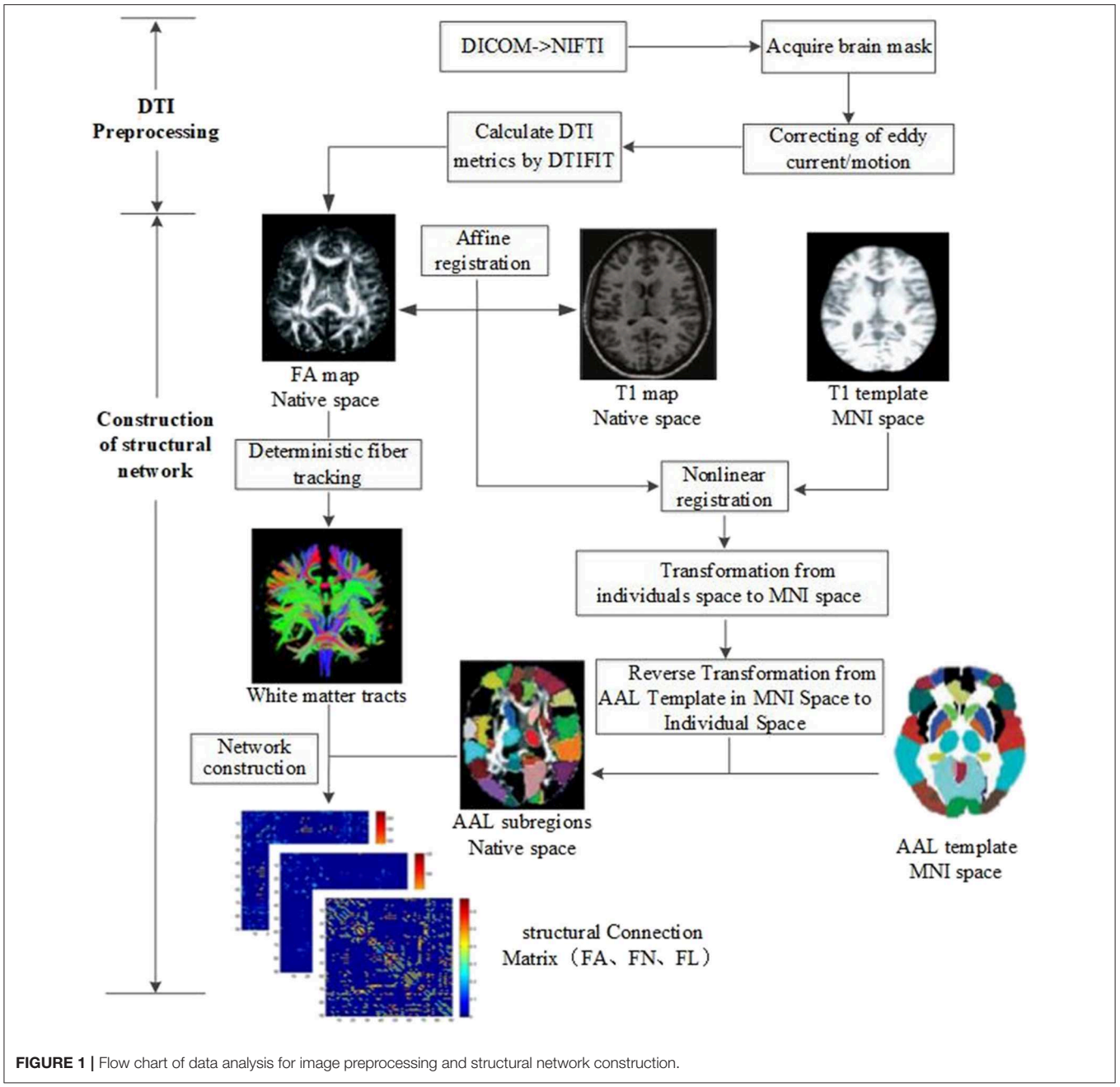

FIGURE 1 | Flow chart of data analysis for image preprocessing and structural network construction.

Construction of White Matter Structural Networks

After preprocessing, white matter structural networks were constructed. (1) Affine transformation was used to match FA map and its corresponding T1 image in individual space. (2) The transformed T1 map was non-linearly registered into MNI space by T1 template. (3) Based on the above two steps, non-linear transformation from DTI individual space to MNI standard space and its inverse transformation were obtained. The Automated Anatomical Labeling (AAL) template (14) including 90 brain subregions in MNI space was registered into individual space by inverse transformation. Ninety subregions in the individual space were then segmented and labeled. (4) White matter fibers were tracked with deterministic tracking algorithm. When FA < 0.2 or direction change $> 45°$, the white matter fiber tracking was terminated to acquire the whole brain tractography. (5) Based on the whole brain tractography, white matter structural networks could be constructed by defining FA, FN, and FL as edge weight and 90 subregions as nodes.

Network Analysis

Graph theoretical network analysis was performed to investigate potential differences in structural network topological characteristics between HTA and LTA groups. Edges with

FN value <3 and FA < 0.2 were excluded to eliminate the pseudoconnection or noise of the network (15). Accordingly, FA-weighted, FN-weighted, and FL-weighted matrix for the following analysis were obtained. The metrics of these networks such as global efficiency (Eg), local efficiency (Eloc), clustering coefficient (Cp), characteristic path length (Lp), and small-world property (Sigma) were calculated by GRETNA software (16). Global efficiency refers to the average inverse shortest path length, which reflects the overall efficiency of information transmission in the network. Clustering coefficient was described as the prevalence of clustered connectivity around individual nodes. The average shortest path length between all pairs of nodes in the network was called the characteristic path length (17). Local efficiency was defined as the average efficiency of the subnetwork, which described the information exchange efficiency of subnetworks. Small-world property indicated a network with high global efficiency and local efficiency (18).

In addition, edges of the three white matter connectivity matrices (FA, FN, and FL) between HTA and LTA groups were compared to identify alterations in fiber connection. The different connections were displayed using Brainnet viewer software (19).

Statistical Analysis

Differences in structural network properties (Sigma, Eg, Eloc, Cp, and Lp) and white matter connectivities between HTA and LTA groups were assessed by two-sample *t*-test. The false discovery rate (FDR) correction for multiple comparisons was used. In addition, given that depression may influence the results, the Beck Depression Inventory (BDI) score was regarded as a covariate. The above analysis was performed by GRETNA software.

RESULTS

Demographic Characteristics and Behavioral Data

Demographic characteristics and behavioral data of the subjects were compared (**Table 1**). No significant differences in age, gender, and CRT were observed between HTA and LTA groups.

TABLE 1 | Statistics of the demographic and behavioral data (mean and SD).

Characteristics	HTA	LTA	Test statistic	*p*-value
Gender (male/female)	38 (19/19)	34 (14/20)	$\chi^2 = 0.563$	0.453
Age (years)	20.237 ± 1.384	20.471 ± 2.078	$t = -0.567$	0.572
TAI	54.50 ± 2.628	26.177 ± 2.516	$t = 46.58$	<0.001*
SAI	43.026 ± 9.356	24.882 ± 3.883	$t = 10.947$	<0.001*
BDI	13.421 ± 7.366	2.294 ± 2.877	$t = 8.608$	<0.001*
CRT	66.263 ± 4.157	66.088 ± 3.108	$t = 0.204$	0.839

*SD, standard deviation; HTA, high trait anxiety; LTA, low trait anxiety; TAI, trait anxiety inventory; SAI, State Anxiety Inventory; BDI, Beck's Depression Inventory; CRT, combined Raven's matrix test. *p < 0.001.*

Alterations in Structural Networks

The topological properties of the three structural networks were not significantly different. However, some altered connections were detected in FA- and FN-weighted networks.

Fractional Anisotropy-Weighted Network

Twenty-five connections featured by FA value decreased significantly in the HTA group compared with the LTA group (**Table 2** and **Figure 2**) ($p < 0.01$, FDR corrected). The most different connections primarily comprised the connectivity of the left inferior orbitofrontal gyrus to the right inferior frontal gyrus (triangular), the right superior orbitofrontal gyrus to the right hippocampus, the right medial orbitofrontal gyrus to the right lenticular nucleus (putamen), the left hippocampus to the left posterior cingulate gyrus, the left thalamus, the right calcarine, the right superior temporal gyrus to the left posterior cingulate gyrus, and the right middle occipital gyrus to the right precentral gyrus ($p < 0.001$, FDR corrected).

Fiber Number-Weighted Network

Twenty connections were detected to have differences ($p < 0.01$, FDR corrected, **Table 3** and **Figure 3**). The most different connections primarily comprised the connectivity of the left inferior frontal gyrus (opercular) to the right inferior frontal gyrus (opercular), the right inferior frontal gyrus (triangular) to the left inferior orbitofrontal gyrus, the right superior orbitofrontal gyrus to the right hippocampus, the left hippocampus to the right calcarine and the left posterior cingulate gyrus, the right middle occipital gyrus to the right precentral gyrus, and the right superior temporal gyrus to the left posterior cingulate gyrus ($p < 0.001$, FDR corrected).

DISCUSSION

To our knowledge, the investigation on white matter structural connectivity in young healthy people with high trait anxiety is limited. Our group previously used tract-based spatial statistics method to detect the changes of white matter in young healthy populations with high trait anxiety (8). In this study, our results showed widespread abnormal connections in brain regions, but no significant difference in the network property was detected. Alterations in white matter structural connectivity were primarily located in the inter-hemispheric frontal lobe, the frontal-limbic lobe in the right hemisphere, and the frontal-temporal lobe in the ipsilateral hemisphere.

Patients with generalized anxiety disorder exhibited decreased brain signal variability in widespread regions, including the visual network, the sensorimotor network, the fronto-parietal network, the limbic system, and the thalamus (20). It should be noted that in our study, all subjects are young healthy populations. Although the HTA group has a higher trait anxiety score, they are still healthy populations, and their brains have no significant decline yet in ability their deliver global information. It may be the primary reason why the global properties of the structural brain networks did not show alterations. The abnormal connections

TABLE 2 | Different connections in FA-weighted network.

Different connections		*p*-value
Frontal lobe–frontal lobe		
Inferior frontal gyrus (opercular)_L	Inferior frontal gyrus (opercular)_R	0.001866*
Inferior frontal gyrus (opercular)_L	Inferior frontal gyrus (triangular)_R	0.001003*
Inferior orbitofrontal gyrus_L	Inferior frontal gyrus (triangular)_R	0.000043**
Frontal lobe–limbic lobe		
Superior orbitofrontal gyrus_R	Hippocampus_R	0.000768**
Superior orbitofrontal gyrus_R	Lenticular nucleus, pallidum_R	0.002447*
Inferior frontal gyrus (opercular)_R	Lenticular nucleus, putamen_R	0.007135*
Supplementary motor area_R	Thalamus_L	0.008487*
Medial orbitofrontal gyrus_R	Lenticular nucleus, putamen_R	0.000383**
Paracentral lobule_R	Thalamus_R	0.006736*
Frontal lobe–temporal lobe		
Inferior orbitofrontal gyrus _R	Inferior temporal gyrus_R	0.002246*
Middle frontal gyrus_L	Middle temporal gyrus_L	0.007896*
Middle orbitofrontal gyrus_L	Temporal_Pole_Mid_L	0.009882*
Rectus gyrus_R	Inferior temporal gyrus_R	0.005715*
Hippocampus–brain regions		
Hippocampus_L	Posterior cingulate gyrus_L	0.000014**
Hippocampus_L	Thalamus_L	0.000824**
Hippocampus_L	Calcarine_R	0.000043**
ParaHippocampal gyrus_R	Middle temporal gyrus_R	0.002421*
Temporal lobe–brain regions		
Superior temporal gyrus_R	Posterior cingulate gyrus_L	0.000043**
Fusiform gyrus_R	Middle temporal gyrus_R	0.003185*
Occipital lobe–brain regions		
Middle occipital gyrus_R	Precentral gyrus_R	0.000436**
Cuneus_R	Lenticular nucleus, putamen_R	0.007813*
Calcarine_R	Inferior occipital gyrus_R	0.003976*
Insula–brain regions		
Insula_L	Middle occipital gyrus_L	0.009393*
Insula_R	Postcentral gyrus_R	0.005002*
Insula_R	Superior temporal gyrus_R	0.005260*

FA, fractional anisotropy; FDR, false discovery rate; L, left hemisphere; R, right hemisphere.
*$p < 0.01$, **$p < 0.001$; FDR corrected.*

may only influence the local information transmission a bit or even has no significant influence. Another reason may be that they are young adults aged only 20 years, and their brains will have more plasticity during their development or maturity. At the early stage, the global network properties have no such sensitivity as the biomarker to describe the brain structural change. However, the results showed that some different connections occurred in FA and FN networks. These different connections may support to elucidate our understanding of the pathological mechanism of trait anxiety in young populations.

Thalamus-Related Connections

In our previous voxel-wise study on highly anxious population, alterations in the anterior corona radiata (ACR)–thalamus pathway have been detected, as manifested by decreased FA values in the bilateral corona radiata and anterior thalamic radiation regions. This study also showed abnormal connectivity between the left hippocampus and the thalamus. The cortical–thalamus–limbic pathway is closely associated with emotional behavior and regulation related to posttraumatic stress disorder (21). Giménez et al. found that patients with social anxiety disorder showed significant functional connections between the thalamo-cortical and fronto-striatal circuits with task induction (22). These findings suggest that thalamus-related connections may be a vulnerable marker in young healthy individuals with high anxiety.

Temporal Lobe/Hippocampus

A large number of studies reported the importance of the hippocampus/temporal lobe for negative emotionality. Montag et al. found that four white matter tracts linking the temporal lobe/hippocampus to other brain regions were strongly correlated with trait anxiety in male participants only (23). Similarly, we demonstrated that population with high anxiety manifested significant abnormalities in 11 white matter tracts linking the temporal lobe/hippocampus to several brain regions. This study also demonstrated the abnormal connectivity of the hippocampus regions to the posterior cingulate gyrus in highly anxious populations.

Insula

The main function of the insula is emotional processing. Baur et al. stated that the anterior insula and basolateral amygdala constitute a network that is significantly related to anxiety (6). They also supposed that the resting-state functional connection of the anterior insula to the basolateral amygdala was highly related to anxiety. Hamm et al. found that the connection of the right amygdala to the insula showed significantly increased connectivity among pediatrics with anxiety disorders (24). Yang et al. found the abnormal functional architecture of the supramarginal gyrus network and the superior parietal gyrus network in patients with anxiety disorder (25). Dennis et al. found that the enhanced connection of the left anterior insula to the default network in healthy populations with anxiety, but connections of the parahippocampal and posterior cingulate gyrus to the default network increased in adults but not in youth (26). In addition, correlations were reported between insula activity and Liebowitz Social Anxiety Scale (LSAS) (27) or Social Phobia Inventory (SPIN) (28). We also found that the connections of the insula to the occipital and parietal lobes showed abnormality in the FA- and FN-weighted networks (the left insula to the left middle occipital gyrus, the right insula to the right postcentral gyrus in FA-weighted network, the left insula to the left superior parietal gyrus, the right insula to the right postcentral gyrus, and the left insula to left middle occipital gyrus in the FN-weighted network).

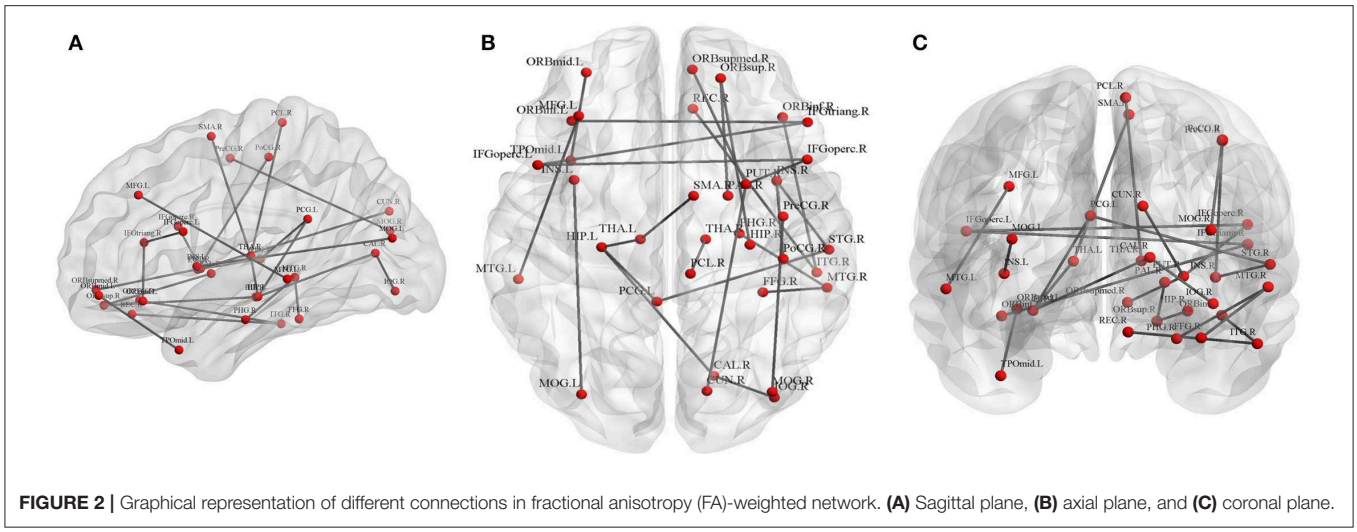

FIGURE 2 | Graphical representation of different connections in fractional anisotropy (FA)-weighted network. **(A)** Sagittal plane, **(B)** axial plane, and **(C)** coronal plane.

TABLE 3 | Different connections in FN-weighted network.

Different connections		*p*-value
Frontal lobe–frontal lobe		
Inferior frontal gyrus (opercular)_L	Inferior frontal gyrus (opercular)_R	0.000009**
Inferior frontal gyrus (triangular)_R	Inferior orbitofrontal gyrus _L	0.000043**
Frontal lobe–limbic lobe		
Superior orbitofrontal gyrus_R	Hippocampus_R	0.000025**
Superior orbitofrontal gyrus_R	Lenticular nucleus, pallidum_R	0.006374*
Paracentral lobule_R	Thalamus_R	0.005746*
Supplementary motor area_R	Lenticular nucleus, putamen_R	0.001449*
Medial orbitofrontal gyrus_R	Lenticular nucleus, putamen_R	0.005243*
Hippocampus–brain regions		
Hippocampus_L	Calcarine_R	0.000043**
ParaHippocampal gyrus_R	Lingual gyrus_R	0.004239*
Hippocampus_L	Posterior cingulate gyrus_L	0.000092**
Middle cingulate gyrus_R	Precuneus_L	0.006184*
Insula–brain regions		
Insula_L	Superior parietal gyrus_L	0.009418*
Insula_R	Postcentral gyrus_R	0.003178*
Insula_L	Middle occipital gyrus_L	0.003504*
Occipital lobe–brain regions		
Calcarine_L	Temporal pole:Superior temporal pole_L	0.009510*
Lingual gyrus_R	Superior orbitofrontal gyrus_R	0.006624*
Middle occipital gyrus_R	Precentral gyrus_R	0.000493**
Precuneus_L	Postcentral gyrus_L	0.002417*
Temporal lobe–brain regions		
Middle temporal gyrus_L	Middle frontal gyrus_L	0.008624*
Superior temporal gyrus_R	Posterior cingulate gyrus_L	0.000043**

FN, fiber number; FDR, false discovery rate; L, left hemisphere; R, right hemisphere.
*$p < 0.01$, **$p < 0.001$, FDR corrected.*

Frontal Cortex and Limbic Areas

The orbitofrontal cortex and the prefrontal cortex located in the anterior–inferior frontal lobe play a crucial role in modulation of fear *via* the amygdala (29). Baur et al. found that the volume of the left uncinate fasciculus decreased in individuals with social anxiety disorder; this finding suggests deficient structural connectivity from high-level control areas in the orbitofrontal cortex to more basal limbic areas, such as the amygdala (30). A study on functional and structural connectivity demonstrated the relationship between trait anxiety and axial diffusivity and reported a direct pathway from the anterior insula to the basolateral amygdala (6). In our study, the observed abnormalities of several frontal lobe connections comprising connectivity linking the orbitofrontal to the limbic regions may be a trait marker in white matter structural network for young healthy individuals. In the FA- and FN-weighted network, individuals with high anxiety manifested abnormalities in the three similar pathways, including the connections of the right superior frontal gyrus (orbital part) to the limbic regions (right hippocampus, pallidum, and putamen).

Basten et al. found that some regions (inferior frontal junction areas, dorsal anterior cingulate gyrus, and left fusiform gyrus) showed significantly weaker task-specific coupling for highly anxious subjects than for those with low anxiety level (31). Kim et al. found a negative functional connectivity of amygdala–dorsal to medial prefrontal cortex in subjects with high anxiety and a positive correlation with activity at rest in subjects with low anxiety (32). Hamm et al. found that anxiety disorders showed a high connection between the left amygdala and the ventromedial prefrontal cortex and posterior cingulate cortex (24). A meta-analysis of fMRI studies investigating emotional processing in individuals who excessively worry demonstrated the convergent abnormalities at the middle frontal gyrus, the inferior frontal gyrus, and the anterior insula compared with normal controls (33). During anticipation of uncertain threat, individuals with high trait anxiety level showed significantly abnormal functional activation in the thalamus, middle temporal

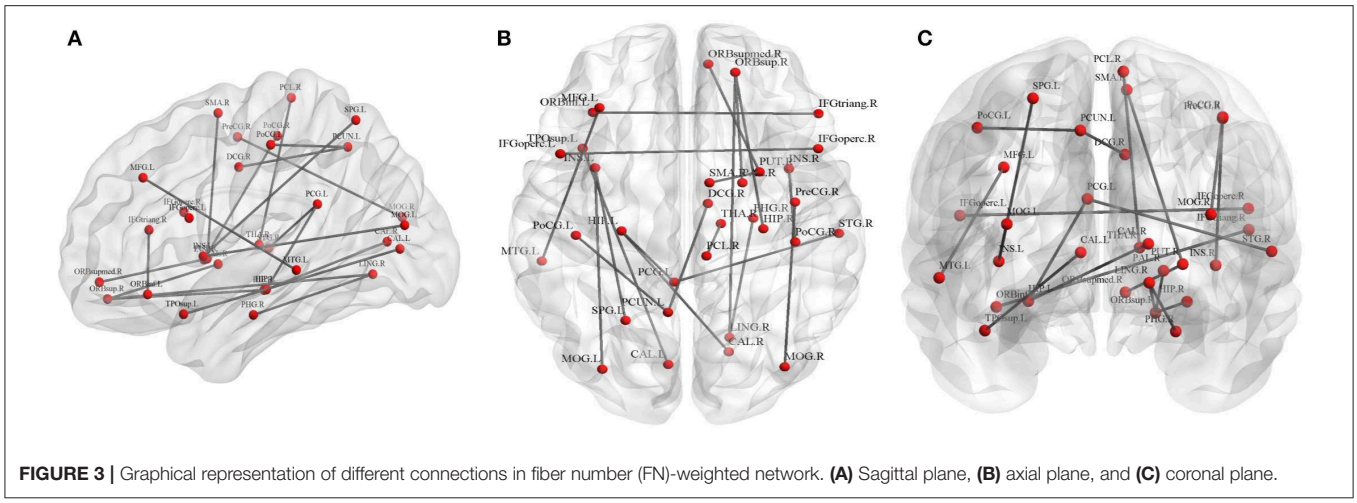

FIGURE 3 | Graphical representation of different connections in fiber number (FN)-weighted network. **(A)** Sagittal plane, **(B)** axial plane, and **(C)** coronal plane.

gyrus, dorsomedial prefrontal cortex, and precuneus (34). Du et al. found that functional connectivity changed in the frontal–limbic–striatal and default-mode networks (35). In predicting uncertain threats for individuals with high trait anxiety level, it was found that the activation of the thalamus, the medial temporal gyrus, and the dorsolateral prefrontal cortex increased significantly, whereas that of the precuneus decreased (34). We also found aberrant connections in precuneus regions in high anxiety populations through an analysis of the FN-weighted network.

Amygdala

The amygdala is a key center for processing threats and plays an important role in generation, recognition, and regulation of emotions. The amygdala is located on the medial dorsal side of the anterior temporal lobe and is a part of the limbic system. Functional brain imaging studies showed that the level of amygdala activation was higher in anxious patients than in healthy controls; moreover, increased amygdala response in clinical and healthy individuals was associated with trait anxiety (36). Makovac et al. found reduced connections of the amygdala to the prefrontal cortex in people with generalized anxiety disorders (36). Similarly, Xue et al. found that high state anxiety level was associated with decreased connectivity of the amygdala to the precuneus/posterior cingulate cortex in adults with anxiety disorders (37).

In their fMRI study, Bishop et al. found that threat-related distractors activated the rostral anterior cingulate cortex in patients with anxiety. In addition, the rostral anterior cingulate cortex and the functions of lateral–prefrontal cortex activities decreased in participants with high anxiety level (38). Similarly, the medial prefrontal cortex and anterior cingulate cortex play important roles in coping with negative emotional stimuli (emotional processing in anterior cingulate and medial prefrontal cortex). Klumpp et al. found that the bilateral anterior insula of patients with generalized social anxiety disorder exhibited strong responses to fear (39). Yang et al. found that functional connectivity among the dorsolateral prefrontal cortex, the ventral medial prefrontal cortex, and the limbic regions was enhanced in the frontal marginal circuit of emotional regulation in patients with social anxiety disorder (40). Jacob et al. found that in people with social anxiety disorders, emotion was associated with decreased connectivity between the amygdala and the prefrontal cortex (41). A task-based fMRI study concerning social anxiety disorders reported abnormal emotion processing areas (e.g., amygdala and insula) (42). However, other scholars believed that the nature of trait anxiety is related to attitudes and strategies and not to situational incentives (4). On the contrary, our results showed no abnormalities of the connections associated with the amygdala. Although the amygdala was an important brain region for anxiety disorders, it has not been structurally altered in healthy people with trait anxiety.

This study has several limitations. First, we only evaluated Chinese undergraduate students who were right-handed and had no history of mental illness. The other similar young healthy populations like those with a relatively low educational level may have results that contrast the current results. Second, the sample size of the current study is still not large enough, which may influence the precision of the results. Third, our study did not report the correlation of functional connection with our structural connection results. Nevertheless, we believe that our data provide strong support for white matter structural connectivity in young healthy individuals with high anxiety level. Results may be helpful to develop interventions before the manifestation of morbidity in young individuals with anxious disorders and to establish a microstructural biomarker of anxiety-related diseases.

DATA AVAILABILITY STATEMENT

Publicly available datasets were analyzed in this study. This data can be found here: The Southwest University Longitudinal Imaging Multimodal, Brain Data Repository (http://fcon_1000.projects.nitrc.org/indi/retro/southwestuni_qiu_index.html).

ETHICS STATEMENT

This study was carried out in accordance with the recommendations of the Declaration of Helsinki (1989) and the Research Ethics Committee of the Brain Imaging Center of Southwest University. The protocol was approved by the Research Ethics Committee of the Brain Imaging Center of Southwest University. All subjects gave written informed consent in accordance with the Declaration of Helsinki.

AUTHOR CONTRIBUTIONS

CY and YZ made contributions to the conception, design, and analysis of DTI data and drafted the manuscript. ML interpreted and discussed the DTI data. JR and ZL made contributions to the revision of the final manuscript. All authors read and approved the final manuscript.

FUNDING

This work was supported by Beijing Nova Program (CN) (no. Z161100004916157); the National Natural Science Foundation of China (nos. 31640035, 71661167001, and 81601126); the Beijing Municipal Commission of Education (no. PXM2017_014204_500012); the Natural Science Foundation of Beijing (no. 4162008); and research fund for CAAE-UCB program, no. 2017010.

ACKNOWLEDGMENTS

Thanks to the Intelligent Physiological Measurement and Clinical Translation, Beijing International Base, for their scientific and technological cooperation. Similarly, thanks also to the Southwest University Longitudinal Imaging Multimodal, Brain Data Repository (China).

REFERENCES

1. Hsiao CY, Tsai HC, Chi MH, Chen KC, Chen PS, Lee IH, et al. The Association between baseline subjective anxiety rating and changes in cardiac autonomic nervous activity in response to tryptophan depletion in healthy volunteers. *Medicine*. (2016) 95:e3498. doi: 10.1097/MD.0000000000003498
2. Dodd HF, Vogt J, Turkileri N, Notebaert L. Task relevance of emotional information affects anxiety-linked attention bias in visual search. *Biol Psychol*. (2017) 122:13–20. doi: 10.1016/j.biopsycho.2016.01.017
3. Zhu H, Qiu C, Meng Y, Yuan M, Zhang Y, Ren Z, et al. Altered topological properties of brain networks in social anxiety disorder: a resting-state functional MRI study. *Sci Rep*. (2017) 7:43089. doi: 10.1038/srep43089
4. Pacheco-Unguetti AP, Acosta A, Callejas A, Lupianez J. Attention and anxiety: different attentional functioning under state and trait anxiety. *Psychol Sci*. (2010) 21:298–304. doi: 10.1177/0956797609359624
5. Liao W, Xu Q, Mantini D, Ding J, Machado-de-Sousa JP, Hallak JE, et al. Altered gray matter morphometry and resting-state functional and structural connectivity in social anxiety disorder. *Brain Res*. (2011) 1388:167–77. doi: 10.1016/j.brainres.2011.03.018
6. Baur V, Hänggi J, Langer N, Jäncke L. Resting-state functional and structural connectivity within an insula–amygdala route specifically index state and trait anxiety. *Biol Psychiatr*. (2013) 73:85–92. doi: 10.1016/j.biopsych.2012.06.003
7. Xing M, Tadayonnejad R, MacNamara A, Ajilore O, Phan KL, Klumpp H, Leow A. EEG based functional connectivity reflects cognitive load during emotion regulation. In: *IEEE 13th International Symposium on Biomedical Imaging (ISBI)*. Chicago, IL (2016). doi: 10.1109/isbi.2016.7493380
8. Lu M, Yang C, Chu T, Wu S. Cerebral white matter changes in young healthy individuals with high trait anxiety: a tract-based spatial statistics study. *Front Neurol*. (2018) 9:704. doi: 10.3389/fneur.2018.00704
9. Liu W, Wei D, Chen Q, Yang W, Meng J, Wu G, et al. Longitudinal test-retest neuroimaging data from healthy young adults in southwest China. *Sci Data*. (2017) 4:170017. doi: 10.1038/sdata.2017.17
10. Spielberger CD, Gorsuch RL. *Manual for the State-Trait Anxiety Inventory (form Y): ("Self-Evaluation Questionnaire")*. Palo Alto, CA: Consulting Psychologists Press, Incorporated (1983).
11. Li D, Hu KD, Chen GP, Jin Y, Li M. The testing results report on the combined Raven's test in Shanghai. *Psychol Sci*. (1988) 4:27–31.
12. Eden AS, Schreiber J, Anwander A, Keuper K, Laeger I, Zwanzger P, et al. Emotion regulation and trait anxiety are predicted by the microstructure of fibers between amygdala and prefrontal cortex. *J Neurosci*. (2015) 35:6020–7. doi: 10.1523/JNEUROSCI.3659-14.2015
13. Cui Z, Zhong S, Xu P, Gong G, He Y. PANDA: a pipeline toolbox for analyzing brain diffusion images. *Front Hum Neurosci*. (2013) 7:42. doi: 10.3389/fnhum.2013.00042
14. Tzourio-Mazoyer N, Landeau B, Papathanassiou D, Crivello F, Etard O, Delcroix N, et al. Automated anatomical labeling of activations in spm using a macroscopic anatomical parcellation of the MNI MRI single-subject brain. *NeuroImage*. (2002) 15:273–89. doi: 10.1006/nimg.2001.0978
15. Li Y, Liu Y, Li J, Qin W, Li K, Yu C, et al. Brain anatomical network and intelligence. *NeuroImage*. (2009) 5:e1000395. doi: 10.1371/journal.pcbi.1000395
16. Wang J, Wang X, Xia M, Liao X, Evans A, He Y. GRETNA: a graph theoretical network analysis toolbox for imaging connectomics. *Front Hum Neurosci*. (2015) 9:386. doi: 10.3389/fnhum.2015.00386
17. Rubinov M, Sporns O. Complex network measures of brain connectivity: uses and interpretations. *NeuroImage*. (2010) 52:1059–69. doi: 10.1016/j.neuroimage.2009.10.003
18. Latora V, Marchiori M. Efficient behavior of small-world networks. *Phys Rev Lett*. (2001) 87:198701. doi: 10.1103/PhysRevLett.87.198701
19. Xia M, Wang J, He Y. BrainNet viewer: a network visualization tool for human brain connectomics. *PLoS ONE*. (2013) 8:e68910. doi: 10.1371/journal.pone.0068910
20. Li L, Wang Y, Ye L, Chen W, Huang X, Cui Q, et al. Altered brain signal variability in patients with generalized anxiety disorder. *Front Psychiatr*. (2019) 10:84. doi: 10.3389/fpsyt.2019.00084
21. Schuff N, Zhang Y, Zhan W, Lenoci M, Ching C, Boreta L, et al. Patterns of altered cortical perfusion and diminished subcortical integrity in posttraumatic stress disorder: an MRI study. *NeuroImage*. (2011) 54:S62–8. doi: 10.1016/j.neuroimage.2010.05.024
22. Giménez M, Pujol J, Ortiz H, Soriano-Mas C, López-Solà M, Farré M, et al. Altered brain functional connectivity in relation to perception of scrutiny in social anxiety disorder. *Psychiatr Res Neuroimaging*. (2012) 202:214–23. doi: 10.1016/j.pscychresns.2011.10.008
23. Montag C, Reuter M, Weber B, Markett S, Schoene-Bake JC. Individual differences in trait anxiety are associated with white matter tract integrity in the left temporal lobe in healthy males but not females. *Neuroscience*. (2012) 217:77–83. doi: 10.1016/j.neuroscience.2012.05.017
24. Hamm LL, Jacobs RH, Johnson MW, Fitzgerald DA, Fitzgerald KD, Langenecker SA, et al. Aberrant amygdala functional connectivity at rest in pediatric anxiety disorders. *Biol Mood Anxiety Disord*. (2014) 4:15. doi: 10.1186/s13587-014-0015-4
25. Yang F, Fan L, Zhai T, Lin Y, Wang Y, Ma J, et al. Decreased intrinsic functional connectivity in first-episode, drug-naive adolescents with generalized anxiety disorder. *Front Hum Neurosci*. (2019) 12:539. doi: 10.3389/fnhum.2018.00539
26. Dennis EL, Gotlib IH, Thompson PM, Thomason ME. Anxiety modulates insula recruitment in resting-state functional magnetic resonance imaging in youth and adults. *Brain Connectivity*. (2011) 1:245–54. doi: 10.1089/brain.2011.0030

27. Liebowitz MR. Social phobia. Modern problems of pharmacopsychiatry. (1987) 22:141–73. doi: 10.1159/000414022
28. Connor KM, Davidson JR, Churchill LE, Sherwood A, Foa E, Weisler RH. Psychometric properties of the Social Phobia Inventory (SPIN). *Br J Psychiatr*. (2000) 176:379–86. doi: 10.1192/bjp.176.4.379
29. Quirk GJ, Likhtik E, Pelletier JG, Paré D. Stimulation of medial prefrontal cortex decreases the responsiveness of central amygdala output neurons. *J Neurosci*. (2003) 23:8800–7. doi: 10.1523/JNEUROSCI.23-25-08800.2003
30. Baur V, Brühl AB, Herwig U, Eberle T, Rufer M, Delsignore A, et al. Evidence of frontotemporal structural hypoconnectivity in social anxiety disorder: a quantitative fiber tractography study. *Hum Brain Mapp*. (2011) 34:437–46. doi: 10.1002/hbm.21447
31. Basten U, Stelzel C, Fiebach CJ. Trait anxiety modulates the neural efficiency of inhibitory control. *J Cogn Neurosci*. (2011) 23:3132–45. doi: 10.1162/jocn_a_00003
32. Kim MJ, Gee DG, Loucks RA, Davis FC, Whalen PJ. Anxiety dissociates dorsal and ventral medial prefrontal cortex functional connectivity with the amygdala at rest. *Cereb Cortex*. (2010) 21:1667–73. doi: 10.1093/cercor/bhq237
33. Weber-Goericke F, Muehlhan M. A quantitative meta-analysis of fMRI studies investigating emotional processing in excessive worriers: application of activation likelihood estimation analysis. *J Affect Disord*. (2018) 243:348–59. doi: 10.1016/j.jad.2018.09.049
34. Geng H, Wang Y, Gu R, Luo YJ, Xu P, Huang Y, et al. Altered brain activation and connectivity during anticipation of uncertain threat in trait anxiety. *Hum Brain Mapp*. (2018) 39:3898–914. doi: 10.1002/hbm.24219
35. Du MY, Liao W, Lui S, Huang XQ, Li F, Kuang WH, Gong QY. Altered functional connectivity in the brain default-mode network of earthquake survivors persists after 2 years despite recovery from anxiety symptoms. *Soc Cogn Affect Neurosci*. (2015) 10:1497–505. doi: 10.1093/scan/nsv040
36. Makovac E, Mancini M, Fagioli S, Watson DR, Meeten F, Rae CL, et al. Network abnormalities in generalized anxiety pervade beyond the amygdala-pre-frontal cortex circuit: Insights from graph theory. *Psychiatr Res Neuroimaging*. (2018) 281:107–16. doi: 10.1016/j.pscychresns.2018.09.006
37. Xue S, Lee T, Guo Y. Spontaneous activity in medial orbitofrontal cortex correlates with trait anxiety in healthy male adults. *J Zhejiang Univ Sci B*. (2018) 19:643–53. doi: 10.1631/jzus.B1700481
38. Bishop S, Duncan J, Brett M, Lawrence AD. Prefrontal cortical function and anxiety: controlling attention to threat-related stimuli. *Nat Neurosci*. (2004) 7:184–8. doi: 10.1038/nn1173
39. Klumpp H, Angstadt M, Phan KL. Insula reactivity and connectivity to anterior cingulate cortex when processing threat in generalized social anxiety disorder. *Biol Psychol*. (2012) 89:273–6. doi: 10.1016/j.biopsycho.2011.10.010
40. Yang X, Liu J, Meng Y, Xia M, Cui Z, Wu X, et al. Network analysis reveals disrupted functional brain circuitry in drug-naive social anxiety disorder. *NeuroImage*. (2017) 190:213–23. doi: 10.1016/j.neuroimage.2017.12.011.
41. Jacob Y, Shany O, Goldin PR, Gross JJ, Hendler T. Reappraisal of interpersonal criticism in social anxiety disorder: a brain network hierarchy perspective. *Cereb Cortex*. (2018) 29:3154–67. doi: 10.1093/cercor/bhy181
42. Brühl AB, Delsignore A, Komossa K, Weidt S. Neuroimaging in social anxiety disorder—A meta-analytic review resulting in a new neurofunctional model. *Neurosci Biobehav Rev*. (2014) 47:260–80. doi: 10.1016/j.neubiorev.2014.08.003

Conflict of Interest: The authors declare that the research was conducted in the absence of any commercial or financial relationships that could be construed as a potential conflict of interest.

frontiers in Neurology

REVIEW
published: 25 February 2020
doi: 10.3389/fneur.2020.00143

Manganese-Enhanced Magnetic Resonance Imaging: Application in Central Nervous System Diseases

Jun Yang and Qinqing Li**

Department of Radiology, The Third Affiliated Hospital of Kunming Medical University, Yunnan Cancer Hospital & Cancer Center, Kunming, China

Manganese-enhanced magnetic resonance imaging (MEMRI) relies on the strong paramagnetism of Mn^{2+}. Mn^{2+} is a calcium ion analog and can enter excitable cells through voltage-gated calcium channels. Mn^{2+} can be transported along the axons of neurons via microtubule-based fast axonal transport. Based on these properties, MEMRI is used to describe neuroanatomical structures, monitor neural activity, and evaluate axonal transport rates. The application of MEMRI in preclinical animal models of central nervous system (CNS) diseases can provide more information for the study of disease mechanisms. In this article, we provide a brief review of MEMRI use in CNS diseases ranging from neurodegenerative diseases to brain injury and spinal cord injury.

Keywords: manganese, MEMRI, central nervous system, neurodegeneration, brain injury

OPEN ACCESS

Edited by:
Achim Gass,
University Medical Center Mannheim, Germany

Reviewed by:
Galit Saar,
National Institute of Neurological Disorders and Stroke (NINDS), United States
Yutong Liu,
University of Nebraska Medical Center, United States

****Correspondence:***
Jun Yang
imdyang@qq.com
Qinqing Li
qinqing_81@163.com

Specialty section:
This article was submitted to Applied Neuroimaging, a section of the journal Frontiers in Neurology

Received: *25 September 2019*
Accepted: *07 February 2020*
Published: *25 February 2020*

Citation:
Yang J and Li Q (2020) Manganese-Enhanced Magnetic Resonance Imaging: Application in Central Nervous System Diseases. Front. Neurol. 11:143. doi: 10.3389/fneur.2020.00143

INTRODUCTION

Central nervous system (CNS) lesions are serious diseases affecting human health. Many imaging methods are currently available for the diagnosis and treatment of CNS diseases, and magnetic resonance imaging (MRI) is the most widely used imaging method. In addition to conventional T1-weighted imaging (T1WI) and T2-weighted imaging (T2WI), the continuous development of multiple MRI functional imaging methods [such as diffusion-weighted imaging (DWI), diffusion tensor imaging (DTI), and blood-oxygen-level dependent (BOLD) imaging] has enabled a better understanding and investigation of the occurrence, development, and prognosis of CNS diseases. Manganese enhanced magnetic resonance imaging (MEMRI) is a special MR functional imaging method, which is different from other imaging methods. For example, DWI has a limited ability to detect complex fiber connections and has low sensitivity in tracking subcortical fibers, leading to underestimation of nerve fiber connections, whereas MEMRI can produce results comparable to histological results (1). DTI can be used to evaluate neural connectivity and the integrity of nerve fiber tract, but cannot assess the dynamics of axonal transport, whereas MEMRI can measure axonal transport functions (2–4). BOLD imaging provides a hemodynamic-dependent measurement of the spatial location and extent of neuronal activity but with poor specificity, whereas MEMRI directly measures neuronal activity in brain areas by assessing dynamic changes in calcium signals (5). PET and SPECT only measure brain activity through an assessment of metabolic changes, but the spatial resolution is low; thus, the ability of this technique to distinguish brain microstructures is limited.

Mn^{2+} has strong paramagnetism, significantly reduces the T1 relaxation time, and exhibits a high signal on T1WI, which is the basis of MEMRI. Mn^{2+} is a Ca^{2+} analog that is absorbed by excitable cells through voltage-gated calcium channels [particularly L-type $Ca_v1.2$ channels (6)], Na^+-Ca^{2+} exchangers on the cell membrane (7–10) in addition to other routes of Na^+/Mg^{2+} antiporters, transferrin and divalent metal transporter-1 (DMT1) (11–13). At present, MEMRI is

mainly used in three areas: studies of anatomy and cellular structure (14–18), tracing of neural connections (5, 19, 20), and brain function (21–26). After entering into cells, Mn^{2+} is transported along neurons via microtubule-dependent axonal transport and reaches secondary neurons by transport across synapses, thereby enabling anterograde tracing of associated neural pathways (27–29). For the study of brain function, activity-induced manganese-dependent MRI (AIM-MRI) is a kind of MEMRI method used to detect preferentially active neural regions during a task such as light, odor, pain, sensory, drug or behavioral stimulation (30, 31). This method is directly dependent on the activity of neurons and is independent of hemodynamics (32). Many types of CNS diseases exist, and animal experiments are required to investigate such diseases in most cases. Due to the unique advantages of MEMRI, its applications are gradually increasing in studies relevant to CNS diseases. This review focuses on animal models of CNS diseases.

Mn^{2+} ADMINISTRATION METHOD

The routes of Mn^{2+} administration in MEMRI are mainly local administration (LA) and systemic administration (SA). SA is performed through oral gavage or intravenous, intraperitoneal, subcutaneous, or intramuscular injection and enables observation of the scopes and boundaries of anatomical structures (33). Intracerebral administration has been used to inject Mn^{2+} into different regions of the brain to study connectivity and axonal transport. A summary of MEMRI studies using local Mn^{2+} administration is provided in **Table 1**. Other methods of administration include nasal lavage and intravitreal, intrathecal, subdural, inner ear, subarachnoid, and intraventricular injection (60, 61, 65, 71, 74–76).

SA is mainly used in preclinical experimental studies. Most Mn^{2+} reaches the brain parenchyma through the blood-brain barrier (BBB) and blood-cerebrospinal fluid barrier [(77, 78); **Figure 1A**], thus enhancing visualization of neuronal structures and highlighting functionally active brain regions. An intravenous injection of mangafodipir (a manganese-based chelate contrast agent) in healthy volunteers provided good visualization of the choroid plexus, anterior pituitary, and exocrine glands in the head and neck (79). Oral administration is mainly used to study the hepatobiliary system and is rarely used to examine the CNS. Qiu et al. (80) studied differences in cerebral development between male and female mice, and MEMRI was performed in neonatal mice after they ingested Mn^{2+} in milk produced by the lactating mother. A major challenge with SA is the adverse effects of Mn^{2+}, which will be discussed in the toxicity section.

Nasal administration is an effective LA method for examination of the CNS using MEMRI (**Figure 2**). Nasal administration avoids the adverse effects of SA. In the study by Fa et al. (23), the visual cortex of rats was observed using AIM-MRI after perfusion of $MnCl_2$ in the nasal cavity, and Mn^{2+} migrated from the olfactory bulb to the visual cortex. When the rats were presented with different odors after intranasal instillation of $MnCl_2$, differences in the signal intensity of Mn^{2+} were observed in the primary olfactory cortex of rats depending on these odors (25). The signal intensity of MEMRI generally increases as the $MnCl_2$ concentration increases, but the signal intensity can be saturated. Moreover, the application of $MnCl_2$ solutions with excessively high concentrations in the nasal cavity will also cause olfactory damage (81), which is occasionally accompanied by inflammatory reactions (82).

Mn^{2+} administration via the visual pathway is also an LA route and mainly includes intraocular injection and a local drip. Intraocular injections are more frequently used, and MRI after an intravitreal injection of $MnCl_2$ allows researchers to observe the entire visual pathway from the retina, optic nerve, optic chiasm, lateral geniculate nucleus, and superior colliculus to the visual cortex (**Figures 1B–D**). Administration of low-dose $MnCl_2$ produces good enhancement on MEMRI without significant damage to the ocular structure, but administration of Mn^{2+} doses >1,500 nmol decreased the number of retinal ganglion cells (RGCs) (83). Local drip is a noninvasive method and is currently being used in experimental research. After a local drip of a $MnCl_2$ solution, Mn^{2+} is rapidly distributed to the aqueous humor, while the concentration of Mn^{2+} in the vitreous body exhibits fewer fluctuations throughout the process (84). According to Sun et al. (85), locally dripped $MnCl_2$ solutions (1 and 1.5 M) did not diffuse into the vitreous cavity, possibly reached the retina through the capillary circulation after iris absorption, and were then transported to the superior colliculus. This method is safe and does not damage the visual system. The authors further showed that an acidic $MnCl_2$ solution produced more pronounced MEMRI signal intensity than a neutral solution, and the use of longer intervals between repeated local Mn^{2+} doses can reduce adverse effects (86). In addition, $MnCl_2$ can be injected through the anterior chamber for imaging (87, 88) and subsequently reveals the structure of the visual system. However, this method is used less frequently because it is more invasive than local drip administration and does not result in direct retinal uptake of Mn^{2+} in contrast to intravitreal injection.

TOXICITY

Manganese is one of the basic trace elements needed for development, but excess manganese intake can cause poisoning. Excess manganese often accumulates in organs such as the liver, pancreas, bones, kidneys, and brain, causing liver damage, neurotoxicity, impaired cardiovascular function, and even death (89). In the chronic stage, excessive manganese accumulation in the brain striatum can lead to Parkinson's disease-like symptoms (29). Currently, the main reason why manganese-containing contrast agents have not been widely used in clinical practice is the neurotoxic effect of Mn^{2+}. Researchers administer Mn contrast agents through either systemic routes or local routes to study the CNS. SA is simple and noninvasive and can be repeated as needed. However, one major disadvantage is that the dose of $MnCl_2$ is significantly higher than the dose used for LA, and Mn^{2+} reaches the liver, heart, and kidney before reaching the brain, increasing the risk of acute toxicity (90).

TABLE 1 | Summary of MEMRI studies using local administration of Mn^{2+}.

Animal strains	Injection site	Dose	MRI	Interest	References
C57BL/6J mice	Hippocampus	0.25 μl, 5–200 mM	2.35 T	Neural pathways	(14, 34)
Lewis rats	Visual cortex	60 μg/kg, 60 mg/kg	4.7 T	Visual cortex; corpus callosum	(35)
Wistar rats	Entorhinal cortex	40 nl, 1 M	4.7T	Hippocampus	(36)
SD rats	Entorhinal cortex	100 nl, 100 mM	4.7 T	Hippocampo-thalamic network	(37)
SD rats	Raphe interpositus nucleus	0.4 μl, 0.08 M	4.7 T	Lateral habenula	(38)
Mice	Hippocampus	3-5 nl, 200 mM	11.7 T	Hippocampal to basal forebrain transport	(39)
Marmoset	Forelimb primary motor cortex	0.16 μl, 800, 400, 40, and 8 nmol	3.0 T	Corticospinal tract	(40)
Mice	Prefrontal cortex	5 nl, 600 mM	11.7 T	Neurocircuitry	(41, 42)
SD rats	Ventral tegmental area	100 nl, 200 mM	4.7 T	Neuronal projections from ventral tegmental area to forebrain	(43)
Monkey	Orbitofrontal/ anterior cingulate cortex	0.2 ∼ 0.5 μl, 800 or 120 mM	4.7 T	Prefrontal circuits	(44)
Wistar rats	Sensorimotor cortex	0.2 μl, 1 M	4.7 T	Neuronal connectivity	(45, 46)
SD rats	Sensorimotor cortex	0.2 μl, 1 M	3.0 T	Neuronal connective pathways	(47)
SD rats	Intracortical/ Motor cortex	0.2 μl, 1 M	9.4 T	Spinal cord/ Corticospinal tract	(48, 49)
C57/BL6 mice	Striatum/ Amygdala	10 nl, 5 mM	11.7 T	Tract tracing from striatum and amygdala	(19)
Mice	Hippocampus	5 nl, 500 mM	11.7 T	Hippocampal circuitry	(50)
C57BL6	Primary somatosensory cortex	60 nl, 100 mM	7.0 T	Somatosensory cortex	(51)
SD rats	Lateral geniculate nucleus/ visual cortex	30 nl, 100 mM; 100 nl, 100 mM	7.0 T	Lateral geniculate nucleus; visual cortex	(20)
SD rats	Somatosensory cortex	200 nl, 60 mM	11.7 T	Corticocortical and thalamocortical connectivity	(52)
SD rats	Habenular nucleus	0.005 μl, 4 M	7.0 T	Habenular nucleus tract	(53)
SD rats	Raphe nucleus	0.15 μl, 0.1 M	7.0 T	Dorsal raphe forebrain tract	(54)
SD rats	Thalamus	200 nl, 10 ∼60 mM	11.7 T	Cortical laminar architecture	(15)
SD rats	Orbitofrontal cortex	200 nl, 80 mM	4.7 T	Orbitofrontal neuronal activity	(55)
SD rats	Somatosensory cortex	∼10 nl, 0.8 M	3.0 T	Major brain projection systems	(56)
Rhesus macaques	Frontal eye fields	0.3 μl, 120 mM or 300 mM	7.0 T	Frontal eye fields connections	(1)
SD rats	Spinal cord	10 nl, 25 mmol/l	9.4 T	Spinal cord	(57)
SD rats	Spinal cord	30 or 60 nl, 100 or 800 mM	7.0 T	Spinal cord	(58)
Wistar rats	Spinal cord	50 nl, 10 mM	4.7 T	Spinal cord	(59)
SD rats	Cisterna magna	50 μl, 25 mM; 25 μl, 50 mM	4.7 T	Brain	(60)
SD rats	Subarachnoid space	50 μl, 10 mM	4.7 T	Spinal cord	(61)
SD rats	Cisterna magna	80 μl, 0.8 mM	1.5 T	Spinal cord	(62)
SD rats	Cisterna magna	80 μl, 0.8 M	1.5 T	Spinal cord	(63)
Mice	Cisterna magna, Lateral ventricles	0.5 μl, 0.8 M; 0.25 μl, 0.8 M	1.5 T	Spinal cord	(64)
C57/BL6 mice	Lateral ventricle	0.25 μl, 5mM	2.35 T	Neural pathways	(14)
SD rats	Lateral ventricles	2 μl, 0.2 mol/l	3.0 T; 7.0 T	Brain and spinal cord; spinal injury	(65, 66)
SD rats, Wistar rats	Lateral ventricle	6 μl, 0.17 M	4.7 T	Spinal cord	(67–69)
Wistar rats	Lateral ventricle	10 μl, 50 mM	4.7 T	Hippocampal	(70)
Wistar rats	Below the dura	200 nl, 0.3 M	7.0 T	Corticothalamic pathway	(71)
SD rats	Transcranial	500 mM or 250 mM	11.7 T	Traumatic brain injury	(72)
SD rats	Transcranial	∼50μl, 100, 250, 500 mM	11.7 T	Neuronal tract tracing	(73)

The use of fractional or continuous infusions of low doses for SA has been shown to reduce the toxic effects of $MnCl_2$. Some studies have used low-dose, fractional administration methods to achieve good imaging effects while avoiding the toxic side effects of $MnCl_2$ (26, 91, 92). Using subcutaneous or intraperitoneal implantation of micro-osmotic pumps to continuously administer low doses of $MnCl_2$ can produce a better enhancement effect than bolus or fractional administration

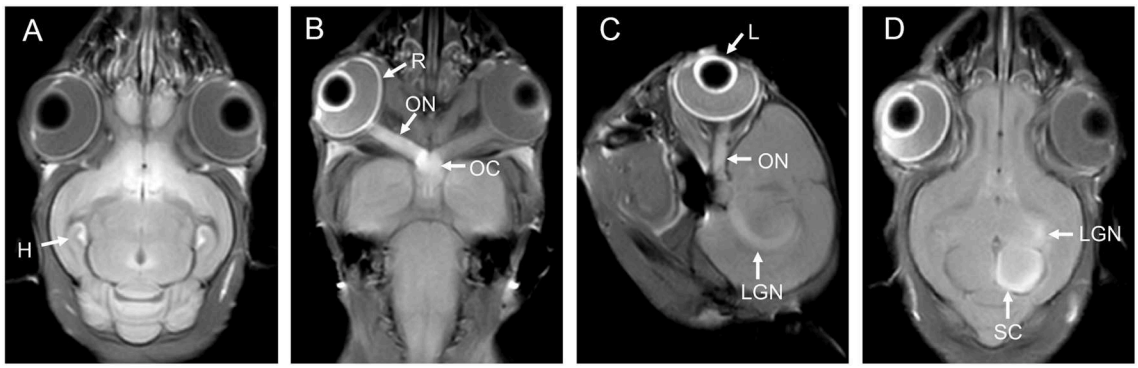

FIGURE 1 | (A) is the brain of a tree shrew in MEMRI after $MnCl_2$ intraperitoneal administration 24 h. The hippocampus can be observed enhancement. **(B–D)** are the visual pathways of a tree shrew in MEMRI. MEMRI can be used to observe visual pathways from the retina, optic nerve, optic chiasm, lateral geniculate nucleus, and superior colliculus after intravitreal injection of $MnCl_2$ in a tree shrew (a kind of squirrel-like mammal which is the closest to primates). H, hippocampus; R, retina; L, lens; ON, optic nerve; OC, optic chiasm; LGN, lateral geniculate nucleus; SC, superior colliculus.

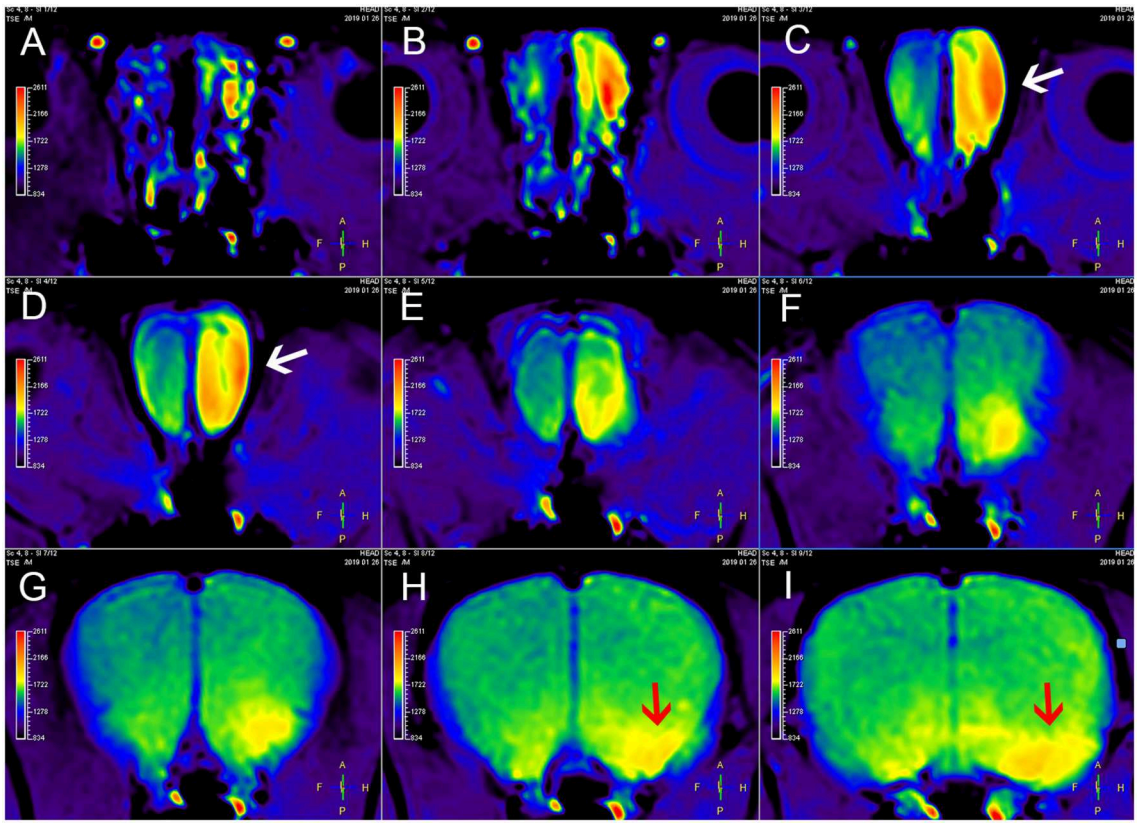

FIGURE 2 | MEMRI of a rat using left nasal administration of $MnCl_2$. Mn^{2+} uptake into the olfactory bulb (white arrows) and transport to olfactory cortex along the olfactory pathway. The red arrows indicate the lateral olfactory tract with unilateral enhancement. From **(A–I)** are axial continuous images of rat brain MRI.

(93–95). Local injections reduce the systemic toxic side effects of manganese but cause certain trauma during the administration process, and the technical requirements for administration are high. For example, precise stereotaxic positioning is required to reach the target area when injecting manganese into a specific brain region. Different studies have used different doses and routes of administration, but the lowest doses that achieve the desired MRI signals should be used to reduce the systemic and local toxic side effects of Mn^{2+}. The signal intensity of MEMRI is related to the concentration of Mn^{2+}, but excessive Mn^{2+} levels can damage different tissues. Thus, the concentration must be balanced according to the actual experimental situation.

NEURODEGENERATIVE DISEASES

Alzheimer's Disease (AD)

AD is a neurodegenerative disease and the most common cause of dementia. Neuropathological features of AD include neurofibrillary tangles (NFTs) and the formation of neuritic amyloid-β (Aβ) plaques. The brains of patients with AD contain a large amount of hyperphosphorylated tau protein. Under these conditions, the normal functions of the tau protein are either inhibited or lost, and paired helical filaments or NFTs associated with synaptic damage begin to appear (96). MEMRI can detect neuronal dysfunction at an early stage and contributes to early detection of the disease. Fontaine et al. used a quantitative ΔR1 value ($\Delta R1 = R1_{6h}\text{-}R1_{baseline}$) and intraperitoneal $MnCl_2$ injection to detect markedly abnormal elevations in ΔR1 in the hippocampal CA1 and CA3 regions before the onset of cognitive deficits in tau protein transgenic mice (rTg4510) (97). In another AD model (5XFAD mice), MEMRI with SA of Mn^{2+} showed increased signal intensity in brain areas associated with spatial cognition in the early stages of the disease (2–5 months of age); this increased intensity was associated with impaired learning and memory in behavioral tests (98). The increase in the degree of MEMRI enhancement may be related to abnormal changes in brain waves, and changes in electroencephalograms occur earlier than abnormal changes in memory (99). Moreover, $MnCl_2$ absorption may be increased due to inflammatory responses as Mn^{2+} enhancement is increased in the presence of increasing inflammation in a stroke model (100). MEMRI also detects depolarization due to reduced calcium influx after oxidative stress-mediated damage to the L-type calcium channel in the hippocampus (CA1d region) of 5xFAD mice via SA of Mn^{2+} (101). Notably, in another study using an APPxPS1 knock-in AD mouse model, MEMRI did not recognize abnormal neuronal activity in various brain regions probably due to increased Mn^{2+} diffusion associated with increased BBB permeability in the AD model and the lack of correlation between Mn^{2+} deposition and local neuronal activity (102).

Rhinencephalon-based MEMRI is widely used to study AD and is mainly used to detect structural changes in the olfactory bulb and the axonal transport function and to evaluate therapeutic effects after treatment. Smith et al. (103) used nasal Mn^{2+} administration for MEMRI to quantitatively evaluate the axonal transport function in animals with tau protein lesions. In this study, the axonal transport rate in Tg2576 mice (an AD animal model) was normal before Aβ deposition, decreased significantly as the Aβ level increased before plaque formation, and substantially decreased after plaque formation. Aβ deposition in the olfactory bulb occurs earlier than in other brain region and is responsible for the decrease in olfactory function observed in subjects with early AD (104). Overexpression of amyloid precursor protein (APP) is also a hallmark of AD, leading to elevated levels of Aβ42 and the formation of neuritic plaques that result in oxidative stress, inflammatory responses, and subsequent neuronal damage (105). Saar et al. (106) used an AD mouse model overexpressing APP and observed changes in the signal intensity in the olfactory bulb following SA via tail vein injection. Since overexpressed APP damages the layered structure of the olfactory bulb, the glomerular layer of the olfactory bulb presents reduced Mn^{2+} enhancement and volume. The Mn^{2+} enhancement of the glomerular layer is increased 1 week after doxycycline-inhibited APP overexpression and gradually returns to normal after 3 weeks. Based on this finding, changes in MEMRI signal intensity in the layers of the olfactory bulb can be used to monitor neurodegenerative changes. In some studies, intranasal perfusion of $MnCl_2$ was used for imaging. MEMRI detected a decrease in the axonal transport rate of the rhinencephalon before the formation of Aβ plaques. The axonal transport rate showed a continuous decrease with the formation of Aβ plaques, and the transport function was gradually restored after treatment (107). In a similar study, MEMRI with nasal administration of Mn^{2+} in rTg4510 transgenic mice revealed an age-dependent axonal transport defect in the rhinencephalon, which was observed beginning at 3 months and until the formation of pathological tau proteins (108). Other similar studies using AD animal models (APP-knockout mice, 3xTg-AD mice, and JNPL3 tauopathy mice) have revealed axonal transport disorders in the brain prior to the formation of Aβ plaques (2, 109), and the axonal transport of Mn^{2+} decreases with the pathological increase in the levels of the tau protein (110). Treatment of Tg2576 mice with R-flurbiprofen (a selective Aβ42-reducing agent) before the formation of Aβ plaques increased the axonal transport of Mn^{2+}, and mice that were treated after plaques formed also showed an improved axonal transport capacity. However, the mechanisms are different, and the latter treatment strategy mainly relies on reducing tau hyperphosphorylation (111).

In addition to SA and nasal administration, Mn^{2+} can be directly injected into specific brain regions to trace neuronal connections in the brain and has been used to detect impairments in the intracellular transport function. In an APP-knockout mouse model, Mn^{2+} transport from the hippocampus to the septal nucleus and amygdala was reduced 7 h after $MnCl_2$ injection into the CA3 region, and Mn^{2+} transport to the contralateral hippocampus was reduced after 25 h (50), suggesting that the transport function was impaired. A similar study analyzed the transport function in mice at different ages by injecting Mn^{2+} into the CA3 region of APP SwInd transgenic mice and wild-type mice. Mn^{2+} transport along the hippocampus to the basal forebrain pathway was decreased with aging, and the decrease was more pronounced in aged APP SwInd transgenic mice. Thus, with aging, the natural degeneration of neurons is further aggravated by APP overexpression and Aβ plaque formation (112). Medina et al. studied the mechanism underlying the decrease in axonal transport and found that knockout of microtubule motor kinesin light chain-1 (KLC-1) decreases Mn^{2+} transport from the hippocampus to the forebrain, but this effect is weak (39), and other kinesins or motor molecules may also play a role in axonal transport.

Parkinson's Disease (PD)

PD is a slowly progressive, neurodegenerative dyskinesia with clinical manifestations of bradykinesia and additional motor symptoms including muscle stiffness, static tremor, and progressive posture and gait instability (113). The most important pathological feature of PD is the degeneration and death of dopaminergic neurons in the substantia nigra pars compacta (SNc) of the midbrain, resulting in a significant reduction in the striatal dopamine content and subsequent disease onset.

An animal model of PD was established using MPTP (1-methyl-4-phenyl-1,2,4,5-tetrahydropyridine) to induce dopaminergic (DAergic) neuron death in the SNc (114). In rats with MPTP-induced PD, MPTP injury resulted in a decrease in neuronal activity and density in the nigrostriatal DAergic system and CA1, CA3, and dentate gyrus (DG) regions of the hippocampus, as well as a decrease in neurogenesis in the DG, but an increase in the activity of the subthalamic nucleus (STN). The hippocampal R1 value on MEMRI following systemic injection of $MnCl_2$ was positively correlated with the neuron density, and the R1 value of the STN was positively correlated with neuronal activity but negatively correlated with the density of DAergic neurons in the SNc. The R1 value on MEMRI was proposed as an indicator of PD severity and treatment outcomes (115). In mice with MPTP-induced PD (intraperitoneal administration of Mn^{2+}), an increase in Mn^{2+} uptake during the first few days was postulated to be caused by increased astrocyte reactivity due to early striatum terminal degeneration, whereas the enhancement of the MEMRI signal was reduced after anti-inflammatory treatment using vasoactive intestinal peptide receptor 2 agonists, thus facilitating neuronal protection (116). Quantitative AIM-MRI uses a quantitative T1 value (or R1 value $= T1^{-1}$) to quantify the neuronal activity map of the entire brain, revealing the patterns and locations of changes in neuronal activity in animal models of PD. In particular, a quantitative analysis of the R1 value in the dorsal caudate-putamen determines the severity of PD and thus facilitates proper treatment (117). Unilateral SNc injury in the rat model of 6-hydroxydopamine (OHDA)-induced PD causes bilateral changes, and the T2 relaxation time of the bilateral SNc increases on MRI. Meanwhile, DTI reveals changes in the axial and radial diffusivities of 6-OHDA in the SNc reticulata and cortex at three and 14 days after 6-OHDA injection, indicating changes in the microstructures of these regions. In addition, MEMRI (local injection of Mn^{2+} into the STN) shows a decrease in the axonal transport function from the ipsilateral STN to the ventral globus pallidus (118). Some researchers have used MEMRI to study neural connections in PD models. In the rat model of 6-OHDA-induced PD, Mn^{2+} infusion into the SNc revealed an enhanced signal in the anterior thalamus and habenular nucleus, and an injection of Mn^{2+} into the habenular nucleus revealed an enhanced signal in the interpeduncular nucleus and raphe, suggesting increased connectivity between the hemispheres of the basal ganglia (119) and reduced connectivity between the raphe and the lateral habenular nucleus, DG, thalamus, and hypothalamus. Apomorphine treatment (a dopamine replacement therapy) partially restores the raphe connections and reduces depressive symptoms (38). Based on these studies, MEMRI not only detects neurodegeneration and dysfunction but also serves as an imaging method to monitor the efficacy of drug treatment.

Amyotrophic Lateral Sclerosis (ALS)

ALS is a neurodegenerative disease that affects human motor neurons and other neuronal cells, leading to severe disability, and some critically ill patients eventually die of respiratory failure. The diagnosis of ALS is based on a painless and progressive functional decline and upper and lower motor neuron dysfunction (120). Mutations in some genes [tubulin alpha 4A (TUBA4A), profilin 1 (PFN1), dynactin 1 (DCTN1), and neurofilament heavy subunit (NEFH)] that are expressed during the progression of pathogenesis may cause axonal transport dysfunction (121). Additional studies have used conventional MRI, such as T2 mapping, DWI, and DTI, to study axonal changes in animal models, whereas studies using MEMRI are relatively rare. In the ALS model of SOD1-G93A mice, MEMRI (nasal administration of $MnCl_2$) was used to estimate the axonal transport rate, and anterograde axonal transport was significantly reduced in the rhinencephalon of ALS mice but returned to normal after acute treatment with davunetide (a neuroprotective compound that facilitates microtubule stabilization and repair). In addition, tau hyperphosphorylation associated with microtubule dysfunction and impaired axonal transport was observed in ALS mice, and chronic treatment with davunetide significantly reduced tau hyperphosphorylation (122). By achieving a better understanding of axonal transport dysfunction in ALS patients, MEMRI will be increasingly used in future studies to assess the axonal transport function and for post-treatment evaluations.

Multiple Sclerosis (MS)

MS is an autoimmune disease in the CNS characterized by demyelination and simultaneous axonal and neuronal degeneration. Optic neuritis is one of the most common manifestations of MS and can gradually lead to vision loss. MEMRI has been used in animal models of optic neuritis and MS and can be used to assess the axonal transport function of the optic nerve (3, 123). Experimental autoimmune encephalomyelitis (EAE) is a chronic inflammation model and a major animal model of MS (124). As shown in the study by Boretius et al. using a rat EAE model, the high signal intensity on T2WI and enhancement mediated by the conventional MRI contrast agent Gd-DTPA are highly sensitive to optic nerve damage. However, the technique was unable to distinguish between mild, moderate, and severe lesions, while MEMRI signal enhancement was positively correlated with the severity of axonal loss, and Mn^{2+} tended to accumulate in the central part of the inflamed optic nerve possibly due to intracellular Ca^{2+} overload (123). In the group with moderate and severe optic neuritis, the rate of Mn^{2+} accumulation and the axonal transport rate (intravitreal injection of $MnCl_2$) were significantly lower than those in the control group, and the change in axonal transport was associated with visual function and structural damage (3). The mechanism by which this inflammation causes axonal degeneration may be direct damage caused by Ca^{2+} influx to the

axon from N-type voltage-dependent calcium channels and/or activated macrophages/microglia, thereby promoting secondary axonal injury (125). Treatment with calpain inhibitors not only reduces calpain activity but also protects RGCs from preclinical degeneration (126).

In clinical practice, corpus callosum atrophy is observed in patients with MS. Another study used an EAE mouse model to study changes in corpus callosum connections. Mn^{2+} was directly injected into the visual cortex, and MEMRI was used to track changes in the corpus callosum over time. At 7 h after Mn^{2+} injection, the signal intensity along the corpus callosum and contralateral visual cortex was higher in the EAE group than that in the control group. At 12–14 h after Mn^{2+} injection, the signal enhancement of the EAE group was significantly higher than that of the control group. This difference may be due to the significant increase in the intracellular Ca^{2+} concentration, thus resulting in an ion imbalance (35).

Glaucoma

Glaucoma is one of the main causes of irreversible blindness. Because the disease can progress for many years before symptoms occur, it is called the "sneaky thief of sight" (127). Glaucoma is characterized by progressive degeneration of RGCs. MEMRI was conducted 2-5 h after intravitreal injection of Mn^{2+} at 2 and 6 weeks after establishment of a rat glaucoma model. MEMRI revealed a delayed increase in signal intensity at 6 weeks. In addition, Mn^{2+} accumulated in the vitreous body, and the concentration was particularly high in the optic disc and retina. The higher signal intensity observed in the vitreous humor may be due to blockage of the trabecular pathway for scleral and limbal vein drainage due to photocoagulation during model establishment (128), the combined effects of RGC apoptosis, a decreased number and density of optic nerve axons, or blockade of axonal transport in the head of the ganglion despite the presence of living cells (129). In a hereditary glaucoma model using DBA/2J mice (whose optic nerve axonal degeneration and intraocular pressure depend on age), the periocular circumference is related to the total retinal thickness, retinal inner layer thickness, ciliary body area, optic disc width, and angulus iridocornealis. Retinal Mn^{2+} uptake decreases with age in old DBA/2J mice, and loss of axonal transport occurs before changes in retinal thickness (130). The visual pathway showed a significant reduction in Mn^{2+} enhancement at 9 months and little enhancement by 12 months in DBA/2J mice (131), and early axonal transport may be impaired before elevated intraocular pressure develops (132). These MEMRI findings help us understand the pathogenesis of glaucoma and monitor the effects of drug interventions and provide an *in vivo* global perspective for investigations of the primary visual conduction system in rats. MEMRI is expected to serve as an important complement to examinations of visual function in subjects with glaucoma.

Retinopathy

MEMRI has been used to observe changes in the function of the retina, degenerative changes in the retina, and diabetic retinopathy. Berkowitz et al. did not detect a significant difference in the signal intensity in the light/dark states between the inner and outer layers of the retina on conventional MRI, but MEMRI revealed that the change in signal intensity between light/dark conditions was significantly greater in the outer layer of the retina than that in the inner layer of the retina, facilitating observations of the physiological response of the normal retina (133). MEMRI was also used to assess changes in retinal function and post-treatment efficacy by measuring ion channel activity (134). In addition to displaying changes in retinal function, MEMRI reveals changes in the retinal structure. In rats with degenerative changes in retinal photoreceptors, MEMRI detected structure changes in the retina layers, and the outer plexiform layer, outer nuclear layer, and photoreceptor inner and outer segment layers disappeared (135). The thickness of the retina and the degree of Mn^{2+} uptake differ at different stages of degenerative changes due to changes in ion regulation within the retina (136). In addition, excitotoxicity is associated with the pathogenesis of various ocular diseases and the pathogenesis of retinal ischemia. In a glutamate excitotoxic retinal injury model, MEMRI reveals a decrease in the Mn^{2+} transport function of the visual pathway, and when combined with DTI and optical coherence tomography, MEMRI provides information about temporal and spatial changes in white matter integrity, as well as relationships between changes in eye-brain and structure-physiology relationships in the visual system (137).

Diabetic mice present a gradual decrease in the thickness of the central region of the retina with increasing age (138). Mn^{2+} uptake in the retinas of these animals is reduced but can return to normal after vascular inhibitor treatment with lipoic acid (139). In streptozotocin-induced diabetic rat retinas, MEMRI detected a decrease in calcium ion activity in the outer layer of the retina 14 days after the onset of early hyperglycemia and decreased activity of the choroid, the latter of which returned to normal after 30 days (140). Similar studies have revealed differences in the retinal uptake of Mn^{2+} at different intervals in diabetic mouse models. Mn^{2+} uptake is initially lower than normal in mice at early stages of the disease (diabetes for 1.5–4 months) and then gradually increases (diabetes for more than 5.5 months) (138). Early diabetes had little effect on the axonal transport function, and at week 4, MEMRI did not detect abnormalities in visual conduction pathways from the retina to the lateral geniculate and superior colliculus (141).

BRAIN INJURY

Stroke

The ischemic penumbra that forms after stroke is defined as the impaired but rescuable ischemic brain tissue around the irreversibly damaged core region (142). MEMRI shows high signal intensity in the ischemic area of the cerebral cortex, reflecting the intracellular Ca^{2+} influx caused by hypoxic depolarization. The area with an enhanced Mn^{2+} signal is the central area of ischemia and is smaller than the area detected using the apparent diffusion coefficient (ADC). MEMRI is expected to become the main imaging method used to detect cerebral ischemia in the hyperacute phase (143). From a few days and a few weeks after stroke, MEMRI showed an increase

in Mn^{2+} enhancement in peri-ischemic tissue mainly due to the inflammatory responses of surrounding tissues and the proliferation of reactive astrocytes (47, 100). This manifestation indicates nerve repair.

MEMRI has also been used to monitor and assess changes in neurological function after stroke and can facilitate assessment of the extent of the loss of function and recovery after stroke. Most studies use local brain injection of Mn^{2+} to study changes in neural connections and functions after stroke. After establishing a rat model of stroke induced by unilateral middle cerebral artery occlusion, manganese was injected into the ipsilateral sensorimotor cortex 2 weeks later, and MEMRI showed decreased enhancement in subcortical areas such as the caudate-putamen, SNc, and thalamus (increased R1 values), suggesting disruptions in the neural connections in the motor cortex (45). In addition to local neural connections, distant neural connections are also affected. A stroke in the sensorimotor cortex that is located farther away from the hippocampus has been shown to alter the neural connections between the hippocampus and thalamus as evidenced by impaired Mn^{2+} transport and Mn^{2+} aggregation in the thalamus (37). At 10 weeks after unilateral establishment of large-area stroke in rats, the functional connections between the contralateral primary motor cortex (M1) and the ipsilateral sensorimotor cortex region were reduced, which was accompanied by reduced translocation of Mn^{2+} from the contralateral M1 to the ipsilateral sensorimotor cortex (24). According to these studies, MEMRI can assess temporal and spatial changes in neurological connections after stroke. Longitudinal MEMRI has been used to dynamically observe the integrity of the post-stroke cortico-thalamic pathway and is helpful to understanding the recovery of brain function after stroke and to visualize plastic changes in cortical-hypothalamic connections (71).

Traumatic Brain Injury (TBI)

TBI is the most common cause of long-term disability and death in trauma patients and imposes a substantial socioeconomic and health care burden. Neuroimaging biomarkers provide a method to noninvasively visualize structural and functional abnormalities in the brains of subjects with TBI. For example, DTI is used to observe changes in the white matter microstructure (144), MRI angiography is used to observe changes in cerebral blood flow (145), magnetic resonance spectroscopy (MRS) is used to observe changes in neuronal metabolism (146), and susceptibility-weighted imaging (SWI) has been used to observe micro bleeding in subjects with diffuse axonal injury. MEMRI is also potentially useful for TBI research because MEMRI provides high-contrast and detailed information about structural and functional changes in the brain *in vivo,* and Mn^{2+} remains in the body for several days, which is beneficial for continuous and dynamic observations.

The volume of the rat brain was measured after fluid percussion injury using MEMRI. The volumes of the whole brain, hippocampus, and cortex decreased gradually from 1 to 6 months after injury, but changes in Mn^{2+} enhancement were observed only in the hippocampus. In particular, the enhancement was significantly increased in the DG on the injured side at 1 month post injury, which may represent an active region involved in subacute neuronal remodeling (147). Calcium channel dysfunction is associated with secondary TBI. Mn^{2+} is a calcium ion analog, and MEMRI has been used to study calcium ion channel-related problems. In the hyperacute phase, MEMRI (SA of Mn^{2+} through the tail vein) can detect early excitotoxic damage and early signs of BBB destruction before vasogenic edema; thus, MEMRI allows earlier and more sensitive detection than T2WI. In the subacute phase, MEMRI detects reactive astrocyte proliferation around the lesion (148). MEMRI (intraperitoneal administration of Mn^{2+}) has also been used to diagnose explosive blast-induced TBI, and an increase in MEMRI signal intensity serves as a biomarker for mild-to-moderate explosive blast-induced TBI (149). In a study of tinnitus caused by explosive blast-induced TBI, MEMRI data showed increased activity along the bilateral auditory pathway and certain peripheral regions in rats with tinnitus compared with that in the age-matched control group (150). In addition to observing changes in TBI, MEMRI has been used to observe changes after TBI treatment. Tang et al. and Jiang et al. used MEMRI to monitor the activity and function of stem cells after neural stem cell transplantation in TBI rats (151, 152).

Hypoxic-Ischemic Encephalopathy (HIE)

Neonatal HIE is a type of hypoxic-ischemic brain damage caused by neonatal asphyxia during the perinatal period, which can cause neurodevelopmental disorders and lead to varying degrees of disability, resulting in high morbidity and mortality rates. After systemic Mn^{2+} injection into a mild HIE model, MEMRI showed enhanced signals in cerebral cortical lesions, which persisted from acute to late phases. The enhanced signals were associated with increased immunological activity of glutamine synthetase (GS) and manganese superoxide dismutase (Mn-SOD) (these two enzymes are conjugated enzymes that protect against glutamate toxicity and oxidative stress during neurodegeneration), and MEMRI detected late-stage mild HIE in damaged gray matter, which cannot be detected using conventional methods (153). MEMRI also detects neurodegenerative changes caused by HIE. In a neonatal HIE model of 1-week-old rats, ipsilateral lesions did not show Mn^{2+} enhancement on T1WI, and histology showed no Mn-SOD or GS production in the acute phase (first 2 days). Mn^{2+} enhancement occurred in the cortex, basal ganglia, and hippocampus in the medium phase (starting from day 3), which was associated with increased local Mn-SOD and GS activity. However, in the late stage, the enhanced region was mainly confined to the basal ganglia and areas around the cortex, and the signal gradually weakened (154). Thus, changes in the activities of the Mn-SOD and GS enzymes can be monitored using MEMRI for early determination of neurodegenerative changes caused by HIE.

Delayed death of neurons and secondary inflammatory reactions occur several days after the onset of neonatal HIE. In another study using the same HIE model of one-week-old rats, MEMRI (intraperitoneal administration of $MnCl_2$) showed no increase in enhancement on days 1 and 3, but Mn^{2+} enhancement increased in the cortex, hippocampus, and thalamus on day 7. Histology revealed delayed neuronal death

and inflammation in these areas, and a large number of activated microglia were present in these regions with high enhancement. Based on these findings, late-stage Mn^{2+} enhancement may be associated with inflammatory processes rather than cell death (155). This group subsequently performed a continuous MEMRI study (1, 3, 7, and 42 days after HIE) and discovered liquefaction on day 42 in areas showing enhancement on day 7 (the hippocampus, thalamus, and basal ganglia), and the main areas with Mn^{2+} enhancement on day 42 were the calcified areas surrounded by activated microglia and reactive astrocytes in the residual thalamus (156). Meanwhile, anti-inflammatory treatment with doxycycline reduces long-term brain tissue loss and white matter damage after neonatal HIE (157). In some studies, MEMRI and DTI were combined to observe gray and white matter damage in the brain caused by HIE and hyperbaric oxygen therapy (158). MEMRI enables researchers to observe *in vivo* pathological processes after HIE and to evaluate the efficacy of HIE treatments.

Chemical and Physical Brain Injury

Chemotherapy can improve the long-term survival rate of patients with cancer, but chemotherapy can also cause brain damage, leading to chemotherapy-related cognitive dysfunction, which is commonly known as chemo brain or chemo fog and is a common side effect of chemotherapy (159). Short-term memory is significantly impaired by chemotherapy and is often associated with impaired neurogenesis, inflammation, and mitochondrial dysfunction in the hippocampus (160). The chemotherapy-treated mice showed a significant decrease in MEMRI signal intensity in the hippocampal subregions, suggesting a decrease in neuronal activity in this region (161). Resveratrol is a natural polyphenol that prevents cognitive impairment caused by chemotherapy. Resveratrol treatment in mice with chemotherapy-induced brain injury improves chemotherapy-induced cognitive impairment and leads to a significantly increased intensity of the MEMRI signal in the prefrontal cortex, whole hippocampus, and the cortex of the CA3 hippocampal subregion (162). Based on these findings, MEMRI is a useful tool to assess the conditions of chemotherapy-induced brain injury and the efficacy of treatments. In addition to brain damage caused by active chemotherapy, passive brain damage is caused by poisoning, such as pesticide poisoning. Organic phosphates are widely used as pesticides in agriculture. Ingestion of organic phosphates causes poisoning or even death, and chronic intake causes neurological damage. Hernandez et al. studied the effects of chlorpyrifos on axonal transport in rat brains and found that repeated exposure to chlorpyrifos resulted in a sustained change in axonal transport in the brains of living mammals, with reduced transport of Mn^{2+} from the optic nerve to the superior colliculus (4). Repeated exposure to diisopropylfluorophosphate also resulted in destruction of the structure of myelinated axons and a sustained decrease in axonal transport in the rat brain (163).

MEMRI is also used in radiation brain injury research, particularly for subjects with CNS diseases induced by prenatal radiation exposure. Mn^{2+} uptake was decreased in the rat brain in the radiation-exposed group at 2 weeks after birth and was mainly associated with decreased cell viability (apoptotic alteration) and decreased cell density after prenatal radiation exposure (164). In another study, 3-week-old rats exposed to prenatal radiation showed a decrease in brain volume, significant expansion of the lateral ventricles, a decrease in the MEMRI-enhanced area in the hippocampus, and disappearance of the MEMRI signal in the CA1/2 region due to destruction of the CA1/2 pyramidal cell layer by invading ectopic cell clusters. However, Mn^{2+} enhancement was still present in the CA3 and DG regions, mainly due to glial cell activation, but was below normal levels (165). In a study of tumor radiotherapy, MEMRI detected cellular changes at an early stage (24 h) (166). Thus, MEMRI provides valuable information regarding neurological damage and functional changes after radiation-induced brain injury.

Epilepsy

Animal models of temporal lobe epilepsy include kainic acid (KA)-, pilocarpine-, and pentylenetetrazol-induced epilepsy models, which are divided into an acute phase and a latent phase. Different stages of disease development are associated with different neurobiological changes, such as hippocampal sclerosis, mossy fiber sprouting, inflammation, and neurodegeneration (114).

In a KA-induced rat model, an MEMRI (administration of Mn^{2+} through the tail vein) study showed an increase in the enhancement of the CA3 pyramidal cell layer after KA treatment that was associated with astrocyte proliferation, and the enhancement on MEMRI was reduced after treatment with the L-type calcium channel blocker diltiazem due to focal edema and decreased neuronal swelling (167). When pilocarpine-induced temporal lobe epilepsy in rats lasted for 30 min, a decrease in the Mn^{2+}-enhanced signal was detected in the DG and CA3 regions (compared to the control group), and this reduction was associated with cerebral edema (168) rather than apoptosis (169). Furthermore, 3–5 days after Mn^{2+} injection into the entorhinal cortex, the MEMRI signals in the ipsilateral and contralateral hippocampal DG and CA3 regions gradually increased, and this enhancement was associated with histologically confirmed mossy fiber sprouting (36). In the chronic phase of epilepsy (2 months after KA induction), MEMRI revealed increases in the signal intensity of the CA1 region and DG after SA of Mn^{2+}, but the increase was not obvious at early time points (4 days or less). The changes in the MEMRI signal in the hippocampus were attributed to an increase in axonal density following mossy fiber sprouting rather than neurodegeneration or proliferation of astrocytes or microglia (170). Direct injections of Mn^{2+} into the lateral ventricle of a rat model of temporal lobe epilepsy induced by KA revealed a gradual increase in the enhancement of the CA3, CA1, and DG regions in the hippocampus from 48 h to 6 weeks, but the enhancement was negatively correlated with the frequency of seizures (70). Similar studies have reported a significant reduction in Mn^{2+} enhancement in the early stages of epilepsy and gradual recovery of Mn^{2+} enhancement in the latent and chronic phases (171). According to these studies, the features of changes observed in different stages of MEMRI reflect

pathophysiological changes during the development of epilepsy, including cell damage and repair, as well as changes in neuronal activity. Systemic intravenous infusion of mesenchymal stem cells in rats during epilepsy onset can reduce the occurrence of epileptic episodes, and the degree of Mn^{2+} enhancement in the hippocampus changed from high to low, which was related to inhibition of mossy fiber sprouting (172). Researchers postulate that changes in MEMRI signals will be used as an index to evaluate treatment efficacy.

Neuroinflammation and Drug Abuse

Neuroinflammation not only plays a role in CNS damage involving infection and trauma but also plays a key role in autoimmunity and neurodegenerative diseases (173). MEMRI also has important application value in neuroinflammation. MEMRI can be used in the following cases and in diseases with neuroinflammation characteristics such as MS, optic neuritis, and post-stroke neuroinflammation. MEMRI can reflect brain pathology during progressive HIV-1 infection in mice, and the signal intensity corresponded to the levels of HIV-1 infection, neuroinflammation, and neuronal injury (174). In addition, MEMRI is also used to detect changes in neuronal activity caused by neuroinflammation in metabolic diseases. Thinschmidt et al. found a significant reduction in basal hypothalamic neuronal activity in 8-month-old $Ins2^{Akita}$ diabetic mice using MEMRI (175).

Drug abuse (including alcohol and nicotine) is an important health issue among society. MEMRI is sensitive to neuronal activities affected by drug abuse and is a very useful for understanding the mechanism and treatment of drug abuse. Dudek et al. demonstrated the extensive brain activation associated with voluntary alcohol drinking in rats using MEMRI, which may be a useful imaging tool for investigating modulation of alcohol-related brain activation by drugs (176). They also found that the caudal linear nucleus controls alcohol preferences and consumption in alcohol-preferring rats, and its activity can be revealed by MEMRI (177). In addition, MEMRI mapping may be a useful translational tool for developing and evaluating pharmacotherapies for alcohol use disorders (178). Smoking is a major public health problem. MEMRI can be used as a non-invasive biomarker to monitor acute and chronic nicotine exposure-induced neuronal activities in cortical and subcortical regions (179).

Spinal Cord Injury

Spinal cord injury (SCI) is another serious CNS disease with high mortality and disability rates. MRI has important application value in SCI. MEMRI has been used to assess the type, extent, and dysfunction conditions of SCI and to track the integrity of the corticospinal tract (48, 59, 64). The Mn^{2+} signal intensity is significantly correlated with motor function, and no enhancement is observed at the injury site or at the caudal end (63). By comparing changes in spinal axonal transport rates, nerve regeneration was studied *in vivo* at different stages (65). MEMRI was correlated with and used to determine the severity of SCI. The signal intensity of MEMRI (lateral ventricle $MnCl_2$ injection) was positively correlated with the myelin load in the acute phase of SCI (66). In the rat spinal cord with electrical injury, MEMRI (lateral ventricle $MnCl_2$ injection) showed an interruption in spinal cord enhancement in the thoracic region, and histology confirmed a more significant reduction in the number of neurons in the ventral horn than that in the dorsal horn (67). MEMRI has also been used to monitor the efficacy of SCI treatment. The MEMRI signal intensity (cisterna magna $MnCl_2$ injection) was significantly higher in rats with acute SCI than that in the control group after short-term erythropoietin treatment. The intensity of the MEMRI signal was significantly correlated with the recovery of function in rats, which is potentially useful for early monitoring and treatment (62). Similarly, MEMRI showed a significant increase in relative signal intensity after SCI was treated with cell transplantation, suggesting the repair and regeneration of axons (68, 69).

CONCLUSIONS

This review describes the applications of MEMRI in CNS diseases and provides a visual approach to study the pathophysiological processes of such diseases. Mn^{2+} is a calcium ion analog that enters cells and represents a unique functional imaging tool used to visualize changes *in vivo*, allowing the detection of subtle, early changes in the body. MEMRI has been used to assess cellular/structural integrity, functional activity, and neural connectivity, thus enabling early detection of neuronal function, the intracellular ion balance, and axonal transport. MEMRI also helps determine disease severity and evaluate treatment efficacy.

As in-depth studies are conducted, MEMRI will have increasing applications in preclinical research on the nervous system, which may reveal the relationship between neurological function and injury and between plasticity and repair. The combination of MEMRI with other imaging methods will provide complementary techniques to reveal the pathophysiological processes of diseases. However, the toxic effects of $MnCl_2$ limit the use of MEMRI in humans, and only a few studies have used the Food and Drug Administration (FDA)-approved agent mangafodipir in humans. When conditions permit, local administration of a low dose is the preferred method due to reduced toxic effects. The sensitivity of PET is much higher than that of MRI, and PET uses a lower dose of manganese for imaging. In particular, the emergence of Mn-PET/MRI will be beneficial for clinical applications of Mn^{2+} (180, 181). Further developments in material science are expected to produce safe manganese-containing contrast agents. Together with highly sensitive MRI using lower doses of Mn^{2+}, these contrast agents will provide broad prospects and endless possibilities for MEMRI clinical applications.

AUTHOR CONTRIBUTIONS

JY proposed the topic and wrote the manuscript. QL edited the manuscript.

FUNDING

This study was supported by the National Natural Science Foundation of China (Grant No. 81703155), the Yunnan Applied Basic Research Projects-Kunming Medical University Joint Special Project [Grant No. 2017FE468 (-071)], Yunnan Health Training Project of High Level Talents (H-2017005), and the Education Department of Yunnan Province (2019J1280).

REFERENCES

1. Schaeffer DJ, Johnston KD, Gilbert KM, Gati JS, Menon RS, Everling S. *In vivo* manganese tract tracing of frontal eye fields in rhesus macaques with ultra-high field MRI: comparison with DWI tractography. *Neuroimage.* (2018) 181:211–8. doi: 10.1016/j.neuroimage.2018.06.072
2. Kim J, Choi IY, Michaelis ML, Lee P. Quantitative *in vivo* measurement of early axonal transport deficits in a triple transgenic mouse model of Alzheimer's disease using manganese-enhanced MRI. *Neuroimage.* (2011) 56:1286–92. doi: 10.1016/j.neuroimage.2011.02.039
3. Lin TH, Kim JH, Perez-Torres C, Chiang CW, Trinkaus K, Cross AH, et al. Axonal transport rate decreased at the onset of optic neuritis in EAE mice. *Neuroimage.* (2014) 100:244–53. doi: 10.1016/j.neuroimage.2014.06.009
4. Hernandez CM, Beck WD, Naughton SX, Poddar I, Adam BL, Yanasak N, et al. Repeated exposure to chlorpyrifos leads to prolonged impairments of axonal transport in the living rodent brain. *Neurotoxicology.* (2015) 47:17–26. doi: 10.1016/j.neuro.2015.01.002
5. Cloyd RA, Koren SA, Abisambra JF. Manganese-enhanced magnetic resonance imaging: overview and central nervous system applications with a focus on neurodegeneration. *Front Aging Neurosci.* (2018) 10:403. doi: 10.3389/fnagi.2018.00403
6. Bedenk BT, Almeida-Correa S, Jurik A, Dedic N, Grunecker B, Genewsky AJ, et al. Mn(2+) dynamics in manganese-enhanced MRI (MEMRI): Cav1.2 channel-mediated uptake and preferential accumulation in projection terminals. *Neuroimage.* (2018) 169:374–82. doi: 10.1016/j.neuroimage.2017.12.054
7. Drapeau P, Nachshen DA. Manganese fluxes and manganese-dependent neurotransmitter release in presynaptic nerve endings isolated from rat brain. *J Physiol.* (1984) 348:493–510. doi: 10.1113/jphysiol.1984.sp015121
8. Narita K, Kawasaki F, Kita H. Mn and Mg influxes through Ca channels of motor nerve terminals are prevented by verapamil in frogs. *Brain Res.* (1990) 510:289–95. doi: 10.1016/0006-8993(90)91379-U
9. Pautler RG, Koretsky AP. Tracing odor-induced activation in the olfactory bulbs of mice using manganese-enhanced magnetic resonance imaging. *Neuroimage.* (2002) 16:441–8. doi: 10.1006/nimg.2002.1075
10. Takeda A. Manganese action in brain function. *Brain Res Brain Res Rev.* (2003) 41:79–87. doi: 10.1016/S0165-0173(02)00234-5
11. Aschner M, Gannon M. Manganese (Mn) transport across the rat blood-brain barrier: saturable and transferrin-dependent transport mechanisms. *Brain Res Bull.* (1994) 33:345–9. doi: 10.1016/0361-9230(94)90204-6
12. Crossgrove J, Zheng W. Manganese toxicity upon overexposure. *NMR Biomed.* (2004) 17:544–53. doi: 10.1002/nbm.931
13. Au C, Benedetto A, Aschner M. Manganese transport in eukaryotes: the role of DMT1. *Neurotoxicology.* (2008) 29:569–76. doi: 10.1016/j.neuro.2008.04.022
14. Watanabe T, Frahm J, Michaelis T. Functional mapping of neural pathways in rodent brain *in vivo* using manganese-enhanced three-dimensional magnetic resonance imaging. *NMR Biomed.* (2004) 17:554–68. doi: 10.1002/nbm.937
15. Silva AC, Lee JH, Wu CW, Tucciarone J, Pelled G, Aoki I, et al. Detection of cortical laminar architecture using manganese-enhanced MRI. *J Neurosci Methods.* (2008) 167:246–57. doi: 10.1016/j.jneumeth.2007.08.020
16. Chuang KH, Belluscio L, Koretsky AP. *In vivo* detection of individual glomeruli in the rodent olfactory bulb using manganese enhanced MRI. *Neuroimage.* (2010) 49:1350–6. doi: 10.1016/j.neuroimage.2009.09.060
17. Gutman DA, Magnuson M, Majeed W, Keifer OPJr, Davis M, Ressler KJ, et al. Mapping of the mouse olfactory system with manganese-enhanced magnetic resonance imaging and diffusion tensor imaging. *Brain Struct Funct.* (2013) 218:527–37. doi: 10.1007/s00429-012-0413-6
18. Sajja BR, Bade AN, Zhou B, Uberti MG, Gorantla S, Gendelman HE, et al. Generation and disease model relevance of a manganese enhanced magnetic resonance imaging-based NOD/scid-IL-2Rgammac(null) mouse brain atlas. *J Neuroimmune Pharmacol.* (2016) 11:133–41. doi: 10.1007/s11481-015-9635-8
19. Pautler RG, Mongeau R, Jacobs RE. *In vivo* trans-synaptic tract tracing from the murine striatum and amygdala utilizing manganese enhanced MRI (MEMRI). *Magn Reson Med.* (2003) 50:33–9. doi: 10.1002/mrm.10498
20. Chan KC, Wu EX. *In vivo* manganese-enhanced MRI for visuotopic brain mapping. *Conf Proc IEEE Eng Med Biol Soc.* (2012) 2012:2279–82. doi: 10.1109/EMBC.2012.6346417
21. Bissig D, Berkowitz BA. Manganese-enhanced MRI of layer-specific activity in the visual cortex from awake and free-moving rats. *Neuroimage.* (2009) 44:627–35. doi: 10.1016/j.neuroimage.2008.10.013
22. Chuang KH, Lee JH, Silva AC, Belluscio L, Koretsky AP. Manganese enhanced MRI reveals functional circuitry in response to odorant stimuli. *Neuroimage.* (2009) 44:363–72. doi: 10.1016/j.neuroimage.2008.08.046
23. Fa Z, Zhang P, Huang F, Li P, Zhang R, Xu R, et al. Activity-induced manganese-dependent functional MRI of the rat visual cortex following intranasal manganese chloride administration. *Neurosci Lett.* (2010) 481:110–4. doi: 10.1016/j.neulet.2010.06.063
24. Van Meer MP, Van Der Marel K, Otte WM, Berkelbach Van Der Sprenkel JW, Dijkhuizen RM. Correspondence between altered functional and structural connectivity in the contralesional sensorimotor cortex after unilateral stroke in rats: a combined resting-state functional MRI and manganese-enhanced MRI study. *J Cereb Blood Flow Metab.* (2010) 30:1707–11. doi: 10.1038/jcbfm.2010.124
25. Lehallier B, Rampin O, Saint-Albin A, Jerome N, Ouali C, Maurin Y, et al. Brain processing of biologically relevant odors in the awake rat, as revealed by manganese-enhanced MRI. *PLoS ONE.* (2012) 7:e48491. doi: 10.1371/journal.pone.0048491
26. Gálosi R, Szalay C, Aradi M, Perlaki G, Pál J, Steier R, et al. Identifying non-toxic doses of manganese for manganese-enhanced magnetic resonance imaging to map brain areas activated by operant behavior in trained rats. *Magn Reson Imaging.* (2017) 37:122–33. doi: 10.1016/j.mri.2016.11.017
27. Pautler RG, Silva AC, Koretsky AP. *In vivo* neuronal tract tracing using manganese-enhanced magnetic resonance imaging. *Magn Reson Med.* (1998) 40:740–8. doi: 10.1002/mrm.1910400515
28. Murayama Y, Weber B, Saleem KS, Augath M, Logothetis NK. Tracing neural circuits *in vivo* with Mn-enhanced MRI. *Magn Reson Imaging.* (2006) 24:349–58. doi: 10.1016/j.mri.2005.12.031
29. Massaad CA, Pautler RG. Manganese-Enhanced Magnetic Resonance Imaging (MEMRI). In: Modo M, Bulte JWM, editors. *Magnetic Resonance Neuroimaging: Methods and Protocols*. Totowa, NJ: Humana Press (2011). p. 145–74.
30. Auffret M, Samim I, Lepore M, Gruetter R, Just N. Quantitative activity-induced manganese-dependent MRI for characterizing cortical layers in the primary somatosensory cortex of the rat. *Brain Struct Funct.* (2016) 221:695–707. doi: 10.1007/s00429-014-0933-3
31. Schroeder MP, Weiss C, Procissi D, Wang L, Disterhoft JF. Activity-induced manganese-dependent MRI (AIM-MRI) and functional MRI in awake rabbits during somatosensory stimulation. *Neuroimage.* (2016) 126:72–80. doi: 10.1016/j.neuroimage.2015.11.033
32. Aoki I, Tanaka C, Takegami T, Ebisu T, Umeda M, Fukunaga M, et al. Dynamic activity-induced manganese-dependent contrast magnetic resonance imaging (DAIM MRI). *Magn Reson Med.* (2002) 48:927–33. doi: 10.1002/mrm.10320
33. Aoki I, Wu YJ, Silva AC, Lynch RM, Koretsky AP. *In vivo* detection of neuroarchitecture in the rodent brain using manganese-enhanced MRI. *Neuroimage.* (2004) 22:1046–59. doi: 10.1016/j.neuroimage.2004.03.031

34. Watanabe T, Radulovic J, Spiess J, Natt O, Boretius S, Frahm J, et al. *In vivo* 3D MRI staining of the mouse hippocampal system using intracerebral injection of MnCl2. *Neuroimage.* (2004) 22:860–7. doi: 10.1016/j.neuroimage.2004.01.028
35. Chen CC, Zechariah A, Hsu YH, Chen HW, Yang LC, Chang C. Neuroaxonal ion dyshomeostasis of the normal-appearing corpus callosum in experimental autoimmune encephalomyelitis. *Exp Neurol.* (2008) 210:322–30. doi: 10.1016/j.expneurol.2007.11.008
36. Nairismagi J, Pitkanen A, Narkilahti S, Huttunen J, Kauppinen RA, Grohn OH. Manganese-enhanced magnetic resonance imaging of mossy fiber plasticity *in vivo*. *Neuroimage.* (2006) 30:130–5. doi: 10.1016/j.neuroimage.2005.09.007
37. Baumgartner P, El Amki M, Bracko O, Luft AR, Wegener S. Sensorimotor stroke alters hippocampo-thalamic network activity. *Sci Rep.* (2018) 8:15770. doi: 10.1038/s41598-018-34002-9
38. Sourani D, Eitan R, Gordon N, Goelman G. The habenula couples the dopaminergic and the serotonergic systems: application to depression in Parkinson's disease. *Eur J Neurosci.* (2012) 36:2822–9. doi: 10.1111/j.1460-9568.2012.08200.x
39. Medina CS, Biris O, Falzone TL, Zhang X, Zimmerman AJ, Bearer EL. Hippocampal to basal forebrain transport of Mn(2+) is impaired by deletion of KLC1, a subunit of the conventional kinesin microtubule-based motor. *Neuroimage.* (2017) 145:44–57. doi: 10.1016/j.neuroimage.2016.09.035
40. Demain B, Davoust C, Plas B, Bolan F, Boulanouar K, Renaud L, et al. Corticospinal Tract Tracing in the Marmoset with a Clinical Whole-Body 3T Scanner Using Manganese-Enhanced MRI. *PLoS ONE.* (2015) 10:e0138308. doi: 10.1371/journal.pone.0138308
41. Zhang X, Bearer EL, Boulat B, Hall FS, Uhl GR, Jacobs RE. Altered neurocircuitry in the dopamine transporter knockout mouse brain. *PLoS ONE.* (2010) 5:e11506. doi: 10.1371/journal.pone.0011506
42. Bearer EL, Zhang X, Janvelyan D, Boulat B, Jacobs RE. Reward circuitry is perturbed in the absence of the serotonin transporter. *Neuroimage.* (2009) 46:1091–104. doi: 10.1016/j.neuroimage.2009.03.026
43. Li Y, Fang F, Wang X, Lei H. Neuronal projections from ventral tegmental area to forebrain structures in rat studied by manganese-enhanced magnetic resonance imaging. *Magn Reson Imaging.* (2009) 27:293–9. doi: 10.1016/j.mri.2008.07.011
44. Simmons JM, Saad ZS, Lizak MJ, Ortiz M, Koretsky AP, Richmond BJ. Mapping prefrontal circuits *in vivo* with manganese-enhanced magnetic resonance imaging in monkeys. *J Neurosci.* (2008) 28:7637–47. doi: 10.1523/JNEUROSCI.1488-08.2008
45. Van Der Zijden JP, Wu O, Van Der Toorn A, Roeling TP, Bleys RL, Dijkhuizen RM. Changes in neuronal connectivity after stroke in rats as studied by serial manganese-enhanced MRI. *Neuroimage.* (2007) 34:1650–7. doi: 10.1016/j.neuroimage.2006.11.001
46. Van Der Zijden JP, Van Der Toorn A, Van Der Marel K, Dijkhuizen RM. Longitudinal *in vivo* MRI of alterations in perilesional tissue after transient ischemic stroke in rats. *Exp Neurol.* (2008) 212:207–12. doi: 10.1016/j.expneurol.2008.03.027
47. Hao XZ, Yin LK, Zhang XX, Tian JQ, Li CC, Feng XY, et al. Combining systemic and stereotactic MEMRI to detect the correlation between gliosis and neuronal connective pathway at the chronic stage after stroke. *J Neuroinflammation.* (2016) 13:156. doi: 10.1186/s12974-016-0622-7
48. Bilgen M. Imaging corticospinal tract connectivity in injured rat spinal cord using manganese-enhanced MRI. *BMC Med Imaging.* (2006) 6:15. doi: 10.1186/1471-2342-6-15
49. Bilgen M, Peng W, Al-Hafez B, Dancause N, He YY, Cheney PD. Electrical stimulation of cortex improves corticospinal tract tracing in rat spinal cord using manganese-enhanced MRI. *J Neurosci Methods.* (2006) 156:17–22. doi: 10.1016/j.jneumeth.2006.02.001
50. Gallagher JJ, Zhang X, Ziomek GJ, Jacobs RE, Bearer EL. Deficits in axonal transport in hippocampal-based circuitry and the visual pathway in APP knock-out animals witnessed by manganese enhanced MRI. *Neuroimage.* (2012) 60:1856–66. doi: 10.1016/j.neuroimage.2012.01.132
51. Daoust A, Bohic S, Saoudi Y, Debacker C, Gory-Faure S, Andrieux A, et al. Neuronal transport defects of the MAP6 KO mouse - a model of schizophrenia - and alleviation by Epothilone D treatment, as observed using MEMRI. *Neuroimage.* (2014) 96:133–42. doi: 10.1016/j.neuroimage.2014.03.071
52. Tucciarone J, Chuang KH, Dodd SJ, Silva A, Pelled G, Koretsky AP. Layer specific tracing of corticocortical and thalamocortical connectivity in the rodent using manganese enhanced MRI. *Neuroimage.* (2009) 44:923–31. doi: 10.1016/j.neuroimage.2008.07.036
53. Hsu YH, Chen CC, Zechariah A, Yen CC, Yang LC, Chang C. Neuronal dysfunction of a long projecting multisynaptic pathway in response to methamphetamine using manganese-enhanced MRI. *Psychopharmacology.* (2008) 196:543–53. doi: 10.1007/s00213-007-0990-x
54. Chiu CH, Siow TY, Weng SJ, Hsu YH, Huang YS, Chang KW, et al. Effect of MDMA-induced axotomy on the dorsal raphe forebrain tract in rats: an *in vivo* manganese-enhanced magnetic resonance imaging study. *PLoS ONE.* (2015) 10:e0138431. doi: 10.1371/journal.pone.0138431
55. Sun N, Li Y, Tian S, Lei Y, Zheng J, Yang J, et al. Dynamic changes in orbitofrontal neuronal activity in rats during opiate administration and withdrawal. *Neuroscience.* (2006) 138:77–82. doi: 10.1016/j.neuroscience.2005.10.034
56. Leergaard TB, Bjaalie JG, Devor A, Wald LL, Dale AM. *In vivo* tracing of major rat brain pathways using manganese-enhanced magnetic resonance imaging and three-dimensional digital atlasing. *Neuroimage.* (2003) 20:1591–600. doi: 10.1016/j.neuroimage.2003.07.009
57. Bilgen M, Dancause N, Al-Hafez B, He YY, Malone TM. Manganese-enhanced MRI of rat spinal cord injury. *Magn Reson Imaging.* (2005) 23:829–32. doi: 10.1016/j.mri.2005.06.004
58. Huereca DJ, Bakoulas KA, Ghoddoussi F, Berkowitz BA, Holt AG, Mueller PJ. Development of manganese-enhanced magnetic resonance imaging of the rostral ventrolateral medulla of conscious rats: importance of normalization and comparison with other regions of interest. *NMR Biomed.* (2018) 31:e3887. doi: 10.1002/nbm.3887
59. Bonny JM, Mailly P, Renou JP, Orsal D, Benmoussa A, Stettler O. Analysis of laminar activity in normal and injured rat spinal cord by manganese enhanced MRI. *Neuroimage.* (2008) 40:1542–51. doi: 10.1016/j.neuroimage.2008.01.050
60. Liu CH, D'arceuil HE, De Crespigny AJ. Direct CSF injection of MnCl(2) for dynamic manganese-enhanced MRI. *Magn Reson Med.* (2004) 51:978–87. doi: 10.1002/mrm.20047
61. Cha M, Lee K, Won JS, Lee BH. Manganese-enhanced magnetic resonance imaging of the spinal cord in rats with formalin-induced pain. *Neurosci Res.* (2019) 149:14–21. doi: 10.1016/j.neures.2019.01.007
62. Freitag MT, Marton G, Pajer K, Hartmann J, Walder N, Rossmann M, et al. Monitoring of short-term erythropoietin therapy in rats with acute spinal cord injury using manganese-enhanced magnetic resonance imaging. *J Neuroimaging.* (2015) 25:582–9. doi: 10.1111/jon.12202
63. Walder N, Petter-Puchner AH, Brejnikow M, Redl H, Essig M, Stieltjes B. Manganese enhanced magnetic resonance imaging in a contusion model of spinal cord injury in rats: correlation with motor function. *Invest Radiol.* (2008) 43:277–83. doi: 10.1097/RLI.0b013e318162f1bd
64. Stieltjes B, Klussmann S, Bock M, Umathum R, Mangalathu J, Letellier E, et al. Manganese-enhanced magnetic resonance imaging for *in vivo* assessment of damage and functional improvement following spinal cord injury in mice. *Magn Reson Med.* (2006) 55:1124–31. doi: 10.1002/mrm.20888
65. Martirosyan NL, Bennett KM, Theodore N, Preul MC. Manganese-enhanced magnetic resonance imaging in experimental spinal cord injury: correlation between T1-weighted changes and Mn(2+) concentrations. *Neurosurgery.* (2010) 66:131–6. doi: 10.1227/01.NEU.0000361997.08116.96
66. Martirosyan NL, Turner GH, Kaufman J, Patel AA, Belykh E, Kalani MY, et al. Manganese-enhanced MRI offers correlation with severity of spinal cord injury in experimental models. *Open Neuroimag J.* (2016) 10:139–47. doi: 10.2174/1874440001610010139
67. Seo CH, Jeong JH, Lee DH, Kang TC, Jin ES, Lee DH, et al. Radiological and pathological evaluation of the spinal cord in a rat model of electrical injury-induced myelopathy. *Burns.* (2012) 38:1066–71. doi: 10.1016/j.burns.2012.02.016
68. Suh HI, Min J, Choi KW, Kim KS, Jeon SR. Axonal regeneration effects of Wnt3a-secreting fibroblast transplantation in spinal cord-injured rats. *Acta Neurochir.* (2011) 153:1003–10. doi: 10.1007/s00701-011-0945-1

69. Park JH, Min J, Baek SR, Kim SW, Kwon IK, Jeon SR. Enhanced neuroregenerative effects by scaffold for the treatment of a rat spinal cord injury with Wnt3a-secreting fibroblasts. *Acta Neurochir.* (2013) 155:809–16. doi: 10.1007/s00701-013-1663-7
70. Dedeurwaerdere S, Fang K, Chow M, Shen YT, Noordman I, Van Raay L, et al. Manganese-enhanced MRI reflects seizure outcome in a model for mesial temporal lobe epilepsy. *Neuroimage.* (2013) 68:30–8. doi: 10.1016/j.neuroimage.2012.11.054
71. Soria G, Wiedermann D, Justicia C, Ramos-Cabrer P, Hoehn M. Reproducible imaging of rat corticothalamic pathway by longitudinal manganese-enhanced MRI (L-MEMRI). *Neuroimage.* (2008) 41:668–74. doi: 10.1016/j.neuroimage.2008.03.018
72. Roth TL, Nayak D, Atanasijevic T, Koretsky AP, Latour LL, Mcgavern DB. Transcranial amelioration of inflammation and cell death after brain injury. *Nature.* (2014) 505:223–8. doi: 10.1038/nature12808
73. Atanasijevic T, Bouraoud N, Mcgavern DB, Koretsky AP. Transcranial manganese delivery for neuronal tract tracing using MEMRI. *Neuroimage.* (2017) 156:146–54. doi: 10.1016/j.neuroimage.2017.05.025
74. Chuang KH, Koretsky AP. Accounting for nonspecific enhancement in neuronal tract tracing using manganese enhanced magnetic resonance imaging. *Magn Reson Imaging.* (2009) 27:594–600. doi: 10.1016/j.mri.2008.10.006
75. Yang J, Li Q, Wang M, Cao X, Ding Y, Wang G, et al. Semiquantitative assessment of optic nerve injury using manganese-enhanced MRI. *Jpn J Radiol.* (2016) 34:356–65. doi: 10.1007/s11604-016-0533-7
76. Tang Z, Wu L, Xiao Z, Feng X, Sun X, Tang W, et al. Manganese-enhanced MRI (ME MRI) in evaluation of the auditory pathway in an experimental rat model. *NMR Biomed.* (2017) 30. doi: 10.1002/nbm.3677
77. Aschner M, Guilarte TR, Schneider JS, Zheng W. Manganese: recent advances in understanding its transport and neurotoxicity. *Toxicol Appl Pharmacol.* (2007) 221:131–47. doi: 10.1016/j.taap.2007.03.001
78. Bornhorst J, Wehe CA, Huwel S, Karst U, Galla HJ, Schwerdtle T. Impact of manganese on and transfer across blood-brain and blood-cerebrospinal fluid barrier *in vitro*. *J Biol Chem.* (2012) 287:17140–51. doi: 10.1074/jbc.M112.344093
79. Sudarshana DM, Nair G, Dwyer JT, Dewey B, Steele SU, Suto DJ, et al. Manganese-Enhanced MRI of the Brain in Healthy Volunteers. *AJNR Am J Neuroradiol.* (2019) 40:1309–16. doi: 10.3174/ajnr.A6152
80. Qiu LR, Fernandes DJ, Szulc-Lerch KU, Dazai J, Nieman BJ, Turnbull DH, et al. Mouse MRI shows brain areas relatively larger in males emerge before those larger in females. *Nat Commun.* (2018) 9:2615. doi: 10.1038/s41467-018-04921-2
81. Lehallier B, Coureaud G, Maurin Y, Bonny JM. Effects of manganese injected into rat nostrils: implications for *in vivo* functional study of olfaction using MEMRI. *Magn Reson Imaging.* (2012) 30:62–9. doi: 10.1016/j.mri.2011.08.009
82. Foster ML, Rao DB, Francher T, Traver S, Dorman DC. Olfactory toxicity in rats following manganese chloride nasal instillation: a pilot study. *Neurotoxicology.* (2018) 64:284–90. doi: 10.1016/j.neuro.2017.09.004
83. Thuen M, Berry M, Pedersen TB, Goa PE, Summerfield M, Haraldseth O, et al. Manganese-enhanced MRI of the rat visual pathway: acute neural toxicity, contrast enhancement, axon resolution, axonal transport, and clearance of Mn(2+). *J Magn Reson Imaging.* (2008) 28:855–65. doi: 10.1002/jmri.21504
84. Liang S, Liang M, Zhu Y, Cheng J, Yang Z. The distribution of Mn2+ in rabbit eyes after topical administration for manganese-enhanced MRI. *Int J Clin Exp Pathol.* (2015) 8:836–41.
85. Sun SW, Campbell B, Lunderville C, Won E, Liang HF. Noninvasive topical loading for manganese-enhanced MRI of the mouse visual system. *Invest Ophthalmol Vis Sci.* (2011) 52:3914–20. doi: 10.1167/iovs.10-6363
86. Sun SW, Thiel T, Liang HF. Impact of repeated topical-loaded manganese-enhanced MRI on the mouse visual system. *Invest Ophthalmol Vis Sci.* (2012) 53:4699–709. doi: 10.1167/iovs.12-9715
87. Lindsey JD, Scadeng M, Dubowitz DJ, Crowston JG, Weinreb RN. Magnetic resonance imaging of the visual system *in vivo*: transsynaptic illumination of V1 and V2 visual cortex. *Neuroimage.* (2007) 34:1619–26. doi: 10.1016/j.neuroimage.2006.07.048
88. Lindsey JD, Grob SR, Scadeng M, Duong-Polk K, Weinreb RN. Ocular integrity following manganese labeling of the visual system for MRI. *Magn Reson Imaging.* (2013) 31:865–74. doi: 10.1016/j.mri.2012.11.012
89. Chen P, Bornhorst J, Aschner M. Manganese metabolism in humans. *Front Biosci.* (2018) 23:1655–79. doi: 10.2741/4665
90. Malheiros JM, Paiva FF, Longo BM, Hamani C, Covolan L. Manganese-enhanced MRI: biological applications in neuroscience. *Front Neurol.* (2015) 6:161. doi: 10.3389/fneur.2015.00161
91. Bock NA, Paiva FF, Silva AC. Fractionated manganese-enhanced MRI. *NMR Biomed.* (2008) 21:473–8. doi: 10.1002/nbm.1211
92. Grunecker B, Kaltwasser SF, Peterse Y, Samann PG, Schmidt MV, Wotjak CT, et al. Fractionated manganese injections: effects on MRI contrast enhancement and physiological measures in C57BL/6 mice. *NMR Biomed.* (2010) 23:913–21. doi: 10.1002/nbm.1508
93. Eschenko O, Canals S, Simanova I, Beyerlein M, Murayama Y, Logothetis NK. Mapping of functional brain activity in freely behaving rats during voluntary running using manganese-enhanced MRI: implication for longitudinal studies. *Neuroimage.* (2010) 49:2544–55. doi: 10.1016/j.neuroimage.2009.10.079
94. Sepulveda MR, Dresselaers T, Vangheluwe P, Everaerts W, Himmelreich U, Mata AM, et al. Evaluation of manganese uptake and toxicity in mouse brain during continuous MnCl2 administration using osmotic pumps. *Contrast Media Mol Imaging.* (2012) 7:426–34. doi: 10.1002/cmmi.1469
95. Poole DS, Doorenweerd N, Plomp JJ, Mahfouz A, Reinders MJT, Van Der Weerd L. Continuous infusion of manganese improves contrast and reduces side effects in manganese-enhanced magnetic resonance imaging studies. *Neuroimage.* (2017) 147:1–9. doi: 10.1016/j.neuroimage.2016.09.030
96. Chandra A, Dervenoulas G, Politis M. Magnetic resonance imaging in Alzheimer's disease and mild cognitive impairment. *J Neurol.* (2019) 266:1293–302. doi: 10.1007/s00415-018-9016-3
97. Fontaine SN, Ingram A, Cloyd RA, Meier SE, Miller E, Lyons D, et al. Identification of changes in neuronal function as a consequence of aging and tauopathic neurodegeneration using a novel and sensitive magnetic resonance imaging approach. *Neurobiol Aging.* (2017) 56:78–86. doi: 10.1016/j.neurobiolaging.2017.04.007
98. Tang X, Wu D, Gu LH, Nie BB, Qi XY, Wang YJ, et al. Spatial learning and memory impairments are associated with increased neuronal activity in 5XFAD mouse as measured by manganese-enhanced magnetic resonance imaging. *Oncotarget.* (2016) 7:57556–70. doi: 10.18632/oncotarget.11353
99. Kam K, Duffy AM, Moretto J, Lafrancois JJ, Scharfman HE. Interictal spikes during sleep are an early defect in the Tg2576 mouse model of beta-amyloid neuropathology. *Sci Rep.* (2016) 6:20119. doi: 10.1038/srep20119
100. Kawai Y, Aoki I, Umeda M, Higuchi T, Kershaw J, Higuchi M, et al. *In vivo* visualization of reactive gliosis using manganese-enhanced magnetic resonance imaging. *Neuroimage.* (2010) 49:3122–31. doi: 10.1016/j.neuroimage.2009.11.005
101. Berkowitz BA, Lenning J, Khetarpal N, Tran C, Wu JY, Berri AM, et al. *In vivo* imaging of prodromal hippocampus CA1 subfield oxidative stress in models of Alzheimer disease and Angelman syndrome. *FASEB J.* (2017) 31:4179–86. doi: 10.1096/fj.201700229R
102. Androuin A, Abada YS, Ly M, Santin M, Petiet A, Epelbaum S, et al. Activity-induced MEMRI cannot detect functional brain anomalies in the APPxPS1-Ki mouse model of Alzheimer's disease. *Sci Rep.* (2019) 9:1140. doi: 10.1038/s41598-018-37980-y
103. Smith KD, Kallhoff V, Zheng H, Pautler RG. *In vivo* axonal transport rates decrease in a mouse model of Alzheimer's disease. *Neuroimage.* (2007) 35:1401–8. doi: 10.1016/j.neuroimage.2007.01.046
104. Wesson DW, Levy E, Nixon RA, Wilson DA. Olfactory dysfunction correlates with amyloid-beta burden in an Alzheimer's disease mouse model. *J Neurosci.* (2010) 30:505–14. doi: 10.1523/JNEUROSCI.4622-09.2010
105. Harrington CR. The molecular pathology of Alzheimer's disease. *Neuroimaging Clin N Am.* (2012) 22:11–22, vii. doi: 10.1016/j.nic.2011.11.003
106. Saar G, Cheng N, Belluscio L, Koretsky AP. Laminar specific detection of APP induced neurodegeneration and recovery using MEMRI in an olfactory based Alzheimer's disease mouse model. *Neuroimage.* (2015) 118:183–92. doi: 10.1016/j.neuroimage.2015.05.045

107. Wang FH, Appelkvist P, Klason T, Gissberg O, Bogstedt A, Eliason K, et al. Decreased axonal transport rates in the Tg2576 APP transgenic mouse: improvement with the gamma-secretase inhibitor MRK-560 as detected by manganese-enhanced MRI. *Eur J Neurosci.* (2012) 36:3165–72. doi: 10.1111/j.1460-9568.2012.08258.x
108. Majid T, Ali YO, Venkitaramani DV, Jang MK, Lu HC, Pautler RG. *In vivo* axonal transport deficits in a mouse model of fronto-temporal dementia. *Neuroimage Clin.* (2014) 4:711–7. doi: 10.1016/j.nicl.2014.02.005
109. Smith KD, Peethumnongsin E, Lin H, Zheng H, Pautler RG. Increased human wildtype tau attenuates axonal transport deficits caused by loss of APP in mouse models. *Magn Reson Insights.* (2010) 4:11–8. doi: 10.4137/MRI.S5237
110. Bertrand A, Khan U, Hoang DM, Novikov DS, Krishnamurthy P, Rajamohamed Sait HB, et al. Non-invasive, *in vivo* monitoring of neuronal transport impairment in a mouse model of tauopathy using MEMRI. *Neuroimage.* (2013) 64:693–702. doi: 10.1016/j.neuroimage.2012.08.065
111. Smith KD, Paylor R, Pautler RG. R-flurbiprofen improves axonal transport in the Tg2576 mouse model of Alzheimer's disease as determined by MEMRI. *Magn Reson Med.* (2011) 65:1423–9. doi: 10.1002/mrm.22733
112. Bearer EL, Manifold-Wheeler BC, Medina CS, Gonzales AG, Chaves FL, Jacobs RE. Alterations of functional circuitry in aging brain and the impact of mutated APP expression. *Neurobiol Aging.* (2018) 70:276–90. doi: 10.1016/j.neurobiolaging.2018.06.018
113. Kalia LV, Lang AE. Parkinson's disease. *Lancet.* (2015) 386:896–912. doi: 10.1016/S0140-6736(14)61393-3
114. Saar G, Koretsky AP. Manganese enhanced MRI for use in studying neurodegenerative diseases. *Front Neural Circuits.* (2019) 12:114. doi: 10.3389/fncir.2018.00114
115. Weng JC, Tikhonova MA, Chen JH, Shen MS, Meng WY, Chang YT, et al. Ceftriaxone prevents the neurodegeneration and decreased neurogenesis seen in a Parkinson's disease rat model: an immunohistochemical and MRI study. *Behav Brain Res.* (2016) 305:126–39. doi: 10.1016/j.bbr.2016.02.034
116. Olson KE, Bade AN, Schutt CR, Dong J, Shandler SJ, Boska MD, et al. Manganese-enhanced magnetic resonance imaging for detection of vasoactive intestinal peptide receptor 2 agonist therapy in a model of Parkinson's disease. *Neurotherapeutics.* (2016) 13:635–46. doi: 10.1007/s13311-016-0449-z
117. Kikuta S, Nakamura Y, Yamamura Y, Tamura A, Homma N, Yanagawa Y, et al. Quantitative activation-induced manganese-enhanced MRI reveals severity of Parkinson's disease in mice. *Sci Rep.* (2015) 5:12800. doi: 10.1038/srep12800
118. Soria G, Aguilar E, Tudela R, Mullol J, Planas AM, Marin C. *In vivo* magnetic resonance imaging characterization of bilateral structural changes in experimental Parkinson's disease: a T2 relaxometry study combined with longitudinal diffusion tensor imaging and manganese-enhanced magnetic resonance imaging in the 6-hydroxydopamine rat model. *Eur J Neurosci.* (2011) 33:1551–60. doi: 10.1111/j.1460-9568.2011.07639.x
119. Pelled G, Bergman H, Ben-Hur T, Goelman G. Manganese-enhanced MRI in a rat model of Parkinson's disease. *J Magn Reson Imaging.* (2007) 26:863–70. doi: 10.1002/jmri.21051
120. Oskarsson B, Gendron TF, Staff NP. Amyotrophic lateral sclerosis: an update for 2018. *Mayo Clin Proc.* (2018) 93:1617–28. doi: 10.1016/j.mayocp.2018.04.007
121. Chia R, Chio A, Traynor BJ. Novel genes associated with amyotrophic lateral sclerosis: diagnostic and clinical implications. *Lancet Neurol.* (2018) 17:94–102. doi: 10.1016/S1474-4422(17)30401-5
122. Jouroukhin Y, Ostritsky R, Assaf Y, Pelled G, Giladi E, Gozes I. NAP (davunetide) modifies disease progression in a mouse model of severe neurodegeneration: Protection against impairments in axonal transport. *Neurobiol Dis.* (2013) 56:79–94. doi: 10.1016/j.nbd.2013.04.012
123. Boretius S, Gadjanski I, Demmer I, Bahr M, Diem R, Michaelis T, et al. MRI of optic neuritis in a rat model. *Neuroimage.* (2008) 41:323–34. doi: 10.1016/j.neuroimage.2008.02.021
124. Wekerle H, Kojima K, Lannes-Vieira J, Lassmann H, Linington C. Animal models. *Ann Neurol.* (1994) 36(Suppl):S47–53. doi: 10.1002/ana.410360714
125. Gadjanski I, Boretius S, Williams SK, Lingor P, Knoferle J, Sattler MB, et al. Role of n-type voltage-dependent calcium channels in autoimmune optic neuritis. *Ann Neurol.* (2009) 66:81–93. doi: 10.1002/ana.21668
126. Hoffmann DB, Williams SK, Bojcevski J, Muller A, Stadelmann C, Naidoo V, et al. Calcium influx and calpain activation mediate preclinical retinal neurodegeneration in autoimmune optic neuritis. *J Neuropathol Exp Neurol.* (2013) 72:745–57. doi: 10.1097/NEN.0b013e31829c7370
127. Fiedorowicz M, Dyda W, Rejdak R, Grieb P. Magnetic resonance in studies of glaucoma. *Med Sci Monit.* (2011) 17:RA227–32. doi: 10.12659/MSM.881973
128. Chan KC, Fu QL, Hui ES, So KF, Wu EX. Evaluation of the retina and optic nerve in a rat model of chronic glaucoma using *in vivo* manganese-enhanced magnetic resonance imaging. *Neuroimage.* (2008) 40:1166–74. doi: 10.1016/j.neuroimage.2008.01.002
129. Dandona L, Hendrickson A, Quigley HA. Selective effects of experimental glaucoma on axonal transport by retinal ganglion cells to the dorsal lateral geniculate nucleus. *Invest Ophthalmol Vis Sci.* (1991) 32:1593–9.
130. Calkins DJ, Horner PJ, Roberts R, Gradianu M, Berkowitz BA. Manganese-enhanced MRI of the DBA/2J mouse model of hereditary glaucoma. *Invest Ophthalmol Vis Sci.* (2008) 49:5083–8. doi: 10.1167/iovs.08-2205
131. Yang XL, Van Der Merwe Y, Sims J, Parra C, Ho LC, Schuman JS, et al. Age-related changes in eye, brain and visuomotor behavior in the DBA/2J mouse model of chronic glaucoma. *Sci Rep.* (2018) 8:4643. doi: 10.1038/s41598-018-22850-4
132. Fiedorowicz M, Orzel J, Kossowski B, Welniak-Kaminska M, Choragiewicz T, Swiatkiewicz M, et al. Anterograde transport in axons of the retinal ganglion cells and its relationship to the intraocular pressure during aging in mice with hereditary pigmentary glaucoma. *Curr Eye Res.* (2018) 43:539–46. doi: 10.1080/02713683.2017.1416147
133. Berkowitz BA, Roberts R, Goebel DJ, Luan H. Noninvasive and simultaneous imaging of layer-specific retinal functional adaptation by manganese-enhanced MRI. *Invest Ophthalmol Vis Sci.* (2006) 47:2668–74. doi: 10.1167/iovs.05-1588
134. Schur RM, Sheng L, Sahu B, Yu G, Gao S, Yu X, et al. Manganese-enhanced MRI for preclinical evaluation of retinal degeneration treatments. *Invest Ophthalmol Vis Sci.* (2015) 56:4936–42. doi: 10.1167/iovs.15-16522
135. Berkowitz BA, Grady EM, Khetarpal N, Patel A, Roberts R. Oxidative stress and light-evoked responses of the posterior segment in a mouse model of diabetic retinopathy. *Invest Ophthalmol Vis Sci.* (2015) 56:606–15. doi: 10.1167/iovs.14-15687
136. Berkowitz BA, Gradianu M, Schafer S, Jin Y, Porchia A, Iezzi R, et al. Ionic dysregulatory phenotyping of pathologic retinal thinning with manganese-enhanced MRI. *Invest Ophthalmol Vis Sci.* (2008) 49:3178–84. doi: 10.1167/iovs.08-1720
137. Ho LC, Wang B, Conner IP, Van Der Merwe Y, Bilonick RA, Kim SG, et al. *In vivo* evaluation of white matter integrity and anterograde transport in visual system after excitotoxic retinal injury with multimodal MRI and OCT. *Invest Ophthalmol Vis Sci.* (2015) 56:3788–800. doi: 10.1167/iovs.14-15552
138. Berkowitz BA, Gradianu M, Bissig D, Kern TS, Roberts R. Retinal ion regulation in a mouse model of diabetic retinopathy: natural history and the effect of Cu/Zn superoxide dismutase overexpression. *Invest Ophthalmol Vis Sci.* (2009) 50:2351–8. doi: 10.1167/iovs.08-2918
139. Berkowitz BA, Roberts R, Stemmler A, Luan H, Gradianu M. Impaired apparent ion demand in experimental diabetic retinopathy: correction by lipoic acid. *Invest Ophthalmol Vis Sci.* (2007) 48:4753–8. doi: 10.1167/iovs.07-0433
140. Muir ER, Chandra SB, De La Garza BH, Velagapudi C, Abboud HE., Duong TQ. Layer-specific manganese-enhanced MRI of the diabetic rat retina in light and dark adaptation at 11.7 Tesla. *Invest Ophthalmol Vis Sci.* (2015) 56:4006–12. doi: 10.1167/iovs.14-16128
141. Kancherla S, Kohler WJ, Van Der Merwe Y, Chan KC. *In Vivo* Evaluation of the Visual Pathway in Streptozotocin-Induced Diabetes by Diffusion Tensor MRI and Contrast Enhanced MRI. *PLoS ONE.* (2016) 11:e0165169. doi: 10.1371/journal.pone.0165169
142. Astrup J, Siesjo BK, Symon L. Thresholds in cerebral ischemia - the ischemic penumbra. *Stroke.* (1981) 12:723–5. doi: 10.1161/01.STR.12.6.723
143. Aoki I, Ebisu T, Tanaka C, Katsuta K, Fujikawa A, Umeda M, et al. Detection of the anoxic depolarization of focal ischemia using manganese-enhanced MRI. *Magn Reson Med.* (2003) 50:7–12. doi: 10.1002/mrm.10528
144. Hoogenboom WS, Rubin TG, Ye K, Cui MH, Branch KC, Liu J, et al. Diffusion tensor imaging of the evolving response

to mild traumatic brain injury in rats. *J Exp Neurosci.* (2019) 13:1179069519858627. doi: 10.1177/1179069519858627
145. Kazam JJ, Tsiouris AJ. Brain magnetic resonance imaging for traumatic brain injury: why, when, and how? *Top Magn Reson Imaging.* (2015) 24:225–39. doi: 10.1097/RMR.0000000000000061
146. Meyer EJ, Stout JN, Chung AW, Grant PE, Mannix R, Gagoski B. Longitudinal changes in magnetic resonance spectroscopy in pediatric concussion: a pilot study. *Front Neurol.* (2019) 10:556. doi: 10.3389/fneur.2019.00556
147. Bouilleret V, Cardamone L, Liu YR, Fang K, Myers DE, O'brien TJ. Progressive brain changes on serial manganese-enhanced MRI following traumatic brain injury in the rat. *J Neurotrauma.* (2009) 26:1999–2013. doi: 10.1089/neu.2009.0943
148. Talley Watts L, Shen Q, Deng S, Chemello J, Duong TQ. Manganese-enhanced magnetic resonance imaging of traumatic brain injury. *J Neurotrauma.* (2015) 32:1001–10. doi: 10.1089/neu.2014.3737
149. Rodriguez O, Schaefer ML, Wester B, Lee YC, Boggs N, Conner HA, et al. Manganese-enhanced magnetic resonance imaging as a diagnostic and dispositional tool after mild-moderate blast traumatic brain injury. *J Neurotrauma.* (2016) 33:662–71. doi: 10.1089/neu.2015.4002
150. Ouyang J, Pace E, Lepczyk L, Kaufman M, Zhang J, Perrine SA, et al. Blast-induced tinnitus and elevated central auditory and limbic activity in rats: a manganese-enhanced MRI and behavioral study. *Sci Rep.* (2017) 7:4852. doi: 10.1038/s41598-017-04941-w
151. Tang HL, Sun HP, Wu X, Sha HY, Feng XY, Zhu JH. Detection of neural stem cells function in rats with traumatic brain injury by manganese-enhanced magnetic resonance imaging. *Chin Med J.* (2011) 124:1848–53. doi: 10.3760/cma.j.issn.0366-6999.2011.12.016
152. Jiang L, Li R, Tang H, Zhong J, Sun H, Tang W, et al. MRI tracking of iPS cells-induced neural stem cells in traumatic brain injury rats. *Cell Transplant.* (2018) 28:747–55. doi: 10.1177/0963689718819994
153. Yang J, Wu EX. Detection of cortical gray matter lesion in the late phase of mild hypoxic-ischemic injury by manganese-enhanced MRI. *Neuroimage.* (2008) 39:669–79. doi: 10.1016/j.neuroimage.2007.09.009
154. Yang J, Khong PL, Wang Y, Chu AC, Ho SL, Cheung PT, et al. Manganese-enhanced MRI detection of neurodegeneration in neonatal hypoxic-ischemic cerebral injury. *Magn Reson Med.* (2008) 59:1329–39. doi: 10.1002/mrm.21484
155. Wideroe M, Olsen O, Pedersen TB, Goa PE, Kavelaars A, Heijnen C, et al. Manganese-enhanced magnetic resonance imaging of hypoxic-ischemic brain injury in the neonatal rat. *Neuroimage.* (2009) 45:880–90. doi: 10.1016/j.neuroimage.2008.12.007
156. Wideroe M, Brekken C, Kavelaars A, Pedersen TB, Goa PE, Heijnen C, et al. Longitudinal manganese-enhanced magnetic resonance imaging of delayed brain damage after hypoxic-ischemic injury in the neonatal rat. *Neonatology.* (2011) 100:363–72. doi: 10.1159/000328705
157. Wideroe M, Havnes MB, Morken TS, Skranes J, Goa PE, Brubakk AM. Doxycycline treatment in a neonatal rat model of hypoxia-ischemia reduces cerebral tissue and white matter injury: a longitudinal magnetic resonance imaging study. *Eur J Neurosci.* (2012) 36:2006–16. doi: 10.1111/j.1460-9568.2012.08114.x
158. Morken TS, Wideroe M, Vogt C, Lydersen S, Havnes M, Skranes J, et al. Longitudinal diffusion tensor and manganese-enhanced MRI detect delayed cerebral gray and white matter injury after hypoxia-ischemia and hyperoxia. *Pediatr Res.* (2013) 73:171–9. doi: 10.1038/pr.2012.170
159. Moore HC. An overview of chemotherapy-related cognitive dysfunction, or 'chemobrain'. *Oncology.* (2014) 28:797–804.
160. Matsos A, Johnston IN. Chemotherapy-induced cognitive impairments: a systematic review of the animal literature. *Neurosci Biobehav Rev.* (2019) 102:382–99. doi: 10.1016/j.neubiorev.2019.05.001
161. Shi DD, Huang YH, Lai CSW, Dong CM, Ho LC, Wu EX, et al. Chemotherapy-induced cognitive impairment is associated with cytokine dysregulation and disruptions in neuroplasticity. *Mol Neurobiol.* (2019) 56:2234–43. doi: 10.1007/s12035-018-1224-4
162. Shi DD, Dong CM, Ho LC, Lam CTW, Zhou XD, Wu EX, et al. Resveratrol, a natural polyphenol, prevents chemotherapy-induced cognitive impairment: Involvement of cytokine modulation and neuroprotection. *Neurobiol Dis.* (2018) 114:164–73. doi: 10.1016/j.nbd.2018.03.006
163. Naughton SX, Hernandez CM, Beck WD, Poddar I, Yanasak N, Lin PC, et al. Repeated exposures to diisopropylfluorophosphate result in structural disruptions of myelinated axons and persistent impairments of axonal transport in the brains of rats. *Toxicology.* (2018) 406–407:92–103. doi: 10.1016/j.tox.2018.06.004
164. Saito S, Aoki I, Sawada K, Suhara T. Quantitative assessment of central nervous system disorder induced by prenatal X-ray exposure using diffusion and manganese-enhanced MRI. *NMR Biomed.* (2012) 25:75–83. doi: 10.1002/nbm.1715
165. Saito S, Sawada K, Aoki I. Prenatal irradiation-induced hippocampal abnormalities in rats evaluated using manganese-enhanced MRI. *Front Neural Circuits.* (2018) 12:112. doi: 10.3389/fncir.2018.00112
166. Saito S, Hasegawa S, Sekita A, Bakalova R, Furukawa T, Murase K, et al. Manganese-enhanced MRI reveals early-phase radiation-induced cell alterations *in vivo*. *Cancer Res.* (2013) 73:3216–24. doi: 10.1158/0008-5472.CAN-12-3837
167. Hsu YH, Lee WT, Chang C. Multiparametric MRI evaluation of kainic acid-induced neuronal activation in rat hippocampus. *Brain.* (2007) 130:3124–34. doi: 10.1093/brain/awm207
168. Malheiros JM, Longo BM, Tannus A, Covolan L. Manganese-enhanced magnetic resonance imaging in the acute phase of the pilocarpine-induced model of epilepsy. *Einstein.* (2012) 10:247–52. doi: 10.1590/S1679-45082012000200023
169. Malheiros JM, Persike DS, Castro LU, Sanches TR, Andrade Lda C, Tannus A, et al. Reduced hippocampal manganese-enhanced MRI (MEMRI) signal during pilocarpine-induced status epilepticus: edema or apoptosis? *Epilepsy Res.* (2014) 108:644–52. doi: 10.1016/j.eplepsyres.2014.02.007
170. Immonen RJ, Kharatishvili I, Sierra A, Einula C, Pitkanen A, Grohn OH. Manganese enhanced MRI detects mossy fiber sprouting rather than neurodegeneration, gliosis or seizure-activity in the epileptic rat hippocampus. *Neuroimage.* (2008) 40:1718–30. doi: 10.1016/j.neuroimage.2008.01.042
171. Alvestad S, Goa PE, Qu H, Risa O, Brekken C, Sonnewald U, et al. *In vivo* mapping of temporospatial changes in manganese enhancement in rat brain during epileptogenesis. *Neuroimage.* (2007) 38:57–66. doi: 10.1016/j.neuroimage.2007.07.027
172. Fukumura S, Sasaki M, Kataoka-Sasaki Y, Oka S, Nakazaki M, Nagahama H, et al. Intravenous infusion of mesenchymal stem cells reduces epileptogenesis in a rat model of status epilepticus. *Epilepsy Res.* (2018) 141:56–63. doi: 10.1016/j.eplepsyres.2018.02.008
173. Quarantelli M. MRI/MRS in neuroinflammation: methodology and applications. *Clin Transl Imaging.* (2015) 3:475–89. doi: 10.1007/s40336-015-0142-y
174. Bade AN, Gorantla S, Dash PK, Makarov E, Sajja BR, Poluektova LY, et al. Manganese-enhanced magnetic resonance imaging reflects brain pathology during progressive HIV-1 infection of humanized mice. *Mol Neurobiol.* (2016) 53:3286–97. doi: 10.1007/s12035-015-9258-3
175. Thinschmidt JS, Colon-Perez LM, Febo M, Caballero S, King MA, White FA, et al. Depressed basal hypothalamic neuronal activity in type-1 diabetic mice is correlated with proinflammatory secretion of HMBG1. *Neurosci Lett.* (2016) 615:21–7. doi: 10.1016/j.neulet.2016.01.014
176. Dudek M, Abo-Ramadan U, Hermann D, Brown M, Canals S, Sommer WH, et al. Brain activation induced by voluntary alcohol and saccharin drinking in rats assessed with manganese-enhanced magnetic resonance imaging. *Addict Biol.* (2015) 20:1012–21. doi: 10.1111/adb.12179
177. Dudek M, Hyytia P. Alcohol preference and consumption are controlled by the caudal linear nucleus in alcohol-preferring rats. *Eur J Neurosci.* (2016) 43:1440–8. doi: 10.1111/ejn.13245
178. Dudek M, Canals S, Sommer WH, Hyytia P. Modulation of nucleus accumbens connectivity by alcohol drinking and naltrexone in alcohol-preferring rats: a manganese-enhanced magnetic resonance imaging study. *Eur Neuropsychopharmacol.* (2016) 26:445–55. doi: 10.1016/j.euroneuro.2016.01.003

179. Bade AN, Gendelman HE, Boska MD, Liu Y. MEMRI is a biomarker defining nicotine-specific neuronal responses in subregions of the rodent brain. *Am J Transl Res.* (2017) 9:601–10.
180. Topping GJ, Schaffer P, Hoehr C, Ruth TJ, Sossi V. Manganese-52 positron emission tomography tracer characterization and initial results in phantoms and *in vivo*. *Med Phys.* (2013) 40:042502. doi: 10.1118/1.4793756
181. Saar G, Millo CM, Szajek LP, Bacon J, Herscovitch P, Koretsky AP. Anatomy, functionality, and neuronal connectivity with manganese radiotracers for positron emission tomography. *Mol Imaging Biol.* (2018) 20:562–74. doi: 10.1007/s11307-018-1162-6

Conflict of Interest: The authors declare that the research was conducted in the absence of any commercial or financial relationships that could be construed as a potential conflict of interest.

frontiers in Neurology

BRIEF RESEARCH REPORT
published: 14 August 2020
doi: 10.3389/fneur.2020.00854

The Impact of Covariates in Voxel-Wise Lesion-Symptom Mapping

Deepthi Rajashekar[1,2], Matthias Wilms[1,2], Kent G. Hecker[3], Michael D. Hill[4], Sean Dukelow[4], Jens Fiehler[5] and Nils D. Forkert[1,2,4,6]*

[1] Department of Radiology, University of Calgary, Calgary, AB, Canada, [2] Hotchkiss Brain Institute, University of Calgary, Calgary, AB, Canada, [3] Departments of Community Health Sciences and Veterinary Clinical, and Diagnostic Sciences, University of Calgary, Calgary, AB, Canada, [4] Department of Clinical Neurosciences, University of Calgary, Calgary, AB, Canada, [5] Department of Diagnostic and Interventional Neuroradiology, University Medical Center Hamburg-Eppendorf, Hamburg, Germany, [6] Alberta Children's Hospital Research Institute, University of Calgary, Calgary, AB, Canada

Background: Voxel-wise lesion-symptom mapping (VLSM) is a statistical technique to infer the structure-function relationship in patients with cerebral strokes. Previous VLSM research suggests that it is important to adjust for various confounders such as lesion size to minimize the inflation of true effects. The aim of this work is to investigate the regional impact of covariates on true effects in VLSM.

Methods: A total of 222 follow-up datasets of acute ischemic stroke patients with known NIH Stroke Scale (NIHSS) score at 48-h post-stroke were available for this study. Patient age, lesion volume, and follow-up imaging time were tested for multicollinearity using variance inflation factor analysis and used as covariates in VLSM analyses. Covariate importance maps were computed from the VLSM results by standardizing the beta coefficients of general linear models.

Results: Covariates were found to have distinct regional importance with respect to lesion eloquence in the brain. Age has a relatively higher importance in the superior temporal gyrus, inferior parietal lobule, and in the pre- and post-central gyri. Volume explains more variability in the opercular area of the insula, inferior frontal gyrus, and caudate. Follow-up imaging time accounts for most of the variance in the globus pallidus, ventromedial- and dorsolateral putamen, dorsal caudate, pre-motor thalamus, and the dorsal insula.

Conclusions: This is the first study investigating and revealing distinctive regional patterns of importance for covariates typically used in VLSM. These covariate importance maps can improve our understanding of the lesion-deficit relationships in patients and could prove valuable for patient-specific treatment and rehabilitation planning.

Keywords: brain, lesion symptom mapping, analysis of variance, general linear model, stroke

OPEN ACCESS

Edited by:
Roland Beisteiner, Medical University of Vienna, Austria

Reviewed by:
Andrea Federspiel, University of Bern, Switzerland
Peipeng Liang, Capital Normal University, China

****Correspondence:***
Deepthi Rajashekar
deepthi.rajasheka1@ucalgary.ca

Specialty section:
This article was submitted to Applied Neuroimaging, a section of the journal Frontiers in Neurology

Received: *21 April 2020*
Accepted: *07 July 2020*
Published: *14 August 2020*

Citation:
Rajashekar D, Wilms M, Hecker KG, Hill MD, Dukelow S, Fiehler J and Forkert ND (2020) The Impact of Covariates in Voxel-Wise Lesion-Symptom Mapping. Front. Neurol. 11:854. doi: 10.3389/fneur.2020.00854

INTRODUCTION

Voxel-wise lesion symptom mapping (VLSM) is a statistical framework that can be used to quantify the regional relationship of structural integrity of the brain (post-stroke) to a clinical outcome of interest. In the context of acute ischemic strokes, previous literature has investigated these lesion-deficit relationships at the regional or voxel level using various measures of stroke

severity of varying granularity ranging from gross outcomes, like the modified Rankin scale (1, 2), to finer measures of impairment, for example to assess language (3, 4), spatial neglect (5), and proprioception (6). The results from VLSM are population-specific observations that can provide new insights into mechanisms underlying stroke recovery and, therefore, have potential to guide future research in stroke precision medicine.

Various factors such as lesion size, lesion location (7), age (8), sex (9), time to treatment (10, 11), blood pressure (12), and prevailing medical conditions (13) of the patient have been previously identified to be important parameters for stroke treatment decision making. The effects of these (and other) confounding variables might be related to either the extent of structural damage or the severity of clinical outcome (the relationship studied in the VLSM analyses). This suggests that VLSM analyses should take these confounders into account to produce maps of the true regional eloquence, i.e., the underlying structure-function relationship that indicates the brain regions that are highly critical (eloquent) with respect to the clinical outcome of interest. This can, for example, be practically implemented in voxel-level methods by including the confounders as covariates in a regression model. To date, the VLSM literature has dominantly considered age, sex, and lesion volume as covariates with relevance to stroke (14).

However, to the best of our knowledge, there is no work that quantifies the relative importance each covariate has on the voxel-level statistic of the VLSM output. Therefore, the aim of this work is to estimate the importance of each covariate at a voxel level using a VLSM technique. The proposed covariate importance maps add complementary information to the standard VLSM output, which could be a valuable tool for acute treatment decision making as well as tailored rehabilitation planning.

METHODS

Datasets

The datasets available and used for this study are obtained from the two multi-center ESCAPE (15) and IKNOW (2) trials, which enrolled patients with middle cerebral artery stroke (MCA). In this work, patients with severe white matter hyperintensities, bilateral strokes, and remote hemorrhagic transformations are excluded. Patients who obtained a follow-up FLAIR MRI or non-contrast CT imaging (18 hours−7 days from baseline) and had a complete clinical assessment within 48-hours of symptom onset are included in this study. The final sample contains 222 subjects (98 women) with an average age of 68.6 ± 12.6 years. The clinical outcome of interest used in this work is the NIH Stroke Scale (NIHSS) assessed at 48-hours post-stroke. NIHSS is a commonly used secondary stroke outcome score involving assessments for (in decreasing order of representation) voluntary motor function, level of consciousness, vision, language, sensory function, and spatial neglect. The 48-hours timepoint is selected to avoid biases in the results due to comorbidities unrelated to stroke and complications arising from in-hospital treatment at later assessment timepoints. All datasets used in this study were made available for this secondary study after complete anonymization.

Pre-processing

All lesions are segmented by an experienced observer using ITK-SNAP (16). After this, all datasets are skull-stripped and registered non-linearly to a common FLAIR and NCCT atlas (17) using cost function masking, implemented in the ANTs toolkit (18). Subsequently, the computed deformation field that maps the native patient scan to the atlas image is applied to the corresponding binary lesion mask for that patient. Since the dataset is pooled from multicenter trials, there is considerable variability in: in-plane resolution [0.37–1.4 mm^2], slice thickness [2–10 mm], and the number of slices acquired [4–87]. Registering all native patient scans to a common atlas not only helps to minimize image acquisition related differences but also removes anatomical differences between all patients and allows for an unbiased statistical analysis within the common atlas space.

All datasets were visually inspected to ensure that no motion or other imaging artifacts are present, signal to noise ratio was suitable, and the acquisitions were complete covering the whole brain. Likewise, the registration results were visually checked and datasets with sub-optimal registration quality were excluded from this LSM analysis.

Voxel-Wise Lesion Symptom Mapping

Voxel-wise lesion symptom mapping (VLSM) is a statistical technique to generate eloquence maps that quantify the difference between patients with a lesion and those without a lesion in each voxel (3) with respect to a clinical outcome score. The result of VLSM is a parametric map that displays the eloquence of each voxel with respect to the clinical outcome score of interest, known as the lesion-symptom map.

Practically, this can be implemented by a voxel-wise statistical test comparing the distributions of the outcome scores in patients with a lesion in a voxel to patients without a lesion in the same voxel. This procedure results in a t-score, indicating how critical that voxel is with respect to the outcome score of interest. Voxels with higher t-scores are deemed to be more eloquent (i.e. critically associated) to the outcome score (here the 48-hours NIHSS), thereby quantifying the structure-function relationship. In other words, a high average t-score within a brain region implies that a lesion in this brain region likely leads to more severe clinical deficits. In this work, each voxel is modeled as a general linear model (GLM) for VLSM, which is one of the traditional methods to quantify lesion-deficit relationships (3). Correction for multiple comparisons was done using the permutation based thresholding approach (19). The proposed framework for variance estimation is an extension of the VLSM source code released by Bates et al. (3).

Variable Importance

In this work, patient age, lesion volume, and the time from symptom onset to follow-up imaging are selected as covariates to explore regional covariate importance.

These covariates are tested for collinearity in a first step using the Spearman's correlation, which is further confirmed by a variance inflation factor analysis (20) using a linear regression model to predict NIHSS. Once ensured that the covariates are unrelated, the VLSM analyses involved modeling

the independent voxel-wise GLMs (21) as shown below and correcting for multiple comparisons.

$$S_i = \beta_{i,1} * L_i + \beta_{i,2} * age + \beta_{i,3} * vol + \beta_{i,4} * fup + \epsilon_i \quad (1)$$

Here, for each voxel location *i*, an independent regression model that predicts the eloquence score S_i at that spatial location using presence of lesion at that location (L_i), age, lesion volume, and follow-up imaging time (fup) as inputs is estimated. However, only voxels that survived the permutation threshold (maximum t-threshold = 5.06 from the non-parametric null max distribution over 1,000 permutations at alpha = 0.05) are considered to remove false positives.

The relative importance of covariates is inferred from the standardized beta coefficients for each covariate *j* at the voxel location *i* ($\beta s_{i,j}$). Practically, the non-standardized beta coefficient of a covariate ($\beta_{i,j}$) is normalized by the variance of the covariate and the mean squared error at the voxel location *i* as follows (22).

$$\beta s_{i,j} = \frac{\beta_{i,j}}{\sqrt{var\left(\beta_{i,j}\right)} * MSE_i} \quad (2)$$

Subsequently, the standardized beta coefficients for a covariate at each true positive eloquent voxel is written out into a separate covariate importance map, resulting in age-, volume-, and follow-up time-specific covariate importance maps. These individual covariate importance maps are linearly normalized to the range 0–1 to enable comparison.

For ease of interpretation, the parcellation defined in the Brainnetome atlas (23) is used to calculate average regional covariate importance estimates. Finally, hierarchical clustering is employed to group brain regions based on the average region-level importance measures for each covariate. An important advantage of using hierarchical clustering is that, unlike flat clustering techniques, it provides a structural grouping of cerebral subregions. In order to avoid isolated eloquent regions with few voxels biasing the clustering algorithm, an overlap analysis is conducted. More precisely, all brain regions as defined by the Brainnetome atlas are ordered by the volume of overlap with the VLSM output and only those regions that have at least a volume overlap of 400 voxels (50th percentile) are included in the clustering analysis.

RESULTS

Of the 222 subjects, there are 100 right hemispheric strokes. The average volume of lesions on the left and right hemisphere was 42.04 and 43.65 cm^3, respectively. The overlap of all transformed lesions on the common FLAIR and NCCT atlas shows a typical distribution for MCA occlusions, shown in **Figure 1**.

The correlation coefficients (r_s) comparing all covariates at the patient level are <0.1 ($p > 0.05$) suggesting that there is no monotonic association between any two covariates (r_s values: age vs. lesion volume: −0.086; age vs. follow-up time: −0.051; volume vs. follow-up time: 0.043). This finding is further confirmed by their variance inflation values being <5.0 in a linear regression model to predict the 48-hours NIHSS, which is typically considered to indicate the absence of multicollinearity in the input data (24).

The normalized VLSM output is shown in **Figure 2A**. Brain regions with relatively higher t-score values are considered more eloquent with respect to the NIHSS outcome scale, which means that even a small lesion volume in these regions is likely to result in a worse outcome. In this work, the eloquent clusters that survived the correction for multiple comparisons are located around the sub-cortical left hemispheric regions. No eloquence in the right hemisphere is observed.

The importance maps are substantially different for the covariates investigated in this work (see **Figures 2B–D**). Age has a relatively higher importance in the superior temporal gyrus, inferior parietal lobule, and in the pre- and post-central gyri. Lesion volume has the highest relative importance in the opercular area of the inferior frontal gyrus, ventral caudate, and the ventral agranular insula. Finally, follow-up time was found to be the most important covariate in the globus pallidus, ventromedial- and dorsolateral putamen, dorsal caudate, pre-motor thalamus, and dorsal insula.

The result from the hierarchical clustering algorithm is shown in **Figure 3A**. Here, the heatmap from the clustering algorithm is represented as a dendrogram in **Figure 3B** outlining the sub-regions with considerable overlap with the VLSM map. In the heatmap, each covariate is color-coded (age in orange, lesion volume in blue, and follow-up time in green) with darker hues representing higher average covariate importance for a given brain region. It is clear from the heatmap that for each covariate, the set of brain regions with high relative importance is nearly exclusive.

DISCUSSION

The main finding of this study is that covariates typically used within VLSM analyses show distinctive patterns of regional importance for modeling lesion eloquence.

Of the eloquent brain regions mainly influenced by age, the superior temporal gyrus and inferior parietal lobule have been previously reported to display age-specific changes in cerebral blood flow (CBF) patterns in healthy elderly (61.05 ± 13.17 years of age) (25). Specifically, it was previously reported that the CBF in the superior temporal gyrus increases with age as a compensatory response to cognitive tasks, i.e., increased neural activity. Contrary to this, the CBF in the inferior parietal lobule was shown to have a negative correlation with age resulting from the reduction in neuronal activity and deterioration of microvasculature. Other studies using various imaging modalities to investigate age-related perfusion changes have also led to comparable conclusions in these regions (26, 27). The age-related changes in CBF, microvasculature, and neuronal and synaptic activity may deem these cortical structures more susceptible to brain damage in elderly including ischemic stroke, thereby also explaining the likelihood of superior temporal gyrus and inferior parietal lobule not only being eloquent to stroke severity metrics, but also their structure-function relationship most explained by age.

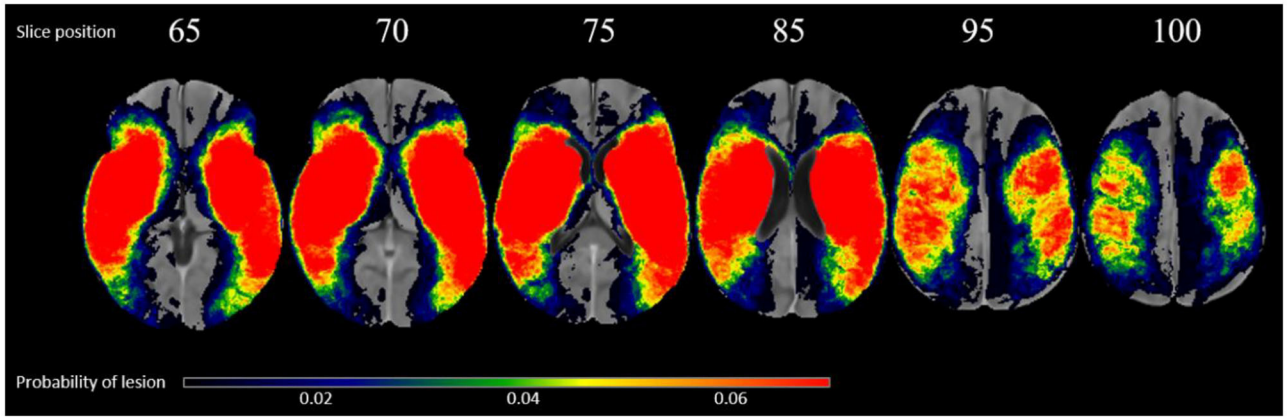

FIGURE 1 | Overlap of all patients lesions in the common atlas space ($N = 222$) in radiological convention.

From a connectivity perspective, the hippocampus, basal ganglia structures, and insula are highly connected structures (*a.k.a.,* rich-club structures) (28), indicating that any insult to these regions is likely to result in a poor clinical outcome. This supports the current finding that lesion volume is the most important covariate for these rich-club brain structures or structures that link to a rich club node, such as the caudate and insula (29).

The brain regions that have been previously reported to have the highest ischemic vulnerability (i.e., increase in infarct per unit reduction in CBF) are the caudate body, putamen nucleus, insular ribbon, middle frontal gyrus, precentral gyrus, and the frontal lobe subcortical white-matter and paracentral lobule (30). Furthermore, the insular ribbon has been described as the most vulnerable brain region of the left hemisphere (30). While it is important to include follow-up imaging time as a covariate to account for potential lesion growth/shrinkage, secondary injuries, and water accumulation differences over time, the importance of follow-up imaging time (or the post-treatment scan time) in the insular gyrus specifically, remains unclear, requiring further research. In general, the regions that are common in variance importance maps have an overall high eloquence, i.e., critical to the outcome of interest. From **Figure 3B**, it is clear that even though there are common regions in the importance maps for each covariate, there are differences in average importance across regions, suggesting that one covariate is likely to be relatively more important than the other two covariates.

There is a strong evidence in the stroke literature pertaining to the bias of the NIHSS assessment. More precisely, the NIHSS is biased toward the left hemisphere because of the language domains and the fact that the consciousness domains are weighted to language. The right hemisphere is reported to have a relatively less weight in NIHSS. Particularly, it was shown that the volume of a right hemispheric lesion has to be far greater than a left hemispheric insult to result in the same severity of outcome on the NIHSS scale (31). A recent VLSM analysis conducted on 216 subjects from the MR CLEAN study showed that the inclusion of lesion volume as a covariate eliminates the eloquence signal in the right hemisphere (1). They described the resulting LSM maps from three scenarios: (1) using the outcome score alone, (2) using the outcome score as the target variable and sex and age as covariates; and (3) using the outcome score as the target variable and sex, age, and lesion volume as covariates [see Figure 2 in Ernst et al. (1)]. The results clearly indicate that the right hemispheric eloquence is no longer present when lesion volume is added as a covariate in the LSM analysis using the modified Rankin score as the outcome score. Therefore, the absence of eloquence in the right hemisphere in this study is likely to stem from either the lateralization of the NIHSS assessment, the effects of lesion volume as a covariate, or both.

The limitations of the proposed method to estimate variance importance of covariates in a lesion symptom mapping approach should be discussed. First, this work should be considered exploratory in terms of the choice of covariates to be adjusted for or included in the analysis. Although the covariates selected in this work are motivated by previous clinical stroke literature and are typically considered in LSM analyses, this selection does not cover the entire repertoire of confounders that could potentially bias an LSM study. For example, sex was intentionally excluded from this study since there are established sex-specific associations with other clinical and lifestyle behaviors (9). Nevertheless, the results of this study suggest that it is of clinical interest to investigate the regional importance of covariates, and more co-variates should be investigated in future studies to improve our understanding of the structure-function relationship. Furthermore, the current implementation does not account for potential interaction terms. However, the proposed method could be extended to include interaction effects between covariates as part of the GLM as an additional regression term as follows.

$$S_i = \beta_{i,1} * L_i + \beta_{i,2} * age + \beta_{i,3} * vol + \beta_{i,4} * fup + \beta_{i,5} * (age * vol) + \beta_{i,5} * (vol * fup) + \epsilon_i \quad (3)$$

However, interpretation of interaction effects is often complicated and requires that VLSM literature accumulates

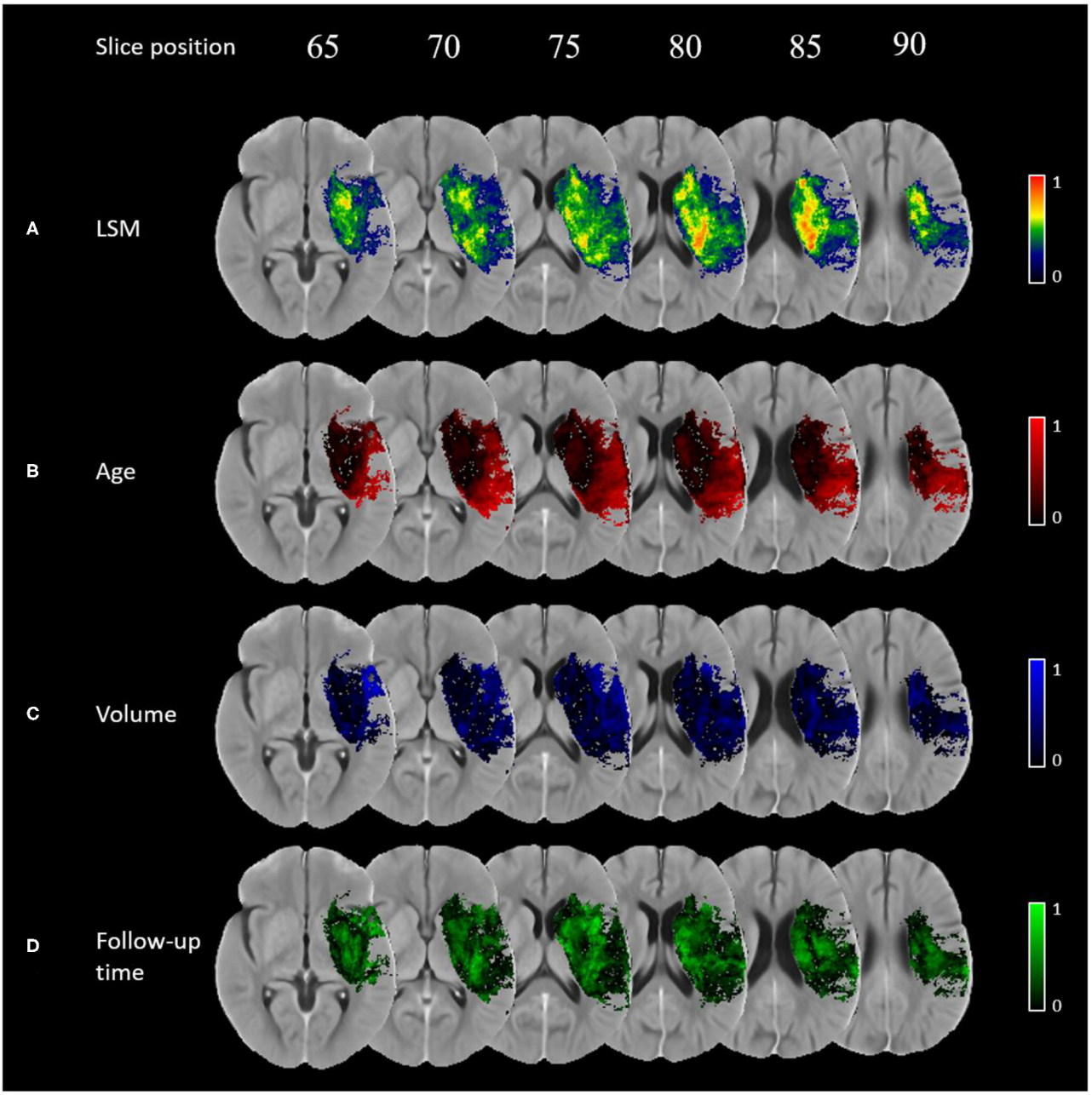

FIGURE 2 | Importance maps for each covariate using voxel-wise generalized linear models corrected for multiple corrections using permutation-based thresholding (p-value < 0.05): **(A)** normalised VLSM result, **(B)** age, **(C)** lesion volume, **(D)** follow-up imaging time.

sufficient evidence of the independent effects of clinically relevant covariates.

Furthermore, voxel-wise LSM requires multiple comparisons correction leading to a low statistical power (32, 33) while not accounting for similar functional deficits induced by non-overlapping lesions (i.e., the partial injury problem) (34). While LSM research is leading toward multivariate models (35, 36) to resolve these issues, the general understanding of the influence of covariates in defining the structure-function relationship in these multivariate models remains unclear. Finally, the results reported in this study may be population-specific. That is, a different sample size, unreliable segmentations of the lesions, or different lesion distributions could likely influence the VLSM analysis, and their impact cannot be easily quantified. Overall, this work should be considered as a first important step in the estimation of voxel-wise variance using the most traditional VLSM technique – general linear regression.

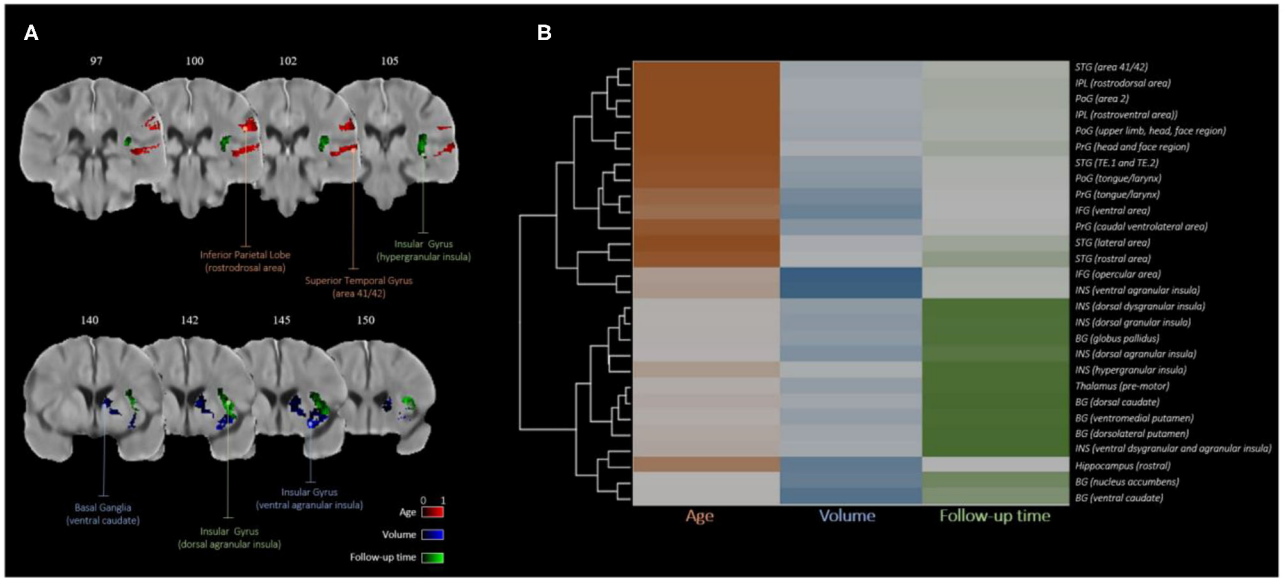

FIGURE 3 | Covariate importance estimates consolidated by hierarchical clustering: **(A)** regions with higher average importance for age (red), volume (blue), and follow-up time (green); **(B)** dendrogram of brain regions clustered by relative covariate importance.

CONCLUSIONS

To the best of our knowledge, this is the first study investigating the regional importance of covariates typically used in VLSM. Using the proposed method, distinctive patterns of regional importance of age, lesion volume, and follow-up time were found. The generated covariate importance maps can help to improve our understanding of the lesion-deficit relationships in patients and could prove valuable for patient-specific treatment and rehabilitation planning.

DATA AVAILABILITY STATEMENT

The data analyzed in this study is subject to the following licenses/restrictions: The acquisition of the data sets for the two trials was approved by the respective local ethics board at each site contributing to the two trials. All data sets used in this secondary study were made available after complete anonymization. Requests to access these datasets should be directed to Nils Forkert, nils.forkert@ucalgary.

ETHICS STATEMENT

Ethical review and approval was not required for the study on human participants in accordance with the local legislation and institutional requirements, as all datasets were fully anonymized prior to transfer and processing. Our paper is a retrospective (secondary) study, not requiring review and approval.

AUTHOR CONTRIBUTIONS

DR and MW: study design, image processing, data analysis, drafting the manuscript, and revising it critically. NF, KH, and SD: drafting the manuscript and revising it critically. JF and MH: data acquisition and revising the manuscript critically. All authors contributed to the article and approved the submitted version.

FUNDING

This work is supported by the Heart and Stroke Foundation of Canada Grant in aid [G-17-0018368] as well as by the River Fund at Calgary Foundation.

ACKNOWLEDGMENTS

We thank the Hotchkiss Brain Institute at the University of Calgary (in partnership with Alberta Health Services) for all the support and encouragement in fostering collaborative brain research.

REFERENCES

1. Ernst M, Boers AMM, Forkert ND, Berkhemer OA, Roos YB, Dippel DWJ, et al. Impact of ischemic lesion location on the mrs score in patients with ischemic stroke: a voxel-based approach. *Am J Neuroradiol.* (2018) 39:1989–94. doi: 10.3174/ajnr.A5821
2. Cheng B, Forkert ND, Zavaglia M, Hilgetag CC, Golsari A, Siemonsen S, et al. Influence of stroke infarct location on functional

outcome measured by the modified rankin scale. *Stroke.* (2014) 45:1695–702. doi: 10.1161/STROKEAHA.114.005152
3. Bates E, Wilson SM, Saygin AP, Dick F, Sereno MI, Knight RT, et al. Voxel-based lesion–symptom mapping. *Nat Neurosci.* (2003) 6:448–50. doi: 10.1038/nn1050
4. Dronkers NF, Wilkins DP, Van Valin RD, Redfern BB, Jaeger JJ. Lesion analysis of the brain areas involved in language comprehension. *Cognition.* (2004) 92:145–77. doi: 10.1016/j.cognition.2003.11.002
5. Karnath HO, Rennig J, Johannsen L, Rorden C. The anatomy underlying acute versus chronic spatial neglect: a longitudinal study. *Brain.* (2011) 134:903–12. doi: 10.1093/brain/awq355
6. Findlater SE, Hawe RL, Semrau JA, Kenzie JM, Yu AY, Scott SH, et al. Lesion locations associated with persistent proprioceptive impairment in the upper limbs after stroke. *NeuroImage Clin.* (2018) 20:955–71. doi: 10.1016/j.nicl.2018.10.003
7. Laredo C, Zhao Y, Rudilosso S, Renú A, Pariente JC, Chamorro Á, et al. Prognostic significance of infarct size and location: the case of insular stroke. *Sci Rep.* (2018) 8:1–10. doi: 10.1038/s41598-018-27883-3
8. Willey JZ, Ortega-Gutierrez S, Petersen N, Khatri P, Ford AL, Rost NS, et al. Impact of acute ischemic stroke treatment in patients >80 years of age. *Stroke.* (2012) 43:2369–75. doi: 10.1161/STROKEAHA.112.660993
9. Lisabeth LD, Reeves MJ, Baek J, Skolarus LE, Brown DL, Zahuranec DB, et al. Factors influencing sex differences in poststroke functional outcome. *Stroke.* (2015) 46:860–3. doi: 10.1161/STROKEAHA.114.007985
10. Kamal N, Sheng S, Xian Y, Matsouaka R, Hill MD, Bhatt DL, et al. Delays in door-to-needle times and their impact on treatment time and outcomes in get with the guidelines-stroke. *Stroke.* (2017) 48:946–54. doi: 10.1161/STROKEAHA.116.015712
11. Muchada M, Rodriguez-Luna D, Pagola J, Flores A, Sanjuan E, Meler P, et al. Impact of time to treatment on tissue-type plasminogen activator–induced recanalization in acute ischemic stroke. *Stroke.* (2014) 45:2734–8. doi: 10.1161/STROKEAHA.114.006222
12. Maïer B, Fahed R, Khoury N, Guenego A, Labreuche J, Taylor G, et al. Association of blood pressure during thrombectomy for acute ischemic stroke with functional outcome. *Stroke.* (2019) 50:2805–12. doi: 10.1161/STROKEAHA.119.024915
13. Morris Jane G, Duffis E. Jesus and Fisher Marc. Cardiac workup of ischemic stroke. *Stroke.* (2009) 40:2893–8. doi: 10.1161/STROKEAHA.109.551226
14. de Haan B, Karnath HO. A hitchhiker's guide to lesion-behaviour mapping. *Neuropsychologia.* (2018) 115:5–16. doi: 10.1016/j.neuropsychologia.2017.10.021
15. Demchuk AM, Goyal M, Menon BK, Eesa M, Ryckborst KJ, Kamal N, et al. Endovascular treatment for small core and anterior circulation proximal occlusion with emphasis on minimizing ct to recanalization times (escape) trial: methodology. *Int J Stroke.* (2015) 10:429–38. doi: 10.1111/ijs.12424
16. Yushkevich PA, Piven J, Hazlett HC, Smith RG, Ho S, Gee JC, et al. User-guided 3D active contour segmentation of anatomical structures: significantly improved efficiency and reliability. *NeuroImage.* (2006) 31:1116–28. doi: 10.1016/j.neuroimage.2006.01.015
17. Rajashekar D, Wilms M, MacDonald ME, Ehrhardt J, Mouches P, Frayne R, et al. High-resolution T2-FLAIR and non-contrast CT brain atlas of the elderly. *Sci Data.* (2020) 7:1–7. doi: 10.1038/s41597-020-0379-9
18. Avants BB, Tustison NJ, Song G, Cook PA, Klein A, Gee JC. A reproducible evaluation of ANTs similarity metric performance in brain image registration. *Neuroimage.* (2011) 54:2033–44. doi: 10.1016/j.neuroimage.2010.09.025
19. Mirman D, Landrigan JF, Kokolis S, Verillo S, Ferrara C, Pustina D Corrections for multiple comparisons in voxel-based lesion-symptom mapping. *Neuropsychologia.* (2017) 115:112–23. doi: 10.1016/j.neuropsychologia.2017.08.025
20. Fox J, Monette G. Generalized collinearity diagnostics. *Journal Am Stat Assoc.* (1992) 87:17883. doi: 10.2307/2290467
21. Darlington RB. Multiple regression in psychological research and practice. *Psycholo. Bull.* (1968) 69:161–82. doi: 10.1037/h0025471
22. Hastie T, Tibshirani R, Friedman J. *The Elements of Statistical Learning: Data Mining, Inference, and Prediction, Second Edition.* Springer Science & Business Media (2009) 757.
23. Jiang T. Brainnetome: a new -ome to understand the brain and its disorders. *NeuroImage.* (2013) 80:263–72. doi: 10.1016/j.neuroimage.2013.04.002
24. James G, Witten D, Hastie T, Tibshirani R. Linear regression. In: James G, Witten D, Hastie T, Tibshirani R. editor. *An Introduction to Statistical Learning: With Applications in R*. New York, NY: Springer (2013). p. 59–126.
25. Zhang N, Gordon ML, Ma Y, Chi B, Gomar JJ, Peng S, et al. The age-related perfusion pattern measured with arterial spin labeling MRI in healthy subjects. *Front Aging Neurosci.* (2018) 10:214 doi: 10.3389/fnagi.2018.00214
26. Chen JJ, Rosas HD, Salat DH. Age-associated reductions in cerebral blood flow are independent from regional atrophy. *NeuroImage.* (2011) 55:468–78. doi: 10.1016/j.neuroimage.2010.12.032
27. Takahashi K, Yamaguchi S, Kobayashi S, Yamamoto Y. Effects of aging on regional cerebral blood flow assessed by using technetium Tc 99m hexamethylpropyleneamine oxime single-photon emission tomography with 3d stereotactic surface projection analysis. *Am J Neuroradiol.* (2005) 26:2005–9.
28. van den Heuvel MP, Sporns O. Rich-club organization of the human connectome. *J Neurosci.* (2011) 31:15775–86. doi: 10.1523/JNEUROSCI.3539-11.2011
29. Schirmer MD, Ktena SI, Nardin MJ, Donahue KL, Giese AK, Etherton MR, et al. Rich-Club organization: an important determinant of functional outcome after acute ischemic stroke. *Front Neurol.* (2019) 10:956. doi: 10.3389/fneur.2019.00956
30. Payabvash S, Souza LC, Wang Y, Schaefer PW, Furie KL, Halpern EF, et al. Regional ischemic vulnerability of the brain to hypoperfusion. *Stroke.* (2011) 42:1255–60. doi: 10.1161/STROKEAHA.110.600940
31. Woo D, Broderick JP, Kothari RU, Lu M, Brott T, Lyden PD, et al. Does the national institutes of health stroke scale favor left hemisphere strokes? *Stroke.* (1999) 30:2355–9. doi: 10.1161/01.STR.30.11.2355
32. Sperber C, Karnath H-O. On the validity of lesion-behaviour mapping methods. *Neuropsychologia.* (2017) 115:17–24. doi: 10.1016/j.neuropsychologia.2017.07.035
33. Karnath HO, Sperber C, Rorden C. Mapping human brain lesions and their functional consequences. *NeuroImage.* (2018) 165:180–9. doi: 10.1016/j.neuroimage.2017.10.028
34. Rorden C, Fridriksson J, Karnath H-O. An evaluation of traditional and novel tools for lesion behavior mapping. *NeuroImage.* (2009) 44:1355–62. doi: 10.1016/j.neuroimage.2008.09.031
35. Pustina D, Avants B, Faseyitan OK, Medaglia JD, Coslett HB. Improved accuracy of lesion to symptom mapping with multivariate sparse canonical correlations. *Neuropsychologia.* (2017) 115:154–66. doi: 10.1016/j.neuropsychologia.2017.08.027
36. Zhang Y, Kimberg DY, Coslett HB, Schwartz MF, Wang Z. Support vector regression based multivariate lesion-symptom mapping. In: *2014 36th Annual International Conference of the IEEE Engineering in Medicine and Biology Society*. (2014). p. 5599–5602.

Conflict of Interest: The authors declare that the research was conducted in the absence of any commercial or financial relationships that could be construed as a potential conflict of interest.

frontiers in Neurology

MINI REVIEW
published: 10 September 2020
doi: 10.3389/fneur.2020.01024

Brain MRI Pattern Recognition in Neurodegeneration With Brain Iron Accumulation

Jae-Hyeok Lee[1], *Ji Young Yun*[2], *Allison Gregory*[3], *Penelope Hogarth*[3] and *Susan J. Hayflick*[3]*

[1] Department of Neurology, Research Institute for Convergence of Biomedical Science and Technology, Pusan National University Yangsan Hospital, Pusan National University School of Medicine, Yangsan-si, South Korea, [2] Department of Neurology, Ewha Womans University Seoul Hospital, Ewha Womans University College of Medicine, Seoul, South Korea, [3] Departments of Molecular and Medical Genetics, Oregon Health and Science University, Portland, OR, United States

Most neurodegeneration with brain iron accumulation (NBIA) disorders can be distinguished by identifying characteristic changes on magnetic resonance imaging (MRI) in combination with clinical findings. However, a significant number of patients with an NBIA disorder confirmed by genetic testing have MRI features that are atypical for their specific disease. The appearance of specific MRI patterns depends on the stage of the disease and the patient's age at evaluation. MRI interpretation can be challenging because of heterogeneously acquired MRI datasets, individual interpreter bias, and lack of quantitative data. Therefore, optimal acquisition and interpretation of MRI data are needed to better define MRI phenotypes in NBIA disorders. The stepwise approach outlined here may help to identify NBIA disorders and delineate the natural course of MRI-identified changes.

Keywords: neurodegeneration, iron, NBIA, magnetic resonance imaging, pattern

OPEN ACCESS

Edited by:
Nobutaka Hattori,
Juntendo University, Japan

Reviewed by:
Luca Marsili,
University of Cincinnati, United States
Carlos Raúl Ferreira,
National Human Genome Research Institute (NHGRI), United States

***Correspondence:**
Susan J. Hayflick
hayflick@ohsu.edu

Specialty section:
This article was submitted to Applied Neuroimaging, a section of the journal Frontiers in Neurology

Received: *25 May 2020*
Accepted: *05 August 2020*
Published: *10 September 2020*

Citation:
Lee J-H, Yun JY, Gregory A, Hogarth P and Hayflick SJ (2020) Brain MRI Pattern Recognition in Neurodegeneration With Brain Iron Accumulation. Front. Neurol. 11:1024. doi: 10.3389/fneur.2020.01024

INTRODUCTION

Neurodegeneration with brain iron accumulation (NBIA) is a group of inherited disorders with hallmark features that include abnormal iron accumulation in the basal ganglia, mainly the globus pallidus (GP) and substantia nigra (SN) (1). Ten associated genes have been identified [**Table 1**; (2)]. The four most common NBIA disorders include pantothenate kinase-associated neurodegeneration (PKAN), phospholipase A_2-associated neurodegeneration (PLAN), mitochondrial membrane protein-associated neurodegeneration (MPAN), and beta-propeller protein-associated neurodegeneration (BPAN) (3). Recently, new candidate genes have been described with the advent of next-generation sequencing (4). However, the scarcity of cases makes it impossible to determine their relevance to NBIA disorders (5).

Evidence by magnetic resonance imaging (MRI) of excessive brain iron indicates the possibility of NBIA. One established hallmark MRI feature of NBIA is the presence of T2 hypointense lesions in the GP and SN on T2-weighted images (T2WI) (3, 6). Certain MRI abnormalities may help distinguish among the NBIA disorders and facilitate more definitive diagnosis (1, 7). However, mutations in NBIA-related genes may not always lead to pronounced iron deposition (1, 7, 8). A significant number of patients confirmed to have an NBIA disorder by genetic testing have MRI features that are atypical for their specific disease (7, 9, 10). The appearance of specific MRI patterns depends on the stage of the disease and the patient's age at evaluation (1, 10), and evidence for iron

TABLE 1 | MRI characteristics of NBIA subtypes.

Disease	Gene/ inheritance	Iron distribution	Core features	Early features	Additional features
PKAN	*PANK2*/AR	GP, SN, STN	Eye-of-the-tiger sign in GP (typically, the surrounding T2 hypointensity)	Linear T2 hyperintense streak along the medial border of GP in infancy [10] Isolated hyperintense center during early childhood [10]	Basal ganglia calcification
MPAN	*C19orf12*/AR, AD	GP, SN	Preserved isointense signal in medial medullary lamina of GP	Three signal layers in GP (T2*WI) T2 hyperintense "dot" in the central part of GP [9]	Diffuse brain atrophy Variable degree of WM involvement
BPAN	*WDR45*/XD	SN, GP	Halo sign in SN	Thin corpus callosum Myelination delay T2 hyperintensity and swelling in SN, GP, deep cerebellar nuclei [41] T2 (or SWI) hypointensity, predominantly in SN and/or T1 hyperintensity	Diffuse brain atrophy Basal ganglia calcification Variable degree of WM involvement
PLAN	*PLA2G6*/AR	GP, SN	Disproportionate cerebellar atrophy and/or cerebellar cortical hyperintensity	Vertically oriented thin corpus callosum [54] Hypertrophy of the clavum [71]	Supratentorial atrophy Variable degree of WM involvement Hypoplastic optic tracts and chiasms
FAHN	*FA2H*/AR	GP, SN	WM hyperintensities (periventricular, parietal predominance) Pontocerebellar atrophy Thin corpus callosum		Supratentorial atrophy
Neuroferritinopathy	*FTL*/AD	Widespread, basal ganglia, thalamus, cerebellum, cerebral cortex	Cavitation involving GP and putamen	SWI hypointensity in GP, SN, thalamus, red nucleus, and dentate nucleus, without cavitation, and cortical pencil lining sign [45]	Diffuse brain atrophy WM hyperintensities
Aceruloplaminemia	*CP*/AR	Widespread, uniform basal ganglia, thalamus, cerebellum, cerebral cortex	Iron accumulation in the brain, liver, pancreas, and myocardium		Diffuse brain atrophy WM hyperintensities
Woodhouse-Sakati syndrome	*DCAF17*/AR	GP, SN	WM hyperintensities (frontoparietal/ periventricular WM)		Small pituitary gland
Kufor-Rakeb syndrome	*ATP13A2*/AR	Putamen, caudate, GP			Diffuse brain atrophy
CoPAN	*COASY*/AR	GP, SN			T2 hyperintensity of caudate, putamen, and thalamus Swollen putamen and caudate GP calcification

PKAN, pantothenate kinase-associated neurodegeneration; MPAN, mitochondrial membrane protein-associated neurodegeneration; BPAN, beta-propeller protein-associated neurodegeneration; PLAN, PLA2G6-associated neurodegeneration; FAHN, fatty acid hydroxylase-associated neurodegeneration; CoPAN, COASY protein-associated neurodegeneration; AR, autosomal recessive; AD, autosomal dominant; XD, X-linked dominant; GP, globus pallidus; SN, substantia nigra; WM, white matter.

accumulation may be absent or subtle early in the disease course. This phenomenon is particularly common in younger patients, where whole exome sequencing often leads to early diagnosis (3). Minor lesions visible in the early stages of disease and more extensive lesions in the late stages often are non-specific.

MRI interpretation can be challenging in rare brain diseases and can be limited by heterogeneously acquired MRI datasets, individual interpreter bias, and a lack of quantitative and longitudinal data. Therefore, optimal acquisition and interpretation of MRI data are needed to better define MRI phenotypes in the NBIA disorders. We describe here the evolution of MRI characteristics and provide a practical approach to identify NBIA subtypes.

IDENTIFICATION OF IRON-SPECIFIC BASAL GANGLIA T2 HYPOINTENSITY

A routine brain MRI, without iron-sensitive sequences, is often suboptimal for evaluating for a possible NBIA disorder (7). Iron-sensitive sequences, especially susceptibility weighted imaging

(SWI) and T2*-weighted imaging (T2*WI), can more clearly depict the increase and extent of iron deposition, even in small gray matter nuclei (10, 11). High-field strength MRI can detect iron with improved sensitivity (12).

To correctly diagnose abnormal brain iron accumulation, the interpreting physician should have a working knowledge of normal age-dependent signal hypointensities on MRI (7). The GP and SN normally become hypointense on T2WI around the end of the first decade of life when compared with signal in the adjacent normal-appearing white matter (13). Iron concentration in the basal ganglia increases with age. An "internal signal-intensity reference" that we empirically use to determine if iron is indeed increased over "normal" is to compare the GP and SN to the red nucleus (RN). They normally appear slightly more hypointense relative to the RN based on their higher iron content at all ages (14). If the signal in GP or SN is significantly more hypointense than in RN, then there is likely to be increased iron. To correct for inconsistencies in the reference standard, signal hypointensity can also be normalized by dividing the structure signal intensity by the mean signal intensity of the cerebrospinal fluid (15, 16).

Once T2 hypointensity is identified, iron-sensitive sequences should be reviewed to distinguish excessive iron deposition from other causes of T2 hypointensity. Hypointense basal ganglia have been observed in hypomyelinating leukodystrophy, lysosomal storage disorders, and other metal accumulation disorders (17). Due to the paramagnetic property of iron, the degree of signal loss is profoundly enhanced in iron-sensitive sequences. Manganese is also paramagnetic, and its deposition typically causes high signal intensity on T1WI (11). Although iron has a T1-shortening effect that can appear as high signal intensity on T1WI, the degree of T1 hyperintensity is variable and is influenced by the status of iron and T1WI parameters (11). Computed tomography (CT) scans may be more useful than MRI in differentiating calcifications from iron deposits. Basal ganglia calcification can co-exist with iron accumulation in NBIA cases, although its frequency is unknown (18–21).

REGIONAL DISTRIBUTION OF EXCESSIVE IRON ACCUMULATION

In most forms of NBIA, excessive iron deposition is mainly confined to the GP and SN (**Table 1**). Other iron-rich deep nuclei in the gray matter, like the dentate nucleus, can occasionally be affected to a lesser extent but only in specific NBIA disorders (22).

In PKAN, iron-related hypointense signals on SWI are restricted to the GP, SN, and subthalamic nucleus (STN) and the fiber tracts between these structures (10). In BPAN, the earliest and most intense iron deposition occurs in the SN as opposed to the GP, unlike PKAN and other NBIA disorders (7). Widespread brain iron accumulation involving the basal ganglia nuclei, thalami, dentate nuclei, and cerebral and cerebellar cortices may develop in aceruloplasminemia and neuroferritinopathy (7, 22). The symptom onset for both of these diseases has been described in adults (1). All basal ganglia and thalami are more uniformly involved in aceruloplasminemia (22). Cortical iron deposition appears as thin hypointense lines on SWI, referred to as pencil-lining in neuroferritinopathy (23, 24). Even in an asymptomatic mutation carrier for this autosomal dominant disease, a characteristic pattern of iron deposition can be seen on iron-sensitive sequences (25). Of the limited number of patients reported, only a small portion of cases with Kufor-Rakeb syndrome had iron accumulation within the putamen and caudate nuclei (26, 27).

EVOLUTION OF PALLIDONIGRAL ABNORMALITIES

The characteristic pallidonigral lesions of the major NBIA disorders are established diagnostic clues (**Table 1**). These include the "eye-of-the-tiger" sign in PKAN, preservation of isointense signal in the medial medullary lamina in the GP of MPAN patients, the "halo" sign in the SN of BPAN patients, and "cavitation" in neuroferritinopathy. Other NBIA disorders do not have distinct pallidonigral lesions. However, the morphological patterns of pallidonigral lesions can vary according to the patient's age. Typical findings may not appear until adolescence or early adulthood and are therefore not usually useful in infancy or early childhood. For these reasons, the frequency of MRI clues varied across studies.

The detection of these specific MRI signs can also be influenced by MRI acquisition settings (10). Image planes and levels for optimal visualization should be selected for efficient identification of the signs (**Figure 1**).

Eye-of-the-tiger Sign in PKAN

The hallmark of PKAN is the eye-of-the-tiger sign that comprises a round hyperintense center and surrounding hypointensity in the GP on T2WI. This sign in its classic form is not observed in other NBIA disorders, including in patients with *COASY* protein-associated neurodegeneration (CoPAN), which affects coenzyme A metabolism, similar to PKAN (21, 28).

The earliest change observed in infancy was the linear hyperintense streak along the medial border of the GP. During early childhood, T2WI mostly shows the isolated hyperintense center in the anteromedial region, which is typically visible at the level of the anterior commissure (29). The surrounding T2 hypointensity tends to increase in size and decrease in signal intensity with age (**Figures 1A,B**). Signal hypointensity on SWI was first detected in a 3-year-old patient, and advanced from the medial to the lateral portion of the GP (10, 18). In adult patients, the hyperintense center varies in shape, from small and round to streaked, or is lost entirely. Furthermore, the T2 hyperintense area of the sign may be obscured by diamagnetic calcium deposits (10, 18).

This sign has been reported to occur as an imaging phenocopy in other conditions, such as carbon monoxide intoxication, neuroferritinopathy, MPAN, Wilson's disease, multiple system atrophy, as well as in healthy adults (10, 30–32). The combination of T2 hypointense and hyperintense lesions, resulting from iron deposition and gliosis, respectively, can mimic the eye-of-the-tiger sign. The PKAN-specific eye-of-the-tiger sign is better defined by the region-specific pattern of iron deposition on SWI (10).

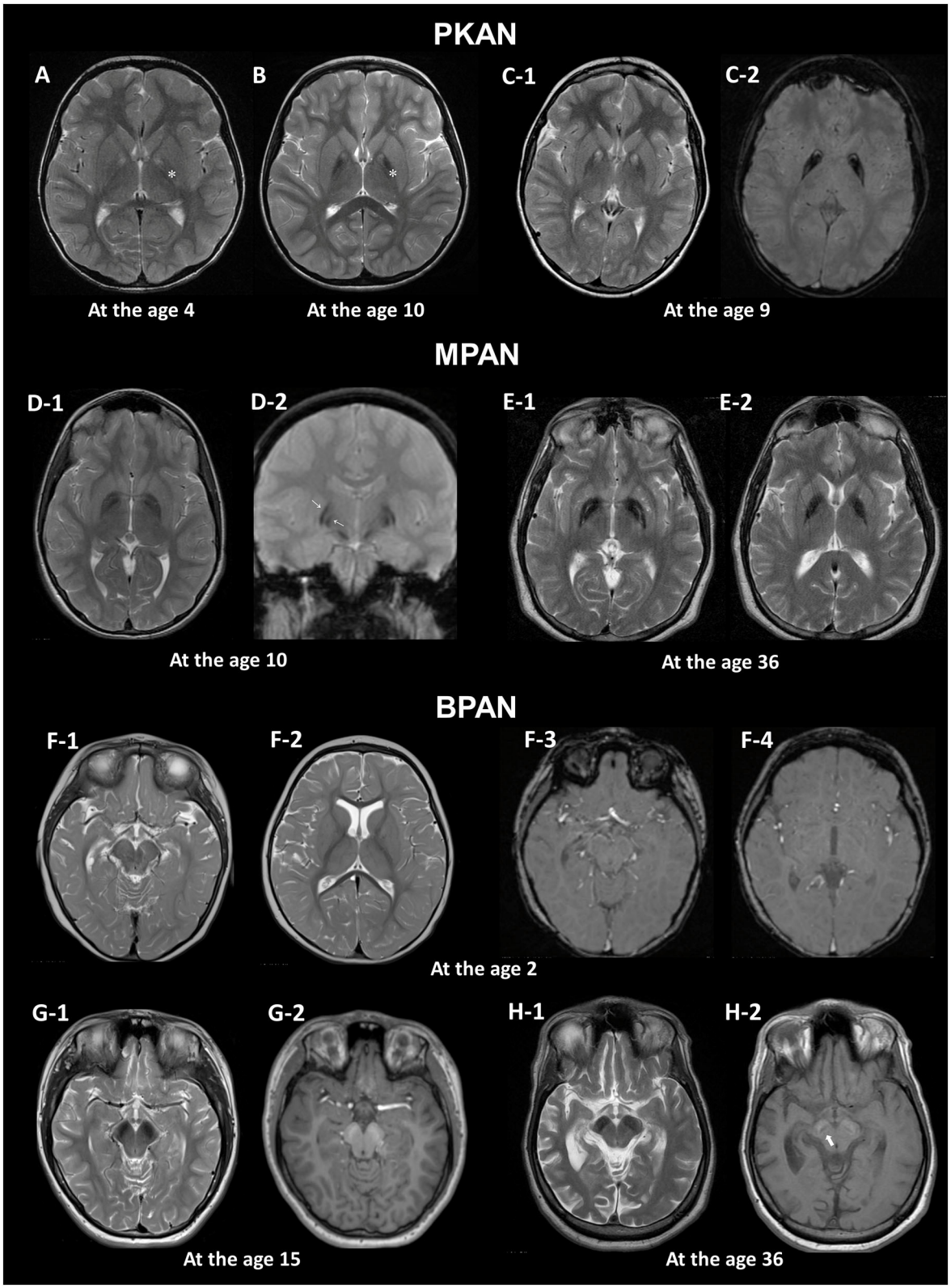

FIGURE 1 | MRI hallmarks of PKAN **(A–C)**, MPAN **(D,E)**, and BPAN **(F–H)**. In a PKAN patient with serial MRIs, the surrounding T2 hypointensity decreases in signal intensity with age (**A,B**, asterix). The PKAN-specific eye-of-the-tiger sign at the level of the anterior commissure **(C-1)** is better defined by the region-specific pattern of

(Continued)

FIGURE 1 | iron deposition on susceptibility-weighted image **(C-2)**. In a younger patient with MPAN, T2- and T2*-weighted images shows preservation of isointense signal in the middle of inner and outer layers of iron accumulation (**D-1, D-2**, thin arrows). The typical streaking of the medial medullary lamina on T2-weighted image becomes more pronounced as signal intensity in the GP decreases, which is typically visible at the level of the anterior commissure **(D-1, E-1)**. Brain MRI scans of three BPAN patients at different ages show age-related MRI changes. Brain MRI of a patient with BPAN at the age of 2 shows no abnormality on T2-weighted **(F-1, F-2)** and susceptibility-weighted **(F-3, F-4)** images. The substantia nigra is seen as hypointense on T2-weighted image **(G-1, H-1)** and hyperintense on T1-weighted image, whereas the central hypointense band is not demonstrated **(G-2)**. T1-weighted image demonstrates hyperintensity of the substantia nigra and cerebral peduncle surrounding a central linear band of hypointensity, also known as the halo sign (**H-2**, thick arrow).

Preserved Isointense Signal in Medial Medullary Lamina in MPAN

Iron accumulation in the GP, followed by the SN, is evident on MRI (1). A characteristic feature in MPAN is T2 iso- to hyperintense streaking in the region of the medial medullary lamina between the abnormally hypointense GP interna and externa (33, 34), typically visible at the level of the anterior commissure (**Figure 1**). However, this MRI finding is present only in some MPAN patients (33, 35, 36). In recent reports, this sign was detectable in about half of patients and brain MRI may be normal in the early stages of MPAN (9, 37, 38).

Typical linear streaking (**Figure 1E**) develops over time and becomes more pronounced as signal intensity in the GP decreases due to iron accumulation. Initially, the GP appears as three signal layers consisting of the isointense signal layer in the middle of the hypointense inner and outer signal layers of iron accumulation, and is more contrasted on iron-sensitive T2*WI (**Figure 1D**).

Substantia Nigra Halo Sign in BPAN

A unique feature of BPAN is the presence of a hyperintense halo surrounding a central band of hypointensity on axial T1WI within the SN [**Figure 1H**; (19, 39, 40)]. T1 hyperintensity extends to the cerebral peduncles. T2WI shows prominent hypointense signal in the SN and cerebral peduncles. The SN is more hypointense relative to the GP, indicating higher levels of iron.

MRI changes in BPAN develop as age-dependent phenomena (**Figures 1F–H**). A serial MRI study demonstrated that SWI hypointensity in the GP and SN was observed after 2–7 years old, whereas T2 hypointensity after 4–7 years old (41). Here, the T1 hyperintense signal in the SN was detectable by early in the second decade of life (40, 42, 43). A characteristic halo sign appears later in the disease course, particularly as parkinsonism becomes evident in early adulthood (1).

Cavitation in Neuroferritinopathy

Cavitation involving the GP and putamen is unique to neuroferritinopathy among the NBIA disorders. A neuropathological study has demonstrated fluid accumulation within these cysts (22). Cavitary lesions with T2 hyperintensity are lined by hypointense rims secondary to prominent iron deposition (23). In a case report, Fluid-attenuated inversion recovery (FLAIR) images exhibited a tri-lamellar intensity consisting of an outer layer with iron deposition, a middle layer with gliosis, and a cystic core (44). This may represent different stages of expanding pathology. Cavitary lesions occur late in the disease, usually after excessive iron deposition, and evolve with time (22, 45).

NON-IRON AND EXTRAPALLIDAL ABNORMALITIES

Besides excessive iron, extrapallidal MRI abnormalities are helpful to facilitate diagnoses [**Table 1**; (7, 17)]. Neuroradiographic anatomic regions where non-iron and extrapallidal abnormalities are common in the NBIA disorders are summarized in **Supplementary Figure 1**.

The Extent and Magnitude of the Cerebral Atrophy

The extent of atrophy may depend on the nature of the underlying pathology (8, 46). Widespread α-synuclein-positive Lewy pathology has been identified in PLAN and MPAN (47, 48). Tau-positive neurofibrillary tangles are common in the brains of patients with BPAN (49). Indeed, pathologic α-synuclein and tau can spread extensively across the brain using a prion-like mechanism of propagation (50). Therefore, neurodegenerative changes can be more widely distributed throughout the brain. Serial MRI studies showed that brain atrophy progresses with the disease course (9, 34). On the contrary, in PKAN, neuronal loss, and astrogliosis are largely restricted to the GP in the absence of misfolded protein aggregates (49).

Visual rating scales are useful tools in assessing the severity of atrophy objectively. An established 4-point rating scale (51–53) is applicable for the assessment of cerebral and cerebellar cortical atrophy in NBIA disorders. In addition, planimetric analysis using sagittal T1WI can be used to evaluate volumetric changes in midsagittal structures including the corpus callosum, cerebellar vermis, and brainstem.

Disproportionate Cerebellar Atrophy in PLAN

In the majority of NBIA disorders, brain atrophy, if present, is usually generalized and has been commonly described without regional dominance. Cerebellar atrophy is a hallmark feature in PLAN, and is often the earliest sign on MRI (7, 54). It has been seen in up to 95% of patients with *PLA2G6* mutations (55). In infantile neuroaxonal dystrophy (NAD) and childhood-onset PLAN (juvenile NAD), cerebellar atrophy is a near universal feature (56, 57). Patients with an earlier disease onset showed a more severe cerebellar atrophy, which was assessed using the ratio of the mid-sagittal vermis size over the total posterior cranial fossa size (57). T2 or FLAIR hyperintensity in the cerebellar cortex often accompanies cerebellar atrophy (54, 58). In contrast, excessive iron deposition in the GP is seen in only up to half of PLAN cases (7, 55). Disproportionate cerebellar atrophy and iron deposition can be absent in adult-onset PLAN

(56, 59, 60), where there may be only frontally predominant atrophy (61) and MRI may even appear normal (56).

Thin Corpus Callosum

Thinning of the corpus callosum is a uniform feature in fatty acid hydroxylase-associated neurodegeneration (FAHN) (7, 62). Abnormal posterior corpus callosum that are thin and vertically oriented were noted in some cases of PLAN (54). Corpus callosum thinning may be an early sign of BPAN in the absence of excessive iron during infancy and early childhood (39, 40, 63).

It is important to evaluate the thickness and the morphology of corpus callosum in association with other findings observed in NBIA disorders, such as cerebral atrophy, myelination defect, or white matter damage (64).

White Matter Hyperintensities

T2 hyperintensities in white matter have been reported in most NBIA subtypes (1, 7, 8, 17) and are prominent in FAHN, Woodhouse-Sakati syndrome (WSS), and aceruloplasminemia. In a large cohort of patients with FAHN, the most common findings were white matter changes (100%), followed by ponto-cerebellar atrophy, GP hypointensity, and thin corpus callosum (62). T2 hyperintense white matter abnormalities were consistently found in the periventricular white matter with parietal predominance. In WSS, frontoparietal and periventricular white matter lesions were the most common non-iron abnormalities (65). And, older age was associated with a more severe degree of white matter lesions. In this study, the extent of white matter lesions was graded as none, mild (small focal), moderate (patchy scattered), or severe (diffuse confluent) according to their site, shape, confluency, and multifocality (65, 66). Prominent white matter hyperintensity is frequently noted in aceruloplasminemia (7). White matter hyperintensities in the posterior frontal and parieto-occipital regions extend caudally to the brainstem along the corticospinal tracts in a patient with aceruloplasminemia (67). Confluent T2 hyperintensities in white matter, localized mostly to the periventricular region, may be observed to a lesser extent in MPAN, BPAN, PLAN, and neuroferritinopathy (7–9, 40).

Although white matter T2 hyperintensity may be observed in NBIA disorders, diffuse cerebral hypomyelination is generally not a feature of these disorders (17). Delayed myelination has been reported in some cases of BPAN diagnosed in infancy and childhood (63, 68). However, the MRI findings in these cases were not described in enough detail to assess myelination. Hypomyelination is defined as an unchanged pattern of deficient myelination on two successive MRI scans at least 6 months apart in a child older than 1 year (69, 70). Myelinated white matter structures have a higher signal than do gray matter structures on T1WI and a lower signal on T2WI (69).

Miscellaneous Findings

Apparent hypertrophy of the clavum has been proposed as an important early feature of PLAN and may precede cerebellar atrophy (57, 71). Confirmation of clavum enlargement was made by comparison of its largest anteroposterior dimension on mid-sagittal T1WI with age-matched controls (71). Hypoplastic optic tracts and chiasms are seen in infantile NAD (72). SN swelling in the absence of iron deposition has been described as an early sign of BPAN (73), although the reason for SN enlargement is unknown. In a serial MRI study, transient T2 hyperintensity and swelling in the SN, GP, and/or deep cerebellar nuclei was observed during the episodes of pyrexia and seizures (41). Similarly, swelling and T2 hyperintensity of the caudate nucleus, putamen, and thalamus have been found in CoPAN (28). Small pituitary glands are common MRI abnormalities in WSS (65).

CURRENT LIMITATIONS AND FUTURE DIRECTIONS

Visual inspection of MRI can be highly subjective, and results can be varied. Objective interpretation is limited due to a lack of consistent methods to quantify the severity of MRI findings. A feasible way to objectively assess MRI severity is to use established visual rating scales or planimetric analysis as described above.

Iron quantification can be challenging, particularly within routine clinical settings. T2WI and SWI do not directly reflect iron concentrations (74). Instead, both the transverse relaxation rate (R2*) and quantitative susceptibility mapping are highly sensitive and accurate for measuring iron content in the brain (75). In a recent randomized trial of deferiprone for PKAN, iron concentrations in the GP were measured by MRI-R2* mapping (76). Diffusion-tensor imaging study demonstrated a significant increase of FA in patients with PKAN suggest the presence of abnormal iron in deep gray matter nuclei, even in the absence of its demonstration on T2*WI (77). An optimized protocol for quantitative MRI analysis is needed to monitor disease progression and treatment response.

Finally, studies that have investigated the pathological correlates of MRI signal alterations are rare. In some NBIA disorders, excessive iron deposition has not yet been demonstrated pathologically due to lack of autopsy-proven cases. Further research is needed to verify the exact underlying pathology of MRI abnormalities.

CONCLUSION

Specific NBIA disorders can be diagnosed by identifying characteristic MRI changes in combination with clinical findings. If an NBIA disorder is suspected or in the differential diagnosis, then iron-sensitive sequences should be included in an initial MRI. It is important to consider that MRI features specific to each NBIA disorder develop in an age-dependent manner and evolve during the disease course. The stepwise pattern-recognition approach outlined here may help to distinguish specific NBIA disorders as well as to delineate the natural course of MRI changes.

AUTHOR CONTRIBUTIONS

J-HL and SH: design and conceptualization of the study, analysis and interpretation of the data, drafting the manuscript, and final approval of the manuscript. PH: design and conceptualization of the study and final approval of the manuscript. AG and JY:

acquisition of the data and final approval of the manuscript. All authors reviewed the manuscript.

FUNDING

This study was supported by Research Institute for Convergence of biomedical science and technology Grant No. (30-2018-009), Pusan National University Yangsan Hospital.

SUPPLEMENTARY MATERIAL

The Supplementary Material for this article can be found online at: https://www.frontiersin.org/articles/10.3389/fneur.2020.01024/full#supplementary-material

Supplementary Figure 1 | Neuroradiographic anatomic regions where non-iron and extrapallidal abnormalities are common in the NBIA disorders. A normal MRI is used to show structures. The specific NBIA disorders are listed under each abnormality.

REFERENCES

1. Hogarth P. Neurodegeneration with brain iron accumulation: diagnosis and management. *J Mov Disord*. (2015) 8:1–13. doi: 10.14802/jmd.14034
2. Meyer E, Kurian MA, Hayflick SJ. Neurodegeneration with brain iron accumulation: genetic diversity and pathophysiological mechanisms. *Annu Rev Genomics Hum Genet*. (2015) 16:257–79. doi: 10.1146/annurev-genom-090314-025011
3. Hayflick SJ, Kurian MA, Hogarth P. Neurodegeneration with brain iron accumulation. *Handb Clin Neurol*. (2018) 147:293–305. doi: 10.1016/B978-0-444-63233-3.00019-1
4. Levi S, Tiranti V. Neurodegeneration with brain iron accumulation disorders: valuable models aimed at understanding the pathogenesis of iron deposition. *Pharmaceuticals*. (2019) 12:27. doi: 10.3390/ph12010027
5. Tello C, Darling A, Lupo V, Pérez-Dueñas B, Espinós C. On the complexity of clinical and molecular bases of neurodegeneration with brain iron accumulation. *Clin Genet*. (2018) 93:731–40. doi: 10.1111/cge.13057
6. Keogh MJ, Chinnery PF. Current concepts and controversies in neurodegeneration with brain iron accumulation. *Semin Pediatr Neurol*. (2012) 19:51–6. doi: 10.1016/j.spen.2012.03.004
7. Amaral LL, Gaddikeri S, Chapman PR, Roy R, Gaddikeri RS, Marussi VH, et al. Neurodegeneration with brain iron accumulation: clinicoradiological approach to diagnosis. *J Neuroimaging*. (2015) 25:539–51. doi: 10.1111/jon.12195
8. Kruer MC, Boddaert N, Schneider SA, Houlden H, Bhatia KP, Gregory A, et al. Neuroimaging features of neurodegeneration with brain iron accumulation. *Am J Neuroradiol*. (2012) 33:407–14. doi: 10.3174/ajnr.A2677
9. Skowronska M, Kmiec T, Jurkiewicz E, Malczyk K, Kurkowska-Jastrzebska I, Czlonkowska A. Evolution and novel radiological changes of neurodegeneration associated with mutations in C19orf12. *Parkinsonism Relat Disord*. (2017) 39:71–6. doi: 10.1016/j.parkreldis.2017.03.013
10. Lee JH, Gregory A, Hogarth P, Rogers C, Hayflick SJ. Looking deep into the eye-of-the-tiger in pantothenate kinase-associated neurodegeneration. *Am J Neuroradiol*. (2018) 39:583–8. doi: 10.3174/ajnr.A5514
11. Kanda T, Nakai Y, Aoki S, Oba H, Toyoda K, Kitajima K, et al. Contribution of metals to brain MR signal intensity: review articles. *Jpn J Radiol*. (2016) 34:258–66. doi: 10.1007/s11604-016-0532-8
12. Dusek P, Mekle R, Skowronska M, Acosta-Cabronero J, Huelnhagen T, Robinson SD, et al. Brain iron and metabolic abnormalities in C19orf12 mutation carriers: a 7.0 tesla MRI study in mitochondrial membrane protein-associated neurodegeneration. *Mov Disord*. (2020) 35:142–50. doi: 10.1002/mds.27827
13. Barkovich AJ. *Pediatric Neuroimaging*. 4th ed. Philadelphia, PA: Lippincott Williams and Wilkins (2005). p. 17–75.
14. Yan SQ, Sun JZ, Yan YQ, Wang H, Lou M. Evaluation of brain iron content based on magnetic resonance imaging (MRI): comparison among phase value, R2* and magnitude signal intensity. *PLoS ONE*. (2012) 7:e31748. doi: 10.1371/journal.pone.0031748
15. Zhang Y, Zabad R, Wei X, Metz L, Hill M, Mitchell J. Deep grey matter "black T2" on 3 tesla magnetic resonance imaging correlates with disability in multiple sclerosis. *Mult Scler*. (2007) 13:880–3. doi: 10.1177/1352458507076411
16. Gupta D, Saini J, Kesavadas C, Sarma PS, Kishore A. Utility of susceptibility-weighted MRI in differentiating Parkinson's disease and atypical parkinsonism. *Neuroradiology*. (2010) 52:1087–94. doi: 10.1007/s00234-010-0677-6
17. Kruer MC, Boddaert N. Neurodegeneration with brain iron accumulation: a diagnostic algorithm. *Semin Pediatr Neurol*. (2012) 19:67–74. doi: 10.1016/j.spen.2012.04.001
18. Wu YW, Hess CP, Singhal NS, Groden C, Toro C. Idiopathic basal ganglia calcifications: an atypical presentation of PKAN. *Pediatr Neurol*. (2013) 49:351–4. doi: 10.1016/j.pediatrneurol.2013.06.021
19. Saitsu H, Nishimura T, Muramatsu K, Kodera H, Kumada S, Sugai K, et al. *De novo* mutations in the autophagy gene WDR45 cause static encephalopathy of childhood with neurodegeneration in adulthood. *Nat Genet*. (2013) 45:445–9. doi: 10.1038/ng.2562
20. Van Goethem G, Livingston JH, Warren D, Oojageer AJ, Rice GI, Crow YJ. Basal ganglia calcification in a patient with beta-propeller protein-associated neurodegeneration. *Pediatr Neurol*. (2014) 51:843–5. doi: 10.1016/j.pediatrneurol.2014.08.017
21. Dusi S, Valletta L, Haack TB, Tsuchiya Y, Venco P, Pasqualato S, et al. Exome sequence reveals mutations in CoA synthase as a cause of neurodegeneration with brain iron accumulation. *Am J Hum Genet*. (2014) 94:11–22. doi: 10.1016/j.ajhg.2013.11.008
22. McNeill A, Birchall D, Hayflick SJ, Gregory A, Schenk JF, Zimmerman EA, et al. T2* and FSE MRI distinguishes four subtypes of neurodegeneration with brain iron accumulation. *Neurology*. (2008) 70:1614–9. doi: 10.1212/01.wnl.0000310985.40011.d6
23. Kumar N, Rizek P, Jog M. Neuroferritinopathy: pathophysiology, presentation, differential diagnoses and management. *Tremor Other Hyperkinet Mov*. (2016) 6:355. doi: 10.7916/D8KK9BHF
24. Batla A, Adams ME, Erro R, Ganos C, Balint B, Mencacci NE, et al. Cortical pencil lining in neuroferritinopathy: a diagnostic clue. *Neurology*. (2015) 84:1816–8. doi: 10.1212/WNL.0000000000001511
25. Chinnery PF, Crompton DE, Birchall D, Jackson MJ, Coulthard A, Lombès A, et al. Clinical features and natural history of neuroferritinopathy caused by the FTL1 460InsA mutation. *Brain*. (2007) 130:110–9. doi: 10.1093/brain/awl319
26. Schneider SA, Paisan-Ruiz C, Quinn NP, Lees AJ, Houlden H, Hardy J, et al. ATP13A2 mutations (PARK9) cause neurodegeneration with brain iron accumulation. *Mov Disord*. (2010) 25:979–84. doi: 10.1002/mds.22947
27. Gregory A, Hayflick S. Neurodegeneration with brain iron accumulation disorders overview. In: Adam MP, Ardinger HH, Pagon RA, Wallace SE, Bean LJH, Stephens K, Amemiya A, editors. *GeneReviews®*. Seattle, WA: University of Washington (2019).
28. Evers C, Seitz A, Assmann B, Opladen T, Karch S, Hinderhofer K, et al. Diagnosis of CoPAN by whole exome sequencing: waking up a sleeping tiger's eye. *Am J Med Genet A*. (2017) 173:1878–86. doi: 10.1002/ajmg.a.38252
29. Hayflick SJ, Hartman M, Coryell J, Gitschier J, Rowley H. Brain MRI in neurodegeneration with brain iron accumulation with and without PANK2 mutations. *Am J Neuroradiol*. (2006) 27:1230–3.
30. Yoganathan S, Sudhakar SV, Thomas M, Dutta AK, Danda S. "Eye of tiger sign" mimic in an adolescent boy with mitochondrial membrane protein associated neurodegeneration (MPAN). *Brain Dev*. (2016) 38:516–9. doi: 10.1016/j.braindev.2015.10.017
31. Litwin T, Karlinski M, Skowrońska M, Dziezyc K, Gołębiowski M, Członkowska A. MR image mimicking the "eye of the tiger" sign in Wilson's disease. *J Neurol*. (2014) 261:1025–7. doi: 10.1007/s00415-014-7322-y

32. Chang MH, Hung WL, Liao YC, Lee YC, Hsieh PF. Eye of the tiger-like MRI in parkinsonian variant of multiple system atrophy. *J Neural Transm*. (2009) 116:861–6. doi: 10.1007/s00702-009-0234-9
33. Hogarth P, Gregory A, Kruer MC, Sanford L, Wagoner W, Natowicz MR, et al. New NBIA subtype: genetic, clinical, pathologic, and radiographic features of MPAN. *Neurology*. (2013) 80:268–75. doi: 10.1212/WNL.0b013e31827e07be
34. Gregory A, Hartig M, Prokisch H, Kmiec T, Hogarth P, Hayflick SJ. Mitochondrial membrane protein-associated neurodegeneration. In: Adam MP, Ardinger HH, Pagon RA, Wallace SE, Bean LJH, Stephens K, Amemiya A, editors. *GeneReviews®*. Seattle, WA: University of Washington (2019).
35. Hartig M, Prokisch H, Meitinger T, Klopstock T. Mitochondrial membrane protein-associated neurodegeneration (MPAN). *Int Rev Neurobiol*. (2013) 110:73–84. doi: 10.1016/B978-0-12-410502-7.00004-1
36. Deutschländer A, Konno T, Ross OA. Mitochondrial membrane protein-associated neurodegeneration. *Parkinsonism Relat Disord*. (2017) 39:1–3. doi: 10.1016/j.parkreldis.2017.03.014
37. Olgiati S, Dogu O, Tufekcioglu Z, Diler Y, Saka E, Gultekin M, et al. The p.Thr11Met mutation in c19orf12 is frequent among adult Turkish patients with MPAN. *Parkinsonism Relat Disord*. (2017) 39:64–70. doi: 10.1016/j.parkreldis.2017.03.012
38. Landouré G, Zhu PP, Lourenço CM, Johnson JO, Toro C, Bricceno KV, et al. Hereditary spastic paraplegia type 43 (SPG43) is caused by mutation in C19orf12. *Hum Mutat*. (2013) 34:1357–60. doi: 10.1002/humu.22378
39. Gregory A, Kurian MA, Haack T, Hayflick SJ, Hogarth P. Beta-propeller protein-associated neurodegeneration. In: Adam MP, Ardinger HH, Pagon RA, Wallace SE, Bean LJH, Stephens K, Amemiya A, editors. *GeneReviews®*. Seattle, WA: University of Washington (2017).
40. Hayflick SJ, Kruer MC, Gregory A, Haack TB, Kurian MA, Houlden HH, et al. β-Propeller protein-associated neurodegeneration: a new X-linked dominant disorder with brain iron accumulation. *Brain*. (2013) 136:1708–17. doi: 10.1093/brain/awt095
41. Kimura Y, Sato N, Ishiyama A, Shigemoto Y, Suzuki F, Fujii H, et al. Serial MRI alterations of pediatric patients with beta-propeller protein associated neurodegeneration (BPAN). *J Neuroradiol*. (2020). doi: 10.1016/j.neurad.2020.04.002. [Epub ahead of print].
42. Ohba C, Nabatame S, Iijima Y, Nishiyama K, Tsurusaki Y, Nakashima M, et al. De novo WDR45 mutation in a patient showing clinically Rett syndrome with childhood iron deposition in brain. *J Hum Genet*. (2014) 59:292–5. doi: 10.1038/jhg.2014.18
43. Long M, Abdeen N, Geraghty MT, Hogarth P, Hayflick S, Venkateswaran S. Novel WDR45 mutation and pathognomonic BPAN imaging in a young female with mild cognitive delay. *Pediatrics*. (2015) 136:e714–17. doi: 10.1542/peds.2015-0750
44. Yoon SH, Kim NY, Kim YJ, Lyoo CH. Novel ferritin light chain gene mutation in a korean patient with neuroferritinopathy. *J Mov Disord*. (2019) 12:63–5. doi: 10.14802/jmd.18062
45. Park CW, Kim NY, Kim YJ, Song SK, Lyoo CH. A patient with neuroferritinopathy presenting with juvenile-onset voice tremor. *J Mov Disord*. (2019) 13:66–8. doi: 10.14802/jmd.19038
46. Kara E, Hardy J, Houlden H. The pallidopyramidal syndromes: nosology, aetiology and pathogenesis. *Curr Opin Neurol*. (2013) 26:381–94. doi: 10.1097/WCO.0b013e3283632e83
47. Schneider SA, Hardy J, Bhatia KP. Syndromes of neurodegeneration with brain iron accumulation (NBIA): an update on clinical presentations, histological and genetic underpinnings, and treatment considerations. *Mov Disord*. (2012) 27:42–53. doi: 10.1002/mds.23971
48. Schneider SA, Alcalay RN. Neuropathology of genetic synucleinopathies with parkinsonism: review of the literature. *Mov Disord*. (2017) 32:1504–23. doi: 10.1002/mds.27193
49. Arber CE, Li A, Houlden H, Wray S. Review: insights into molecular mechanisms of disease in neurodegeneration with brain iron accumulation: unifying theories. *Neuropathol Appl Neurobiol*. (2016) 42:220–41. doi: 10.1111/nan.12242
50. Goedert M, Masuda-Suzukake M, Falcon B. Like prions: the propagation of aggregated tau and α-synuclein in neurodegeneration. *Brain*. (2017) 140:266–78. doi: 10.1093/brain/aww230
51. Pasquier F, Leys D, Weerts JG, Mounier-Vehier F, Barkhof F, Scheltens P. Inter- and intraobserver reproducibility of cerebral atrophy assessment on MRI scans with hemispheric infarcts. *Eur Neurol*. (1996) 36:268–72. doi: 10.1159/000117270
52. Harper L, Barkhof F, Fox NC, Schott JM. Using visual rating to diagnose dementia: a critical evaluation of MRI atrophy scales. *J Neurol Neurosurg Psychiatry*. (2015) 86:1225–33. doi: 10.1136/jnnp-2014-310090
53. Sasaki R, Maki F, Hara D, Tanaka S, Hasegawa Y. Stratification of disease progression in a broad spectrum of degenerative cerebellar ataxias with a clustering method using MRI-based atrophy rates of brain structures. *Cerebellum Ataxias*. (2017) 4:9. doi: 10.1186/s40673-017-0068-4
54. Kurian MA, Morgan NV, MacPherson L, Foster K, Peake D, Gupta R, et al. Phenotypic spectrum of neurodegeneration associated with mutations in the PLA2G6 gene (PLAN). *Neurology*. (2008) 70:1623–9. doi: 10.1212/01.wnl.0000310986.48286.8e
55. Gregory A, Westaway SK, Holm IE, Kotzbauer PT, Hogarth P, Sonek S, et al. Neurodegeneration associated with genetic defects in phospholipase A2. *Neurology*. (2008) 71:1402–9. doi: 10.1212/01.wnl.0000327094.67726.28
56. Kurian MA, McNeill A, Lin JP, Maher ER. Childhood disorders of neurodegeneration with brain iron accumulation (NBIA). *Dev Med Child Neurol*. (2011) 53:394–404. doi: 10.1111/j.1469-8749.2011.03955.x
57. Darling A, Aguilera-Albesa S, Tello CA, Serrano M, Tomás M, Camino-León R, et al. PLA2G6-associated neurodegeneration: new insights into brain abnormalities and disease progression. *Parkinsonism Relat Disord*. (2019) 61:179–86. doi: 10.1016/j.parkreldis.2018.10.013
58. Iodice A, Spagnoli C, Salerno GG, Frattini D, Bertani G, Bergonzini P, et al. Infantile neuroaxonal dystrophy and PLA2G6-associated neurodegeneration: an update for the diagnosis. *Brain Dev*. (2017) 39:93–100. doi: 10.1016/j.braindev.2016.08.012
59. Karkheiran S, Shahidi GA, Walker RH, Paisán-Ruiz C. PLA2G6-associated dystonia-parkinsonism: case report and literature review. *Tremor Other Hyperkinet Mov*. (2015) 5:317. doi: 10.7916/D84Q7T4W
60. Guo YP, Tang BS, Guo JF. PLA2G6-associated neurodegeneration (PLAN): review of clinical phenotypes and genotypes. *Front Neurol*. (2018) 9:1100. doi: 10.3389/fneur.2018.01100
61. Yoshino H, Tomiyama H, Tachibana N, Ogaki K, Li Y, Funayama M, et al. Phenotypic spectrum of patients with PLA2G6 mutation and PARK14-linked parkinsonism. *Neurology*. (2010) 75:1356–61. doi: 10.1212/WNL.0b013e3181f73649
62. Rattay TW, Lindig T, Baets J, Smets K, Deconinck T, Söhn AS, et al. FAHN/SPG35: a narrow phenotypic spectrum across disease classifications. *Brain*. (2019) 142:1561–72. doi: 10.1093/brain/awz102
63. Hoffjan S, Ibisler A, Tschentscher A, Dekomien G, Bidinost C, Rosa AL. WDR45 mutations in Rett (-like) syndrome and developmental delay: case report and an appraisal of the literature. *Mol Cell Probes*. (2016) 30:44–9. doi: 10.1016/j.mcp.2016.01.003
64. Andronikou S, Pillay T, Gabuza L, Mahomed N, Naidoo J, Hlabangana LT, et al. Corpus callosum thickness in children: an MR pattern-recognition approach on the midsagittal image. *Pediatr Radiol*. (2015) 45:258–72. doi: 10.1007/s00247-014-2998-9
65. Abusrair AH, Bohlega S, Al-Semari A, Al-Ajlan FS, Al-Ahmadi K, Mohamed B, et al. Brain MR imaging findings in Woodhouse-Sakati syndrome. *Am J Neuroradiol*. (2018) 39:2256–62. doi: 10.3174/ajnr.A5879
66. King KS, Peshock RM, Warren MW, Alhilali L, Hulsey K, McColl R, et al. Evaluation of a practical visual MRI rating scale of brain white matter hyperintensities for clinicians based on largest lesion size regardless of location. *Am J Neuroradiol*. (2013) 34:797–801. doi: 10.3174/ajnr.A3283
67. Grisoli M, Piperno A, Chiapparini L, Mariani R, Savoiardo M. MR imaging of cerebral cortical involvement in aceruloplasminemia. *Am J Neuroradiol*. (2005) 26:657–61.
68. Stige KE, Gjerde IO, Houge G, Knappskog PM, Tzoulis C. Beta-propeller protein-associated neurodegeneration: a case report and review of the literature. *Clin Case Rep*. (2018) 6:353–62. doi: 10.1002/ccr3.1358
69. Guleria S, Kelly TG. Myelin, myelination, and corresponding magnetic resonance imaging changes. *Radiol Clin North Am*. (2014) 52:227–39. doi: 10.1016/j.rcl.2013.11.009
70. Schiffmann R, van der Knaap MS. Invited article: an MRI-based approach to the diagnosis of white matter disorders. *Neurology*. (2009) 72:750–9. doi: 10.1212/01.wnl.0000343049.00540.c8

71. Al-Maawali A, Yoon G, Feigenbaum AS, Halliday WC, Clarke JT, Branson HM, et al. Validation of the finding of hypertrophy of the clava in infantile neuroaxonal dystrophy/PLA2G6 by biometric analysis. *Neuroradiology*. (2016) 58:1035–42. doi: 10.1007/s00234-016-1726-6
72. Illingworth MA, Meyer E, Chong WK, Manzur AY, Carr LJ, Younis R, et al. PLA2G6-associated neurodegeneration (PLAN): further expansion of the clinical, radiological and mutation spectrum associated with infantile and atypical childhood-onset disease. *Mol Genet Metab*. (2014) 112:183–9. doi: 10.1016/j.ymgme.2014.03.008
73. Russo C, Ardissone A, Freri E, Gasperini S, Moscatelli M, Zorzi G, et al. Substantia nigra swelling and dentate nucleus T2 hyperintensity may be early magnetic resonance imaging signs of β-propeller protein-associated neurodegeneration. *Mov Disord Clin Pract*. (2018) 6:51–6. doi: 10.1002/mdc3.12693
74. Stüber C, Pitt D, Wang Y. Iron in multiple sclerosis and its noninvasive imaging with quantitative susceptibility mapping. *Int J Mol Sci*. (2016) 17:100. doi: 10.3390/ijms17010100
75. Lee JH, Lee MS. Brain iron accumulation in atypical parkinsonian syndromes: *in vivo* MRI evidences for distinctive patterns. *Front Neurol*. (2019) 10:74. doi: 10.3389/fneur.2019.00074
76. Klopstock T, Tricta F, Neumayr L, Karin I, Zorzi G, Fradette C, et al. Safety and efficacy of deferiprone for pantothenate kinase-associated neurodegeneration: a randomised, double-blind, controlled trial and an open-label extension study. *Lancet Neurol*. (2019) 18:631–42. doi: 10.1016/S1474-4422(19)30142-5
77. Awasthi R, Gupta RK, Trivedi R, Singh JK, Paliwal VK, Rathore RK. Diffusion tensor MR imaging in children with pantothenate kinase-associated neurodegeneration with brain iron accumulation and their siblings. *Am J Neuroradiol*. (2010) 31:442–7. doi: 10.3174/ajnr.A1849

Conflict of Interest: The authors declare that the research was conducted in the absence of any commercial or financial relationships that could be construed as a potential conflict of interest.

frontiers in Neurology

ORIGINAL RESEARCH
published: 30 September 2020
doi: 10.3389/fneur.2020.499910

Differences in Advanced Magnetic Resonance Imaging in MOG-IgG and AQP4-IgG Seropositive Neuromyelitis Optica Spectrum Disorders: A Comparative Study

Felix A. Schmidt[1,2,3,4], *Claudia Chien*[1], *Joseph Kuchling*[1,2], *Judith Bellmann-Strobl*[1,5], *Klemens Ruprecht*[2,3], *Nadja Siebert*[1,5], *Susanna Asseyer*[1,5], *Sven Jarius*[6], *Alexander U. Brandt*[1,5,7], *Michael Scheel*[1,4,8†] *and Friedemann Paul*[1,2,5*†]

[1] NeuroCure Clinical Research Center, Charité – Universitätsmedizin Berlin, Corporate Member of Freie Universität Berlin, Humboldt-Universität zu Berlin, and Berlin Institute of Health, Berlin, Germany, [2] Department of Neurology, Charité – Universitätsmedizin Berlin, Corporate Member of Freie Universität Berlin, Humboldt-Universität zu Berlin, and Berlin Institute of Health, Berlin, Germany, [3] Clinical and Experimental Multiple Sclerosis Research Center, Department of Neurology, Charité – Universitätsmedizin Berlin, Berlin, Germany, [4] Berlin Institute of Health, Berlin, Germany, [5] Experimental and Clinical Research Center, Max Delbrueck Center for Molecular Medicine and Charité – Universitätsmedizin Berlin, Corporate Member of Freie Universität Berlin, Humboldt-Universität zu Berlin, and Berlin Institute of Health, Berlin, Germany, [6] Division of Molecular Neuroimmunology, Department of Neurology, University Hospital Heidelberg, Heidelberg, Germany, [7] Department of Neurology, University of California, Irvine, Irvine, CA, United States, [8] Department of Neuroradiology, Charité – Universitätsmedizin Berlin, Berlin, Germany

Aims: To explore differences in advanced brain magnetic resonance imaging (MRI) characteristics between myelin oligodendrocyte (MOG) immunoglobulin (IgG) and aquaporin-4 (AQP4) IgG seropositive (+) neuromyelitis optica spectrum disorders (NMOSD).

Methods: 33 AQP4-IgG and 18 MOG-IgG seropositive NMOSD patients and 61 healthy control (HC) subjects were included. All 112 participants were scanned with the same standardized MRI-protocol on a 3-Tesla MRI-scanner. Brain volume and diffusion tensor imaging (DTI) parameters were assessed.

Results: MOG-IgG+ patients showed reduced parallel diffusivity within white matter tracts compared to HC whereas AQP4-IgG+ showed no significant brain parenchymal damage in DTI analysis. AQP4-IgG+ patients showed reduced whole brain volumes and reduced volumes of several deep gray matter structures compared to HC whereas MOG-IgG+ patients did not show reduced brain or deep gray matter volumes compared to HC.

Conclusions: Microstructural brain parenchymal damage in MOG-IgG+ patients was more pronounced than in AQP4-IgG+ patients, compared with HC, whereas normalized brain volume reduction was more severe in AQP4-IgG+ patients. Longitudinal imaging studies are warranted to further investigate this trend in NMOSD. Our results suggest

OPEN ACCESS

Edited by:
Fabienne Brilot, The University of Sydney, Australia

Reviewed by:
Amy Kunchok, Mayo Clinic, United States
Marco A. Lana-Peixoto, Federal University of Minas Gerais, Brazil

***Correspondence:**
Friedemann Paul
friedemann.paul@charite.de

† These authors have contributed equally to this work and share senior authorship

Specialty section:
This article was submitted to Applied Neuroimaging, a section of the journal Frontiers in Neurology

Received: *23 September 2019*
Accepted: *24 August 2020*
Published: *30 September 2020*

Citation:
Schmidt FA, Chien C, Kuchling J, Bellmann-Strobl J, Ruprecht K, Siebert N, Asseyer S, Jarius S, Brandt AU, Scheel M and Paul F (2020) Differences in Advanced Magnetic Resonance Imaging in MOG-IgG and AQP4-IgG Seropositive Neuromyelitis Optica Spectrum Disorders: A Comparative Study. Front. Neurol. 11:499910. doi: 10.3389/fneur.2020.499910

that MOG-IgG+ and AQP4-IgG+ NMOSD patients differ in cerebral MRI characteristics. Advanced MRI analysis did not help to differentiate between MOG-IgG+ and AQP4-IgG+ patients in our study.

Keywords: NMOSD, AQP4, MOG, MRI, DTI, advanced imaging

INTRODUCTION

Neuromyelitis optica spectrum disorders (NMOSD) are autoimmune diseases that present with longitudinally extensive transverse myelitis (LETM) and or optic neuritis (ON). They can also present with area postrema, diencephalic, cerebral or acute brainstem syndromes (1–6). The proof of serum autoantibodies directed against aquaporin-4 (AQP4-IgG) in around 80% of cases established NMOSD as a distinct disease from multiple sclerosis (MS) (7–10). In a subgroup of AQP4-IgG negative NMOSD patients serum antibodies targeting the myelin oligodendrocyte glycoprotein (MOG-IgG) were detected (11–16). MOG-IgG+ patients with clinical and neuroimaging characteristics of NMOSD are currently discussed as a different disease entity (17–23). Cortical encephalitis and seizures or cranial nerve involvement have also been reported in MOG-IgG+ patients (24–27).

While brain atrophy and microstructural tissue damage occur in MS from earliest disease stages (28–30), non-conventional MRI studies have shown conflicting results in NMOSD (31–35), and advanced imaging, such as diffusion tensor imaging (DTI) analysis, have not been reported from MOG-IgG+ patients.

Thus, the goal of our study was to further investigate possible MRI differences between MOG-IgG+ and AQP4-IgG+ mediated pathology in NMOSD patients and to compare these effects to a group of HCs.

MATERIALS AND METHODS

Study Participants and Controls

Data for this cross-sectional study were extracted from an ongoing longitudinal observational study following patients with NMOSD and HCs performed at the NeuroCure Clinical Research Center, Charité Universitaetsmedizin Berlin.

Inclusion criteria were diagnosis of NMOSD according to the international consensus diagnostic criteria for NMOSD 2015 (36) or positive proof of MOG-IgG serum antibodies in a live cell-based assay and an associated demyelinating CNS disease with a clinical phenotype equivalent to NMOSD diagnosis criteria in patients over 18 years (17). In this regard, we treated MOG-IgG positivity as equivalent to positive AQP4-IgG for fulfilling the diagnostic criteria. All MOG-IgG+ patients met the currently proposed criteria for MOG encephalomyelitis (26). Exclusion criteria were a relapse within 3 months prior to MRI examination. Patients from the outpatient clinics of the Experimental and Clinical Research Center, NeuroCure Clinical Research Center and from the Department of Neurology, Charité – Universitätsmedizin Berlin were screened for eligibility.

Ethics Statement

The study was approved by the Charité-Universitätsmedizin Berlin ethics committee (EA1/041/14) and was conducted in accordance to the Declaration of Helsinki in its currently applicable version and applicable German laws. All participants gave written informed consent to participate in the study.

CLINICAL DATA

Clinical Assessment

The expanded disability status scale (EDSS) and further clinical characteristics were assessed on the day the MRI scan was performed as part of a study protocol. All patients included were enrolled into a prospective observational cohort study of NMOSD at NeuroCure Clinical Research Center and received a MRI scan annually as part of this cohort study. All patients were examined with the same standardized MRI protocol at the same MRI scanner for study purposes. From the majority of patients no MRI at disease onset was available because most of the included patients were referred from other hospitals and the department of neurology - Charité – Universitätsmedizin Berlin.

MRI Acquisition Protocol

The multimodal brain MRIs all were acquired from a 3 T MRI (MAGNETOM Trio Tim, Siemens, Erlangen, Germany) and included a 3-dimensional T1-weighted magnetization prepared rapid acquisition gradient echo (MPRAGE) sequence ($1 \times 1 \times 1$ mm resolution, TR = 1,900 ms, TE = 3.03 ms), a 3-dimensional fluid attenuated inversion recovery (3D FLAIR) sequence ($1 \times 1 \times 1$ mm resolution, TR = 6,000 ms, TE = 388 ms) and a single-shot echo planar imaging DTI sequence (TR/TE = 7,500/86 ms; FOV = 240×240 mm; matrix 96×96, 61 slices no gap, slice thickness 2.3 mm, 64 non-collinear directions, b-value = 1,000 s/mm^2).

MRI-Data Post-processing

Brain and Deep Gray Matter Volumes

Gray and white matter volumes were calculated from MPRAGE scans, after lesion filling, using FSL SIENAX for normalized whole brain gray matter and white matter and with FSL FIRST for deep gray matter volumes (37–40).

DTI PARAMETERS

FSL DTIFIT (41) was used for DTI data processing, which included brain extraction and correction for eddy current distortions. Fractional anisotropy (FA) and parallel diffusivity were calculated by fitting a tensor model to the diffusion data using the tools from FSL. All data were then further processed with the tract based spatial statistics (TBSS) (42, 43).

Statistical Analysis

Statistical analyses was were performed with R version 3.3.0 using the packages geepack and ggplot2 (44). Differences in demographics and clinical characteristics between patients and HC were tested using Welch's two-sample *t*-test. Differences in gender, clinical phenotype and immunosuppressive therapy were tested with the Fisher Exact Test. Group differences (brain volume and DTI measures) were analyzed using a linear regression model, including age, female sex and disease duration as a covariate. A *p*-value of <0.05 was considered significant. Due to the exploratory nature of the study, no correction for multiple comparisons was made.

TABLE 1 | Demographics and clinical characteristics of AQP4-IgG+ and MOG-IgG+ patients.

Parameter	AQP4 ($n = 33$)	MOG ($n = 18$)	*p*-value
Sex (f/m)	30/3	11/7	**0.02**
Age in years	50.3 ± 13.6 (24–72)	44.3 ± 12.2 (22–59)	0.11
EDSS	4 (0–7)	2 (1–6)	**0.01**
Annualized Relapse Rate	0.8 ± 1.2	1.3 ± 1.2	0.28
Total number of relapses	3.6 ± 2.1	3.7 ± 2.5	0.89
Disease Duration in years	8 ± 7	8 ± 11	1.0
Immunosuppressive Therapy	28 (85%)	14 (78%)	0.70
Clinical Phenotype LETM + bilateral ON	14 (42%)	5 (28%)	0.37
Bilateral ON	3 (9%)	4 (22%)	0.23
LETM only	12 (36%)	3 (17%)	0.20

F, female; M, Male; EDSS, Expanded Disability Status Scale; LETM, longitudinal extensive transverse myelitis; ON, optic neuritis. EDSS is presented as median (range). Age, annual relapse rate, total number of previous attacks and disease duration are presented as mean ± standard deviation. Clinical phenotype and immunosuppressive therapy are presented as total numbers and in %.

RESULTS

From the 51 included patients, 33 had a diagnosis of AQP4-IgG seropositive NMOSD according to the 2015 IPND diagnostic criteria (36). From the 18 patients with positive MOG-IgG serology, five patients fulfilled the criteria for AQP4-IgG seronegative NMOSD. Another 13 patients were tested positive for serum MOG-IgG and had recurrent ON or at least one episode of LETM, but did not formally fulfill the 2015 IPND criteria for NMOSD. Demographics and clinical characteristics of AQP4-IG+ and MOG-IgG+ patients are summarized in **Table 1**. AQP4-IgG+ and MOG-IgG+ patients showed differences in sex and EDSS score, with no significant difference in age, disease duration, annualized relapse rate and further clinical characteristics (see **Table 1**).

Brain Volume Analysis

AQP4-IgG+ patients showed a trend for reduced normalized whole brain volumes compared to HC ($p = 0.087$, see **Figure 1**). There was no difference between AQP4-IgG+ patients, MOG-IgG+ patients and HC normalized gray matter volumes and white matter volumes.

Brain Volume Analysis of Deep Gray Matter Structures

MOG-IgG+ patients did not show any volume reduction in deep gray matter structures compared to HC. A significant volume reduction for AQP4-IgG+ patients compared to HC was found in the putamen ($p = 0.035$, see **Figure 2**), the thalamus ($p = 0.019$, see **Figure 3**) and the pallidum ($p = 0.008$, see **Figure 4**).

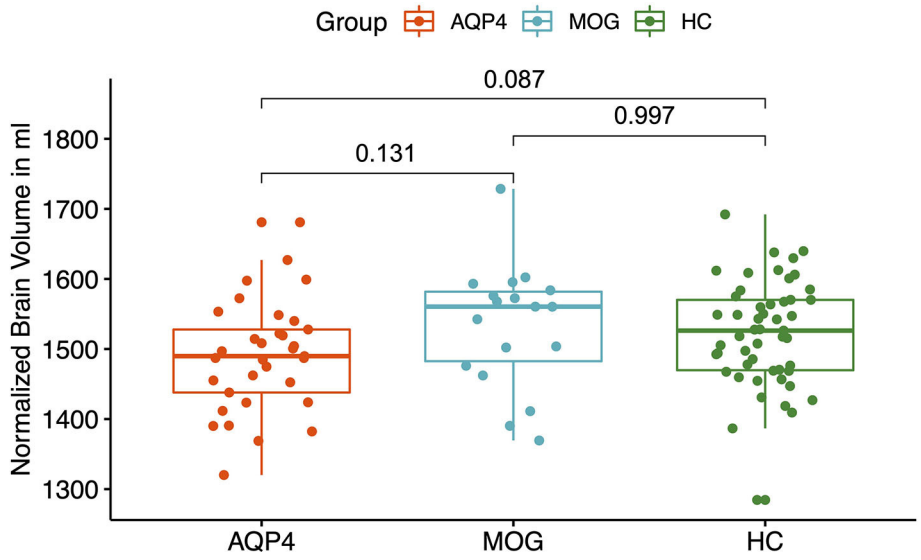

FIGURE 1 | Normalized Brain Volumes. Y-axis: normalized brain volume in ml. X-axis: patient groups and healthy controls. AQP4, Aquaporin-4-IgG+ patients; HC, healthy control; MOG, Myelin oligodendrocyte glycoprotein IgG+ patients.

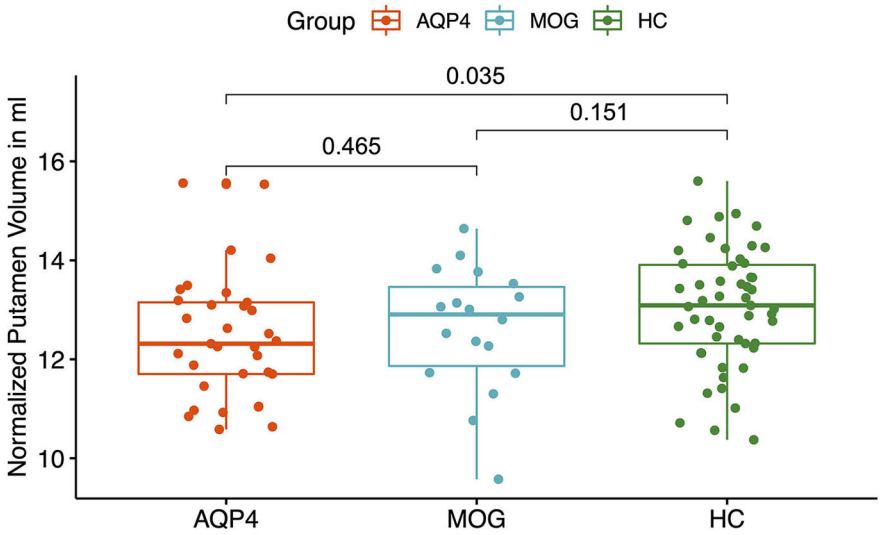

FIGURE 2 | Y-axis: Normalized putamen volume in ml. X-axis: patient groups and healthy controls. AQP4, Aquaporin-4-IgG+ patients; HC, healthy control; MOG, Myelin oligodendrocyte glycoprotein IgG+ patients.

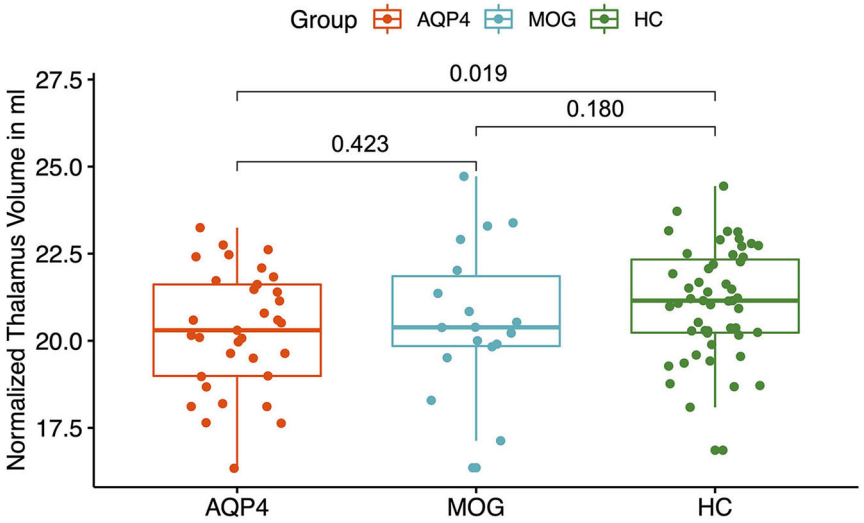

FIGURE 3 | Y-axis: Normalized thalamus volume in ml. X-axis: patient groups and healthy controls. AQP4, Aquaporin-4-IgG+ patients; HC, healthy control; MOG, Myelin oligodendrocyte glycoprotein IgG+ patients.

Diffusion Tensor Imaging

MOG-IgG+ patients showed reduced parallel diffusivity compared to HC while AQP4-IgG+ patients showed no difference in parallel diffusivity compared to HC (see **Figure 5**). No difference was found between AQP4-IgG+ and MOG-IgG+ patients or HC in fractional anisotropy (FA), mean diffusivity, or radial diffusivity measures.

DISCUSSION

How intracranial volume and brain parenchymal damage differ between MOG-IgG+ and AQP4-IgG+ patients has not been investigated in detail before.

MOG-IgG seropositive patients with clinical and neuroimaging features of NMOSD are currently under discussion as being a distinct disease entity (45–51). There are few studies investigating MRI findings of MOG-IgG+ patients, likely due to its recent discovery and rare prevalence (18, 28, 46–48).

This is the first study that compares advanced MRI analysis of a larger cohort of MOG-IgG+ patients against AQP4-IgG+ patients along with HC. Other studies demonstrated that MRI brain lesion distribution criteria may help to distinguish MOG-IgG+ and AQP4-IgG+ patients from multiple sclerosis patients (28, 32, 45, 47, 48, 52). However, these studies did not analyze differences in brain volume and brain parenchymal damage.

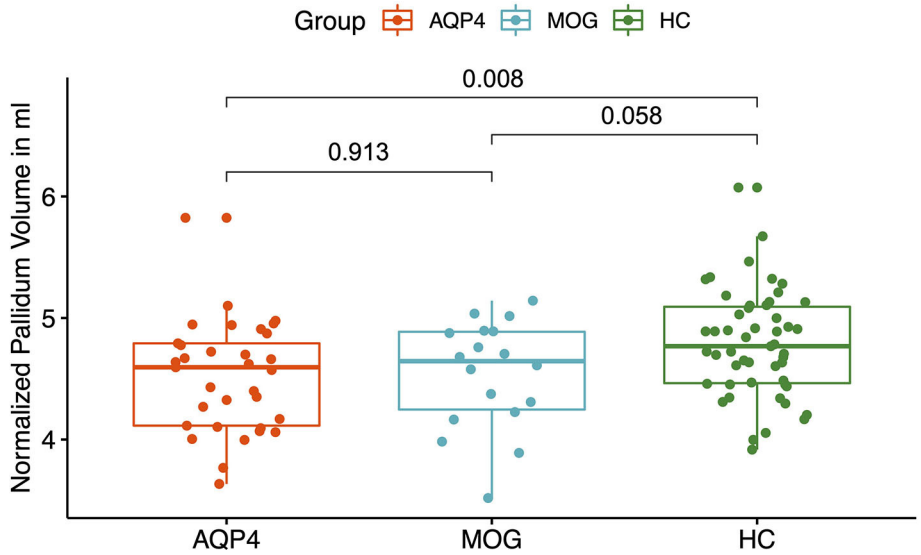

FIGURE 4 | Y-Axis: Normalized pallidum volume in ml. X-axis: patient groups and healthy controls. AQP4, Aquaporin-4-IgG+ patients; HC, healthy control; MOG, Myelin oligodendrocyte glycoprotein IgG+ patients.

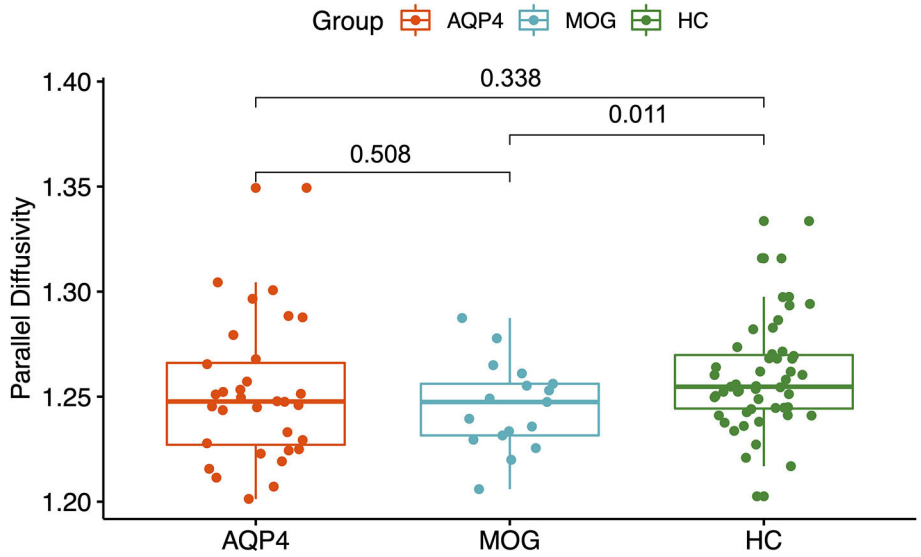

FIGURE 5 | Y-axis: Parallel diffusivity. X-axis: patient groups and healthy controls. AQP4, Aquaporin-4-IgG+ patients; HC, healthy control; MOG, Myelin oligodendrocyte glycoprotein IgG+ patients.

Interestingly, in our brain volume analyses and DTI analysis no significant differences were found between MOG-IgG+ and AQP4-IgG+ patients, although MOG-IgG+ patients showed a reduced parallel diffusivity compared to HC. Our findings of reduced parallel diffusivity in white matter tracts of MOG-IgG+ patients compared to HC are complemented by previous studies investigating C57BL/6 mice with MOG-induced experimental autoimmune encephalomyelitis (EAE) that showed significant parallel diffusivity reduction within optic nerves (53) and within the spinal chord (54) with significant associations to EAE clinical scores and greater amounts of axonal damage as confirmed by quantitative staining. Decreased parallel diffusivity within the optic nerves of human patients after acute optic neuritis (55, 56) further corroborated the notion that decreased parallel diffusivity may be associated with various mechanisms of axonal damage, such as Wallerian degeneration, and diffuse axonal injury (57) that might have similarly occurred within the white matter of our MOG-IgG+ patients. Axonal loss and atrophy might lead to a bulk reduction of the intra-axonal volume and associated anisotropic diffusion profile

(58). However, the exact biophysical mechanisms of reduction in parallel diffusivity still remain uncertain and further *in-* and *ex-vivo* studies are highly warranted to elucidate the exact associations between parallel diffusivity alterations and potentially corresponding axonal damage in patients with MOG-IgG+ encephalomyelitis.

AQP4-IgG+ patients showed a trend for a reduced normalized whole brain volume and a reduced volume of the putamen, pallidum and thalamus compared to HC. In a previous study, a smaller number of AQP4-IgG+ patients from our NMOSD cohort was analyzed and no significant brain volume reduction was found compared to HC with no brain parenchymal damage (34, 59). The differences could be explained by a statistical power problem, since the AQP4-IgG+ patient cohort was smaller.

Several measures were taken to establish a homogeneous study cohort to permit a comparison of these heterogeneous autoimmune disorders. Firstly, only antibody seropositive patients were included. Also, each patient was examined with the same standardized MRI protocol at the same MRI scanner. MRI data was evaluated by the same experienced neuroradiologist blinded to the patients' diagnosis. Further, the current study was restricted to mainly Caucasian patients with NMOSD given that ethnicity likely interacts with NMOSD pathogenicity with regard to possible genetic influence (i.e., Asian opticospinal MS) (60). Finally, AQP4-IgG+ and MOG-IgG+ patients were close in age where there was no significant difference in the means, thus reducing chances of finding differences in brain volume based on age.

A limitation of our study, and most of the previous imaging NMOSD studies, is the limited sample size due to the prevalence of this rare disease, especially in Caucasians (61). One possible solution to this fact, in a rare disease like MOG-IgG+ NMOSD, would be to compile available data in an international study group and pool imaging data in a common database for analysis in multicenter studies. This would allow for the evaluation of brain damage in NMOSD patients with enhanced statistical power. Another limitation are differences in sex and EDSS score between MOG-IgG+ and AQP4-IgG+ patients in our study. Both variables might have an impact on the MRI results.

We conclude that MOG-IgG+ patients in our cohort have more structural brain parenchymal damage, as detected by DTI measures when compared to HC whereas AQP4-IgG+ patients showed reduced whole brain volumes and reduced volumes of several deep gray matter structures compared to HC. Volume sub-analyses of deep gray matter structures and DTI measurements did not help to differentiate between MOG-IgG+- and AQP4-IgG+ patients in our study.

Our results are in favor of an early immunosuppressive treatment of patients with MOG encephalomyelitis whose treatment approaches still are a matter of debate (62). Similar to the treatment strategies for AQP4-IgG+ NMOSD patients, we believe this suggestion is valid because of the increased brain parenchymal damage observed from diffusion tensor imaging measures of parallel diffusivity in MOG-IgG+ patients. Longitudinal imaging studies are warranted to further investigate this trend of increased brain parenchymal damage in MOG-IgG+ patients.

DATA AVAILABILITY STATEMENT

The datasets generated for this study are available on request to the corresponding author.

ETHICS STATEMENT

The studies involving human participants were reviewed and approved by Charité-Universitätsmedizin Berlin ethics committee (EA1/041/14). The patients/participants provided their written informed consent to participate in this study.

AUTHOR CONTRIBUTIONS

Study concept and coordination was performed by FP, AB, and MS. Data acquisition and interpretation were performed by FS and MS. Initial draft was performed by FS. Study supervision by FP, AB, and MS. Critical revision of the manuscript for important intellectual content was performed by FP, MS, AB, CC, KR, JK, NS, JB-S, SA, and SJ. All authors contributed to the article and approved the submitted version.

REFERENCES

1. Jarius S, Wildemann B, Paul F. Neuromyelitis optica: clinical features, immunopathogenesis and treatment. *Clin Exp Immunol.* (2014) 176:149–64. doi: 10.1111/cei.12271
2. Kleiter I, Gahlen A, Borisow N, Fischer K, Wernecke K, Hellwig K, et al. Apheresis therapies for NMOSD attacks: a retrospective study of 207 therapeuthic interventions. *Neurol Neuroimmunol Neuroinflamm.* (2018) 5:e504. doi: 10.1212/NXI.0000000000000504
3. Kremer L, Mealy M, Jacob A, Nakashima I, Cabre P, Bigi S, et al. Brainstem manifestations in neuromyelitis optica: a multicenter study of 258 patients. *Mult Scler.* (2014) 20:843–7. doi: 10.1177/1352458513507822
4. Mori M, Kuwabara S, Paul F. Worldwide prevalence of neuromyelitis optica spectrum disorders. *J Neurol Neurosurg Psychiatry.* (2018) 89:555–56. doi: 10.1136/jnnp-2017-317566
5. Schmidt F, Zimmermann H, Mikolajczak J, Oertel FC, Pache F, Weinhold M, et al. Severe structural and functional visual system damage leads to profound loss of vision-related quality of life in patients with neuromyelitis optica spectrum disorders. *Mult Scler Relat Disord.* (2017) 11:45–50. doi: 10.1016/j.msard.2016.11.008
6. Finke C, Zimmermann H, Pache F, Oertel FC, Chavarro VS, Kramarenko Y, et al. Association of visual impairment in neuromyelitis optica spectrum disorder with visual network reorganization. *JAMA Neurol.* (2018) 75:296–303. doi: 10.1001/jamaneurol.2017.3890
7. Sepúlveda M, Armangué T, Sola-Valls N, Arrambide G, Meca-Lallana J, Orecha-Guevara C, et al. Neuromyelitis optica spectrum disorders: comparison according to the phenotype and serostatus. *Neurol Neuroimmunol Neuroinflamm.* (2016) 3:e225. doi: 10.1212/NXI.0000000000000225
8. Metz I, Beißbarth T, Ellenberger D, Pache F, Stork L, Ringelstein M, et al. Serum peptide reactivities may distinguish neuromyelitis optica subgroups and multiple sclerosis. *Neurol Neuroimmunol Neuroinflamm.* (2016) 3:e204. doi: 10.1212/NXI.0000000000000204

9. Zekeridou A, Lennon VA. Aquaporin-4 autoimmunity. *Neurol Neuroimmunol Neuroinflamm.* (2015) 2:e110. doi: 10.1212/NXI.0000000000000110
10. Jarius S, Ruprecht K, Wildemann B, Kuempfel T, Ringelstein M, Geis Ch, et al. Contrasting disease patterns in seropositive and seronegative neuromyelitis optica: a multicenter study of 175 patients. *J Neuroinflammation.* (2012) 9:14. doi: 10.1186/1742-2094-9-14
11. Sato DK, Callegaro D, Lana-Peixoto MA, Waters P, Jorge F, Takahashi T, et al. Distinction between MOG antibody-positive and AQP4 antibody-positive NMO spectrum disorders. *Neurology.* (2014) 82:474–81. doi: 10.1212/WNL.0000000000000101
12. Jarius S, Metz I, König FB, Ruprecht K, Reindl M, Paul F, et al. Screening for MOG- IgG and 27 other anti-glial and anti-neuronal autoantibodies in 'pattern II multiple sclerosis' and brain biopsy findings in a MOG-IgG-positive case. *Mult Scler.* (2016) 22:1541–49. doi: 10.1177/1352458515622986
13. Zamvill SS, Slavin AJ. Does MOG-Ig positive AQP4-seronegative opticospinal inflammatory disease justify a diagnosis of NMO spectrum disorder? *Neurol Neuroimmunol Neuroinflamm.* (2015) 2:e62. doi: 10.1212/NXI.0000000000000062
14. Narayan R, Simpson A, Fritsche K, Salama S, Pardo S, Mealy M, et al. MOG antibody disease: a review of MOG antibody seropositive neuromyelitis optica spectrum disorder. *Mult Scler Relat Disord.* (2018) 25:66–72. doi: 10.1016/j.msard.2018.07.025
15. Reindl M, Schanda K, Woodhall M, Tea I, Ramanathan S, Sagen S, et al. International multicenter examination of MOG antibody assays. *Neurol Neuroimmunol Neuroinflamm.* (2020) 7:e674. doi: 10.1212/NXI.0000000000000674
16. Cobo-Calvo A, Indy H, Ruiz A, Collongues N, Kremer L, Durant-Dubief F, et al. Frequency of myelin oligodendrocyte glycoprotein antibody in multiple sclerosis: a multicenter cross-sectional study. *Neurol Neuroimmunol Neuroinflamm.* (2020) 7:e649. doi: 10.1212/NXI.0000000000000649
17. Jarius S, Ruprecht K, Kleiter I, Borisow N, Asgari N, Pitarokoilio K, et al. MOG-IgG in NMO and related disorders: a multicenter study. Part 1: Frequency, syndrome specificity, influence of disease activity, long-term course, association with AQP4-IgG, and origin. *J Neuroinflamm.* (2016) 13:279. doi: 10.1186/s12974-016-0717-1
18. Jarius S, Ruprecht K, Kleiter I, Borisow N, Asgari N, Pitarokoilio K, et al. MOG-IgG in NMO and related disorders: a multicenter study. Part 2: Epidemiology, clinical presentation, radiological and laboratory features, treatment, and long-term outcome. *J Neuroinflamm.* (2016) 13:281. doi: 10.1186/s12974-016-0718-0
19. Jarius S, Ruprecht K, Kleiter I, Borisow N, Asgari N, Pitarokoilio K, et al. MOG-IgG in NMO and related disorders: a multicenter study. Part 3: Brainstem involvement - frequency, presentation and outcome. *J Neuroinflamm.* (2016) 13:281. doi: 10.1186/s12974-016-0719-z
20. Pache F, Zimmermann H, Mikolaczak J, Schumacher S, Lacheta A, Oertel FC, et al. MOG-IgG in NMO and related disorders: a multicenter study. Part 4: Afferent visual system damage after optic neuritis in MOG-IgG-seropositive versus AQP4-IgG- seropositive patients. *J Neuroinflamm.* (2016) 13:281. doi: 10.1186/s12974-016-0720-6
21. Cobo-Calvo A, Ruiz A, Maillart E, Audoin B, Zephir H, Bourre B, et al. Clinical spectrum and prognostic value of CNS MOG autoimmunity in adults: the MOGADOR study. *Neurology.* (2018) 90:e1858. doi: 10.1212/WNL.0000000000005560
22. Jurynczyk M, Probert F, Yeo T, Tackley G, Claridge T, Cavey A, et al. Metabolimics reveals distinct, antibody- independent, molecular signatures of MS, AQP4-antibody and MOG-antibody disease. *Acta Neuropathol Commun.* (2017) 5:95. doi: 10.1186/s40478-017-0495-8
23. Cobo-Calvo A, Sepulveda M, Rollot F, Armangue T, Ruiz A, Maillat E, et al. Evaluation of treatment response in adults with relapsing MOG-Ab-associated disease. *J Neuroinflamm.* (2019) 16:134. doi: 10.1186/s12974-019-1525-1
24. Ogawa R, Nakashima I, Takahashi T, Kaneko K, Akaishi T, Takai Y, et al. MOG- antibody positive, benign, unilateral, cerebral cortical encephalities with epilepsy. *Neurol Neuroimmunol Neuroinflamm.* (2017) 4:e322. doi: 10.1212/NXI.0000000000000322
25. Hamid SHM, Whittam D, Saviour M, Alorainy A, Mutzl K, Linaker S, et al. Seizures and encephalitis in myelin oligodentrocyte glycoprotein IgG disease vs AQP4 IgG disease. *JAMA Neurol.* (2018) 75:65–71. doi: 10.1001/jamaneurol.2017.3196
26. Jarius S, Paul F, Aktas O, Asgari N, Dale RC, DSeze J, et al. MOG encephalomyelitis: international recommendations on diagnosis and antibody testing. *J Neuroinflamm.* (2018) 15:134. doi: 10.1186/s12974-018-1144-2
27. Cobo-Calvo A, Ayrignac X, Kerschen P, Hourrellou P, Cotton F, Labauge P, et al. Cranial nerve involvment in patients with MOG antibody-associated disease. *Neurol Neuroimmunol Neuroinflamm.* (2019) 6:e543. doi: 10.1212/NXI.0000000000000543
28. Alcaide-Leon P, Cybulsky K, Sankar S, Casserly C, Leung G, Hohol M, et al. Quantitative spinal chord MRI in radiologically isolated syndrome. *Neurol Neuroimmunol Neuroinflamm.* (2018) 5:e346. doi: 10.1212/NXI.0000000000000436
29. Azevedo CJ, Overton E, Khadka S, Buckley J, Liu S, Sampat M, et al. Early CNS neurodegeneration in radiologically isolated syndrome. *Neurol Neuroimmunol Neuroinflamm.* (2015) 2:e102. doi: 10.1212/NXI.0000000000000102
30. Pawlitzki M, Neumann J, Kaufmann J, Heidel J, Stadler E, Sweeney-Reed C, et al. Loss of corticospinal tract integrity in early MS disease stages. *Neurol Neuroimmunol Neuroinflamm.* (2017) 4:e399. doi: 10.1212/NXI.0000000000000399
31. Van Pelt E, Wong YY, Keteslegers I, Haman D, Hintzen RG. Neuromyelitis optica spectrum disorders: comparison of clinical and magnetic resonance imaging characteristics of AQP4-IgG versus MOG-IgG seropositive cases in the Netherlands. *Eur J Neurol.* (2016) 23:580–7. doi: 10.1111/ene.12898
32. Kremer S, Renard F, Achard S, Peixoto L, Palace J, Asgari N, et al. Use of advanced magnetic resonance imaging techniques in neuromyelitis optica spectrum disorder. *JAMA Neurol.* (2015) 72:815–22. doi: 10.1001/jamaneurol.2015.0248
33. Streitberger KJ, Fehlner A, Pache F, Lacheta A, Papazoglou S, Bellmann-Strobl J, et al. Multifrequency magnetic resonance elastography of the brain reveals tissue degeneration in neuromyelitis optica spectrum disorder. *Eur Radiol.* (2017) 27:2206–15. doi: 10.1007/s00330-016-4561-6
34. Pache F, Zimmermann H, Finke C, Lacheta A, Papazoglu S, Kuchling J, et al. Brain parenchymal damage in neuromyelitis optica spectrum disorder - A multimodal MRI study. *Eur Radiol.* (2016) 26:4413–22. doi: 10.1007/s00330-016-4282-x
35. Pasquier B, Borisow N, Rasche L, Bellman-Strobl, Ruprecht K, Niendorf T, et al. Quantitative 7T MRI does not detect occult brain damage in neuromyelitis optica. *Neurol Neuroimmunol Neuroinflamm.* (2019) 6:e541. doi: 10.1212/NXI.0000000000000541
36. Wingerchuk DM, Banwell B, Bennett JL, Caire P, Carroll W, Chitnis T, et al. International consensus diagnostic criteria for neuromyelitis optica spectrum disorders. *Neurology.* (2015) 85:177–89. doi: 10.1212/WNL.0000000000001729
37. Schmidt P, Gaser C, Arsic M, Buck D, Förschler A, Berthele A, et al. An automated tool for detection of FLAIR- hyperintense white matter lesions in multiple sclerosis. *Neuroimage.* (2012) 59:3774–83. doi: 10.1016/j.neuroimage.2011.11.032
38. Yushkevich PA, Piven J, Hazlett HC, Smith G, Ho S, Gee J, et al. User guided 3D active contour segmentation of anatomical structures: significantly improved efficiency and reliability. *Neuroimmage.* (2006) 31:1116–28. doi: 10.1016/j.neuroimage.2006.01.015
39. Smith SM, Zhang Y, Jenkinson M, Chen J, Matthews PM, Federico A, et al. Accurate, robust, and automated longitudinal and cross-sectional brain change analysis. *Neuroimmage.* (2002) 17:479–89. doi: 10.1006/nimg.2002.1040
40. Patenaude B, Smith SM, Kennedy DN, Jenkinson M. A Bayesian model of shape and appearance for subcortical brain segmentation. *Neuroimmage.* (2011) 56:907–22. doi: 10.1016/j.neuroimage.2011.02.046
41. Behrens TE, Woolrich MW, Jenkinson M, Johansen H, Nunei R, Clare S, et al. Characterization and propagation of uncertainty in diffusion-weighted MR imaging. *Magn Reson Med.* (2003) 50:1077–88. doi: 10.1002/mrm.10609
42. Kuchling J, Backner Y, Oertel F, Raz N, Ruprecht K, Bellman-Strobl J, et al. Comparison of probabilistic tractography and tract based spatial statistics for assessing optic radiation damage in patients with autoimmune inflammatory disorders of the central nervous system. *Neuroimage Clin.* (2018) 19:538–50. doi: 10.1016/j.nicl.2018.05.004

43. Huak K, Zhang J, Wakana S, Jiang H, Li X, Reich D, et al. Tract probability maps in stereotaxic spaces: analysis of white matter anatomy and tract-specific quantification. *Neuroimmage.* (2008) 39:336–47. doi: 10.1016/j.neuroimage.2007.07.053
44. R Development Core Team. *R: A language and Environment for Statistical Computing*. Vienna (2015).
45. Hyun JW, Huh SY, Shin HJ, Woodhall M, Kim S, Irani S, et al. Evaluation of brain distribution criteria at disease onset in differentiating MS from NMOSD and MOG- IgG-associated encephalomyelitis. *Mult Scler.* (2018) 1:1352458518761186. doi: 10.1177/1352458518761186
46. Dos Passos GR, Oliveira LM, da Costa BK, Apostolus S, Callegaro D, Fujihara K, et al. MOG-IgG-associated optic neuritis, encephalitis and myelitis: lessons learned from neuromyelitis optica spectrum disorder. *Front Neurol.* (2018) 9:217. doi: 10.3389/fneur.2018.00217
47. Jurynzcyk M, Geraldes R, Probert F, Woodlhall M, Waters P, Tackley G, et al. Distinct brain imaging characteristics of autoantibody-mediated CNS conditions and multiple sclerosis. *Brain.* (2017) 140:617–27. doi: 10.1093/brain/aww350
48. Jurynzcyk M, Tackley G, Kong Y, Geraldes R, Matthews L, Woodhall M, et al. Brain lesion distribution criteria distinguish MS from AQP4-antibody NMOSD and MOG-antibody disease. *JNNP.* (2017) 88:132–6. doi: 10.1136/jnnp-2016-314005
49. Fan M, Fu Y, Su L, Suen Y, Wood K, Yang l, et al. Comparison of brain and spinal cord magnetic resonance imaging features in neuromyelitis optica spectrum disorders patients with or without aquaporin-4 antibody. *Mult Scler Relat Disord.* (2017) 13:58–66. doi: 10.1016/j.msard.2017.02.003
50. Waters P, Reindl M, Saiz A, Schandu K, Tuller V, Kral V, et al. Multicenter comparison of a diagnostic assay: aquaporin-4 antibodies in neuromyelitis optica. *J Neurol Neurosurg Psyychiatry.* (2016) 87:1005–15. doi: 10.1136/jnnp-2015-312601
51. Melamed E, Levy M, Waters PJ, Sato D, Bennett J, John G. Update on biomarkers in neuromyelitis optica. *Neurol Neuroimmunol Neuroinflamm.* (2015) 2:e134. doi: 10.1212/NXI.0000000000000134
52. Kitley J, Waters P, Woodhall M, Leite I, Murchison A, George J, et al. Neuromyelitis optica spectrum disorders with aquaporin-4 and myelin-oligodentrocyte glycoprotein antibodies. A comparative study. *JAMA Neurol.* (2014) 71:276–83. doi: 10.1001/jamaneurol.2013.5857
53. Sun SW, Liang HF, Schmidt R, Cross A, Song S. Selective vulnerability of cerebral white matter in a murine model of multiple sclerosis detected using diffusion tensor imaging. *Neurobiol Dis.* (2007) 28:30–8. doi: 10.1016/j.nbd.2007.06.011
54. Budde MD, Xie M, Cross AH, Song S. Axial diffusivity is the primary correlate of axonal injury in the experimental autoimmune encephalomyelitis spinal chord: a quantitative pixelwise analysis. *J Neurosci.* (2009) 29:2805–13. doi: 10.1523/JNEUROSCI.4605-08.2009
55. Kolbe S, Bajrazewski C, Chapman C, Nguyen T, Mitchell P, Paine M, et al. Diffusion tensor imaging of the optic radiations after optic neuritis. *Hum Brain Mapp.* (2012) 33:2047–61. doi: 10.1002/hbm.21343
56. Naismith RT, Xu J, Tutlam NT, Lancia S, Trinkaus K, Song S, et al. Diffusion tensor imaging in acute optic neuropathies: predictor of clinical outcomes. *Arch Neurol.* (2012) 69:65–71. doi: 10.1001/archneurol.2011.243
57. Aung WY, Mar S, Benzinger TL. Diffusion tensor MRI as a biomarker in axonal and myelin damage. *Imaging Med.* (2013) 5:427–40. doi: 10.2217/iim.13.49
58. Kolbe S, Chapman C, Nguyen T, Bajraszewski C, Johnston L, Kean M, et al. Optic nerve diffusion changes and atrophy jointly predict visual dysfunction after optic neuritis. *Neuroimage.* (2009) 45:679–86. doi: 10.1016/j.neuroimage.2008.12.047
59. Finke C, Heine J, Pache F, Lacheta A, Borisow N, Kuchling J, et al. Normal volumes and microstructural integrity of deep gray matter structures in AQP4+ NMOSD. *Neurol Neuroimmunol Neuroinflamm.* (2016) 3:e229. doi: 10.1212/NXI.0000000000000229
60. Vanikieti K, Poonyathalang P, Jindhara P, Ladeta A, Fujihara K, Prayoonvivat N, et al. Clinical characteristics and long-term visual outcome of optic neuritis in neuromyelitis optica spectrum disorder: a comparison between Thai and American- Caucasian cohort. *Mult Scler Relat Disord.* (2017) 17:87–91. doi: 10.1016/j.msard.2017.07.013
61. Hor J, Asgari N, Nakashima I, Broadley S, Leite I, Kissani N, et al. Epidemiology of neuromyelitis optica spectrum disorder and its prevalence and incidence worldwide. *Front Neurol.* (2020) 11:501. doi: 10.3389/fneur.2020.00501
62. Borisow N, Mori M, Kuwabara S, Scheel M, Paul F. Diagnosis and treatment of NMO spectrum disorder and MOG-Encephalomyelitis. *Front Neurol.* (2018) 9:888. doi: 10.3389/fneur.2018.00888

Conflict of Interest: FS served on the scientific advisory board of Novartis, received travel funding and/or speaker honoraria from Biogen Idec, Bayer Healthcare, Teva Pharmaceuticals and Sanofi-Aventis/Genzyme. JK received conference registration fees from Biogen and financial research support from Krankheitsbezogenes Kompetenznetzwerk Multiple Sklerose (KKNMS), not related to this work. JB-S received travel funding and speaking fees from Bayer Healthcare, Sanofi-Aventis/Genzyme, and Teva Pharmaceuticals. KR served on the scientific advisory board for Sanofi-Aventis/Genzyme, Novartis, and Roche; received travel funding and/or speaker honoraria from Bayer Healthcare, Biogen Idec, Merck Serono, Sanofi-Aventis/Genzyme, Teva Pharmaceuticals, Novartis, and Guthy Jackson Charitable Foundation; is an academic editor for PLoS ONE; receives publishing royalties from Elsevier; and received research support from Novartis and German Ministry of Education and Research. SA received travel funding from Celgene. AB served on the scientific advisory board for Biogen; received travel funding and/or speaker honoraria from Novartis and Biogen; has patents pending from method and system for optic nerve head shape quantification, perceptive visual computing based postural control analysis, multiple sclerosis biomarker, and perceptive sleep motion analysis; has consulted for Nexus and Motognosis; and received research support from Novartis Pharma, Biogen Idec, BMWi, BMBF, and Guthy Jackson Charitable Foundation. FP serves on the scientific advisory board for Novartis; received speaker honoraria and travel funding from Bayer, Novartis, Biogen Idec, Teva, Sanofi-Aventis/Genzyme, Merck Serono, Alexion, Chugai, MedImmune, and Shire; is an academic editor for PLoS ONE; is an associate editor for Neurology® Neuroimmunology & Neuroinflammation; consulted for SanofiGenzyme, Biogen Idec, MedImmune, Shire, and Alexion; and received research support from Bayer, Novartis, Biogen Idec, Teva, Sanofi-Aventis/Genzyme, Alexion, Merck Serono, German Research Council, Werth Stiftung of the City of Cologne, German Ministry of Education and Research, Arthur Arnstein Stiftung Berlin, EU FP7 Framework Program, Arthur Arnstein Foundation Berlin, Guthy Jackson Charitable Foundation, and National Multiple Sclerosis of the USA. MS holds a patent for manufacturing of phantoms for computed tomography imaging with 3D printing technology and received research support from Federal Ministry of Economics and Technology.

The remaining authors declare that the research was conducted in the absence of any commercial or financial relationships that could be construed as a potential conflict of interest.

The reviewer ML-P declared a past co-authorship with one of the authors FP to the handling editor.

frontiers in Neurology

ORIGINAL RESEARCH
published: 06 October 2020
doi: 10.3389/fneur.2020.529930

Brain Amyloid Burden and Resting-State Functional Connectivity in Late Middle-Aged Hispanics

*Mouna Tahmi[1], Brady Rippon[1], Priya Palta[1,2], Luisa Soto[1], Fernando Ceballos[1], Michelle Pardo[1], Greysi Sherwood[1], Gabriela Hernandez[1], Rodolfo Arevalo[1], Hengda He[3], Amirreza Sedaghat[3], Soroush Arabshahi[3], Jeanne Teresi[4], Herman Moreno[5,6], Adam M. Brickman[7,8,9], Qolamreza R. Razlighi[10] and José A. Luchsinger[1,2]**

[1] Department of Medicine, College of Physicians and Surgeons, Columbia University Irving Medical Center, New York, NY, United States, [2] Department of Epidemiology, Joseph P. Mailman School of Public Health, Columbia University Irving Medical Center, New York, NY, United States, [3] Department of Biomedical Engineering, Columbia University, New York, NY, United States, [4] Research Division, Hebrew Home in Riverdale, Bronx, NY, United States, [5] Departments of Neurology and Physiology/Pharmacology, The Robert F. Furchgott Center for Neural and Behavioral Science, SUNY Downstate Medical Center, New York, NY, United States, [6] Kings County Hospital Neurology, New York, NY, United States, [7] Department of Neurology, College of Physicians and Surgeons, Columbia University Irving Medical Center, New York, NY, United States, [8] Taub Institute for Research on Alzheimer's Disease and the Aging Brain, Columbia University Irving Medical Center, New York, NY, United States, [9] Gertrude H. Sergievsky Center, Columbia University Irving Medical Center, New York, NY, United States, [10] Department of Radiology, Weill Cornell Medicine, New York, NY, United States

OPEN ACCESS

Edited by:
Peter Sörös,
University of Oldenburg, Germany

Reviewed by:
Silvia Tommasin,
Sapienza University of Rome, Italy
Paul Gerson Unschuld,
University of Zurich, Switzerland

***Correspondence:**
José A. Luchsinger
jal94@cumc.columbia.edu

Specialty section:
This article was submitted to Applied Neuroimaging, a section of the journal Frontiers in Neurology

Received: 27 January 2020
Accepted: 02 September 2020
Published: 06 October 2020

Citation:
Tahmi M, Rippon B, Palta P, Soto L, Ceballos F, Pardo M, Sherwood G, Hernandez G, Arevalo R, He H, Sedaghat A, Arabshahi S, Teresi J, Moreno H, Brickman AM, Razlighi QR and Luchsinger JA (2020) Brain Amyloid Burden and Resting-State Functional Connectivity in Late Middle-Aged Hispanics. Front. Neurol. 11:529930. doi: 10.3389/fneur.2020.529930

Non-linear relations of brain amyloid beta (Aβ) with task- based functional connectivity (tbFC) measured with functional magnetic resonance imaging (fMRI) have been reported in late middle age. Our objective was to examine the association between brain Aβ and resting-state functional connectivity (rsFC) in late middle-aged adults. Global brain Aβ burden was ascertained with ^{18}F-Florbetaben Positron Emission Tomography (PET); rsFC was ascertained on 3T Magnetic Resonance Imaging (MRI) among 333 late middle-aged Hispanics adults without dementia in four major brain functional connectivity networks: default mode network (DMN), fronto-parietal control network (FPC), salience network (SAL) and dorsal attention network (DAN). We examined the relationship of global brain Aβ with rsFC using multivariable linear regression adjusted for age, sex, education, and APOE-ε4 genotype. We quantified the non-linear associations both with quadratic terms and by categorizing Aβ into three groups: low Aβ, intermediate Aβ, and positive Aβ. We found no significant linear or non-linear associations between Aβ, measured either continuously or categorically, with rsFC in the examined networks. Our null findings may be explained by the younger age of our participants in whom amyloid burden is relatively low. It is also possible that the recently reported non-linear relationship is exclusive to task fMRI and not rsfMRI.

Keywords: Alzheimer's disease, amyloid beta, RsfMRI, fMRI, functional connectivity, middle-age, hispanic

INTRODUCTION

The deposition of amyloid beta (Aβ) in the brain starts decades before it impacts cognition (1). The effects of Aβ on brain function using resting-state functional connectivity (rsFC) magnetic reasoning imaging (fMRI) have been largely studied in cognitively normal older adults and have yielded conflicting findings with both positive and negative linear relationships reported for Aβ levels and functional connectivity (2–6). Similar results of hyperactivation and hypoactivation in association with brain Aβ are also observed with task activation (7–10). To address these mixed results, a recent study of 62 middle-aged and older adults (mean age: 67.73 years) reported a non-linear quadratic association between levels of Aβ and task-based functional connectivity (tbFC), such that intermediate levels of Aβ are associated with higher activation in regions of the default mode network (DMN), but high levels of Aβ are associated with lower activation (11). Another study from the same group ($n = 68$, mean age: 68.59) replicated these findings using a different functional task paradigm, suggesting that this non-linear relationship between Aβ and FC is task-independent (12). If replicated in rsFC, such a finding would provide evidence for the hypothesis that the brain dose-dependent response to levels of Aβ may also be apparent at rest when no task is performed (12).

Our primary goal in this study was to determine if the non-linear association of Aβ with functional connectivity, recently observed in tbFC, is also present at rest using fMRI in late middle-age, a critical period for the deposition of Aβ (13). Thus, we examined the association of global brain Aβ burden with rsFC among 333 late middle-aged Hispanic adults without dementia in four major cognitive networks: default mode network (DMN), fronto-parietal control network (FPC), dorsal attention network (DAN), and salience network (SAL).

MATERIALS AND METHODS

Participants

This was a cross-sectional analysis of a community-based cohort of 333 late middle-aged Hispanic adults without dementia and with functional connectivity data out of 350 recruited between 03/01/2016 and 07/31/2019 in New York City as part of a study of Alzheimer's disease biomarkers (14). We targeted Hispanics because they are the most common ethnic group in the community surrounding CUIMC (15) and because there is a paucity of AD biomarkers studies in Non-Whites (13). Inclusion criteria included ages between 55 and 69 years, men and women, able to undergo phlebotomy, clinical and neuropsychological assessments, 3T brain magnetic resonance imaging (MRI), and Positron Emission Tomography (PET) with the Aβ radioligand ^{18}F-Florbetaben. Exclusion criteria included dementia diagnosis, cancer other than non-melanoma skin cancer, and MRI contraindications. We screened 659 potential participants; 114 (17.30%) declined to participate, 178 (27.01%) were ineligible, 16 (2.43%) did not complete study procedures; 17 participants (2.58%) were excluded due to incomplete fMRI data and one additional participant (0.15%) was excluded from analyses due to incomplete data on APOE genotype, the most important predictor of *in-vivo* brain amyloid burden (16) (**Figure 1**). The interval between amyloid PET and MRI was 15.79 ± 33.41 days. The Institutional Review Board and the Joint Radiation Safety Commission at CUIMC approved this study. Participants provided written informed consent. Funding sources had no role in study design, data collection, data analyses or interpretation.

Exposure: Global Brain Aβ

Our main exposure of interest was global brain Aβ ascertained with ^{18}F-Florbetaben positron emission tomography (PET). The dose of ^{18}F-Florbetaben was 300 MBq (8.1 mCi), maximum 30 mcg mass dose, administered as a single slow intravenous bolus. Images were acquired over 20 min starting 90 min after injection. Dynamic PET frames (4 scans) were aligned to the first frame using rigid-body registration and a static PET image was obtained by averaging the four registered frames. Additional information on the Aβ PET scan processing protocol has been previously published (17). The standardized uptake value (SUV), defined as the decay-corrected brain radioactivity concentration normalized for injected dose and body weight, was calculated in all regions and each voxel, which subsequently normalized to the SUV in cerebellar gray matter to derive the regional and voxel-wise SUVR. We used a standard approach to calculating global Aβ burden using Alzheimer's Disease Neuroimaging Initiative (ADNI) defined regions of interests (ROIs) to generate four lobar SUVRs (frontal, temporal, cingulate and parietal cortex) (18). We then averaged them to compute an overall mean value of global cortical Aβ. Aβ measures were examined both continuously and categorically. We examined the non-linear association of Aβ measured continuously by incorporating quadratic terms in the model. The threshold for dichotomization into Aβ positive and negative groups was 1.342 and was derived using the K-means clustering method. To classify two groups, the K-means clustering algorithm starts by identifying two Aβ SUVR values from our data at random and subsequently assigns all other observations to the group with the closest mean Aβ SUVR. Once this process has been completed for all observations, it continues to reiterate, checking if observations should be reclassified to the other cluster, until all group assignments are stable. The final classifications should minimize each within-cluster variance, equivalent to the sum of the squared Euclidean distance between each Aβ SUVR value and its within-cluster mean (19). Values under this resulting threshold (SUVR = 1.342) were further dichotomized as intermediate and low using a median split (SUVR = 1.126).

Outcome: Resting-State Functional Connectivity

Resting-state scans were collected on a 3T GE scanner during 10 min of resting state protocol where participants were instructed to lie still, keep their eyes open, and to not think about anything in particular. T1-weighted images of the whole brain were acquired for each participant with a magnetization prepared rapid gradient-echo sequence (Time of Inversion (TI) = 450 ms; Flip angle (FA) =12 degree; Field of view (FOV) = 25.6 × 25.6 cm; Matrix size = 256 × 256). Ten minutes of rsfMRI

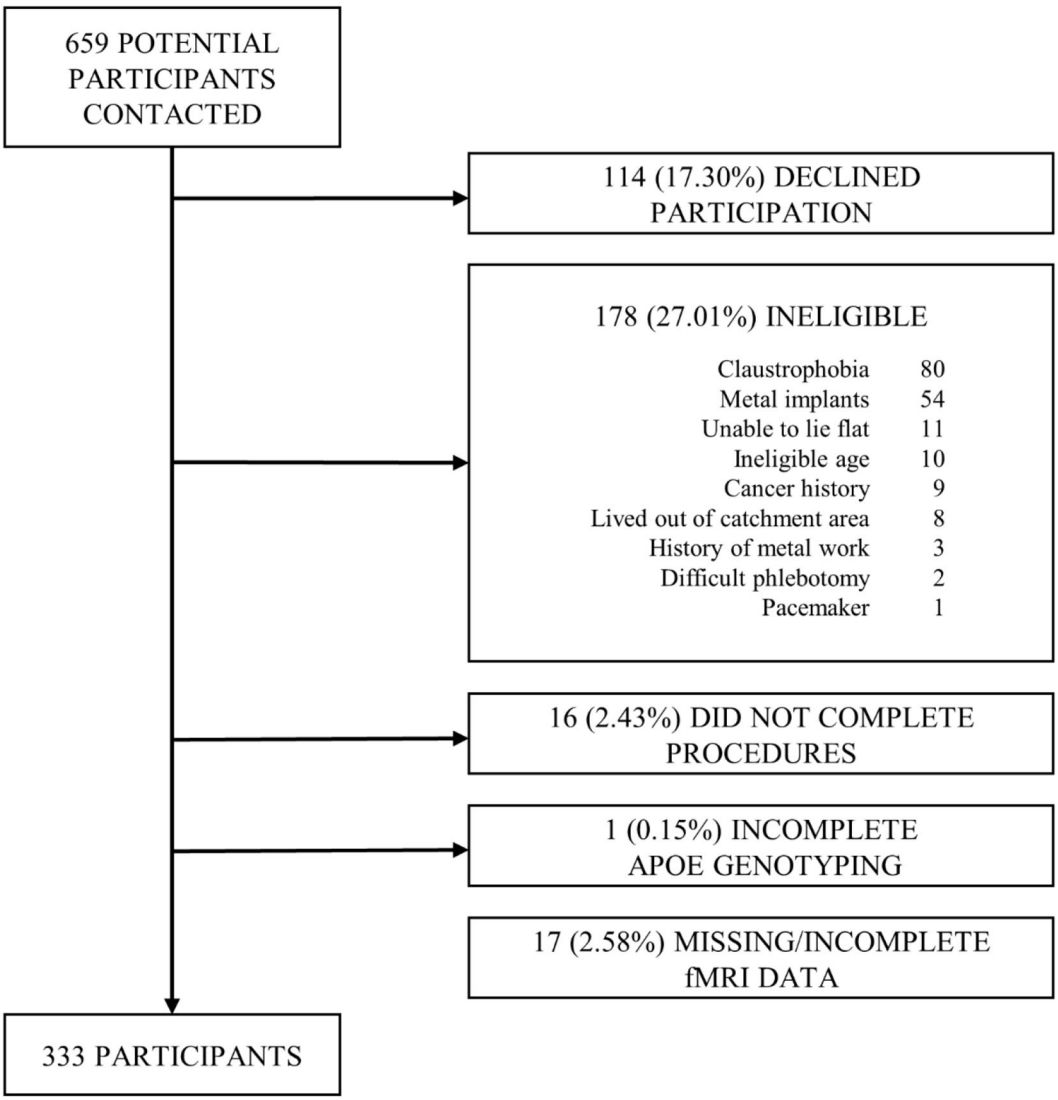

FIGURE 1 | Flow chart of participant recruitment.

scans were collected with GRE-EPI sequence using the following parameters: TR/TE = 2,000/23 ms; FOV =19.2 × 19.2 cm; FA = 77 degree; matrix size = 96 × 96; slice thickness/gap = 3/0 mm; number of slices = 40.

fMRI Data Processing

Images were preprocessed using an in-house developed native space method (20). Briefly, "slice timing correction was done using the FSL slice timing tool (21). We then used *mcflirt* (a motion correction tool available in the FSL package) to register all volumes to a reference image (21, 22). The reference image was generated by registering (6 df, 256 bins mutual information, and *Sinc* interpolation) all volumes to the middle volume and averaging them. We then used the method described in Power et al. (23) to calculate frame-wise displacement (FWD) from the six motion parameters and root mean square difference (RMSD) of the realigned fMRI signal in the consecutive volumes for each subject. To be conservative, we lowered the threshold of our RMSD to 0.3% (it was originally suggested to be 0.5%). RMSD was computed on the motion-corrected volumes before temporal filtering. The contaminated volumes were detected by the criteria FWD > 0.5 mm or RMSD > 0.3%. Identified contaminated volumes were replaced with new volumes generated by linear interpolation of adjacent volumes. Volume replacement was done before band-pass filtering (24). The motion-corrected signals were passed through a band-pass filter with the cutoff frequencies of 0.01 and 0.09 Hz. We used *flsmaths– bptf* to do the filtering in this study (22). Finally, we residualized the motion-corrected, scrubbed, and temporally filtered volumes by regressing out the FWD, RMSD, left and right hemisphere white matter, and lateral ventricular signals (25)."

TABLE 1 | Characteristics of the entire sample and by amyloid β (Aβ) category.

	Total sample ($n = 333$)	Low Aβ ($n = 154$)	Intermediate Aβ ($n = 153$)	Positive Aβ ($n = 26$)	*P*-value[a]
Age, mean (SD), y	64.14 (3.37)	63.76 (3.54)	64.40 (3.19)	64.83 (3.27)	0.14
Sex, Women, *N* (%)	237 (71.17)	86 (55.84)	132 (28.27)	19 (73.08)	<0.0001
Education, mean (SD), y	10.51 (3.95)	10.48 (3.77)	10.34 (4.15)	11.62 (3.80)	0.31
Ethnicity, *N* (%)					0.76
Dominican	286 (85.88)	132 (85.71)	134 (87.58)	20 (76.92)	
Other Caribbean Hispanic	20 (6.0)	9 (5.84)	8 (5.23)	3 (11.54)	
South American	17 (5.10)	9 (5.84)	6 (3.92)	2 (7.69)	
Central American	4 (1.20)	1 (0.65)	3 (1.96)	0 (0)	
Unspecified Hispanic	3 (0.90)	2 (1.30)	1 (0.65)	6 (23.08)	
Spanish speakers, *N* (%)	312 (93.69)	144 (93.51)	144 (94.12)	24 (92.31)	0.93
APOE-ε4 carriers, *N* (%)[a]	117 (35.13)	40 (25.97)	56 (36.60)	21(80.77)	<0.0001

SD, standard deviation; Aβ, Amyloid beta.

[a]*Bivariate comparisons across Aβ categories were made using analysis of variance (ANOVA) for continuous variables. Differences in categorical variables were evaluated using chi-squared tests.*

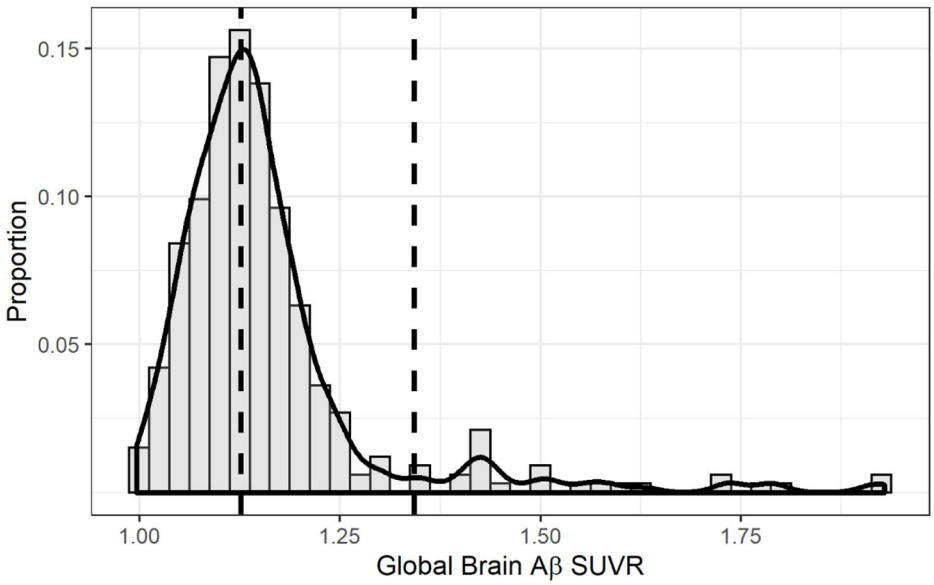

FIGURE 2 | Distribution of global brain amyloid SUVR. The solid line overlaid onto the histogram represents a non-parametric kernel density estimation. The right vertical dashed line marks the threshold for amyloid positivity using the k-means clustering method (1.342) while the left vertical line marks the threshold for intermediate amyloid (1.126).

T1-weighted image segmentation was performed with FreeSurfer (http://surfer.nmr.mgh.harvard.edu/) (26–28) and inspected visually for any inaccuracies. Using the state of the art non-linear registration method, advanced normalization tools (ANTs), we transferred the 264 putative functional coordinates derived from a brainwide graph described by Power et al. (29) from MNI space to subjects' native space. A conjunction mask was obtained as an intersection of a 10 mm radius spherical mask, centered at each coordinate and the native space gray-matter mask. This conjunction mask was used to compute the time-series for each coordinate by averaging the time-series of all voxels that fall within the conjunction mask. To prevent inflation of within-network functional connectivity (correlation), we also averaged all coordinates that fell within each node of the networks. For instance, all the DMN coordinates that were closely located in the left/right angular gyrus and inferior parietal regions were averaged to obtain a single time-series for left/right angular gyrus node of the DMN. This resulted in 53 separate nodes representing all the networks reported in Power et al. (29). The averaged functional time-series of each of the 53 regions were used to compute a correlation matrix for each participant preprocessed rsfMRI scan. Then, the correlations were Fisher z-transformed to generate normalized correlation matrices for each subject. In order to remove correlations between an area

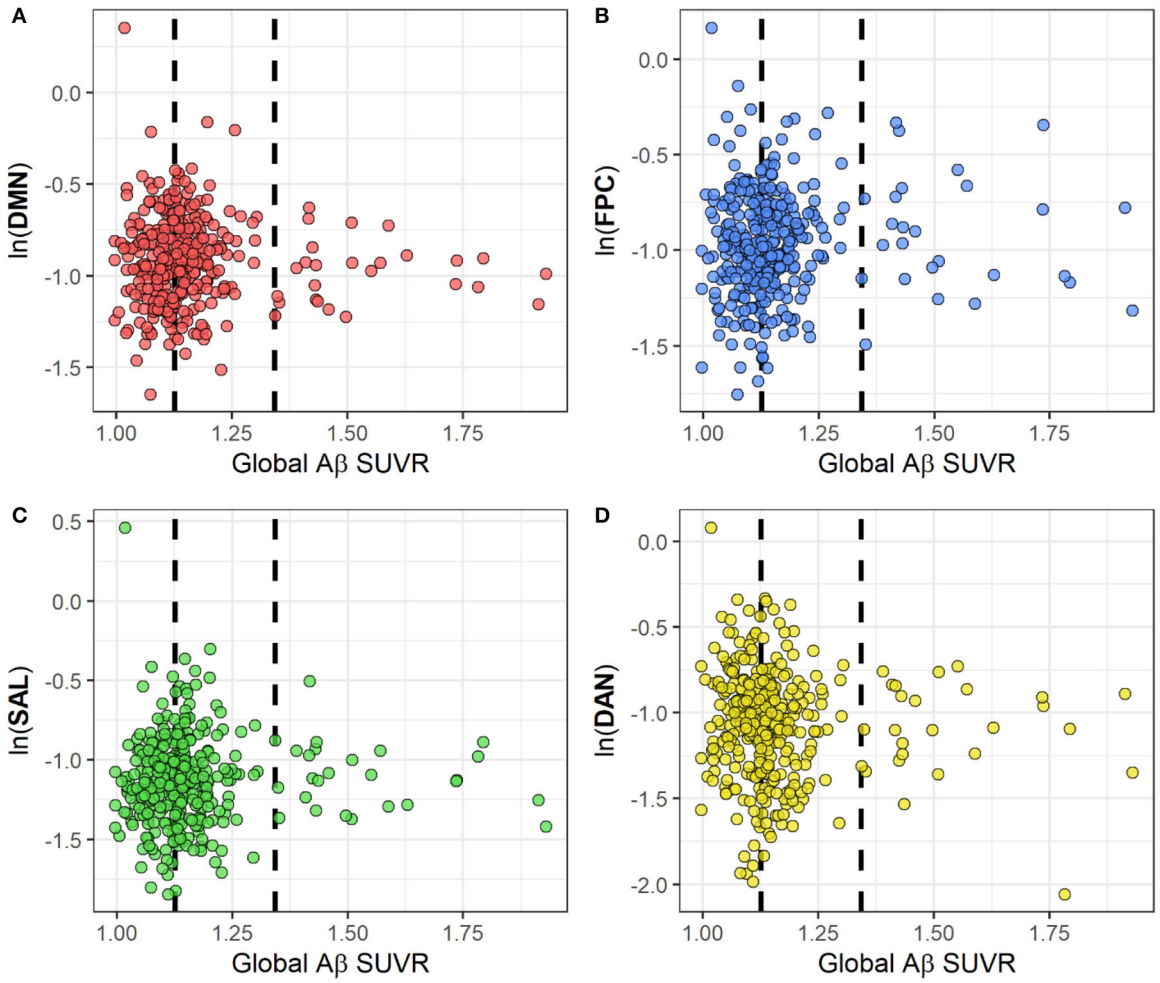

FIGURE 3 | Scatterplots for the association between rsFC and global Aβ SUVRs in four cognitive networks: DMN **(A)**, FPC **(B)**, SAL **(C)** and DAN **(D)**. RsFC for each network has been log-transformed. The two dashed lines represent Aβ thresholds between low and intermediate (SUVR = 1.126) and between intermediate and positive (SUVR = 1.342) categories.?Abbreviations: Ln, natural logarithm; Aβ, amyloid beta; SUVR, Standardized Uptake Value Ratio; rsFC, resting state functional connectivity; DMN, default mode network; FPC, fronto-parietal control; DAN, dorsal attention network; SAL, salience.

and itself, the diagonal of each correlation matrix was set to zero. Regions of interest (ROIs) were labeled based on their network assignment according to Power et al. (29) and within network functional connectivity was computed by averaging the inter-nodal correlation within each network. Four networks were preselected for statistical analysis based on their role on cognitive processes: default mode network (DMN; 9 nodes), salience network (SAL; 9 nodes), fronto-parietal control network (FPC; 9 nodes), and dorsal attention network (DAN; 6 nodes). For details on the location of each node within each network, see **Supplemental Table 1.**

Neuropsychological and Behavioral Assessment

All participants were administered a neuropsychological assessment that included tests of memory, language, visuospatial abilities, and processing speed. A Spanish version of the neuropsychological test battery was used for Spanish-speaking participants (30). The following tests were included: the Buschke Selective reminding Tests (SRT) and its components, including total recall, delayed recall, and delayed recognition (31); the Boston Naming-15 item Test (32); letter fluency; category fluency; the similarities subtest from the Wechsler Adult Intelligence Scale-Revised (33); the repetition and comprehension subtests of the Boston Diagnostic Aphasia Evaluation (34); the recognition and matching components of the Benton Visual Retention Test (35); the Rosen Drawing Test (36); the identities and oddities subtest from the Mattis Dementia Rating Scale (37); Color Trails 1 and 2 (38). To aggregate the neuropsychological test data, we performed a Principal Component Analysis (PCA). PCA is a statistical method most commonly used for data reduction on a set of collinear variables, where each principle component is a linear combination of the centered loading variables (in this case,

TABLE 2 | Coefficients and *p*-values from linear regression for linear and quadratic term of Aβ (SUVR) on rsFC.

	Aβ (SUVR) linear term		Aβ (SUVR) quadratic term	
	β (CI)	*P*	β (CI)	*P*
Model 1				
LnDMN	0.93 (−1.00, 2.85)	0.35	−0.37 (−1.07, 0.34)	0.31
LnFPC	−1.46 (−0.77, 3.69)	0.20	−0.49 (−1.31, 0.33)	0.24
LnDAN	−0.95 (−3.50, 1.60)	0.46	0.28 (−0.66, 1.22)	0.55
LnSAL	1.35 (−0.87, 3.57)	0.23	−0.48 (−1.30, 0.33)	0.25
Model 2				
LnDMN	0.25 (−1.72, 2.22)	0.80	−0.13 (−0.85, 0.59)	0.72
LnFPC	0.88 (−1.41, 3.17)	0.45	−0.30 (−1.13, 0.54)	0.48
LnDAN	−0.37 (−3.02, 2.27)	0.78	0.10 (−0.87, 1.06)	0.84
LnSAL	1.15 (−1.11, 3.41)	0.32	−0.39 (−1.21, 0.35)	0.36

Ln, natural logarithm; Aβ, amyloid beta; SUVR, Standardized Uptake Value Ratio; rsFC, resting state functional connectivity; DMN, default mode network; FPC, fronto- parietal control; DAN, dorsal attention network; SAL, salience.
Model 1 is unadjusted. Model 2 is adjusted for age, sex, education and APOE-ε4.

our neuropsychological test scores) such that the variance of these variables is maximized (39). Each principle component is independent and captures a proportion of the variance in the neuropsychological tests, meaning that 15 principle components would completely capture the variance in our 15 tests. We chose to only retain the first principle component for our analysis as it captured much more variance in our tests than any other component. Additionally, the difference in the variance captured by all other principle components was not appreciable by visual inspection of the scree plot of our components (**Supplemental Figure 1**).

Covariates

Characteristics considered as potential covariates included age, sex, education, and APOE-ε4 genotype. We controlled for age, sex and education due to their known effects on functional connectivity (40, 41). We controlled for APOE-ε4 genotyping because it is a strong determinant of Aβ burden (42). Participants were classified as APOE-ε4 carriers if they were homozygous or heterozygous for APOE-ε4. APOE-ε4 genotyping was conducted by LGC genomics (Beverly, MA) using single nucleotide polymorphisms rs429358 and rs7412.

Statistical Analysis

RsFC values in the four networks examined were right-skewed and required logarithmic transformation to approximate a normal distribution. Bivariate comparisons across Aβ categories were made using analysis of variance (ANOVA) for continuous variables. Differences in categorical variables were evaluated using chi-squared tests. The relationship between global brain Aβ SUVR and rsFC was evaluated with a multivariable linear regression model including continuous Aβ SUVR and squared terms for Aβ SUVR, adjusted for age, sex, education, and APOE-ε4 carrier status. The relationship of Aβ categories (low, intermediate, and positive) with rsFC was examined with linear regression models adjusted for age, sex, education, and APOE-ε4 carrier status. The statistical significance was defined as $p < 0.05$. All statistical analyses were performed using the Statistical Package for the Social Sciences (SPSS) 26 (SPSS, Chicago, IL) and R version 3.6.0.

Sensitivity Analyses

As a sensitivity analysis, we examined the association of Aβ with rsFC among participants who were cognitively normal only. Cognitive impairment was defined according to cutoffs of 1.0 or 1.5 standard deviations below the first principal component of the neuropsychological battery of our sample (43). The rationale for conducting sensitivity analyses restricted to cognitively normal participants was to replicate prior studies, which exclusively examined these associations among cognitively normal participants (11, 12). We validated our assumption that the first principle component of the neuropsychological battery is an appropriate approximation of global cognition by verifying that better performance on all neuropsychological evaluations was significantly positively correlated with increases in this principle component.

RESULTS

Table 1 shows the characteristics of the total sample and across Aβ categories (low, intermediate, positive). The sample consisted of 237 women and 96 men, who had a mean age of 64.14 ± 3.37 years and 10.51 ± 3.95 years of education. There were no significant differences across Aβ groups with respect to age and education. There was a higher proportion of women among the intermediate and positive Aβ categories. As expected, compared to participants without the APOE-ε4 allele, APOE-ε4 carriers had higher odds of being in the intermediate or positive category as compared to the low Aβ category (**Table 1**, **Supplemental Figure 2**). **Figure 2** shows the distribution of global Aβ SUVR in the sample. As expected, Aβ SUVR had a bimodal distribution and the first peak resembled a normal distribution.

Figure 3 represents scatter plots for the association between rsFC in the four networks and global Aβ SUVR. We observed no linear or quadratic association between Aβ and rsFC in the four networks, including the DMN. Results for adjusted and unadjusted associations with continuous Aβ (SUVR) and rsFC are reported in **Table 2**. In **Table 3**, we report associations between dichotomized Aβ categories and rsFC. Results were similar in sensitivity analyses restricted to participants who were cognitively normal only based either on 1.5 ($n = 318$) or 1.0 SD ($n = 291$) below the first PCA of the sample neuropsychological performance.

DISCUSSION

Our goal in the current study was to test if the recent evidence of a dose-dependent relationship between Aβ and tbFC in regions of the DMN (11, 12) are also present at rest. We found that there is no association between Aβ burden and rsFC.

TABLE 3 | Association between Aβ categories (low, intermediate and positive) and rsFC using linear regressions.

	Low to intermediate Aβ		Low to positive Aβ		Intermediate to positive Aβ		*P*-trend
	β (CI)	P	β (CI)	P	β (CI)	P	
Model 1							
LnDMN	0.04 (−0.01, 0.10)	0.13	−0.05 (−0.15, 0.05)	0.36	−0.09 (−0.19, 0.01)	0.08	0.12
LnFPC	0.03 (−0.03, 0.10)	0.27	0.07 (−0.04, 0.19)	0.21	0.04 (−0.08, 0.16)	0.51	0.33
LnDAN	−0.05 (−0.12, 0.02)	0.19	−0.07 (−0.20, 0.07)	0.32	−0.02 (−0.15, 0.11)	0.78	0.34
LnSAL	0.04 (−0.02, 0.10)	0.20	0.05 (−0.07, 0.16)	0.42	0.007 (−0.11, 0.12)	0.91	0.40
Model 2							
LnDMN	0.02 (−0.04, 0.07)	0.57	−0.05 (−0.16, 0.05)	0.31	−0.07 (−0.17, 0.03)	0.18	0.39
LnFPC	0.01 (−0.05, 0.08)	0.69	0.05 (−0.07, 0.18)	0.40	0.04 (−0.08, 0.05)	0.69	0.69
LnDAN	−0.02 (−0.10, 0.05)	0.54	−0.03 (−0.18, 0.11)	0.64	−0.01 (−0.15, 0.13)	0.89	0.79
LnSAL	0.04 (−0.03, 0.10)	0.29	0.09 (−0.03, 0.21)	0.15	0.05 (−0.06, 0.17)	0.37	0.29

Ln, natural logarithm; Aβ, amyloid beta; SUVR, Standardized Uptake Value Ratio; rsFC, resting state functional connectivity; DMN, default mode network; FPC, fronto- parietal control; DAN, dorsal attention network; SAL, salience.
Model 1 is unadjusted. Model 2 is adjusted for age, sex, education and APOE-ε4.

In a study of 62 middle-aged and older adults (mean age=67.73 years), Foster et al. (11) reported that the association between Aβ SUVR and tbFC is quadratic with both hyperactivation and hypoactivation phases in regions of the DMN. These findings were further replicated by the same group using a different functional task paradigm ($n = 68$, mean age: 68.59), suggesting that this non-linear relationship is task independent (12). However, the question on whether this observed association between Aβ and functional connectivity is actually present at rest remains unanswered. The results from our large sample of 333 found no linear or non-linear association between global brain Aβ and functional connectivity in major cognitive networks, including DMN, measured at rest.

There are several possible explanations of our findings. First, it is possible that the reported non-linear association by Foster et al. with task fMRI (11, 12), although independent of the type of task performed, may be dependent on the action of performing a task in general and therefore not an intrinsic effect apparent at rest. The fact that this was observed using different task paradigms does not entirely confirm its task independency. Alternatively, it is possible that the relatively younger age group of our sample is at its initial stages of Aβ accumulation which has not yet affected rsFC. Most of the reported studies on Aβ and rsFC were done in older adults and still yielded different results between a positive and negative associations (2–6). A null association with static rsFC, as was observed in our study, was also reported in a community-based cohort of 133 adults with a mean age of 72 years (44). A follow-up of our cohort will allow for more time for Aβ accumulation, at which point an effect on rsFC may be detected. Finally both Aβ and tau accumulation may be required for the non-linear effects when it comes to the resting brain which has been recently reported in cognitively normal older adults (45). We cannot address the effects of tau in our data. However, we are currently collecting tau PET data in this sample, which will allow us to investigate the interactive roles of tau and Aβ on functional connectivity in future analyses.

Strengths of our study include the relatively large sample of late middle-aged Hispanic adults within a relatively narrow age range, which addresses a gap in studies in late middle age and in ethnic minorities. The main limitation of our study is its cross-sectional design, which limits our ability to infer causality from our findings. It is also possible that our findings are not generalizable to other ethnic groups. However, we could also argue that our findings may be generalized to other ethnics groups since APOE-ε4 in our sample was associated with higher amyloid burden as reported in most Non-Hispanic White samples (46).

In conclusion, we found that no association between brain Aβ burden and rsFC in our cohort of late middle-aged Hispanics without dementia. Continued follow-up of the same cohort is needed to examine future effects of Aβ accumulation on brain functional networks.

DATA AVAILABILITY STATEMENT

The datasets generated for this study are available on request to the corresponding author.

ETHICS STATEMENT

The studies involving human participants were reviewed and approved by the Institutional Review Board at Columbia University Irving Medical Center. The patients/participants provided their written informed consent to participate in this study.

AUTHOR CONTRIBUTIONS

MT conducted statistical analyses, and drafted the initial manuscript. BR performed data curation, advised on data interpretation, and manuscript review. PP advised on data interpretation and manuscript review. LS, FC, MP, GS, GH,

and RA assisted with data collection. HH conducted the PET data processing. AS conducted the fMRI data processing. SA helped with fMRI data processing. JT, HM, and AB advised on data interpretation and manuscript review. QR advised on fMRI/PET data analyses and manuscript review. JL advised on data interpretation and manuscript review and supervised the project. All authors contributed to the article and approved the submitted version.

FUNDING

Support for the reported work was provided by United States National Institutes of Health Grant Nos. R01AG050440, RF1AG051556, and RF1AG051556-01S2. Partial support was also provided by Grant Nos. K24AG045334, P30AG059303, and ULT1TR001873. PP is supported by Grant No. R00 AG052830 from the National Institute of Aging. The views expressed in this manuscript are those of the authors and do not necessarily represent the views of the National Institute of Aging; the National Institutes of Health; or the U.S. Department of Health and Human Services.

SUPPLEMENTARY MATERIAL

The Supplementary Material for this article can be found online at: https://www.frontiersin.org/articles/10.3389/fneur.2020.529930/full#supplementary-material

REFERENCES

1. Gonneaud J, Arenaza-Urquijo EM, Mezenge F, Landeau B, Gaubert M, Bejanin A, et al. Increased florbetapir binding in the temporal neocortex from age 20 to 60 years. *Neurology.* (2017) 89:2438–46. doi: 10.1212/WNL.0000000000004733
2. Hedden T, Van Dijk KR, Becker JA, Mehta A, Sperling RA, Johnson KA, et al. Disruption of functional connectivity in clinically normal older adults harboring amyloid burden. *J Neurosci.* (2009) 29:12686–94. doi: 10.1523/JNEUROSCI.3189-09.2009
3. Sheline YI, Raichle ME, Snyder AZ, Morris JC, Head D, Wang S, et al. Amyloid plaques disrupt resting state default mode network connectivity in cognitively normal elderly. *Biol Psychiatry.* (2010) 67:584–7. doi: 10.1016/j.biopsych.2009.08.024
4. Wang L, Brier MR, Snyder AZ, Thomas JB, Fagan AM, Xiong C, et al. Cerebrospinal fluid Abeta42, phosphorylated Tau181, and resting-state functional connectivity. *JAMA Neurol.* (2013) 70:1242–8. doi: 10.1001/jamaneurol.2013.3253
5. Lim HK, Nebes R, Snitz B, Cohen A, Mathis C, Price J, et al. Regional amyloid burden and intrinsic connectivity networks in cognitively normal elderly subjects. *Brain.* (2014) 137:3327–38. doi: 10.1093/brain/awu271
6. Mormino EC, Smiljic A, Hayenga AO, Onami SH, Greicius MD, Rabinovici GD, et al. Relationships between beta-amyloid and functional connectivity in different components of the default mode network in aging. *Cereb Cortex.* (2011) 21:2399–407. doi: 10.1093/cercor/bhr025
7. Sperling RA, Dickerson BC, Pihlajamaki M, Vannini P, LaViolette PS, Vitolo OV, et al. Functional alterations in memory networks in early alzheimer's disease. *Neuromolecular Med.* (2010) 12:27–43. doi: 10.1007/s12017-009-8109-7
8. Sperling R. Potential of functional MRI as a biomarker in early alzheimer's disease. *Neurobiol Aging.* (2011) 32 Suppl 1:S37–43. doi: 10.1016/j.neurobiolaging.2011.09.009
9. Kennedy KM, Rodrigue KM, Devous MD, Sr., Hebrank AC, Bischof GN, et al. Effects of beta-amyloid accumulation on neural function during encoding across the adult lifespan. *Neuroimage.* (2012) 62:1–8. doi: 10.1016/j.neuroimage.2012.03.077
10. Oh H, Steffener J, Razlighi QR, Habeck C, Stern Y. beta-amyloid deposition is associated with decreased right prefrontal activation during task switching among cognitively normal elderly. *J Neurosci.* (2016) 36:1962–70. doi: 10.1523/JNEUROSCI.3266-15.2016
11. Foster CM, Kennedy KM, Horn MM, Hoagey DA, Rodrigue KM. Both hyper- and hypo-activation to cognitive challenge are associated with increased beta-amyloid deposition in healthy aging: a nonlinear effect. *Neuroimage.* (2018) 166:285–92. doi: 10.1016/j.neuroimage.2017.10.068
12. Kennedy KM, Foster CM, Rodrigue KM. Increasing beta-amyloid deposition in cognitively healthy aging predicts nonlinear change in bold modulation to difficulty. *Neuroimage.* (2018) 183:142–9. doi: 10.1016/j.neuroimage.2018.08.017
13. Jack CR, Jr., Knopman DS, Jagust WJ, Petersen RC, Weiner MW, et al. Tracking pathophysiological processes in alzheimer's disease: an updated hypothetical model of dynamic biomarkers. *Lancet Neurol.* (2013) 12:207–16. doi: 10.1016/S1474-4422(12)70291-0
14. Luchsinger JA, Palta P, Rippon B, Sherwood G, Soto L, Ceballos F, et al. Pre-Diabetes, but not type 2 diabetes, is related to brain amyloid in late middle-age. *J Alzheimers Dis.* (2020) 75:1241–52. doi: 10.3233/JAD-200232
15. Luchsinger JA, Cabral R, Eimicke JP, Manly JJ, Teresi J. glycemia, diabetes status, and cognition in hispanic adults aged 55-64 years. *Psychosom Med.* (2015) 77:653–63. doi: 10.1097/PSY.0000000000000208
16. Ossenkoppele R, Jansen WJ, Rabinovici GD, Knol DL, van der Flier WM, van Berckel BNM, et al. Prevalence of amyloid PET positivity in dementia syndromes: a meta-analysis. *JAMA.* (2015) 313:1939–49. doi: 10.1001/jama.2015.4669
17. Tahmi M, Bou-Zeid W, Razlighi QR. A fully automatic technique for precise localization and quantification of amyloid-beta PET scans. *J Nucl Med.* (2019) 60:1771–9. doi: 10.2967/jnumed.119.228510
18. Landau SM, Horng A, Fero A, Jagust WJ, Alzheimer's Disease Neuroimaging I. Amyloid negativity in patients with clinically diagnosed alzheimer disease and MCI. *Neurology.* (2016) 86:1377–85. doi: 10.1212/WNL.0000000000002576
19. MacQueen J, editor. Some methods for classification and analysis of multivariate observations. In: *Proceedings of the Fifth Berkeley Symposium on Mathematical Statistics and Probability,* Vol. 1: Statistics (1967). Berkeley, CA: University of California Press.
20. Razlighi QR, Habeck C, Steffener J, Gazes Y, Zahodne LB, Mackay-Brandt A, et al. Unilateral disruptions in the default network with aging in native space. *Brain Behav.* (2014) 4:143–57. doi: 10.1002/brb3.202
21. Jenkinson M, Beckmann CF, Behrens TE, Woolrich MW, Smith SM. Fsl. *Neuroimage.* (2012) 62:782–90. doi: 10.1016/j.neuroimage.2011.09.015
22. Jenkinson M, Bannister P, Brady M, Smith S. Improved optimization for the robust and accurate linear registration and motion correction of brain images. *Neuroimage.* (2002) 17:825–41. doi: 10.1006/nimg.2002.1132
23. Power JD, Barnes KA, Snyder AZ, Schlaggar BL, Petersen SE. Spurious but systematic correlations in functional connectivity MRI networks arise from subject motion. *Neuroimage.* (2012) 59:2142–54. doi: 10.1016/j.neuroimage.2011.10.018
24. Carp J. Optimizing the order of operations for movement scrubbing: comment on power et al. *Neuroimage.* (2013) 76:436–8. doi: 10.1016/j.neuroimage.2011.12.061
25. Birn RM, Diamond JB, Smith MA, Bandettini PA. Separating respiratory-variation-related fluctuations from neuronal-activity-related fluctuations in fMRI. *Neuroimage.* (2006) 31:1536–48. doi: 10.1016/j.neuroimage.2006.02.048
26. Dale AM, Fischl B, Sereno MI. Cortical surface-based analysis. I. Segmentation and surface reconstruction. *Neuroimage.* (1999) 9:179–94. doi: 10.1006/nimg.1998.0395

27. Fischl B, Salat DH, Busa E, Albert M, Dieterich M, Haselgrove C, et al. Whole brain segmentation: automated labeling of neuroanatomical structures in the human brain. *Neuron.* (2002) 33:341–55. doi: 10.1016/S0896-6273(02)00569-X
28. Fischl B, van der Kouwe A, Destrieux C, Halgren E, Segonne F, Salat DH, et al. Automatically parcellating the human cerebral cortex. *Cereb Cortex.* (2004) 14:11–22. doi: 10.1093/cercor/bhg087
29. Power JD, Cohen AL, Nelson SM, Wig GS, Barnes KA, Church JA, et al. Functional network organization of the human brain. *Neuron.* (2011) 72:665–78. doi: 10.1016/j.neuron.2011.09.006
30. Siedlecki KL, Manly JJ, Brickman AM, Schupf N, Tang MX, Stern Y. Do neuropsychological tests have the same meaning in Spanish speakers as they do in English speakers? *Neuropsychology.* (2010) 24:402–11. doi: 10.1037/a0017515
31. Buschke H, Fuld PA. Evaluating storage, retention, and retrieval in disordered memory and learning. *Neurology.* (1974) 24:1019–25. doi: 10.1212/WNL.24.11.1019
32. Roth C. Boston naming test. In: Kreutzer JS, DeLuca J, Caplan B, editors. *Encyclopedia of Clinical Neuropsychology.* New York, NY: Springer New York (2011). p. 430–3.
33. Wechsler D, De Lemos MM. *Wechsler Adult Intelligence Scale-Revised* New York, NY: Harcourt Brace Jovanovich (1981).
34. Goodglass H, Kaplan E. *The Assessment of Aphasia and Related Disorders* Philadelphia, PA: Lea & Febiger (1972).
35. Benton AL. *Visual Retention Test*. New York, NY: Psychological Corporation (1974).
36. Rosen W. *The Rosen Drawing Test*. Bronx, NY: Veterans Administration Medical Center. (1981).
37. Mattis S. Mental status examination for organic mental syndrome in the elderly patient. In: Bellack L, Karusu TB, editors. *Geriatric Psychiatry*. New York, NY: Grune & Stratton (1976). p. 77–121.
38. L.F D'Elia PS, C.L Uchiyama TW. *Color Trails Test*. Odessa, FL: Psychological Assessment Resources (1996).
39. Jolliffe IT, Cadima J. Principal component analysis: a review and recent developments. *Philos Trans A Math Phys Eng Sci.* (2016) 374:20150202. doi: 10.1098/rsta.2015.0202
40. Scheinost D, Finn ES, Tokoglu F, Shen X, Papademetris X, Hampson M, et al. Sex differences in normal age trajectories of functional brain networks. *Hum Brain Mapp.* (2015) 36:1524–35. doi: 10.1002/hbm.22720
41. Shen X, Cox SR, Adams MJ, Howard DM, Lawrie SM, Ritchie SJ, et al. Resting-State connectivity and its association with cognitive performance, educational attainment, and household income in the UK biobank. *Biol Psychiatry Cogn Neurosci Neuroimaging.* (2018) 3:878–86. doi: 10.1016/j.bpsc.2018.06.007
42. Sanchez-Juan P, Seshadri S. Dynamic measurements of beta-amyloid accumulation: the early effect of APOE. *Neurology.* (2017) 89:986–7. doi: 10.1212/WNL.0000000000004344
43. Albert MS, DeKosky ST, Dickson D, Dubois B, Feldman HH, Fox NC, et al. The diagnosis of mild cognitive impairment due to alzheimer's disease: recommendations from the national institute on aging-alzheimer's association workgroups on diagnostic guidelines for alzheimer's disease. *Alzheimers Dement.* (2011) 7:270–9. doi: 10.1016/j.jalz.2011.03.008
44. Hahn A, Strandberg TO, Stomrud E, Nilsson M, van Westen D, Palmqvist S, et al. association between earliest amyloid uptake and functional connectivity in cognitively unimpaired elderly. *Cereb Cortex.* (2019) 29:2173–82. doi: 10.1093/cercor/bhz020
45. Schultz AP, Chhatwal JP, Hedden T, Mormino EC, Hanseeuw BJ, Sepulcre J, et al. phases of hyperconnectivity and hypoconnectivity in the default mode and salience networks track with amyloid and tau in clinically normal individuals. *J Neurosci.* (2017) 37:4323–31. doi: 10.1523/JNEUROSCI.3263-16.2017
46. Jansen WJ, Ossenkoppele R, Knol DL, et al. Prevalence of cerebral amyloid pathology in persons without dementia: a meta-analysis. *JAMA.* (2015) 313:1924–38. doi: 10.1001/jama.2015.4668

Conflict of Interest: JL receives a stipend from Wolters Kluwer, N.V. as Editor in Chief of The Journal Alzheimer's Disease and Associated Disorders, and has served as a paid consultant to vTv, In review therapeutics, Inc. and Recruitment Partners. AB is a paid consultant for Regeneron Pharmaceuticals and Cognition Therapeutics, Inc and owns equity in Mars Holding Limited.

The remaining authors declare that the research was conducted in the absence of any commercial or financial relationships that could be construed as a potential conflict of interest.

frontiers in Neurology

ORIGINAL RESEARCH
published: 20 January 2021
doi: 10.3389/fneur.2020.573095

The Spatial and Cell-Type Distribution of SARS-CoV-2 Receptor ACE2 in the Human and Mouse Brains

Rongrong Chen[1†], Keer Wang[1†], Jie Yu[1†], Derek Howard[2], Leon French[2], Zhong Chen[3,4], Chengping Wen[1] and Zhenghao Xu[1*]*

[1] Institute of Traditional Chinese Medicine Clinical Basic Medicine, School of Basic Medical Science, Zhejiang Chinese Medical University, Hangzhou, China, [2] Krembil Centre for Neuroinformatics, Centre for Addiction and Mental Health, Toronto, ON, Canada, [3] Zhejiang Chinese Medical University, Hangzhou, China, [4] Key Laboratory of Medical Neurobiology of National Health Commission and Chinese Academy of Medical Sciences, Institute of Pharmacology and Toxicology, College of Pharmaceutical Sciences, Zhejiang University, Hangzhou, China

OPEN ACCESS

Edited by:
Torben Moos,
Aalborg University, Denmark

Reviewed by:
Konstantinos Kalafatakis,
University of Ioannina, Greece
Kasper Bendix Johnsen,
Technical University of Denmark, Denmark

***Correspondence:**
Chengping Wen
wengcp@163.com
Zhenghao Xu
xuzhenghao@zcmu.edu.cn
orcid.org/0000-0003-0033-525X

[†] These authors have contributed equally to this work

Specialty section:
This article was submitted to Applied Neuroimaging, a section of the journal Frontiers in Neurology

Received: 25 June 2020
Accepted: 14 December 2020
Published: 20 January 2021

Citation:
Chen R, Wang K, Yu J, Howard D, French L, Chen Z, Wen C and Xu Z (2021) The Spatial and Cell-Type Distribution of SARS-CoV-2 Receptor ACE2 in the Human and Mouse Brains. Front. Neurol. 11:573095. doi: 10.3389/fneur.2020.573095

By engaging angiotensin-converting enzyme 2 (ACE2 or Ace2), the novel pathogenic severe acute respiratory syndrome coronavirus 2 (SARS-CoV-2) invades host cells and affects many organs, including the brain. However, the distribution of ACE2 in the brain is still obscure. Here, we investigated the ACE2 expression in the brain by analyzing data from publicly available brain transcriptome databases. According to our spatial distribution analysis, ACE2 was relatively highly expressed in some brain locations, such as the choroid plexus and paraventricular nuclei of the thalamus. According to cell-type distribution analysis, nuclear expression of ACE2 was found in many neurons (both excitatory and inhibitory neurons) and some non-neuron cells (mainly astrocytes, oligodendrocytes, and endothelial cells) in the human middle temporal gyrus and posterior cingulate cortex. A few ACE2-expressing nuclei were found in a hippocampal dataset, and none were detected in the prefrontal cortex. Except for the additional high expression of Ace2 in the olfactory bulb areas for spatial distribution as well as in the pericytes and endothelial cells for cell-type distribution, the distribution of Ace2 in the mouse brain was similar to that in the human brain. Thus, our results reveal an outline of ACE2/Ace2 distribution in the human and mouse brains, which indicates that the brain infection of SARS-CoV-2 may be capable of inducing central nervous system symptoms in coronavirus disease 2019 (COVID-19) patients. Potential species differences should be considered when using mouse models to study the neurological effects of SARS-CoV-2 infection.

Keywords: angiotensin-converting enzyme 2, ACE2, brain, SARS-coronavirus 2, COVID-19

INTRODUCTION

Since December 2019, much attention has focused on the novel severe acute respiratory syndrome coronavirus 2 (SARS-CoV-2) and the related coronavirus disease 2019 (COVID-19) pandemic, which is rapidly spreading around the world and results in a global health emergency (1). In addition to atypical pneumonia, the central nervous system (CNS) symptoms of COVID-19

patients have been observed in the clinic (2). According to a recent retrospective case series study, 53 out of 214 (24.8%) COVID-19 patients had CNS symptoms, including dizziness, headache, impaired consciousness, acute cerebrovascular disease, ataxia, and epilepsy (3). More importantly, it has been found that SARS-CoV, a previously reported similar coronavirus, spreads into the brain after it was cleared from the lung in mice, which could be more concealment than that in the lung (4). Recently, Puelles et al. found that SARS-CoV-2 has an organotropism beyond the respiratory tract, including the kidneys, liver, heart, and brain (5). Thus, it is necessary and urgent to study the CNS infection of SARS-CoV-2.

Angiotensin-converting enzyme 2 (ACE2 or Ace2) has been identified as a key entry receptor for novel pathogenic SARS-CoV-2 invasion, similar to previous SARS-CoV (6). By binding of the spike protein to ACE2, SARS-CoV-2 and SARS-CoV could invade host cells in human organs (7, 8). However, the distribution of ACE2 in the brain is still obscure and even inconsistent. In 2004, Hamming et al. found that ACE2 may be expressed only in the endothelium and vascular smooth muscle cells in the human brain tissue (9). However, some recent studies found that the human endothelial cells expressed low or undetectable levels of ACE2 (10, 11). On the other hand, a previous study has reported that Ace2 could be expressed in the mouse neuron cells, which may contribute to the development of hypertension (12); however, in another neurocytometry study, Ace2 is a potential marker for non-neurons in the zinc-fixed mouse brain cortical section (13). Thus, further clarifying the brain tissue distribution of ACE2 may help to bring to light the CNS infection of the novel SARS-CoV-2 and previous SARS-CoV.

Here, we investigated the distribution of ACE2 in the brain by analyzing publicly available brain transcriptome databases. These databases, such as those produced by the Allen Institute for Brain Science, offer an extremely valuable source of genomic data, whose processing and interpretation may facilitate translational research (14, 15). We revealed an uneven spatial and cell-type distribution of ACE2 in the human and mouse brains.

METHODS

Brain Transcriptome Databases

As listed in **Table 1**, 10 publicly available brain transcriptome databases that can be accessed without specialized computational expertise were used. All these databases offer extremely valuable sources of genomic data freely for academic and other non-commercial purposes. Except for the Single Cell Portal database (https://singlecell.broadinstitute.org), some of these databases have been also introduced in a recent review study (27). All databases and datasets were appropriately used and cited according to their citation policy, license, or terms of use.

Analysis of the Spatial Distribution of ACE2 in the Human Brain

Three databases, including Allen Human Brain Atlas database (http://human.brain-map.org), Human Brain Transcriptome database (https://hbatlas.org), and GTEx Portal database (https://www.gtexportal.org), were used to analyze the spatial distribution of ACE2 in the human brain.

Cell-Type Distribution of ACE2 in the Human Brain

Three single-cell sequencing databases, including Single Cell Portal database (https://singlecell.broadinstitute.org, single-cell sequencing), Allen Cell Types database (http://celltypes.brain-map.org, single-cell sequencing), and Brain RNA-Seq database from Barres labs (https://www.brainrnaseq.org/, RNA-seq of cell types isolated from the human brain), were used. The summary of the included datasets for the human brain is shown in **Table 2**.

Spatial and Cell-Type Distribution of Ace2 in the Mouse Brain

Allen Mouse Brain Atlas database (http://mouse.brain-map.org) was used to analyze the general spatial distribution of Ace2 in the mouse brain. The hippocampus RNA-seq Atlas database (https://hipposeq.janelia.org/), Single Cell Portal database, Mouse Brain Atlas database (http://mousebrain.org), Brain RNA-Seq database from Barres lab (https://www.brainrnaseq.org/), and Brain vascular single-cell database from Betsholtz lab were used for cell-type distribution of Ace2 in the mouse brain. The summary of the used five single-cell sequencing datasets is also shown in **Table 2**.

Data Processing and Statistical Analysis

Datasets were independently searched and analyzed by two authors (RC and JY), and any disagreements were discussed and resolved by consensus with the corresponding author (ZX). The data from the Allen Human Brain Atlas database and Allen Cell Types database were exported to Microsoft Excel 2017 and GraphPad Prism 6.0 for further analysis. ACE2 expression data from the Allen Human and Mouse Brain Atlas databases were imported to Brain Explorer 2.0 software to get visualization. The data from the other databases were analyzed online. Where applicable, data are expressed as median or mean. Interquartile range (IQR), 95% CI, range, and/or all sample points were also provided if possible.

Positive of expression criterion: (1) to minimize false positive of expression as previous studies (32, 33), a gene with calculate counts per million (CPM), transcripts per million (TPM), unique molecular identifier (UMI) count, or fragments per kilobase million (FPKM) >1 were considered to be positive, which also is the same as log10 (CPM), log10 (TPM), or log10 (UMI) ≥ 0 as well as log10 (CPM + 1), log10 (TPM + 1), and log10 (UMI + 1) ≥ 0.3; (2) besides, as a z score being >2 corresponds to a p-value <0.05, a z score of ACE2 expression >2 was considered as high ACE2 expression in the Allen Human Brain Atlas database.

RESULTS

The General Expression of ACE2 in the Human Brain

According to the GTEx Portal database, the general expression of ACE2 was extremely low but not none in the brain according to our positive of expression criterion (**Figure 1A**). Excepted for the lung (38 out of 578, positive rate of 6.57%), the positive samples

TABLE 1 | The database used for the current study.

Analysis	Web Interface	References	Species	Brain area	Method
Spatio-temporal	http://hbatlas.org	(16)	Human	Multi	Microarray
Spatial	http://human.brain-map.org	(17)	Human	Multi	Microarray
Spatial	https://www.gtexportal.org	(18)	Human	Multi	RNA-seq
Spatial	https://mouse.brain-map.org/	(19)	Mouse	Multi	Microarray
Spatial and cell type	https://hipposeq.janelia.org	(20)	Mouse	Hippocampus	RNA-seq
Cell type	http://mousebrain.org	(21)	Mouse	Multi	RNA-seq
Cell type	https://www.brainrnaseq.org/	(22, 23)	Mouse and human	Multi	RNA-seq
Single cell	https://singlecell.broadinstitute.org	Not available	Many	Multi	RNA-seq
Single cell	https://celltypes.brain-map.org/rnaseq/	(24)	Human	Cortex	RNA-seq
Single cell	http://betsholtzlab.org/VascularSingleCells/database.html	(25, 26)	Mouse	Blood vessels	scRNA-seq

were also found in the amygdala (1 out of 152, 0.65%), anterior cingulate cortex (2 out of 176, 1.14%), caudate (3 out of 246, 1.22%), cortex (1 out of 255, 0.39%), frontal cortex (2 out of 209, 0.96%), hippocampus (4 out of 197, 2.03%), hypothalamus (3 out of 202, 1.49%), nucleus accumbens (NAc; 1 out of 246, 0.41%), putamen (1 out of 205, 0.48%), spinal cord (cervical c-1, 4 out of 159, 2.52%), and substantial nigra (5 out of 139, 3.60%), but none in the cerebellum (0 out of 241) and cerebellar hemisphere (0 out of 215).

In addition, according to the Human Brain Transcriptome database, the general expression of ACE2 was also similar among the cortex and other brain regions, which may not change a lot with age (**Figures 1B,C**).

Two-Spatial Distribution of ACE2 in the Human Brain

By providing slice images, the Allen Human Brain Atlas may prove a more detailed spatial distribution of ACE2 in the human brain than the GTEx Portal database and Human Brain Transcriptome database. Two microarray datasets using the different probes of ACE2 (A_23_P252981, CUST_16267_PI416261804) were collected from the Allen Human Brain Atlas database (http://human.brain-map.org/microarray/search). To provide a relatively systematic analysis of the Allen Human Brain Atlas database, we analyzed the data as both separated datasets and pooled them together. By analyzing the z score and intensity of ACE2 expression as two separated datasets, we found that 6 brain areas had high ACE2 expression (with a maximal z score of ACE2 expression >2.0) in both probe datasets, 15 brain areas had high ACE2 expression only in probe 1 dataset, and 9 brain areas had high ACE2 expression only in probe 2 dataset (**Figures 2A,B**).

To further visualize the spatial distribution of ACE2 expression and minimize the influences of the use of two different probes (such as the difference of detective sensitivity), we pooled the expression value of the two datasets and found 23 brain areas with a z score >1.0 and four of them with a z score >2.0 (**Figure 3A**). The spatial distribution of ACE2 expression in the human brain according to the pooled expression data is shown in **Figure 3B**.

Cell-Type Distribution of ACE2 in the Human Brain

We further collected and analyzed single-cell sequencing data, which may provide all mRNAs present in every single cell of the tested brain tissue. By analyzing the single-cell sequencing data of the human middle temporal gyrus (https://celltypes.brain-map.org/rnaseq/human/mtg), human posterior cingulate cortex (https://singlecell.broadinstitute.org/single_cell/study/SCP371), and archived human prefrontal cortex (PFC) and hippocampus samples (https://singlecell.broadinstitute.org/single_cell/study/SCP90/), the expression of ACE2 is relatively high in the human middle temporal gyrus (a total of 2.00% of the ACE2 positive cells, 309 out of 15,603) and posterior cingulate cortex (a total of 1.38% of the ACE2 positive cells, 133 out of 9,635) samples, but it is very low in the archived human PFC (no ACE2 positive cells) and hippocampus samples (a total of 0.21% of the ACE2 positive cells, 2 out of 9,530). Besides, according to the Brain RNA-Seq database from Barres lab, we also found no expression of ACE2 in all kinds of cell subtypes that were isolated from the human anterior temporal lobe cortex and hippocampus (**Supplementary Figure 1**).

For the cell types, most of the ACE2 positive cells were neurons in both the human middle temporal gyrus and the posterior cingulate cortex, especially excitatory neurons (72.1% for the middle temporal gyrus and 66.1% for the posterior cingulate cortex, **Figures 4A,B**) and interneurons (22.4% for the middle temporal gyrus and 9.8% for the posterior cingulate cortex, **Figures 4A,B**). The ACE2 positive percentage of excitatory neurons was also the highest among cell types (2.14% for the middle temporal gyrus and 2.18% for the posterior cingulate cortex, **Figure 4C**). The details of the cell-type distribution of ACE2 in the human brain are shown in **Supplementary Figures 2**, **3**.

Spatial and Cell-Type Distribution of Ace2 in the Mouse Brain

As shown in **Figure 5**, we additionally analyzed the spatial distribution of Ace2 in the mouse brain based on the Allen Mouse Brain Atlas (http://mouse.brain-map.org/gene/show/45849). Similar to the human brain, we found that the Ace2

TABLE 2 | Summary of cell-type or single-cell sequencing databases for the human and mouse brains.

Brain Area	References	Method	Nuclei	Species n (age)	Source
Middle temporal gyrus	(24)	SMART-Seq	15,928	Human $n = 8$ (24–66)	https://celltypes.brain-map.org/rnaseq/human/mtg
Posterior cingulate cortex	(28)	Multiplexing snRNA-seq	9,923	Human $n = 20$ (>65)	https://singlecell.broadinstitute.org/single_cell/study/SCP371
Prefrontal cortex and hippocampus	(29)	DroNc-Seq	19,550	Human $n = 5$ (40–65)	https://singlecell.broadinstitute.org/single_cell/study/SCP90/
Temporal lobe cortex and hippocampus	(22, 23)	RNA-seq of cell types isolated from the human brain	NA	Human $n = 22$ (8–65)	https://www.brainrnaseq.org/
Whole cortex	(30)	10× Chromium, SMART-seq2, DroNc-seq and sci-RNA-seq	13,783	Mouse (1 month old)	https://singlecell.broadinstitute.org/single_cell/study/SCP425/
SNr, SNc, VTA	U19—Huang BICCN data (1U19MH114821-01)[a]	Unclear	13,861	Mouse (unclear)	https://singlecell.broadinstitute.org/single_cell/study/SCP478
Cerebellum	(31)	High-throughput single-nucleus RNA-seq	611,034 (10,000 used)	Mouse 2 female, 4 male (60 days)	https://singlecell.broadinstitute.org/single_cell/study/SCP795
Prefrontal cortex and hippocampus	(29)	DroNc-Seq	29,543	Mouse 4 (adult)	https://singlecell.broadinstitute.org/single_cell/study/SCP60
Hippocampus	(20)	Div-Seq	1,367	Mouse unclear	https://singlecell.broadinstitute.org/single_cell/study/SCP1
Multiple areas (265 clusters of cells)	(21)	Cell-type RNA-seq	509,876 (160,796 used)	Mouse male and female (12–56 days old)	http://mousebrain.org
Vascular and vessel-associated cells (15 of cluster cells)	(25, 26)	scRNA-seq	3,186	Mouse (adult)	http://betsholtzlab.org/VascularSingleCells/database.html

[a] *This dataset is provided by Huang et al. (https://biccn.org/teams/u19-huang) and from the BRAIN Initiative Cell Census Network (BICCN, https://biccn.org/). Multiplexing snRNA-seq: nuclei multiplexing with barcoded antibodies for single-nucleus genomics; Smart-Seq: switching mechanism at 5′ end of the RNA transcript; DroNc-Seq: deciphering cell types in the human archived brain tissues by massively-parallel single-nucleus RNA-seq; sci-RNA-seq: single-cell combinatorial-indexing RNA-sequencing analysis; SNr: substantia nigra pars reticulate; SNc: substantia nigra pars compacta; VTA: ventral tegmental area.*

expression is relatively high in the choroid plexus of the lateral ventricle, substantia nigra pars reticulata (SNr), and some cortical areas (such as the piriform cortex). We additionally found that the ACE2 expression is also relatively high in the olfactory bulb, whereas it was very low in the hippocampal areas.

We further analyze the single-cell sequencing data of the multiple mouse cortex (https://singlecell.broadinstitute.org/single_cell/study/SCP425/); archived mouse brain samples (https://singlecell.broadinstitute.org/single_cell/study/SCP60); mouse hippocampus (https://singlecell.broadinstitute.org/single_cell/study/SCP1); substantia nigra pars reticulate (SNr), substantia nigra pars compacta (SNc), and ventral tegmental area (VTA) areas (https://singlecell.broadinstitute.org/single_cell/study/SCP478); and cerebellum (https://singlecell.broadinstitute.org/single_cell/study/SCP795). Similar to human data, the expression of Ace2 is relatively high in the multiple mouse cortex samples (a total of 0.84% of the Ace2 positive cells, 84 out of 10,000), but it is relatively low in the mixed mouse PFC and hippocampus samples (a total of 0.28% of the Ace2 positive cells, 38 out of 13,313) and the mouse hippocampus samples (a total of 0.1% of the Ace2 positive cells, 2 out of 1,188). Besides, the expression of Ace2 is also found in 0.68% of the cell in the mixed SNr, SNc, and VTA areas as well as 0.52% in the cerebellum.

For the cell-type distribution, different from human brain data, the Ace2 positive rate of the endothelial cells was the highest among different cell types in the mouse brain, including the multiple mouse cortex; mixed PFC and hippocampus; mixed SNr, SNc, and VTA areas; and cerebellum (**Figure 6A**). Similar to human brain data, the Ace2 positive rate of the neurons was also very high among different cell types in the mouse brain, including the multiple cortex (48.8%); mixed PFC and hippocampus (15%); mixed SNr, SNc, and VTA areas (10.5%); and cerebellum (7.69%) (**Figure 6A**). The details of the cell-type distribution of Ace2 in the mouse brain are shown in **Supplementary Figure 4**. Similarly, in a comprehensive atlas of the mouse nervous system, of the 265 cell clusters, 4 had an expression z score >2 (3 pericyte clusters and 1 cluster of arterial endothelial cells, **Figure 6B**). According to the Brain RNA-Seq database from Barres lab,

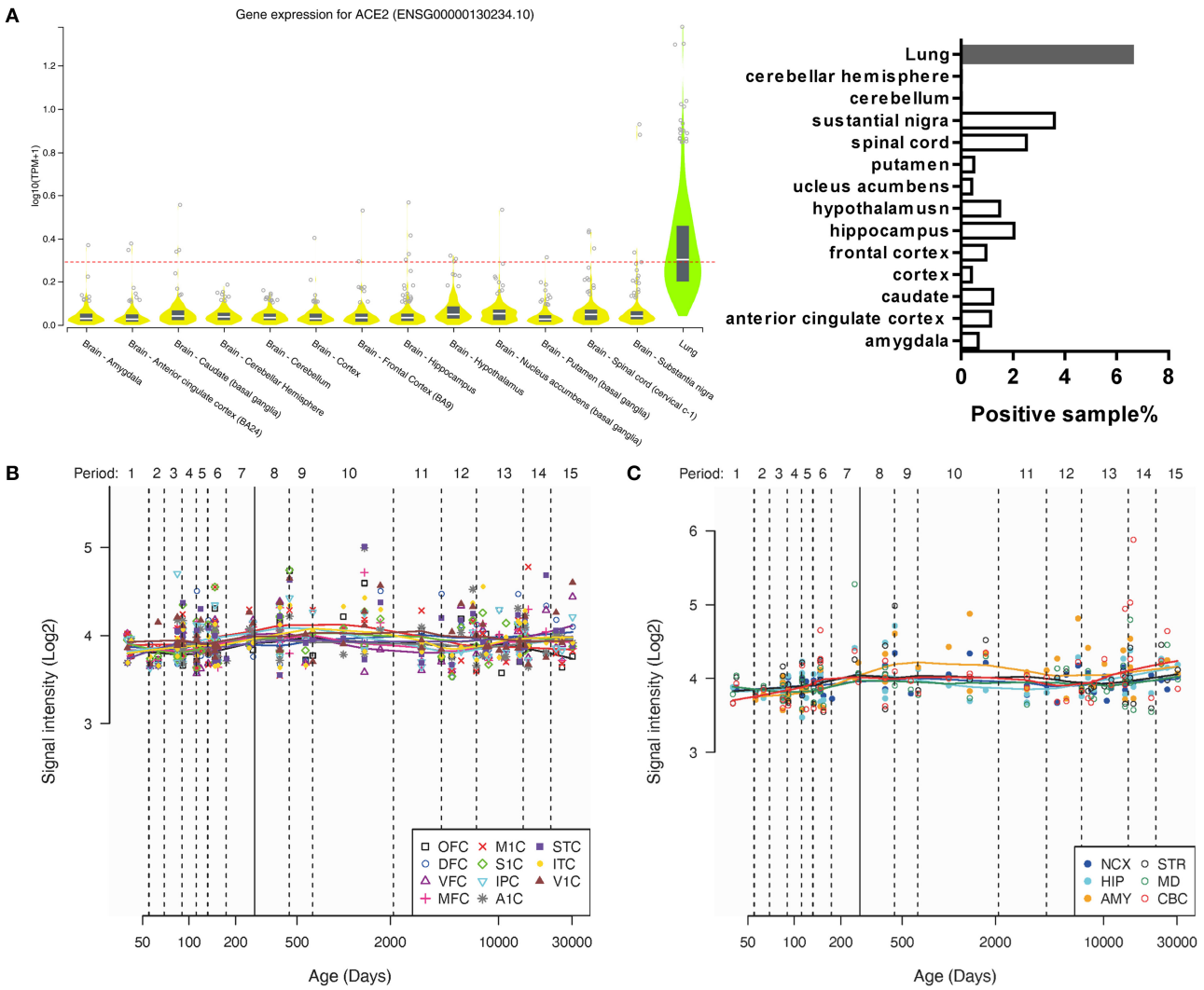

FIGURE 1 | The general expression of ACE2 in different human brain areas. **(A)** The expression of ACE2 in different human brain areas and the lung according to the GTEx Portal database (18). The dotted line means log10(CPM + 1) = 0.3, which means a threshold of the positive sample (>0.3 could be positive). **(B,C)** Change of intensity of ACE2 expression with age in different human brain areas according to the Human Brain Transcriptome database. Data are expressed as median, interquartile range (IQR), and all sample points in **(A)**, whereas data are expressed as mean and all sample points in **(B,C)**.

Ace2 was also highly expressed in the endothelial cells in the mouse brain (**Supplementary Figure 1**). Besides, according to the vascular single-cell transcriptions database from Betsholtz labs (**Supplementary Figure 5**), we further found: (1) ACE2 was only expressed in one kind of the endothelial cells in the brain vascular and (2) the expression level of ACE2 in the endothelial cells was much lower than that in the pericytes, smooth muscle cells, vascular fibroblast-like cells, and brain vascular.

As the inconsistent results were found in the hippocampus based on the single-cell sequencing, we additionally analyzed the expression of Ace2 in a cell-type sequencing database of the mouse hippocampus, the Hippocampus RNA-seq Atlas database (https://hipposeq.janelia.org). As shown in **Supplementary Figure 6**, (1) Ace2 expression was only found in the intermediate and ventral areas of the hippocampus with a mean FPKM <1; (2) Ace2 expression was found in the ventral pyramidal cells but not in the dorsal CA1 pyramidal cells, dorsal CA3 pyramidal cells, dorsal CA2 pyramidal cells, dorsal DG granule cells, dorsal DG mossy cells, ventral CA3 pyramidal cells, and ventral DG granule cells; (3) Ace2 expression was not found in parvalbumin (PV)-positive or somatostatin (SST)-positive interneurons in the hippocampus; and (4) Ace2 expression was not found in any neurons that project to the postsubiculum, NAc, or amygdala.

DISCUSSION

ACE2 is an important entry receptor for SARS-CoV-2 and SARS-CoV infecting host organs (6). Though the infection of

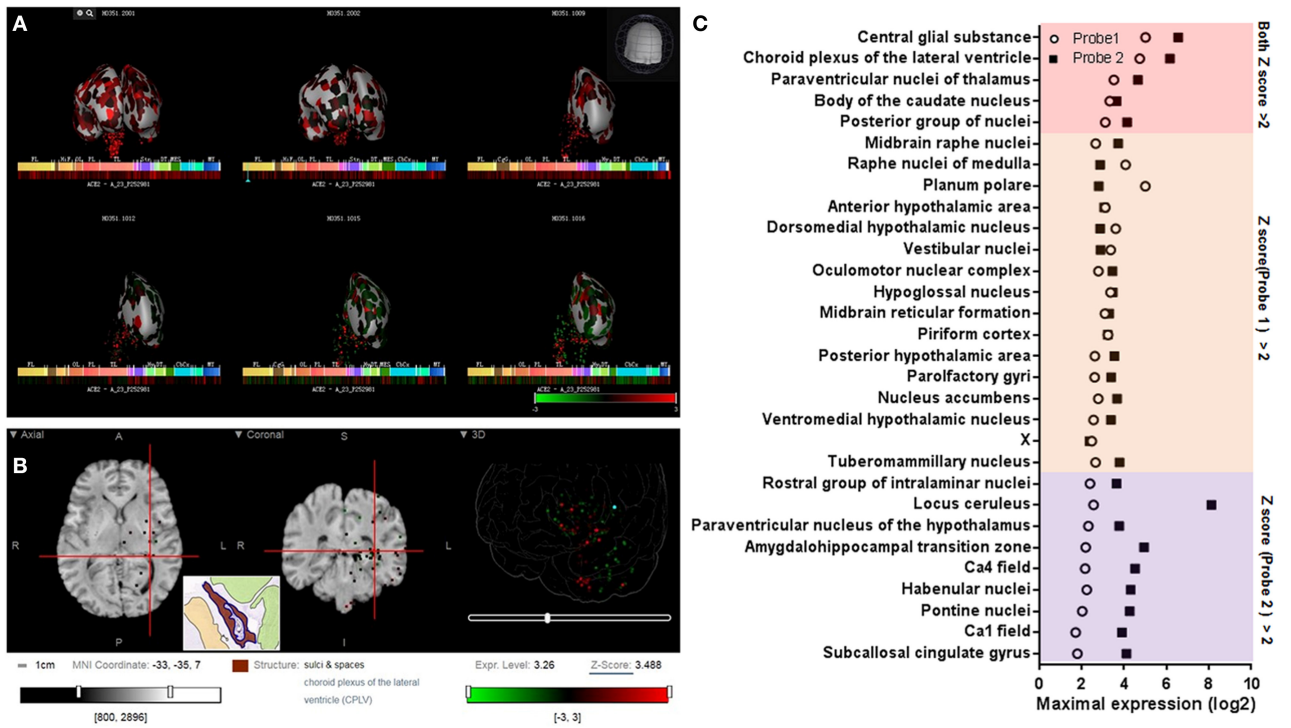

FIGURE 2 | Spatial distribution of ACE2 in the human brain according to the Allen Human Brain Atlas. **(A)** 3D view of the expression of ACE2 in different human brain areas based on the data of probe A_23_P252981 (probe 1). **(B)** Planar view of the expression of ACE2 in the choroid plexus of the lateral ventricle. The inset shows a sampled area of the choroid plexus of the lateral ventricle (the dark area in the inset). **(C)** Log2 intensity of ACE2 expression in the 30 brain areas with a z score >2.0 in at least one probe dataset (probe 1: A_23_P252981; probe 2: CUST_16267_PI416261804). All data were generated from the Allen Human Brain Atlas (http://human.brain-map.org/microarray/search). Images in **(A,B)** were directly from the Allen Human Brain Atlas (© 2010 Allen Institute for Brain Science, Allen Human Brain Atlas, available from: http://human.brain-map.org).

SARS-COV in the brain was reported in the past (34, 35), the distribution of ACE2 in the brain is still unclear. Here, we mainly found: (1) the expression of ACE2 was relatively high in several specific brain areas in human; (2) the expression of ACE2 was mainly located in many neurons (both excitatory and inhibitory neurons) in the human middle temporal gyrus and posterior cingulate cortex, but it was undetectable in the human PFC and very low in the human hippocampus; and (3) except for the additional expression of Ace2 in the olfactory bulb areas for spatial distribution and the pericytes and endothelial cells for cell-type distribution analysis, the main distribution map of Ace2 in the mouse brain was similar to that in human. Thus, our results revealed an outline of ACE2 or Ace2 distribution in the human and mouse brains, which supports the hypothesis that SARS-CoV-2 is capable to infect the brain and lead to CNS symptoms in COVID-19 patients (36). Our results indicate a heterogeneous distribution of ACE2 in different brain areas and cell types, which should be considered in further related studies.

SARS-CoV-2 shares a 77.2% amino acid identity, 72.8% sequence identity, and high structural similarity to previous SARS-CoV (37, 38). Similar to SARS-CoV, experimental affinity measurements show a high affinity of the receptor-binding domain of SARS-CoV-2 and ACE2 (37, 39). According to the GTEx Portal database, we found: (1) the total expression in the brain was much lower than that in the lung and (2) however, ACE2 positive samples were found in many brain areas, especially in the substantial nigra that the ACE2 positive sample rate was almost comparable to that in the lung. According to the Human Brain Transcriptome database, the total expression of ACE2 seems not to change with age. Moreover, according to the Allen Brain Atlas, six brain areas had relatively high expression of ACE2, especially four brain areas had high expression of ACE2 in the pooled data. Some of these high ACE2 expression brain nuclei are very important for normal brain functions, such as the paraventricular nuclei of the thalamus (involved in the control of wakefulness, feeding, appetitive motivation, drug addiction, regulation of stress and negative emotional behavior, and epilepsy) (40, 41), the raphe nuclei (the main serotoninergic nuclei in the brain) (42), and tuberomammillary nucleus (the main histaminergic nuclei in the brain) (43). Therefore, our results highlight the importance of spatial distribution rather than the overall expression of ACE2 in the brain. These results may provide some clues for further study on the brain infection of SARS-CoV-2 in COVID-19 patients and suggest that SARS-CoV-2 may result in serious CNS symptoms in COVID-19 patients (if it would infect these important brain areas by binding ACE2). Brain imaging and long-term follow-up may be required to

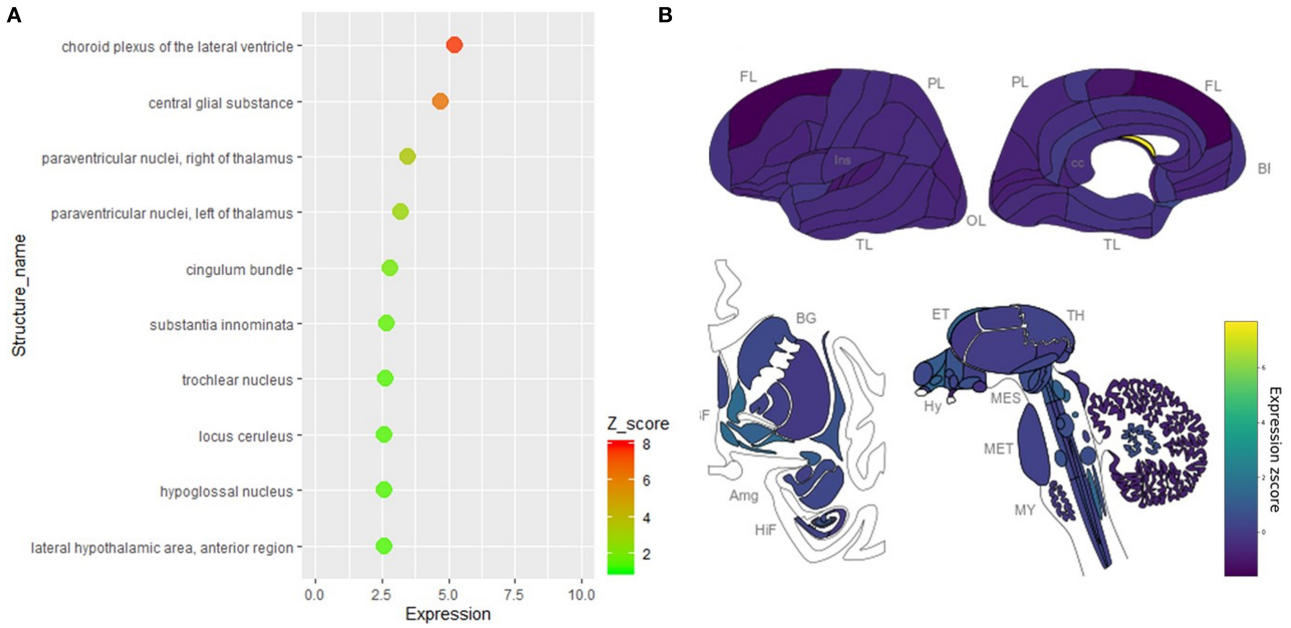

FIGURE 3 | Spatial distribution of ACE2 in the human brain according to the pooled data of the Allen Human Brain Atlas. **(A)** The expression intensity and z score of ACE2 in the top 10 brain areas of the pooled expression data of the two probes. **(B)** The distribution view of ACE2 expression in the human brain according to the pooled expression data of the two probes. Original data are available from the Allen Human Brain Atlas (http://human.brain-map.org/microarray/search). Brain region abbreviations: FL, frontal lobe; PL, parietal lobe; TL, temporal lobe; OL, occipital lobe; BF, basal forebrain; BG, basal ganglia; AmG, amygdala; HiF, hippocampal formation; EP, epithalamus; TH, thalamus; Hy, hypothalamus; MES, mesencephalon; MET, metencephalon; MY, myelencephalon.

confirm the possibility of SARS-CoV-2 brain infection and the following brain disorders in COVID-19 patients.

The routes or pathways for SARS-CoV and novel SARS-CoV-2 entering the brain are still unclear. According to experiments in mice transgenic for human ACE2, intranasal administration of SARS-CoV may enter the brain through the olfactory nerves (44). Consistent with this, we found that the expression of ACE2 in the olfactory bulb is higher than that in most other cortexes (**Figure 3**). In the human brain, we also found that the piriform cortex, a brain area directly connected with the olfactory bulb, had high ACE2 expression. Though no ACE2 expression data of the olfactory bulb in humans were available, our results indirectly support the hypothesis that SARS-CoV-2 might enter the human brain through the olfactory nerves. Recently, Meinhardt et al. found the olfactory transmucosal SARS-CoV-2 invasion as a port of CNS entry in individuals with COVID-19, which supports our finding (45).

On the other hand, we additionally found high ACE2 expression (z score >5) in the central glial substance and choroid plexus of the lateral ventricle in the human brain. Relatively high expression of ACE2 in the choroid plexus of the lateral ventricle was also found in the mouse brain in the current study. The central glial substance refers to an area of gray matter surrounding the central canal, which carries the cerebrospinal fluid (CSF) and helps to transport nutrients to the spinal cord (46). Besides, the choroid plexus of the ventricles is an important brain area for the generation of the CSF (47), the main location of the blood–CSF barrier (48), and serves as a crucial gateway for immune cells entering the brain (49). Recently, SARS-CoV-2 has also been found in CSF samples from a 56-year-old COVID-19 patient by genetic sequencing in China (http://www.ecns.cn/news/society/2020-03-05/detail-ifzuhesu4119860.shtml). SARS-CoV-2 may also infect the brain of a 24-year-old male patient (33). Thus, our results suggest that the high expression of ACE2 in the central glial substance and ventricles may provide another potential pathway for SARS-CoV-2 or SARS-CoV entering the CSF and/or spreading around the brain. This idea has been further confirmed by two recent studies, which found that SARS-CoV-2 infects the brain choroid plexus in human brain organoids (50, 51).

Single-nucleus RNA-seq provides a high resolution of cellular gene expression of each cell (52). According to the single-nucleus RNA-seq data, we further found that ACE2 was located in many neurons (especially excitatory neurons) and some non-neuron cells [especially astrocytes and oligodendrocytes (ODCs)] in both the posterior cingulate cortex and the middle temporal gyrus. The highest number of ACE2 positive cells was in the excitatory neurons, which may be projection neurons that make up many important brain networks. For example, excitatory neurons in the posterior cingulate cortex may project dense connections to the hippocampal formation and parahippocampal cortex, which are related to emotion and memory (53). On the other hand, the percentage of positive cells in some inhibitory neuron subtypes was comparable compared with excitatory neurons, though the total positive cell number of inhibitory neurons is lower than excitatory neurons. Inhibitory neurons are crucial for

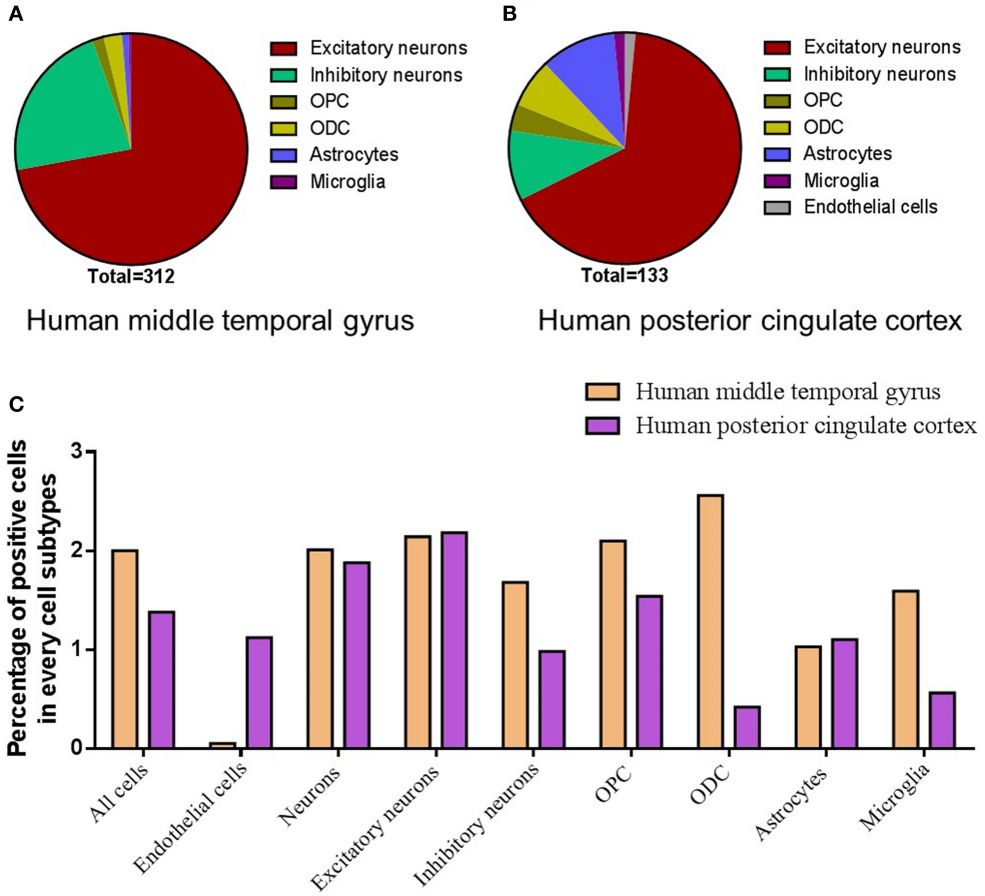

FIGURE 4 | Cell-type distribution of ACE2 in the human brain. **(A)** The cell-type proportion of the total positive cells in the human middle temporal gyrus. **(B)** The cell-type proportion of the total positive cells in the human posterior cingulate cortex. **(C)** The percentage of positive cells in different cell subtypes in the human middle temporal gyrus and posterior cingulate cortex. Original data are from https://celltypes.brain-map.org/rnaseq/human/mtg and https://singlecell.broadinstitute.org.

normal brain function (54). For example, the neurons in the SNr are mainly inhibitory gamma-aminobutyric acid (GABAergic) neurons, which is one important note in the neural circuits that contribute to epilepsy (41). Besides, we also found that some dopaminergic neurons and cerebellar cells in the mouse brain are also ACE2 positive. Thus, our results may help to explain the previous finding that SARS-CoV particles are mainly located in the neurons in the brain samples from SARS patients (34) and suggest that SARS-CoV-2 may also invade many neurons in the human brain and hence contribute to the CNS symptoms in COVID-19 patients.

In addition, single-nucleus RNA-seq showed that the expression of ACE2 was very low in both the endothelial cells and the pericytes from the human brain, whereas the expression of Ace2 was high in the endothelial cells and the pericytes in the mouse brain. According to RNA-seq of isolated subtype cells from the human and mouse brains, we also found that the expression of Ace2 was high in the mouse endothelial cells, but that of ACE2 was none in the human endothelial cells. Of note, previous microarray data show ACE2 expressed in the human endothelium (9), which is mainly a single layer of squamous endothelial cells. One possible reason for these differences might be that most blood vessels were excluded from the tested human brain tissues, whereas they were hard to be removed and left in the mouse brain tissues. However, some recent studies found that the human vascular endothelial cells do not express ACE2 or express relatively low levels of ACE2 (10, 11). Besides, according to the vascular single-cell transcriptions database from Betsholtz labs, the expression of Ace2 only found in one subtype of the vascular endothelial cells in the mouse brain and its level was also very low. On the contrary, the expression of Ace2 in the pericytes is very high in the mouse brain according to the database from Betsholtz labs. Thus, these results taken together suggest: (1) blood vessels may not be the main source of ACE2 expressed endothelial cells in mice; (2) the heterogeneity of ACE2 or Ace2 distribution in the subtypes of the endothelial cells or pericytes may exist in both the human and mouse brains; and (3) such a potential difference between humans and mice should be noted when using mouse models for the SARS-CoV-2 study. Further studies are need to confirm the ACE2 distribution in the specific types of the endothelial cells or pericytes (such as these nonvascular endothelial cells or pericytes in the cerebral

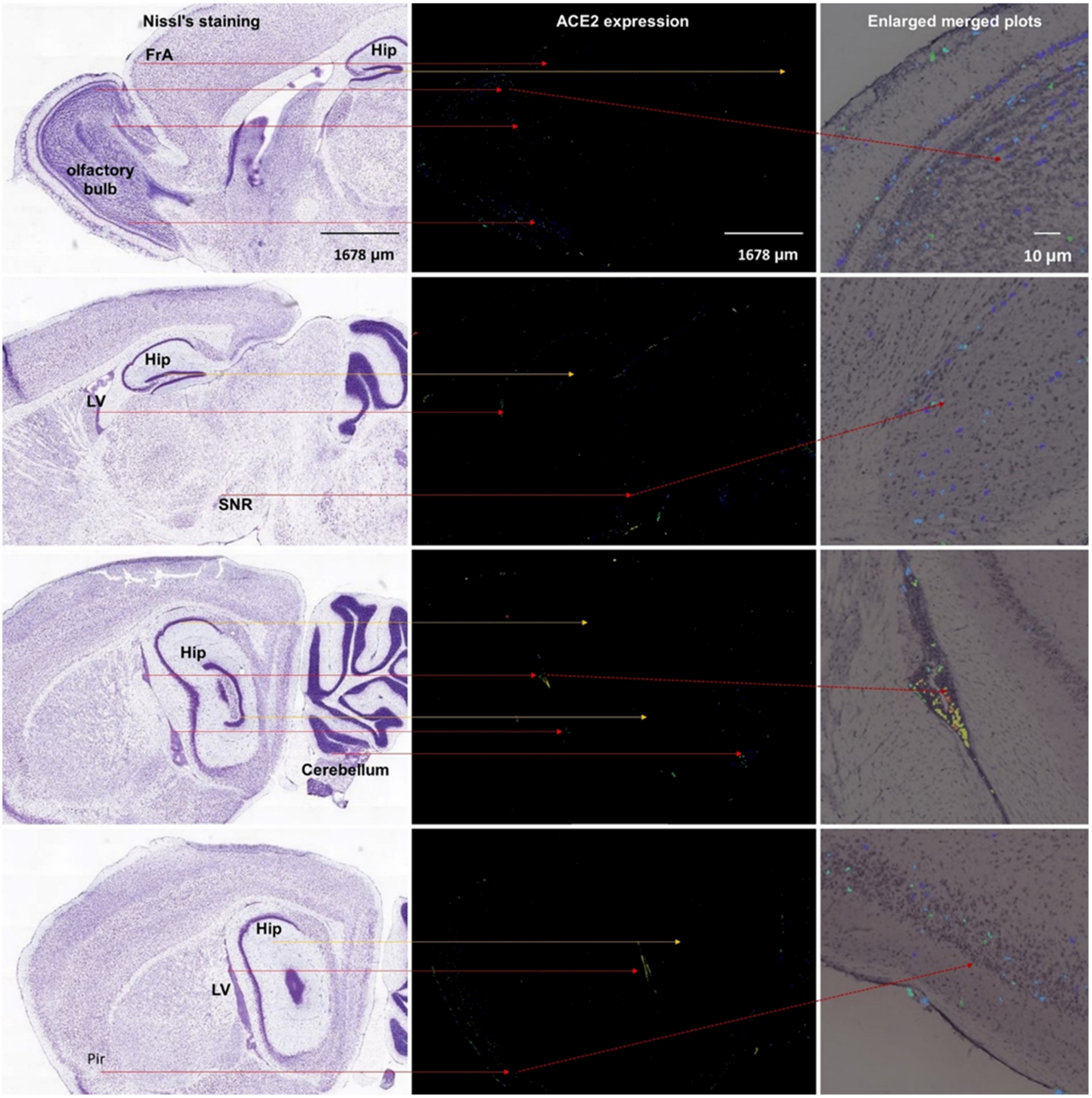

FIGURE 5 | Spatial distribution of ACE2 in the mouse brain. The left column means the Nissl staining of mouse brain slice, the middle column means the ACE2 expression by antisense, and the right column means the enlarged merged plots from the Brain Explorer 2.0 software. Hip, hippocampus; LV, lateral ventricle; SNR, substantia nigra pars reticulate; Pir, piriform cortex. All images are from the Allen Mouse Brain Atlas (© 2004 Allen Institute for Brain Science, Allen Mouse Brain Atlas, available from https://mouse.brain-map.org/).

lymphatic or ventricles), which may help SARS-CoV-2 to enter the brain and contribute to the cerebrovascular events in COVID-19 patients (55–57).

CONCLUSIONS

Our results reveal an outline of ACE2 or Ace2 distribution in the human and mouse brains, which indicates that the brain infection of SARS-CoV-2 might be capable to infect the brain and result in CNS symptoms in COVID-19 patients. The finding of high ACE2 expression in the central glial substance and brain ventricles suggests two potential novel routes for SARS-CoV-2 entering the CSF and/or spreading around the brain. A summary schematic figure is shown in **Figure 7**. In addition, the differences of ACE2/Ace2 distribution between humans and mice may be also useful to further

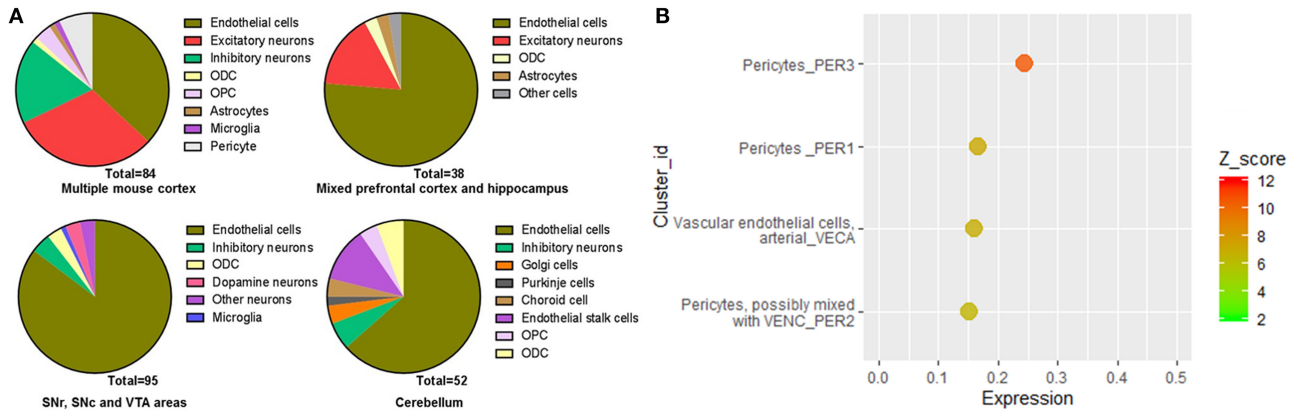

FIGURE 6 | Cell-type distribution of Ace2 in the mice brain. **(A)** Cell-type distribution of Ace2 according to the Single Cell Portal database (https://singlecell.broadinstitute.org/). **(B)** Top cell-type cluster expression of Ace2 according to the Mouse Brain Atlas database (http://mousebrain.org).

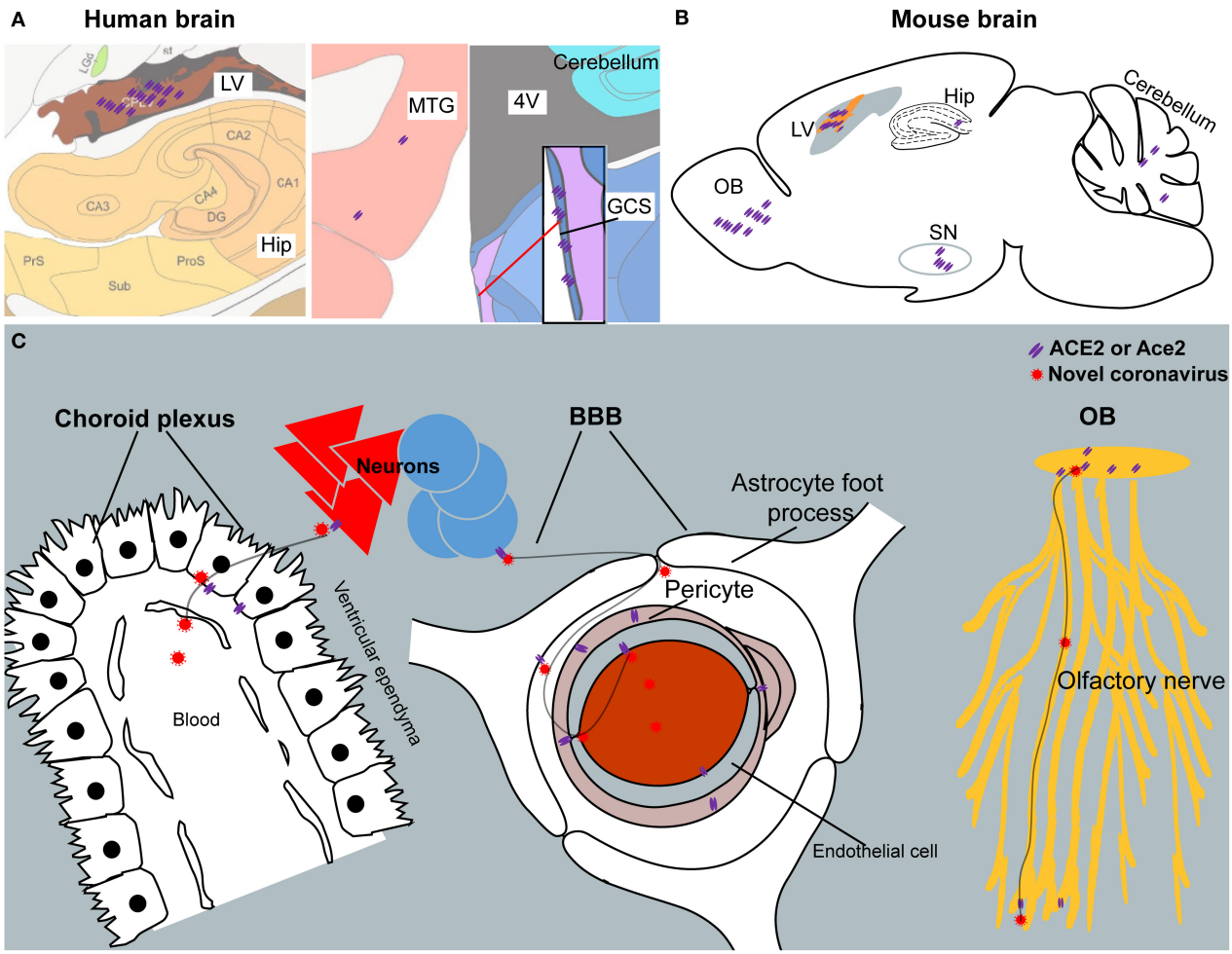

FIGURE 7 | The summary schematic figure. **(A)** The distribution of ACE2 in the choroid plexus of the lateral ventricle (LV), hippocampus (Hip), middle temporal gyrus (MTG), and central glial substance (CGS) in the human brain. Pictures are modified from the human brain atlas (http://atlas.brain-map.org/) of the Allen Brain Atlas. **(B)** Representative ACE2 expression in the olfactory bulb (OB), choroid plexus of the lateral ventricle (LV), hippocampus (Hip), substantia nigra (SN), and cerebellum in the mouse brain. **(C)** Three potential routes for SARS-CoV-2 entering the CSF and/or spreading around the brain. Another potential route for SARS-CoV-2 entering the CSF from the CGS is not listed because of limited information regarding this brain area.

"bench to bedside" translational studies regarding SARS-CoV-2. Our results may help to bring light to the brain infection of the present novel SARS-CoV-2 and previous SARS-CoV. Further studies are warranted to confirm our results and related predictions.

DATA AVAILABILITY STATEMENT

The original contributions presented in the study are included in the article/**Supplementary Material**, further inquiries can be directed to the corresponding author/s.

ETHICS STATEMENT

Ethical review and approval was not required for the study on human participants in accordance with the local legislation and institutional requirements. Written informed consent for participation was not required for this study in accordance with the national legislation and the institutional requirements. Ethical review and approval was not required for the animal study because we just used publicly available brain transcriptome databases.

AUTHOR CONTRIBUTIONS

ZX and CW designed the study. RC, KW, and JY performed the search and analysis. DH and LF contributed to the data analysis for **Figures 1**, **2**. ZX and KW checked the analyzed data. ZX wrote the manuscript in consultation with JY, ZC, CW, DH, and LF. All authors contributed to the article and approved the submitted version.

FUNDING

This work was funded by the Natural Science Foundation of Zhejiang Province (LEZ20H190001) and the National Natural Science Foundation of China (81673623) and partly supported by the Foundation of Zhejiang Chinese Medical University (Q2019Y02 and ZYX2018002).

ACKNOWLEDGMENTS

We would like to thank the Allen Institute for Brain Science (https://alleninstitute.org/), BRAIN Initiative Cell Census Network (BICCN, https://biccn.org/), Brain RNA-Seq database (https://www.brainrnaseq.org/), Brain vascular single-cell database (http://betsholtzlab.org/VascularSingleCells/database.html), GTExportal database (https://www.gtexportal.org), Hippocampus RNA-seq Atlas database (https://hipposeq.janelia.org/), Human Brain Transcriptome (http://hbatlas.org), Human Brain Transcriptome database (https://hbatlas.org), Mouse Brain atlas (http://mousebrain.org), and Single Cell Portal database (https://singlecell.broadinstitute.org).

SUPPLEMENTARY MATERIAL

The Supplementary Material for this article can be found online at: https://www.frontiersin.org/articles/10.3389/fneur.2020.573095/full#supplementary-material

REFERENCES

1. Liu Y, Eggo RM, Kucharski AJ. Secondary attack rate and superspreading events for SARS-CoV-2. *Lancet.* (2020) 395:e47. doi: 10.1016/S0140-6736(20)30462-1
2. Li YC, Bai WZ, Hashikawa T. The neuroinvasive potential of SARS-CoV2 may play a role in the respiratory failure of COVID-19 patients. *J. Med. Virol.* (2020) 92:552–5. doi: 10.1002/jmv.25728
3. Mao L, Wang M, Chen S, He Q, Chang J, Hong C, et al. Neurological manifestations of hospitalized patients with COVID-19 in Wuhan, China: a retrospective case series study. *medRxiv* 2020.2002.2022.20026500 (2020). doi: 10.2139/ssrn.3544840
4. Glass WG, Subbarao K, Murphy B, Murphy PM. Mechanisms of host defense following severe acute respiratory syndrome-coronavirus (SARS-CoV) pulmonary infection of mice. *J. Immunol.* (2004) 173:4030–9. doi: 10.4049/jimmunol.173.6.4030
5. Puelles VG, Lutgehetmann M, Lindenmeyer MT, Sperhake JP, Wong MN, Allweiss L, et al. Multiorgan and renal tropism of SARS-CoV-2. *N. Engl. J. Med.* (2020) 383:590–2. doi: 10.1056/NEJMc2011400
6. Hoffmann M, Kleine-Weber H, Schroeder S, Kruger N, Herrler T, Erichsen S, et al. SARS-CoV-2 cell entry depends on ACE2 and TMPRSS2 and is blocked by a clinically proven protease inhibitor. *Cell.* (2020) 181:271–80.e8 doi: 10.1016/j.cell.2020.02.052
7. Walls AC, Park YJ, Tortorici MA, Wall A, McGuire AT, Veesler D. Structure, function, and antigenicity of the SARS-CoV-2 spike glycoprotein. *Cell.* (2020) 183:1735. doi: 10.1016/j.cell.2020.11.032
8. Yan R, Zhang Y, Li Y, Xia L, Guo Y, Zhou Q. Structural basis for the recognition of the SARS-CoV-2 by full-length human ACE2. *Science.* (2020) 367:1444–8. doi: 10.1126/science.abb2762
9. Hamming I, Timens W, Bulthuis ML, Lely AT, Navis G, van Goor H. Tissue distribution of ACE2 protein, the functional receptor for SARS coronavirus. A first step in understanding SARS pathogenesis. *J. Pathol.* (2004) 203:631–7. doi: 10.1002/path.1570
10. Ahmetaj-Shala B, Peacock TP, Baillon L, Swann OC, Gashaw H, Barclay WS, et al. Resistance of endothelial cells to SARS-CoV-2 infection *in vitro*. *bioRxiv* 2020.2011.2008.372581 (2020). doi: 10.1101/2020.11.08.372581
11. He L, Mäe MA, Muhl L, Sun Y, Pietilä R, Nahar K, Vázquez Liébanas E, et al. Pericyte-specific vascular expression of SARS-CoV-2 receptor ACE2 – implications for microvascular inflammation and hypercoagulopathy in COVID-19. *bioRxiv* 2020.2005.2011.088500 (2020). doi: 10.1101/2020.05.11.088500
12. Xia H, Sriramula S, Chhabra KH, Lazartigues E. Brain angiotensin-converting enzyme type 2 shedding contributes to the development of neurogenic hypertension. *Circ. Res.* (2013) 113:1087–96. doi: 10.1161/CIRCRESAHA.113.301811
13. Martin D, Xu J, Porretta C, Nichols CD. Neurocytometry: flow cytometric sorting of specific neuronal populations from human and rodent brain. *ACS Chem. Neurosci.* (2017) 8:356–67. doi: 10.1021/acschemneuro.6b00374
14. Kalafatakis K, Giannakeas N, Lightman SL, Charalampopoulos I, Russell GM, Tsipouras M, et al. Utilization of the allen gene expression atlas to gain further insight into glucocorticoid physiology in the adult mouse brain. *Neurosci. Lett.* (2019) 706:194–200. doi: 10.1016/j.neulet.2019.05.020
15. Kalafatakis I, Kalafatakis K, Tsimpolis A, Giannakeas N, Tsipouras M, Tzallas A, et al. Using the Allen gene expression atlas of the adult mouse brain to gain further insight into the physiological significance of TAG-1/Contactin-2. *Brain Struct. Funct.* (2020) 225:2045–56. doi: 10.1007/s00429-020-02108-4
16. Johnson MB, Kawasawa YI, Mason CE, Krsnik Z, Coppola G, Bogdanovic D, et al. Functional and evolutionary insights into human brain development through global transcriptome analysis. *Neuron.* (2009) 62:494–509. doi: 10.1016/j.neuron.2009.03.027
17. Hawrylycz MJ, Lein ES, Guillozet-Bongaarts AL, Shen EH, Ng L, Miller JA, et al. An anatomically comprehensive atlas of the adult human brain transcriptome. *Nature.* (2012) 489:391–9. doi: 10.1038/nature11405
18. GTEx Consortium. Human genomics. The Genotype-Tissue Expression (GTEx) pilot analysis: multitissue gene regulation in humans. *Science.* (2015) 348:648–60. doi: 10.1126/science.1262110

19. Lein ES, Hawrylycz MJ, Ao N, Ayres M, Bensinger A, Bernard A, et al. Genome-wide atlas of gene expression in the adult mouse brain. *Nature.* (2007) 445:168–76. doi: 10.1038/nature05453
20. Cembrowski MS, Wang L, Sugino K, Shields BC, Spruston N. Hipposeq: a comprehensive RNA-seq database of gene expression in hippocampal principal neurons. *elife.* (2016) 5:e14997. doi: 10.7554/eLife.14997.028
21. Zeisel A, Hochgerner H, Lonnerberg P, Johnsson A, Memic F, van der Zwan J, et al. Molecular architecture of the mouse nervous system. *Cell.* (2018) 174:999–1014.e1022. doi: 10.1016/j.cell.2018.06.021
22. Zhang Y, Chen K, Sloan SA, Bennett ML, Scholze AR, O'Keeffe S, et al. An RNA-sequencing transcriptome and splicing database of glia, neurons, and vascular cells of the cerebral cortex. *J. Neurosci.* (2014) 34:11929–47. doi: 10.1523/JNEUROSCI.1860-14.2014
23. Zhang Y, Sloan SA, Clarke LE, Caneda C, Plaza CA, Blumenthal PD, et al. Purification and characterization of progenitor and mature human astrocytes reveals transcriptional and functional differences with mouse. *Neuron.* (2016) 89:37–53. doi: 10.1016/j.neuron.2015.11.013
24. Tasic B, Menon V, Nguyen TN, Kim TK, Jarsky T, Yao Z, et al. Adult mouse cortical cell taxonomy revealed by single cell transcriptomics. *Nat. Neurosci.* (2016) 19:335–46. doi: 10.1038/nn.4216
25. Vanlandewijck M, He L, Mäe MA, Andrae J, Ando K, Del Gaudio F, et al. A molecular atlas of cell types and zonation in the brain vasculature. *Nature.* (2018) 554:475–80. doi: 10.1038/nature25739
26. He L, Vanlandewijck M. Single-cell RNA sequencing of mouse brain and lung vascular and vessel-associated cell types. *Sci. Data.* (2018) 5:180160. doi: 10.1038/sdata.2018.160
27. Keil JM, Qalieh A, Kwan KY. Brain transcriptome databases: a user's guide. *J. Neurosci.* (2018) 38:2399–412. doi: 10.1523/JNEUROSCI.1930-17.2018
28. Gaublomme JT, Li B, McCabe C, Knecht A, Yang Y, Drokhlyansky E, et al. Nuclei multiplexing with barcoded antibodies for single-nucleus genomics. *Nat. Commun.* (2019) 10:2907. doi: 10.1038/s41467-019-10756-2
29. Habib N, Avraham-Davidi I, Basu A, Burks T, Shekhar K, Hofree M, et al. Massively parallel single-nucleus RNA-seq with DroNc-seq. *Nat. Methods.* (2017) 14:955–8. doi: 10.1038/nmeth.4407
30. Ding J, Adiconis X, Simmons SK, Kowalczyk MS, Hession CC, Marjanovic ND, et al. Systematic comparative analysis of single cell RNA-sequencing methods. *bioRxiv.* (2019). doi: 10.1101/632216
31. Kozareva V, Martin C, Osorno T, Rudolph S, Guo C, Vanderburg C, et al. A transcriptomic atlas of the mouse cerebellum reveals regional specializations and novel cell types. *bioRxiv* 2020.2003.2004.976407 (2020). doi: 10.1101/2020.03.04.976407
32. Gonzalez-Castellano I, Manfrin C, Pallavicini A, Martinez-Lage A. *De novo* gonad transcriptome analysis of the common littoral shrimp Palaemon serratus: novel insights into sex-related genes. *BMC Genomics.* (2019) 20:757. doi: 10.1186/s12864-019-6157-4
33. Moriguchi T, Harii N, Goto J, Harada D, Sugawara H, Takamino J, et al. A first case of meningitis/encephalitis associated with SARS-Coronavirus-2. *Int. J. Infect. Dis.* (2020) 94:55–8. doi: 10.1016/j.ijid.2020.03.062
34. Gu J, Gong E, Zhang B, Zheng J, Gao Z, Zhong Y, et al. Multiple organ infection and the pathogenesis of SARS. *J. Exp. Med.* (2005) 202:415–24. doi: 10.1084/jem.20050828
35. Xu J, Zhong S, Liu J, Li L, Li Y, Wu X, et al. Detection of severe acute respiratory syndrome coronavirus in the brain: potential role of the chemokine mig in pathogenesis. *Clin. Infect. Dis.* (2005) 41:1089–96. doi: 10.1086/444461
36. Kabbani N, Olds JL. Does COVID19 infect the brain? If so, smokers might be at a higher risk. *Mol. Pharmacol.* (2020) 97:351–3. doi: 10.1124/molpharm.120.000014
37. Brielle ES, Schneidman-Duhovny D, Linial M. The SARS-CoV-2 exerts a distinctive strategy for interacting with the ACE2 human receptor. *bioRxiv* 2020.2003.2010.986398 (2020). doi: 10.1101/2020.03.10.986398
38. Wu F, Zhao S, Yu B, Chen YM, Wang W, Song ZG, et al. A new coronavirus associated with human respiratory disease in China. *Nature.* (2020) 579:265–9. doi: 10.1038/s41586-020-2008-3
39. Lu R, Zhao X, Li J, Niu P, Yang B, Wu H, et al. Genomic characterisation and epidemiology of 2019 novel coronavirus: implications for virus origins and receptor binding. *Lancet.* (2020) 395:565–74. doi: 10.1016/S0140-6736(20)30251-8
40. Ren S, Wang Y, Yue F, Cheng X, Dang R, Qiao Q, et al. The paraventricular thalamus is a critical thalamic area for wakefulness. *Science.* (2018) 362:429–34. doi: 10.1126/science.aat2512
41. Chen B, Xu C, Wang Y, Lin W, Wang Y, Chen L, et al. A disinhibitory nigra-parafascicular pathway amplifies seizure in temporal lobe epilepsy. *Nat. Commun.* (2020) 11:923. doi: 10.1038/s41467-020-14648-8
42. Oikonomou G, Altermatt M, Zhang RW, Coughlin GM, Montz C, Gradinaru V, et al. The serotonergic raphe promote sleep in zebrafish and mice. *Neuron.* (2019) 103:686–701.e688. doi: 10.1016/j.neuron.2019.05.038
43. Hu W, Chen Z. The roles of histamine and its receptor ligands in central nervous system disorders: an update. *Pharmacol. Ther.* (2017) 175:116–32. doi: 10.1016/j.pharmthera.2017.02.039
44. Netland J, Meyerholz DK, Moore S, Cassell M, Perlman S. Severe acute respiratory syndrome coronavirus infection causes neuronal death in the absence of encephalitis in mice transgenic for human ACE2. *J. Virol.* (2008) 82:7264–75. doi: 10.1128/JVI.00737-08
45. Meinhardt J, Radke J, Dittmayer C, Franz J, Thomas C, Mothes R, et al. Olfactory transmucosal SARS-CoV-2 invasion as a port of central nervous system entry in individuals with COVID-19. *Nat. Neurosci.* (2020). doi: 10.1038/s41593-020-00758-5. [Epub ahead of print].
46. Thouvenin O, Keiser L, Cantaut-Belarif Y, Carbo-Tano M, Verweij F, Jurisch-Yaksi N, et al. Origin and role of the cerebrospinal fluid bidirectional flow in the central canal. *elife.* (2020) 9:e47699. doi: 10.7554/eLife.47699
47. Lun MP, Monuki ES, Lehtinen MK. Development and functions of the choroid plexus-cerebrospinal fluid system. *Nat. Rev. Neurosci.* (2015) 16:445–57. doi: 10.1038/nrn3921
48. Ghersi-Egea JF, Strazielle N, Catala M, Silva-Vargas V, Doetsch F, Engelhardt B. Molecular anatomy and functions of the choroidal blood-cerebrospinal fluid barrier in health and disease. *Acta Neuropathol.* (2018) 135:337–61. doi: 10.1007/s00401-018-1807-1
49. Valente LA, Begg LR, Filiano AJ. Updating neuroimmune targets in central nervous system dysfunction. *Trends Pharmacol. Sci.* (2019) 40:482–94. doi: 10.1016/j.tips.2019.04.013
50. Jacob F, Pather SR, Huang WK, Zhang F, Wong SZH, Zhou H, et al. Human pluripotent stem cell-derived neural cells and brain organoids reveal SARS-CoV-2 neurotropism predominates in choroid plexus epithelium. *Cell Stem Cell.* (2020) 27:937–50.e9. doi: 10.1016/j.stem.2020.09.016
51. Pellegrini L, Albecka A, Mallery DL, Kellner MJ, Paul D, Carter AP, et al. SARS-CoV-2 infects the brain choroid plexus and disrupts the blood-CSF barrier in human brain organoids. *Cell Stem Cell.* (2020) 27:951–61.e5. doi: 10.1016/j.stem.2020.10.001
52. Grun D, van Oudenaarden A. Design and analysis of single-cell sequencing experiments. *Cell.* (2015) 163:799–810. doi: 10.1016/j.cell.2015.10.039
53. Leech R, Sharp DJ. The role of the posterior cingulate cortex in cognition and disease. *Brain.* (2014) 137(Pt 1):12–32. doi: 10.1093/brain/awt162
54. Cardin JA. Inhibitory interneurons regulate temporal precision and correlations in cortical circuits. *Trends Neurosci.* (2018) 41:689–700. doi: 10.1016/j.tins.2018.07.015
55. Daneman R, Zhou L, Kebede AA, Barres BA. Pericytes are required for blood-brain barrier integrity during embryogenesis. *Nature.* (2010) 468:562–6. doi: 10.1038/nature09513
56. Sweeney MD, Ayyadurai S, Zlokovic BV. Pericytes of the neurovascular unit: key functions and signaling pathways. *Nat. Neurosci.* (2016) 19:771–83. doi: 10.1038/nn.4288
57. Khosravani H, Rajendram P, Notario L, Chapman MG, Menon BK. Protected code stroke: hyperacute stroke management during the coronavirus disease 2019 (COVID-19) pandemic. *Stroke.* (2020) 51:e156–7. doi: 10.1161/STROKEAHA.120.030243

Conflict of Interest: The authors declare that the research was conducted in the absence of any commercial or financial relationships that could be construed as a potential conflict of interest.

Advantages of publishing in Frontiers

OPEN ACCESS
Articles are free to read for greatest visibility and readership

FAST PUBLICATION
Around 90 days from submission to decision

HIGH QUALITY PEER-REVIEW
Rigorous, collaborative, and constructive peer-review

TRANSPARENT PEER-REVIEW
Editors and reviewers acknowledged by name on published articles

Frontiers
Avenue du Tribunal-Fédéral 34
1005 Lausanne | Switzerland

Visit us: www.frontiersin.org
Contact us: frontiersin.org/about/contact

REPRODUCIBILITY OF RESEARCH
Support open data and methods to enhance research reproducibility

DIGITAL PUBLISHING
Articles designed for optimal readership across devices

FOLLOW US
@frontiersin

IMPACT METRICS
Advanced article metrics track visibility across digital media

EXTENSIVE PROMOTION
Marketing and promotion of impactful research

LOOP RESEARCH NETWORK
Our network increases your article's readership